NUCLEAR MAGNETIC RESONANCE STUDIES OF BIOLOGICAL AND BIOGEOCHEMICAL PROCESSES

by

Sarah Jane Vogt

A dissertation submitted in partial fulfillment
of the requirements for the degree

of

Doctor of Philosophy

in

Engineering

MONTANA STATE UNIVERSITY
Bozeman, Montana

January 2013

APPROVAL

of a dissertation submitted by

Sarah Jane Vogt

This dissertation has been read by each member of the dissertation committee and has been found to be satisfactory regarding content, English usage, format, citation, bibliographic style, and consistency, and is ready for submission to The Graduate School.

Dr. Joseph D. Seymour (Co-chair)

Dr. Sarah L. Codd (Co-chair)

Approved for the Department of Chemical and Biological Engineering

Dr. Jeffrey Heys

Approved for The Graduate School

Dr. Ronald W. Larsen

STATEMENT OF PERMISSION TO USE

In presenting this dissertation in partial fulfillment of the requirements for a doctoral degree at Montana State University, I agree that the Library shall make it available to borrowers under rules of the Library. I further agree that copying of this dissertation is allowable only for scholarly purposes, consistent with "fair use" as prescribed in the U.S. Copyright Law. Requests for extensive copying or reproduction of this dissertation should be referred to ProQuest information and Learning, 300 North Zeeb Road, Ann Arbor, Michigan 48106, to whom I have granted "the exclusive right to reproduce and distribute my dissertation in and from microform along with the non-exclusive right to reproduce and distribute my abstract in any format in whole or in part."

Sarah Jane Vogt

January 2013

TABLE OF CONTENTS

TABLE OF CONTENTS – CONTINUED

TABLE OF CONTENTS – CONTINUED

TABLE OF CONTENTS – CONTINUED

LIST OF FIGURES

LIST OF FIGURES – CONTINUED

LIST OF FIGURES – CONTINUED

LIST OF FIGURES – CONTINUED

LIST OF TABLES

ABSTRACT

The research presented uses nuclear magnetic resonance (NMR) experimental techniques to study systems of geochemical and biological processes. This thesis first presents an introduction to the NMR experimental concepts and data analysis. Several experimental systems are then described in detail: biological reduction of uranium; biofilm growth in porous media; and solutions and gels of alginate, a polymer molecule commonly found in the biofilm polymeric matrix.

Bioremediation of heavy metal contaminants such as uranium around nuclear waste storage sites is an important environmental problem. Uranyl (UO_2^{2+}) is soluble in water, while uraninite (UO_2) precipitates as nanoparticles. Certain types of bacteria are able to use uranium as the electron acceptor and reduce uranyl ions to uraninite. The experiments presented used a solution of uranyl ions that was reduced by a sulfur reducing bacteria and were studied using images and relaxation measurements.

The growth of biofilms in the subsurface may also be used for bioremediation. Biofilms form when bacteria attach to surfaces and then produce and live within a polymeric matrix known as the extracellular polymeric substance (EPS). Experiments were done on a biofilm grown through the pore structure of a model bead pack. During the biofilm growth, displacement-relaxation correlation experiments were performed which were able to separate the biofilm phase from the bulk fluid phase using relaxation information. The results presented show that during biofilm growth very little convective flow occurs through the biofilm phase, while pore clogging causes channeling that increases the flow through non-biofilm filled pores and increases hydrodynamic dispersion.

The EPS matrix of a biofilm contains DNA, proteins, and biologically produced polymers. Some biofilms such as those produced by the bacteria *Pseudomonas aeruginosa* contain the polymer alginate. Three biologically produced alginates were compared: alginate produced by algae, alginate produced by *P. aeruginosa* FRD1153, and alginate produced by *P. aeruginosa* FRD1. A diffusive reaction gelation process was used to produce heterogeneous gels which were analyzed both during and after gelation. Homogeneous gels and solutions were studied using relaxation dispersion techniques. Differences in hydrogen exchange processes, polymer conformation, and gel structure were analyzed.

INTRODUCTION

The research presented in this thesis is an exploration of the use of nuclear magnetic resonance (NMR) experimental techniques to study a variety of systems applicable to the fields of biological engineering, chemical engineering, geosciences, and mathematical modeling [1-11]. A wide array of NMR experiments that enable non-invasive analysis of opaque and heterogeneous samples both static and dynamic were performed for this thesis research including relaxation experiments, magnetic resonance imaging, and dynamic measurements. NMR relaxation measurements are sensitive to a range of sample effects such as the surface to volume ratio and have been used for years as a tool to study heterogeneous samples. In recent years, multi-dimensional correlation experiments have seen increased use as computing power has increased that allows data analysis on personal computers. Magnetic resonance imaging (MRI) is a powerful tool that is used extensively in medicine. MRI is used in this thesis to study the pore structure of porous media such as rocks and bead packs, a system of uranium nanoparticles, and biopolymer gels. Dynamic measurements of diffusion and fluid flow using NMR techniques are used to study systems of fluid flow through porous media and diffusion of colloidal particles in gels.

This thesis first presents an introduction to the experimental concepts and data analysis of magnetic relaxation measurements, multi-dimensional correlation experiments, magnetic resonance images, and dynamic measurements. The basics of magnetic resonance phenomenon including the quantum mechanics that underlie the technique, classical mechanics concepts, and basic pulse sequences are first presented in

Chapter 2. The data analysis of magnetic relaxation measurements and multi-dimensional correlation experiments requires the use of the inverse Laplace transform, the basic concepts of which are presented in Chapter 3. More advanced concepts of magnetic resonance experiments such as relaxation mechanisms, dynamic measurements, and velocity images are explored in Chapter 4.

The experiments performed for this thesis research are presented in Chapters 5-9. The results of the author's work for several large collaborative projects are presented in Chapter 5. Experiments that included magnetic resonance images and two dimensional relaxation correlations were performed on both limestone and sandstone rocks before and after a solution of supercritical CO_2 was pumped through the pore structure of the rocks. The limestone was shown to dissolve along preferential flow pathways, while the pore structure of the sandstone did not change. A manuscript containing this data is being prepared for submission to *Geophysical Research Letters* [9]. In a separate but related project, a biofilm was grown throughout the pore structure of a sandstone and two dimensional relaxation measurements were performed. The biofilm growth was not able to be detected using high field relaxation correlations. This work was published in the journal *Organic Geochemistry* [1]. High resolution velocity images were obtained for a system of fluid flow through a model porous medium. The images were then compared with computational fluid dynamics simulations done by collaborators, and the results are shown to compare very well spatially. This work was submitted for publication in the journal *Advances in Water Resources* [8].

Several experimental systems are then described in detail in Chapter 6-9: biological reduction of uranium; biofilm growth in porous media; and solutions and gels of alginate, a polymer molecule commonly found in the biofilm polymeric matrix. Chapter 6 presents the use of magnetic resonance to study a system of biological reduction of uranium. Bioremediation of heavy metal contaminants such as uranium around nuclear waste storage sites is an important environmental problem. Uranyl (UO_2^{2+}) is soluble in water, while uraninite (UO_2) precipitates as nanoparticles. Precipitation of uranium may be able to reduce contaminant transport through the subsurface. Certain types of bacteria are able to use uranium as the electron acceptor and reduce uranyl ions to uraninite. The experiments presented used a solution of uranyl ions that was reduced by a sulfur reducing bacteria and studied using images and relaxation measurements to show the potential use of NMR as a tool to study these biological reactions. This work was published in the journal *Biotechnology and Bioengineering* [2].

Chapter 7 presents the use of displacement-relaxation correlation experiments to study a system of a biofilm growing within a porous medium. The growth of biofilms in the subsurface is another tactic that may be used for bioremediation. Biofilms form when bacteria attach to surfaces and then produce and live within a polymeric matrix known as the extracellular polymer substance (EPS). The fluid dynamics and nutrient transport during biofilm growth in porous media is an important area of study. Experiments were done on a biofilm grown through the pore structure of a model bead pack. During the biofilm growth, displacement-relaxation correlation experiments were performed. These experiments were able to separate the biofilm phase from the bulk fluid phase using

relaxation information. The results presented show that during biofilm growth very little convective flow occurs through the biofilm phase, while pore clogging causes channeling that increases the flow through non-biofilm filled pores and increases hydrodynamic dispersion. This work will also be published in the journal *Biotechnology and Bioengineering* [6].

The EPS matrix of a biofilm contains DNA, proteins, and biologically produced polymers. Some biofilms such as those produced by the bacteria *Pseudomonas aeruginosa* contain the polymer alginate. To study this constituent of the EPS, experiments were performed on alginate solutions and gels. Three biologically produced alginates were compared: alginate produced by algae, alginate produced by *P. aeruginosa* FRD1153, and alginate produced by *P. aeruginosa* FRD1. The differences between these alginates were studied using relaxation techniques and images. Chapter 8 is a study of heterogeneous gelation of the biopolymer alginate. A diffusive reaction gelation process was used to produce heterogeneous gels which were analyzed both during and after gelation using images and relaxation and diffusion-relaxation correlation experiments. Significant differences were shown between the gel structures produced by the three different alginates. This work was published in the *Journal of Biotechnology* [3]. Chapter 9 is a study of homogeneous gelation of alginate. Homogeneous gels and solutions were studied using relaxation dispersion techniques. Differences in hydrogen exchange processes, polymer conformation, and gel structure were analyzed. This research is ongoing and is being conducted in collaboration with current undergraduate students and will result in future publications.

INTRODUCTION TO NUCLEAR MAGNETIC RESONANCE

The phenomenon of nuclear magnetic resonance (NMR) was first observed in 1945 by Purcell, Torrey, and Pound [12] at Harvard University and Bloch, Hansen, and Packard [13] at Stanford University. The observation of NMR and the physics behind it was an important breakthrough for the validation of some of the concepts of quantum mechanics. The experimental use of this phenomenon has been widely developed in the past 75 years and applied in the fields of medicine, chemistry, and fluid dynamics, in addition to physics, due to the ability to non-invasively study the molecular dynamics of macroscopic samples. This chapter will explain the basic concepts behind the use of NMR, while the next chapter will expand upon these ideas and describe more advanced experiments and data analysis. This introduction will cite original references, but essentially obtains most information from [14] and [15].

Theory of Nuclear Magnetic Resonance: Quantum Mechanics

Nuclear magnetic resonance utilizes the quantum mechanical property of the spin angular momentum of a single nucleus and its response to a magnetic field to study molecular ensemble properties of macroscopic systems containing a large number of nuclei. Since most experiments do not detect single molecules, the experiments discussed in this thesis can mostly be understood using classical physical concepts describing molecular ensemble properties, but some quantum mechanics background is necessary to understand the fundamental phenomena of NMR.

Spin Angular Momentum

Each nuclear isotope has a fundamental property called the spin quantum number *I*, which is a half integer or integer value that depends on the number of protons and neutrons in the nucleus. This quantum number refers to a type of angular momentum that is an intrinsic property, and does not imply that the nucleus is physically rotating or spinning. However, the nucleus does behave mathematically and physically as if it is spinning, so the term "spin angular momentum" is universally used in the literature. The quantum number *I* defines the number of discrete values of the spin angular momentum quantum number *m* that are possible for each nucleus:

$$m = -I, (-I+1), ...(I-1), I \qquad (2.1)$$

For example, for the most abundant isotope of hydrogen ^{1}H, $I = \frac{1}{2}$ and $m = -\frac{1}{2}$ or $m = +\frac{1}{2}$ and two discrete angular momentum values are possible. Hydrogen is the most commonly used nucleus in NMR for a number of reasons that are discussed later, and will be used as the main example. However, a large number of nuclei have $I \neq 0$ and can be studied using NMR experiments.

The angular momentum associated with the spin angular momentum quantum number *m* is represented by a vector, since angular momentum always has a direction associated with it. The fundamental idea of quantum mechanical measurements is that at any time each nucleus is not in one state or another (referred to here as $\vec{m}$), but that each nuclei has some probability a_m that it is in each of the states $\vec{m}$. This leads to the

arbitrary spin state of a nucleus $|\Psi\rangle$ being described by the linear combination of all the values for $\vec{m}$:

$$|\Psi\rangle = \sum_m a_m |\vec{m} \qquad (2.2)$$

However, the act of measuring the molecule's spin state causes it to only exist in one of the discrete states. In the following discussion, the deterministic angular momentum vector will be referred to as $\vec{m}$ while the quantum mechanical spin state will be referred to as $|\Psi\rangle$. The directionality of the angular momentum vector leads to the terms "spin-up" and "spin-down" that represent the two spin states *m* of a $I = \frac{1}{2}$ nucleus. The Schrodinger equation describes the time dependence of the spin state:

$$i\hbar \frac{\partial}{\partial t} |\Psi(t)\rangle = H(t) |\Psi(t)\rangle \qquad (2.3)$$

where $H(t)$ is the Hamiltonian energy operator (which has units of energy) and $\hbar$ is Planck's constant (which has units of energy multiplied by time). For example, if the Hamiltonian is constant with time, such as in the description of a stationary system, this equation is straight-forward to solve:

$$|\Psi(t)\rangle = \exp\left(\frac{-iHt}{\hbar}\right) |\Psi(t)\rangle \qquad (2.4)$$

$$U(t) = \exp\left(\frac{-iHt}{\hbar}\right) \qquad (2.5)$$

where *U(t)* is known as the evolution operator.

Spin Magnetism

In order to find a useful expression for the Hamiltonian energy operator *H*, the nucleus is regarded as a magnetic dipole moment. A magnetic dipole moment exists because the moving electrical charges associated with the electron and proton will interact and produce a magnetic field according to Maxwell's equations relating electricity and magnetism. The magnetic dipole moment $\vec{\mu}$ is proportional to the angular momentum $\hbar\vec{m}$ of the nucleus with the constant of proportionality γ, known as the gyromagnetic ratio, i.e.:

$$\vec{\mu} = \gamma\hbar\vec{m} \qquad (2.6)$$

The gyromagnetic ratio has units of Hz/T or rad/s/T, and is different for every nucleus. The hydrogen proton ^1H has one of the highest values for γ (42.58 MHz/T) and, along with its nearly 100% natural isotopic abundance, helps to explain its common use in NMR experiments.

In a magnetic field $\vec{B}$, these dipole moments will align along the axis of the magnetic field, with the energy needed for this realignment represented by $H = -\vec{\mu}\cdot\vec{B}$. Combining this expression with equation 2.6, the Hamiltonian energy operator for a nucleus in a magnetic field oriented along the *z*-axis ($\vec{B} = B_0\vec{k}$ and $\vec{m} = m\vec{k}$) is:

$$H = -\gamma\hbar B_0 m \quad (2.7)$$

This is known as the Zeeman interaction energy, and is the dominant energy exchange mechanism utilized in NMR experiments. The difference between energy levels of spin states is discrete and is equal to $\gamma\hbar B_0$, since *m* varies only by integer values. The spin

state for $m = \frac{1}{2}$ ("spin-up") has a lower energy than $m = -\frac{1}{2}$ ("spin-down"), as shown in Figure 2.1. Applying energy to the system will cause spins to "flip" from spin-down to spin-up, which disturbs the system from equilibrium. The system will then exchange energy with the environment and return to equilibrium as the spins return to the lower energy state.

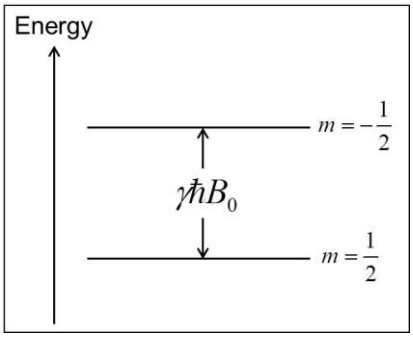

Figure 2.1. Schematic of Zeeman interaction energy for a nucleus with $I = \frac{1}{2}$. $m = \frac{1}{2}$ corresponds to a spin that is aligned with the magnetic field and is the lower energy state.

The evolution operator for the Zeeman interaction found by combining Equations 2.5 and 2.7 is:

$$U(t) = \exp(i\gamma B_0 m t) \qquad (2.8)$$

This function is an example of a rotation operator, with the form:

$$R_z(\phi) = \exp(i\phi m) \qquad (2.9)$$

where $\phi = \gamma B_0 t$ represents the angle of the rotation about the *z*-axis. Therefore, in a

homogeneous, constant magnetic field $B_0\vec{k}$, all of the nuclear spins will rotate, or precess, about the z-axis at a constant frequency known as the Larmor frequency:

$$\omega_0 = \gamma B_0 \qquad (2.10)$$

The precession of the nuclei and the Larmor frequency are very important concepts in understanding NMR and its practical use. The "resonance" in NMR refers to the fact that the application of a small amount of energy at the Larmor frequency will cause a large effect to the magnetization of the sample. A good analogy to think of this effect is a parent pushing a child on a swing. By giving a small push every time the child swings back to the parent (i.e. applying energy at the same frequency) the child will continue to swing until the parent stops pushing.

This discussion of quantum mechanics is the underlying theory of the nuclear magnetic resonance phenomenon, but so far only applies to a single nucleus. No process of measurement can observe just one nucleus, however, so practical measurements will be on the behavior of a large ensemble of nuclei. A discussion of the observation of spin states is beyond the scope of this thesis, but the measurement of an ensemble of spin states is shown by:

$$\left\langle \Psi \middle| I_z \middle| \Psi \right\rangle = \frac{1}{2}\left(\overline{\left|a_{1/2}\right|^2} - \overline{\left|a_{-1/2}\right|^2} \right) \qquad (2.11)$$

where $\left|a_{1/2}\right|$ is the probability of a molecule being in the spin-up state and $\left|a_{-1/2}\right|$ is the probability of a molecule being in the spin-down state. The observation is related to the overall energy of the ensemble since it is the difference in the populations of the spins in

the higher and lower energy states. This energy difference leads to a magnetization of the sample at equilibrium that is utilized and manipulated during NMR experiments. At thermal equilibrium, the high and low energy populations can be calculated by Boltzmann's distribution:

$$\overline{\left|a_{\pm 1/2}\right|^2} = \frac{\exp\left(\pm\frac{\hbar\gamma B_0}{2k_B T}\right)}{\exp\left(-\frac{\hbar\gamma B_0}{2k_B T}\right)+\exp\left(+\frac{\hbar\gamma B_0}{2k_B T}\right)} \qquad (2.12)$$

At room temperature, $k_B T >> \hbar\gamma B_0$, and this expression reduces to:

$$\overline{\left|a_{\pm 1/2}\right|^2} = \frac{1}{2}\left(1 \pm \frac{\hbar\gamma B_0}{2k_B T}\right) \qquad (2.13)$$

Equation 2.13 is important to understand for its practical implications: by increasing γ or B_0 or by decreasing T, the energy difference between the spin populations is increased, and therefore the magnetization at equilibrium is increased (Equation 2.11). This will lead to an increase in the signal-to-noise ratio, which is an important consideration for designing NMR experiments and will be discussed more in a later section. Therefore, the study of nuclei with high γ (such as ^1H) and/or the use of high magnetic fields (such as the 7-17T superconducting magnets used in most laboratories) is common.

Theory of NMR: Classical Mechanics

Excitation

With these concepts from quantum mechanics understood but in the background, most NMR experiments can be explained using macroscopic ideas, first derived by Bloch in 1946 [13]. The bulk magnetization of the ensemble of spins can be represented by a vector $\vec{M}$. As mentioned above, at equilibrium a larger number of spins will align parallel to the magnetic field $\vec{B}_0$ (spin-up) than anti-parallel (spin-down), and $\vec{M}$ will be oriented along the axis of the field. NMR experiments proceed by disturbing this magnetization away from equilibrium, referred to as excitation, and observing how the spin interactions and energy exchange with the environment affect the magnetization as the system returns to equilibrium.

The excitation of the magnetization from equilibrium is caused by pulses of oscillating radio frequency (referred to as "r.f. pulses") administered to the sample while in the static magnetic field. The Larmor frequency (Equation 2.10) of protons in experimental magnetic fields is on the same order of magnitude as the frequency of radio electromagnetic waves (i.e. from kHz to GHz). Applying pulses with the same frequency as the Larmor frequency will result in large changes to the magnetization due to the resonance effects described earlier. These r.f. pulses create an oscillating transverse magnetic field $\vec{B}_1$ within the sample, which is much smaller in magnitude than $\vec{B}_0$. $\vec{B}_1$ can be applied for different amounts of time and in different functional forms in order to control the manipulation of $\vec{M}$.

Using ideas from classical mechanics, the evolution of the $\vec{M}$ vector during excitation can be described in detail by using the fact that the rate of change of the angular momentum, which is related to the magnetization by Equation 2.6 as $\frac{d\hbar\vec{m}}{dt} = \frac{1}{\gamma}\frac{d\vec{M}}{dt}$, is equal to the torque on the magnetization caused by the magnetic field, $\vec{M} \times \vec{B}$, leading to the expression:

$$\frac{d\vec{M}}{dt} = \gamma\vec{M} \times \vec{B} = \gamma \begin{bmatrix} i & j & k \\ M_x & M_y & M_z \\ B_1 \cos(\omega_0 t) & -B_1 \sin(\omega_0 t) & B_0 \end{bmatrix} \quad (2.14)$$

where $\vec{B}_0$ is along the *z*-axis, and $\vec{B}_1$ is in the *xy*-plane, oscillating at the Larmor frequency ω_0. This representation is derived in the "laboratory" frame of reference, but it is also convenient to define a rotating frame of reference in which to view the magnetization. In this notation, the reference frame is rotating at the Larmor frequency, so the $\vec{B}_1$ field is simply along the *x*-axis and the magnetic field seen along the *z*-axis is reduced by what is caused by off-resonant spins, i.e. those rotating at ω instead of ω_0. In this rotating frame of reference, the excitation expression becomes:

$$\frac{d\vec{M}}{dt} = \gamma\vec{M} \times \vec{B} = \gamma \begin{vmatrix} i & j & k \\ M_x & M_y & M_z \\ B_1 & 0 & B_0 - \frac{\omega}{\gamma} \end{vmatrix} \quad (2.15)$$

Or in terms of each component of $\vec{M}$:

$$\frac{dM_x}{dt} = \gamma M_y \left(B_0 - \frac{\omega}{\gamma} \right) \qquad (2.15a)$$

$$\frac{dM_y}{dt} = \gamma M_z B_1 - \gamma M_x \left(B_0 - \frac{\omega}{\gamma} \right) \qquad (2.15b)$$

$$\frac{dM_z}{dt} = -\gamma M_y B_1 \qquad (2.15c)$$

The importance of the off-resonance spins is minimized by applying a pulse with a range of frequencies, or in other words, a pulse with a large bandwidth. The turn angle θ of the pulse is determined for a pulse of duration *t* by: $\theta = \gamma \vec{B}_1 t$, with γ expressed in units of rad/s/T. For example, a $\vec{B}_1$ field applied along the *x*-axis in the rotating frame for a specified amount of time *t* may rotate the $\vec{M}$ vector from its equilibrium along the *z*-axis (caused by the static magnetic field $\vec{B}_0$) onto the *y*-axis through an angle $\theta = \frac{\pi}{2}$.

This process is known as applying a $\frac{\pi}{2}_x$ pulse, as shown in Figure 2.2.

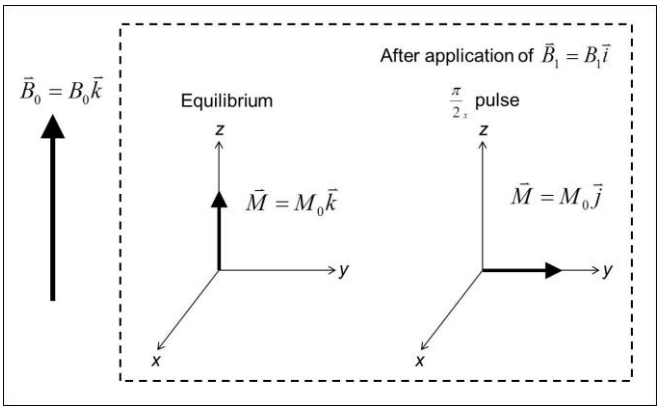

Figure 2.2. Schematic of the process of excitation by application of a r.f. pulse. The bulk magnetization vector begins aligned with the static magnetic field. After the pulse, the magnetization will be along the *y*-axis in the rotating frame of reference.

Relaxation

After the spins in the system have been excited from equilibrium, the system begins to undergo a phenomenon called relaxation. The individual spins are constantly exchanging energy with each other and the environment and the rate at which the magnetization vector $\vec{M}$ returns to equilibrium depends on this energy exchange. There are two different mechanisms for relaxation, known as spin-lattice T_1 relaxation and spin-spin T_2 relaxation. Qualitatively, the two mechanisms refer respectively to the spins returning to thermal equilibrium with the surrounding environment, or lattice, and returning to thermal equilibrium with other spins. Mathematically, the difference between the two mechanisms is explained by introducing the concept of an auto-correlation function of the molecular dipole-dipole interactions and the effect of the molecular motion on the energy exchange in the system. While this discussion concerns the motion of individual molecules, the quantum mechanical properties of the individual spins are neglected, and spins are treated as either being in the spin-up or spin-down state.

Auto-correlation Functions: In general, the auto-correlation function $G(t)$ is the probability that a function $h(t)$ is correlated to itself at another time, $h(t+t')$, and is defined by:

$$G(t) = \int_0^\infty h(t')h(t+t')dt' \qquad (2.16)$$

For an ergodic, stationary system, all starting times are the same and can be set equal to

zero and only the time difference in question is important, so the auto-correlation function can be represented by:

$$G(t) = \overline{h(t)h(0)} \qquad (2.17)$$

Equations 2.16 and 2.17 are general definitions applicable to any system or function. For a system exhibiting Brownian motion, such as the interactions between molecules of water at room temperature, the auto-correlation function decreases exponentially with a time constant τ_c [16]:

$$\tau_c = \frac{\int_0^\infty \overline{h(t)h(0)}dt}{\overline{h(0)^2}} \qquad (2.18)$$

$$G(t) = \overline{h(t)h(0)} \sim \exp\left(\frac{-t}{\tau_c}\right) \qquad (2.19)$$

For the present discussion of magnetic relaxation, the auto-correlation function $G(t)$ is the probability that the fluctuating magnetic fields *h(t)* caused by the individual dipole moments of the diffusing nuclei are correlated to each other after a time *t*. After a short amount of time *t* compared to the time scale of the fluctuation due to thermal motion τ_c, the magnetic field of the nucleus will still depend on its magnetic field at time zero. After a time longer than τ_c there will be little or no correlation with the initial state. As temperature increases, the vibrations and velocity of the nuclei increase and the time constant of the fluctuation of the magnetic fields will decrease, so the auto-correlation function will decay more quickly [14]. Similarly, in more ordered materials such as

solids, the correlation time between the fluctuations is longer and the auto-correlation function of the system takes longer to decay to zero [17].

Spectral Density Functions: The spectral density function $J(\omega)$ is the Fourier transform of the auto-correlation function and describes the frequency dependence of the magnetic field fluctuations. For this discussion of magnetic relaxation, the spectral density is useful to consider as it relates the dependence of the magnetic field fluctuations to frequency of precession more explicitly. The concept of the Fourier transform is used for many applications in NMR and will be important throughout this thesis. In this case, the Fourier transform pair of $G(t)$ and $J(\omega)$ are related by:

$$G(t) = \int_{-\infty}^{\infty} J(\omega)\exp(2\pi i\omega t)d\omega \qquad (2.20)$$

$$J(\omega) = \int_{-\infty}^{\infty} G(t)\exp(-2\pi i\omega t)dt \qquad (2.21)$$

The spectral density, in other words, describes the way that the energy of the magnetic field fluctuations depends on time and frequency of precession. These molecular fluctuations are complex, but a simple model for water is an isotropic, randomly rotating molecule. Energy will exchange between molecules due to dipole-dipole interactions, and this energy exchange will depend on the distance between the molecules R, the time constant for the molecular interactions τ_c, and the precession frequency ω of the molecules [18]. For the purposes of this discussion, the energy exchange will cause the spins to "flip", i.e. to move from the lower energy state to the

higher energy state, or $m = \frac{1}{2}$ to $m = -\frac{1}{2}$, and vice versa. In this model for molecular interactions between two spins, there are three configurations possible after a certain amount of time: no net spin flip $J^{(0)}(\omega)$, one of the spins has flipped $J^{(1)}(\omega)$, or both spins have flipped $J^{(2)}(\omega)$. For this model, the spectral density functions are derived exactly for an isotropic liquid [18]:

$$J^{(0)}(\omega) = \left(\frac{24}{15R^6}\right)\left[\frac{\tau_c}{1+\omega^2\tau_c^2}\right] \quad (2.22)$$

$$J^{(1)}(\omega) = \left(\frac{1}{6}\right)J^{(0)}(\omega) \quad (2.23)$$

$$J^{(2)}(\omega) = \left(\frac{2}{3}\right)J^{(0)}(\omega) \quad (2.24)$$

Using the three spectral density functions, the differences between the two mechanisms for magnetic relaxation can now be explained. The spin-lattice, or T_1, relaxation time at the Larmor frequency ω_0 is represented by:

$$\frac{1}{T_1} = \left(\frac{\mu_0}{4\pi}\right)^2 \gamma^4 \hbar^2 \frac{3}{2} I(I+1)\left[J^{(1)}(\omega_0) + J^{(2)}(2\omega_0)\right] \qquad (2.25)$$

Qualitatively, this means that the T_1 relaxation is only affected by the energy exchange of spins that have flipped, or changed energy states, due to the Zeeman interaction caused by the applied magnetic field which results in spin precession at frequency ω_0, as well as a contribution at a frequency of $2\omega_0$.

The spin-spin, or T_2, relaxation is represented by:

$$\frac{1}{T_2} = \left(\frac{\mu_0}{4\pi}\right)^2 \gamma^4 \hbar^2 \frac{3}{2} I(I+1)\left[\frac{1}{4} J^{(0)}(0) + \frac{5}{2} J^{(1)}(\omega_0) + \frac{1}{4} J^{(2)}(2\omega_0)\right] \qquad (2.26)$$

which qualitatively shows that T_2 relaxation also depends on a zero-frequency term which corresponds to no net spin flip. This term encompasses other energy exchange mechanisms besides the Zeeman interaction energy and causes T_2 to always be shorter than T_1.

For example, a sample of water at room temperature in a magnet operating at 300MHz has a T_1 approximately equal to T_2 because the correlation time of the molecular field fluctuations τ_c is much shorter (on the order of 10^{-13} s) than $\frac{1}{\omega_0}$ (on the order of 10^{-9} s). This system is known as being in the motional averaging regime because the rapid motion of the molecules quickly averages out the magnetic field interactions. As the precession frequency ω_0 increases or the correlation time τ_c of the magnetic field fluctuations increases, the dependence of T_2 on the zero-frequency term increases, and the two relaxation times T_1 and T_2 diverge. The effect of temperature [17] on the two relaxation times is shown schematically in Figure 2.3.

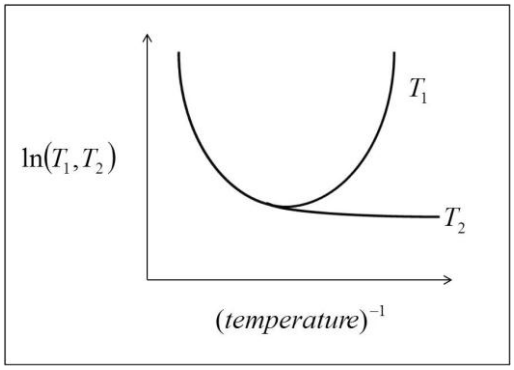

Figure 2.3. Relaxation times as a function of temperature. As the temperature decreases, the zero-frequency term in the equation for T_2 increases and the two relaxation times are no longer approximately equal as they are in the motional averaging regime.

This explanation has so far dealt with the molecular scale dynamics of relaxation, but for the discussion of practical NMR experiments we can use the concept of the bulk magnetization vector $\vec{M}$ to describe the relaxation of the sample magnetization. The following equations apply to spins in the motional averaging regime such as those in a liquid. More complicated relaxation effects will be discussed in the next chapter of this thesis.

The spin-lattice or T_1 relaxation mechanism acts only along the axis of the static magnetic field z since it is only caused by the Zeeman interaction, and is described by:

$$\frac{dM_z}{dt} = \frac{-(M_z - M_0)}{T_1} \quad (2.27)$$

where M_0 is the equilibrium magnetization of the sample. This equation is solved to show:

$$M_z(t) = M_z(0)\exp\left(\frac{-t}{T_1}\right) + M_0\left[1 - \exp\left(\frac{-t}{T_1}\right)\right] \quad (2.28)$$

If $M_z(0)$ is equal to $-M_0$, as immediately following a π r.f. pulse, this equation reduces to:

$$M_z(t) = M_0\left|1 - 2\exp\left(\frac{-t}{T_1}\right)\right| \quad (2.29)$$

These equations show that when $t = T_1(\ln 2)$, the magnetization along the *z*-axis will equal zero. Determination of the T_1 time using this concept is called an inversion recovery experiment and will be discussed later in this chapter.

Spin-spin or T_2 relaxation occurs only in the transverse plane, and is described by the following equations, in both the *x* and *y* directions:

$$\frac{dM_{x,y}}{dt} = \frac{-M_{x,y}}{T_2} \quad (2.30)$$

Equation 2.30 is solved for a homogeneous sample to give:

$$M_{x,y}(t) = M_{x,y}(0)\exp\left(\frac{-t}{T_2}\right) \quad (2.31)$$

By adding these relaxation terms to the excitation equations discussed earlier, we obtain what are called the Bloch equations, which describe the evolution of the magnetization vectors in the rotating frame during the excitation pulse:

$$\frac{dM_x}{dt} = \gamma M_y\left(B_0 - \frac{\omega}{\gamma}\right) - \frac{M_x}{T_2} \quad (2.32a)$$

$$\frac{dM_y}{dt} = \gamma M_z B_1 - \gamma M_x\left(B_0 - \frac{\omega}{\gamma}\right) - \frac{M_y}{T_2} \quad (2.32b)$$

$$\frac{dM_z}{dt} = -\gamma M_y B_1 - \frac{M_z - M_0}{T_1} \quad (2.32c)$$

The Bloch equations are a powerful phenomenological way to examine and understand NMR phenomena and will be expanded upon again in the next chapter of this thesis.

Experimental Background

Experimental Equipment

The equipment needed to perform NMR experiments include the magnet to supply a static magnetic field, a spectrometer to deliver r.f. pulses, and a computer to control the spectrometer. The sample is surrounded by a r.f. coil that administers the r.f. pulses to the sample as homogeneously as possible and also acts as the receiver coil. A "bird-cage" coil is widely used because of the ease in loading the sample into the magnet, but a solenoid coil is the most efficient configuration [14]. The optimization of all of this equipment has been an essential part of NMR experimental development, but will not be a major point of discussion in this thesis and readers are referred to references [17] and [14]

for more information.

Signal Detection

The signal that is detected in an NMR experiment is the voltage produced by the oscillating magnetization in the transverse plane. For example, after applying a $\frac{\pi}{2}$ r.f. pulse to a system with equilibrium magnetization M_0 and Larmor frequency ω_0, the magnetization is described by:

$$\vec{M}(t) = \left[M_0 \cos(\omega_0 t)\vec{i} + M_0 \sin(\omega_0 t)\vec{j}\right]\exp\left(\frac{-t}{T_2}\right) \qquad (2.33)$$

By converting this to exponential notation using Euler's formula, the component of the magnetization in the *x*-direction is described by the real component and in the *y*-direction by the imaginary component. We define the complex magnetization $M^+(t)$ as:

$$M^+(t) = M_0 \exp(i\omega_0 t)\exp\left(\frac{-t}{T_2}\right) \qquad (2.34)$$

In order to detect both the *x* and *y* components of the magnetization, a process called heterodyning is used. The voltage from the sample is mixed with two different reference voltages 90 degrees out of phase with each other, which allows the detection of both the M_x and M_y components. The voltage signal $S(t)$ is then:

$$S(t) = S_0 \exp(i\phi)\exp(i\Delta\omega t)\exp\left(\frac{-t}{T_2}\right) \quad (2.35)$$

where ϕ is the phase of the receiver and $\Delta\omega = \omega_0 - \omega_r$ with ω_r as the reference frequency. This results in an oscillating and decaying voltage signal which is called the Free Induction Decay, or FID, shown in Figure 2.4.

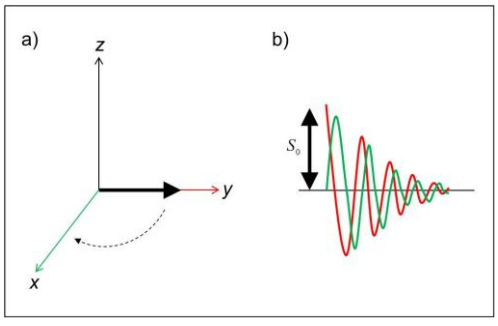

Figure 2.4. a) $\vec{M}$ immediately after a $\frac{\pi}{2}_x$ pulse. The magnetization starts along the *y*-axis and will precess around the *z*-axis as shown. b) Schematic of the Free Induction Decay (FID). The red line is the voltage received along the *y*-axis and the green line is the voltage received along the *x*-axis. The signal oscillates due to $\vec{M}$ precession around the *z*-axis relative to the static detection axis and decays due to the T_2 relaxation process.

This oscillating signal is often Fourier transformed and expressed in terms of frequency using the following relations:

$$F[S(t)] = \int_{-\infty}^{\infty} S(t)\exp(-2\pi i\omega\tau)d\tau \qquad (2.36)$$

$$S(t) = \int_{-\infty}^{\infty} F[S(t)]\exp(2\pi i\omega\tau)d\tau \qquad (2.37)$$

The Fourier transform of a time signal that has an exponential relaxation and one frequency component results in a spectrum $F[S(t)]$ which has a Lorentzian line shape centered on the single frequency value and a Full-Width-Half-Maximum (FWHM) of $\frac{1}{\pi T_2}$. This single pulse experiment to obtain a spectrum is the common result of experiments used in chemistry applications to differentiate hydrogen atoms in different magnetic environments and therefore give information on molecular structure [15]. This type of experiment will be discussed in relation only to specific experiments in a later chapter.

NMR is a low sensitivity technique due to the small difference between populations of spin-up and spin-down nuclei, so an important consideration is the signal-to-noise ratio, or SNR. Many different components in the NMR apparatus and the environment contribute to the noise in an experiment. However, signals from multiple experiments can be added and averaged so that signal adds coherently while noise adds randomly. The SNR improvement by averaging *N* experiments is:

$$\frac{signal}{noise} \equiv SNR \equiv \frac{N}{\sqrt{N}} = \sqrt{N} \qquad (2.38)$$

In addition to signal averaging, the SNR can also be improved by increasing signal and/or decreasing noise. There are many techniques that are applicable, including applying a smoothing function to filter out the noise and optimizing the experimental apparatus to maximize the signal [14].

Basics of Pulse Sequences

Formation of Echoes: With the concepts of r.f. pulses and signal detection understood, the next level of complexity is to consider multiple pulse experiments, or pulse sequences. A common phenomena utilized in many pulse sequences is an "echo". After exciting the spins in a sample with a $\frac{\pi}{2}$ r.f. pulse, inhomogeneity in the magnetic field, either in the B_0 field or within the sample itself, will cause spins in different spatial positions to precess at different Larmor frequencies. The detected signal is from a large number of spins precessing coherently, so when spins are precessing at different frequencies the signal from the bulk magnetization detected along a fixed axis will be smaller, and the signal is said to dephase. If the spins dephase for a time τ after the $\frac{\pi}{2}$ pulse, applying a π r.f. pulse will invert the magnetization within the transverse plane and reverse the sense of precession of the spins so that a "spin echo" will form when the spins reach coherence again at time 2τ, as shown in Figure 2.5. The amplitude of this echo will still be attenuated by T_2 relaxation because this dephasing is caused by stochastic molecular interactions and cannot be refocused. However, dephasing caused by inhomogeneities in the magnetic field or other fluctuations will be refocused by the spin

echo. The use of spin echoes allows the equilibrium magnetization of the sample to be manipulated and re-used until full T_2 relaxation has occurred and all phase coherence is lost.

A good analogy for thinking about this phenomenon is to think of the spins as runners on a track, who start running in the same direction but at different speeds at the time of the $\frac{\pi}{2}$ pulse [19]. At some point (the π pulse at time τ) the runners are told to turn around, but still run at the same speed. At time 2τ, all of the runners will return to the starting line.

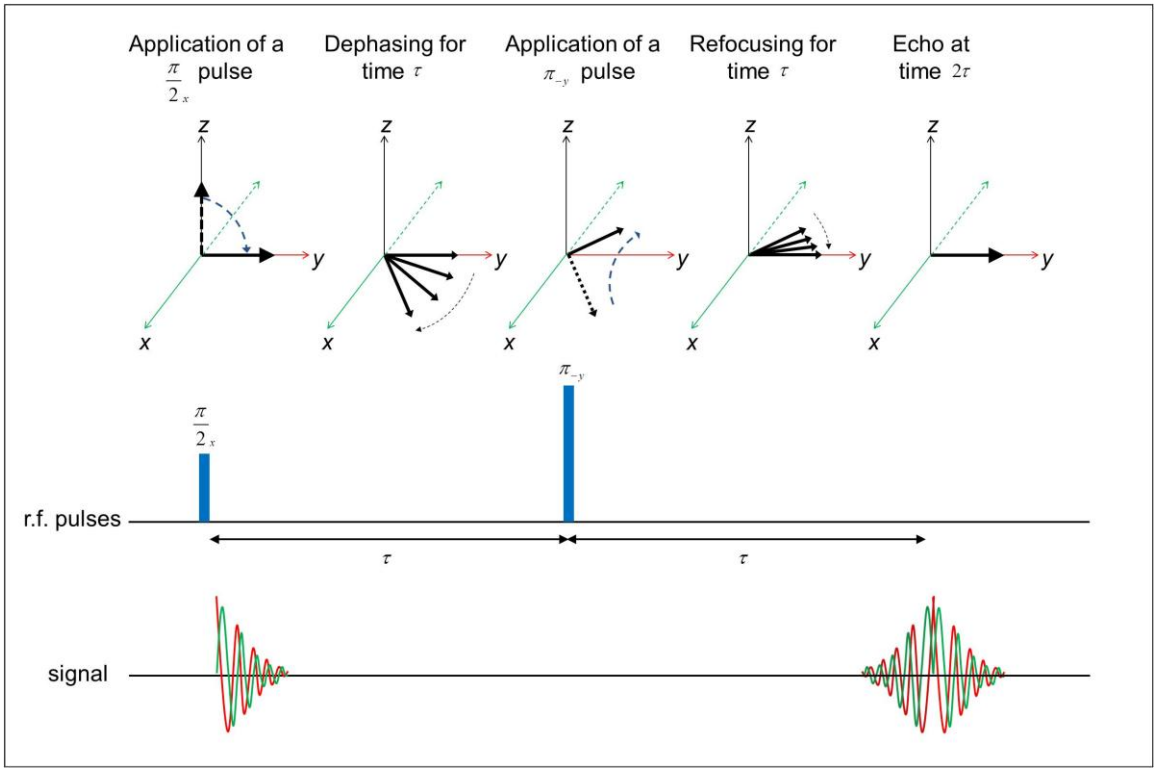

Figure 2.5. Schematic of the spin echo pulse sequence. The first row of images is a depiction of the effects of the r.f. pulses on the magnetization vector. The middle row is the r.f. pulse sequence. The last row is the signal that would be received. There will be a FID after the first r.f. pulse and a spin echo occurring at 2τ.

Another useful technique to form echoes is a pulse sequence called a stimulated echo. In this sequence, instead of using a $\frac{\pi}{2}$ pulse followed by a π pulse to refocus the spins, three $\frac{\pi}{2}$ pulses are used. The first $\frac{\pi}{2}$ pulse excites the magnetization into the transverse plane in both sequences. In the stimulated echo sequence, the second $\frac{\pi}{2}$ pulse returns the magnetization to the *z*-axis, and the third re-excites the magnetization back into the transverse plane. This sequence is useful in samples where the T_2 time is very short but the T_1 time is long, because the signal is "stored" along the *z*-axis where it experiences only T_1 relaxation, as shown in Figure 2.6. The FID after the second pulse is due to magnetization which has relaxed by T_1 relaxation during τ_1 and is re-excited, in addition to signal from spins excited by the second pulse but not the first pulse as discussed in the next section.

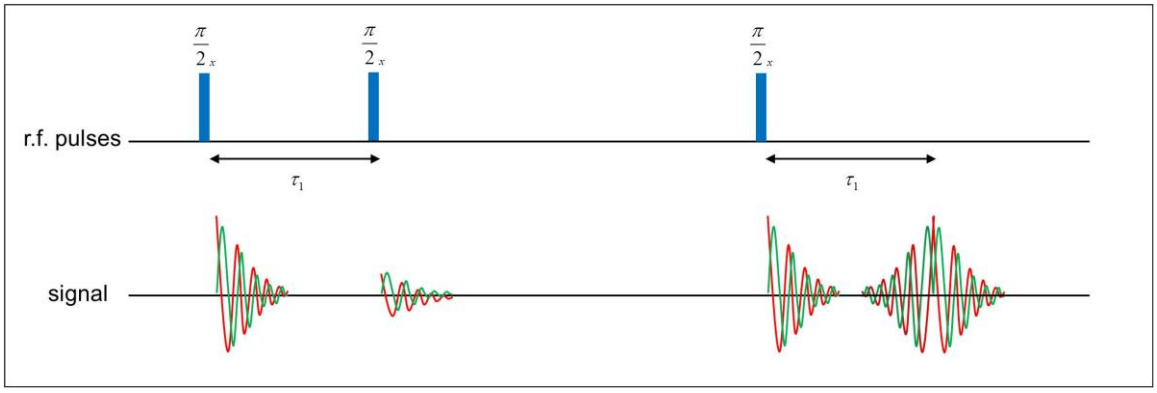

Figure 2.6. Stimulated echo pulse sequence. The signal shown after each pulse is shown to illustrate the need for phase cycling, as explained in the next section. The echo will occur at a time of $2\tau_1$ plus the time between the second and third pulses, which is the amount of time that the magnetization is stored along the *z*-axis.

Phase Cycling: An important consideration in multiple pulse experiments is the concept of phase cycling. The basic idea is that because of the quantum mechanical properties of spins, some spins will experience each r.f. pulse but other spins will not. For example in the stimulated echo sequence, spins that do not experience the first $\frac{\pi}{2}$ pulse but do experience the second will produce a FID during the storage time, as shown in Figure 2.6. By extension, spins that do not experience either of the first two pulses but do experience the third will produce a FID during the echo from signal that has experienced all three pulses. However, the experiment is optimal when only spins which have experienced all three pulses are detected.

To avoid this problem, the phase of the pulses and the detector are chosen and cycled through during multiple experiments so that the desired echoes add together, while the undesired signals are cancelled out. For example, one stimulated echo experiment may use three $\frac{\pi}{2}_{x}$ pulses, resulting in the desired spin echo formed along the –*y*-direction as well as a FID formed in the *y*-direction after each pulse. The next experiment may use two $\frac{\pi}{2}_{-x}$ pulses and a $\frac{\pi}{2}_{x}$ pulse, again resulting in a spin echo along the –*y*-direction but with the FIDs after the first two pulses now along the –*y*-direction. By cycling through the different phases for the pulses and the receiver, the desired signal can be added while the undesired signal can be subtracted. The addition of the signals from multiple experiments also increases the SNR, and the two effects can be addressed at the same time. This process is called signal averaging, and is done in nearly every NMR experiment.

Introduction to Relaxation Measurements: The determination of the T_1 time of a sample is usually done by performing an inversion recovery experiment, shown in Figure 2.7.a. The π pulse moves the magnetization to the –*z*-axis and the $\frac{\pi}{2}$ pulse excites this magnetization into the *xy*-plane for detection. By recording the amount of signal as a function of t_1, the minimum amount of signal will be related to the T_1 time by $t_{1,\min} = T_1(\ln 2)$, as mentioned earlier.

An experimental use of spin echoes is to measure the T_2 time of the sample using a pulse sequence developed by Carr, Purcell, Meiboom and Gill [20], often referred to as the CPMG sequence. This sequence uses a long series of equally spaced π pulses to produce a series of spin echoes (see Figure 2.7.b). The amplitudes of the echoes can be plotted and used to find the T_2 time of the sample using the following relation (see also Equation 2.31):

$$M_y(2\tau) = M_0 \exp\left(\frac{-2\tau}{T_2}\right) \qquad (2.39)$$

Relaxation measurements are a powerful way to examine complicated samples. These applications will be discussed more thoroughly in the next chapter and applied throughout the experiments described in later chapters.

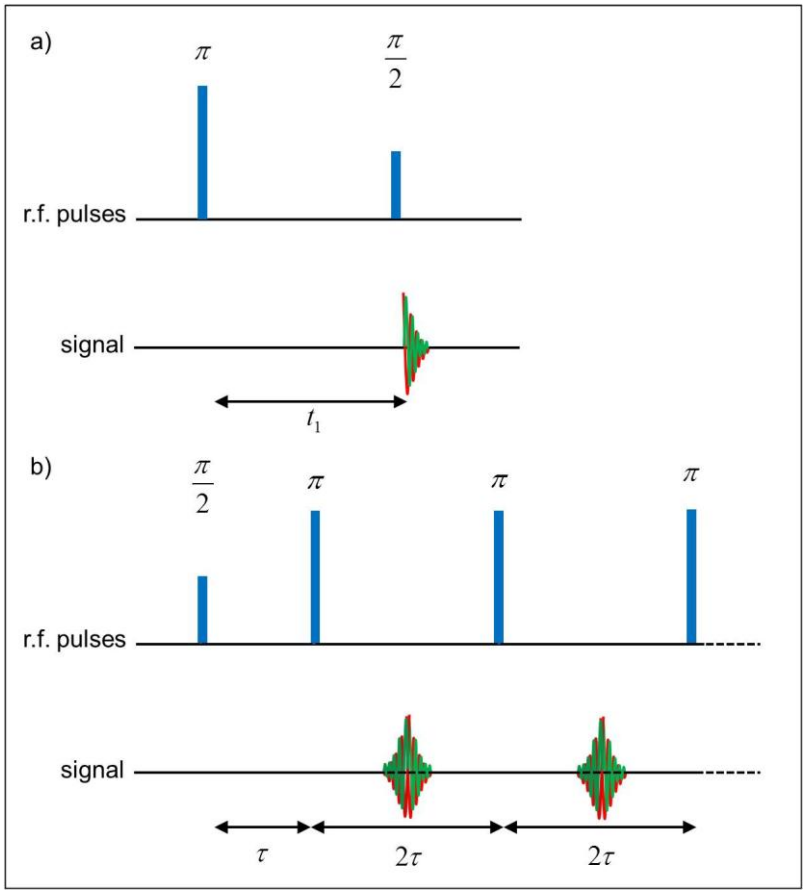

Figure 2.7. a) Inversion recovery pulse sequence, used to determine T_1. The first pulse inverts the equilibrium magnetization which is then excited into the transverse plane for detection after a variable amount of time t_1. b) CPMG pulse sequence, used to determine T_2. The series of echoes may contain thousands of pulses and last several seconds in some cases.

Introduction to Magnetic Resonance Imaging: As mentioned in the discussion of spin echoes, any inhomogeneity in the magnetic field causes the spins to precess at different Larmor frequencies. This phenomenon is utilized and manipulated by linearly varying the magnetic field with respect to position, or applying a gradient in the magnetic field $G(\vec{r})$, as shown in Figure 2.8. This gradient adds to the static B_0 field, but is much

smaller in magnitude; for example, most of the experiments in this thesis were done with a B_0 of 7 T and an available maximum gradient of 1.482T/m.

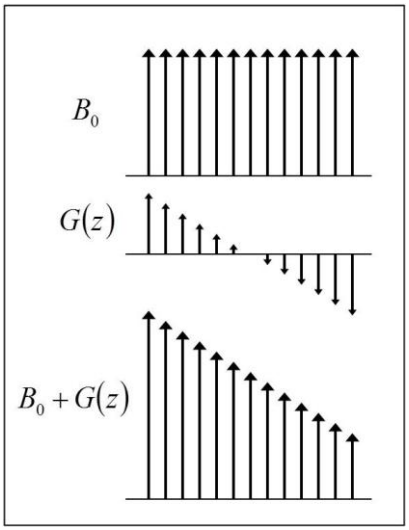

Figure 2.8. Schematic of the application of a magnetic field gradient in the same direction as the static magnetic field B_0.

By applying this gradient to the sample, the spins are encoded based on position:

$$\omega(\vec{r}) = \gamma B_0 + \gamma G(\vec{r}) \cdot \vec{r} \quad (2.40)$$

The first term in this equation is the Larmor frequency, and is subtracted out by using the rotating frame of reference. Using the simplified equation with spatially dependent frequency, the signal received from the sample is then, in complex notation:

$$S(t) = \iiint \rho(\vec{r}) \exp\left[i\gamma G(\vec{r}) \cdot \vec{r} t\right] d\vec{r} \qquad (2.41)$$

where $\rho(\vec{r})$ is the spatial density of the spins in the sample. This equation leads to the

definition of a vector $\vec{k}$, which depends on both the applied gradient and the amount of time that it is applied:

$$\vec{k} = \frac{\gamma G(\vec{r})t}{2\pi} \qquad (2.42)$$

Substitution of the definition of $\vec{k}$ in equation 2.42 into 2.41 results in another Fourier transform relationship, in this case between the signal and the density of the spins:

$$S(\vec{k}) = \iiint \rho(\vec{r}) \exp(2\pi i \vec{k} \cdot \vec{r}) d\vec{r} \qquad (2.43)$$

$$\rho(\vec{r}) = \iiint S(\vec{k}) \exp(-2\pi i \vec{k} \cdot \vec{r}) d\vec{k} \qquad (2.44)$$

These equations describe the acquisition of the NMR signal in the time domain as a function of $\vec{k}$ and how the Fourier transform of this signal returns the spin density or the "image".

The $\vec{k}$ vector depends on both the gradient that is applied, $G(\vec{r})$, and the time *t* over which it is applied. This leads to two different ways to "move through $\vec{k}$ -space": frequency encoding or phase encoding. By keeping the gradient fixed and changing the time, the spins are frequency encoded. This is generally done by applying a steady gradient during the acquisition of the echo signal. This gradient is then referred to as the read gradient, and the direction in space in which the gradient is applied is called the read direction. By keeping the time fixed and changing the magnitude of the applied gradient, the spins are phase encoded. This refers to the fact that only spins from a certain area of

the sample and with a specific frequency defined by $\vec{k}$ will refocus at the same time to form the echo.

For example, by applying a read gradient in one direction a one-dimensional profile is obtained, which is the projection of the spins onto the plane defined by the gradient direction. If the gradient is applied along the *z*-direction, the equations 2.43 and 2.44 become:

$$S(k_z) = \iiint \rho(x, y, z) \exp(2\pi i k_z z) dx dy dz \qquad (2.45)$$

$$F[S(k_z)] = \rho(z) = \iint \rho(x, y, z) dx dy \qquad (2.46)$$

Acquisition of the signal as a function of time and subsequent Fourier transformation leads to the spin density as a function of frequency, which is related to the spatial dimension because of the applied magnetic field gradient. This concept is extended into two dimensions, resulting in a 2D image, by applying a phase gradient in one direction and then applying the read gradient in another direction. Phase encoding in the third dimension results in a 3D image.

To reduce experimental time, rather than phase encoding in the third dimension and acquisition of a full 3D image, a "slice" in the third dimension is excited which results in a 2D image averaged over the specified slice. Instead of exciting all the spins in the sample, referred to as a "hard" pulse, in slice-selection a shaped "soft" pulse is applied during the application of a gradient. Therefore only spins that correspond to the spatial slice of interest are excited. Due to the Fourier relationship involved, to excite a rectangular shaped slice in the sample a sinc shaped pulse is often applied. Slice

selection can occur using several different types of pulse sequences, as shown in Figure 2.9. Since soft pulses occur in the presence of a gradient, a $\frac{\pi}{2}$ excitation pulse requires a gradient to be applied in the opposite direction in order for the excited spins to refocus as required while a π pulse is self-refocusing [14]. The use of a spin echo is desirable for a number of reasons: the inhomogeneous dephasing of the signal is refocused, as discussed

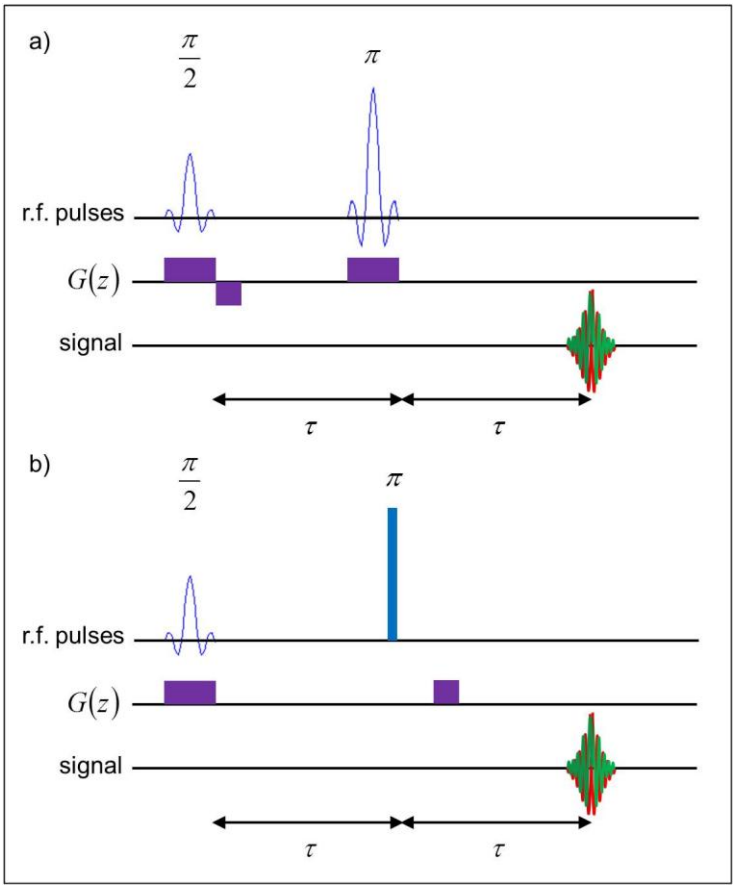

Figure 2.9. a) Slice selection using two slice selective pulses. A soft $\frac{\pi}{2}$ pulse requires an additional refocusing gradient, while a soft π pulse is self-refocusing. b) Slice selection with a slice selective excitation pulse and a non-slice selective refocusing pulse. The refocusing gradient in the slice direction is shown at two different points in the sequence to emphasize that it may be applied at different times while having the same effect.

earlier, and hardware issues related to the finite time that is needed to switch gradients on and off and to start the data acquisition are avoided.

The combination of slice selection and application of gradients to acquire data in 2D *k*-space leads to an example of a standard imaging sequence, shown in Figure 2.10. The pulse sequence consists of slice selection in the *z*-direction using a spin echo (see Figure 2.9.b). A gradient is applied in the phase direction, which moves the starting point of data acquisition up in $\vec{k}$ -space. In this example, the full echo is sampled, so a negative gradient is applied in the read direction to move in the negative *x*-direction in $\vec{k}$ -space (corresponding to (a) in Figure 2.10). Data is then acquired by applying a constant gradient in the read direction, and the points in the k_x direction are acquired by sampling the echo as a function of time (points (b)). Figure 2.10 also illustrates the concept of $\vec{k}$ -space, with the variation of k_y occurring in the phase direction and k_x in the read direction. The dots on the grid correspond to data points that are collected as a function of time. A line of data in the read (k_x) direction is acquired following the application of each amplitude of the phase (k_y) gradient. Two-dimensional Fourier transformation (equation 2.43) yields a 2D image of the spin density of the sample.

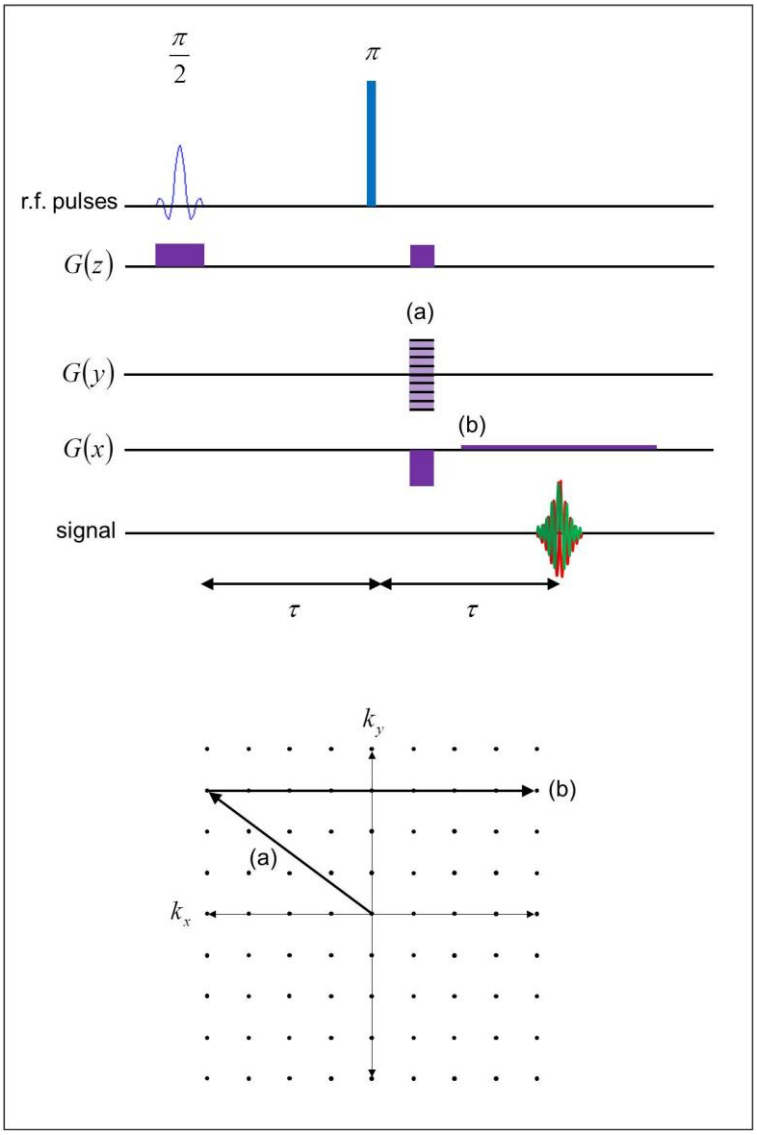

Figure 2.10. Basic imaging pulse sequence with a schematic of $\vec{k}$ -space. A detailed description is contained in the text.

Introduction to Measurement of Molecular Motion: The basic process of observing molecular motion with NMR is that of encoding molecules for their position by applying one or more spatially varying gradients and then observing over a fixed time the effect of the molecular motion on the detected signal. Carr and Purcell [20]

calculated the effect of the application of a steady gradient $G(\vec{r})$ with amplitude G to a sample for a time t with random diffusive motion as:

$$\frac{S(G)}{S(0)} = E(G) = \exp\left(-\frac{1}{3}\gamma^2 G^2 D t^3\right) \quad (2.47)$$

where $E(G)$ is the signal normalized with the signal amplitude at $G = 0$, or the signal attenuation. The steady gradient method of measuring diffusion is limited by this t^3 behavior because only very small amounts of time may be measured before total signal attenuation has occurred.

Stejskal and Tanner [21] developed the pulsed gradient spin echo (PGSE) sequence shown in Figure 2.11. The first pulse excites the spins, then the application of two gradients $G(\vec{r})$ with duration δ and amplitude g spaced time Δ apart encode for molecular motion. If a molecule is at a position defined by the first gradient pulse as $\vec{r}_1$ and stays at $\vec{r}_1$ during the observation time Δ, the second gradient pulse will cancel out the phase effect of the first gradient pulse and signal from the molecule will refocus at the correct time and contribute to the echo. However, if it moves to position $\vec{r}_2$ during Δ, its frequency will have changed and so the signal will have a phase shift, causing it to refocus at a different time. If the molecules are moving randomly (*i.e.* diffusion) they will all refocus at different times due to a random distribution of phase shifts and the intensity of the echo signal will be attenuated. If a large number of spins are moving the same amount (i.e. from $\vec{r}_1$ to $\vec{r}_2$ at velocity $\vec{v}$) they will coherently refocus but at a different time than if $\vec{v} = 0$ and therefore lead to a measureable phase shift in the echo.

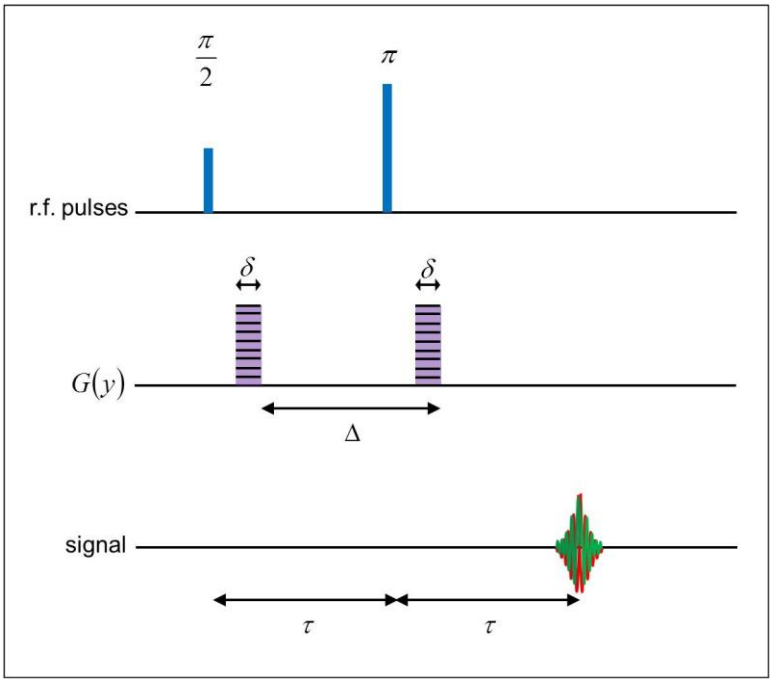

Figure 2.11. PGSE pulse sequence, used to measure molecular motion. In this example, the molecular motion is encoded for in the *y*-direction. The first pulse excites the spins, then the application of two gradients $G(\bar{r})$ with duration δ and amplitude g spaced time Δ apart encode for molecular motion. A refocusing pulse during Δ results in a spin echo which is affected by the molecular motion as described in the text.

The equation for the signal attenuation for the PGSE experiment with molecular diffusion and bulk flow is:

$$E(\bar{g}) = \exp\left[i\gamma\delta\Delta(\bar{g}\cdot\bar{v}) - \gamma^2 g^2 \delta^2 D\left(\Delta - \frac{\delta}{3}\right)\right] \quad (2.48)$$

The random diffusive motion contributes to a signal attenuation while the velocity contributes a phase shift. By varying δ, g, or Δ, different time and length scales of molecular motion can be measured, which makes this pulse sequence much more versatile than the steady gradient method. The PGSE sequence can be modified to use a stimulated echo instead of a spin echo, known as the PGSTE sequence. This allows measurement of molecular motion of samples with short T_2 relaxation.

NMR RELAXATION AND MULTI-DIMENSIONAL RELAXATION AND DISPLACEMENT CORRELATION EXPERIMENTS

Using the basic ideas introduced in the previous chapter, NMR and MRI experiments used for this thesis research are discussed in more depth in the following chapters. This chapter will explain the acquisition and data analysis of relaxation measurements and multi-dimensional relaxation and displacement correlations. Magnetic relaxation is affected by surface interactions, hydrogen exchange, and magnetic field inhomogeneities in addition to the dipolar interactions among nuclei. NMR relaxation measurements have been used for 20 years by the oil industry to study the pore structure of rocks to determine the amount of recoverable oil [22, 23] and by chemists for 60 years to study hydrogen exchange in polymer systems [24]. Multi-dimensional relaxation and diffusion correlation experiments developed more recently have been used to study rocks [25, 26], food [27], contact lenses [28], and concrete [29-31]. The systems studied in this thesis included a variety of samples containing liquid water including porous rock [1], hydrogels [3], biofilm growth in porous media [6], and colloidal suspensions [2].

Data Acquisition: NMR Relaxation Experiments and Multi-Dimensional Correlations

As introduced in Chapter 2, the T_1 and T_2 relaxation times of a liquid depend largely on the stochastic motion of the molecules which mediate dipolar correlations. This relaxation leads to exponential decays of the magnetization in both the direction of the magnetic field (T_1; Equation 2.28) and in the transverse plane (T_2; Equation 2.31)

which can be measured using the pulse sequences shown in Figure 2.7. The motion of the liquid molecules will be present for all experiments, but for complex solutions and geometries described in this thesis additional mechanisms occur. Therefore other sample effects on the magnetization such as surface effects, diffusion, and molecular exchange will also be considered. While these effects will be present in both longitudinal T_1 and transverse T_2 relaxation, the emphasis of this discussion and of the subsequent experiments will be on T_2 measurements using the CPMG experiment.

1D T_2 Relaxation Distributions

The multitude of sample dependent effects on the magnetization can be incorporated and described using the full Bloch-Torrey equation [14]. In Chapter 2, the Bloch equations for relaxation [13] in the rotating frame were presented as Equation 2.32. The effect of diffusion on the bulk magnetization was first taken into account by Torrey [32], and the influence of magnetic field gradients, hydrogen exchange, and fluid velocity can also be incorporated into a single equation. In the rotating frame, the complex magnetization $M_+(\vec{r},t) = M_x + iM_y$ in the transverse plane after excitation is given by:

$$\frac{dM_+}{dt} = -\frac{M_+}{T_2} + D\nabla^2 M_+ - (\vec{v}\cdot\nabla)M_+ - i(\gamma\vec{r}\cdot\vec{g}M_+ - \Delta\omega M_+) \qquad (3.1)$$

where T_2 is the spin-spin magnetic relaxation caused by the dipolar interactions in the liquid, D is the self-diffusion coefficient, v is coherent fluid velocity, g represents any magnetic field gradient present in the sample, and $\Delta\omega$ is a chemical shift difference between different molecular species. If multiple chemical species are present in the

sample $\Delta\omega$ incorporates the effect of hydrogen exchange [33]. The T_2 relaxation effect was discussed in Chapter 2 and is caused by molecular interactions due to dipole induced molecular magnetic field fluctuations. In addition, Equation 3.1 shows how the measurement of the relaxation decay of complex samples contains information about other molecular interactions. The mechanisms of relaxation for these additional effects will be discussed in greater detail in the following chapter.

For the present discussion, data obtained from a CPMG experiment (Figure 2.7.b) on a complex sample may lead to a multi-exponential $M(t)$ decay with a range of apparent T_2 values:

$$M(t) = \int M_0(T_2) \exp\left(\frac{-t}{T_2}\right) dT_2 \qquad (3.2)$$

where $M_0(T_2)$ is the distribution of molecules in the sample as a function of their apparent T_2 decay and is also known as the T_2 spectrum. The range of apparent T_2 values sampled will depend on the sample and on the time scale of the measurement but in general may vary between the shortest resolvable liquid state decay time (about 0.0001 s or 100 μs) and the longest possible T_2 (less than 10 s). In the following discussion, references to different T_2 times will imply the apparent or measured T_2, which incorporates other effects to the magnetization in addition to molecular dipole interactions. For example, molecules of water in smaller pores of a rock have shorter measured T_2 times than molecules in larger pores in the same rock because of surface relaxation effects [34]. An example of a T_2 distribution of a Berea sandstone rock is shown in Figure 3.1. The range of measured T_2 times is between 0.1 ms and 10 s. The

height of the peaks in the distribution corresponds to the amount of water molecules in each T_2 environment $M_0(T_2)$. This sample has a majority of smaller pores, as evidenced by the largest peak of the distribution being centered around 0.001 s. The range of T_2 times up to 1 s can be related to the surface to volume ratio of the porous structure of the rock; this will be discussed further in the next chapter.

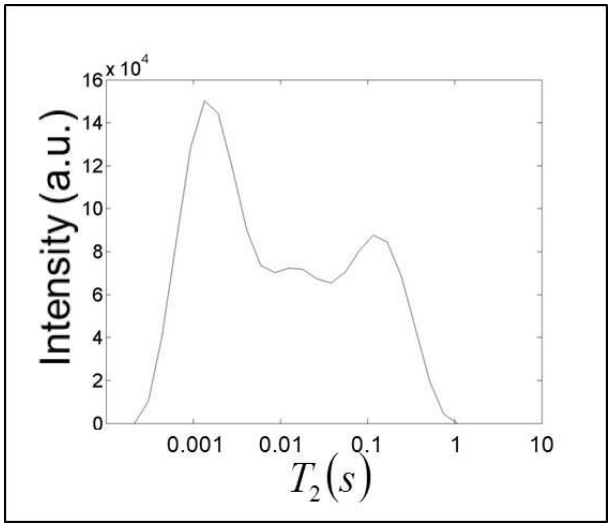

Figure 3.1. Example of a 1D T_2 distribution for a Berea sandstone rock core saturated with brine (salt water). Experimental parameters: τ = 200 μs; 512 echoes. Figures 3.1, 3.3, 3.4, and 3.5 are data obtained for the same rock sample.

1D T_2 distributions are obtained experimentally in two different ways. Figure 3.2.a shows the classic CPMG measurement. The echo signal is collected after a logarithmically varying number of π pulses. The advantage of this method is that the full echo can be collected to obtain molecular spectral information, leading to its use by chemists to study the T_2 relaxation mechanisms of complex molecules. The downside of this method is that for each iteration with a certain number of π pulses, only one data point is collected before the experiment must be repeated. Figure 3.2.b shows what is

sometimes called the "one-shot" CPMG measurement. In this sequence, the signal is collected by sampling the echoes that occur between each π pulse. In this way, the magnetization decay as a function of echoes on the order of thousands and time on the order of seconds can be obtained during one experiment. The T_2 relaxation distributions described in this thesis were almost entirely obtained using the method shown in Figure 3.2.b. This method is faster, but the downside is that due to data acquisition constraints only the amplitude of the echoes is recorded, so spectral information is not obtained.

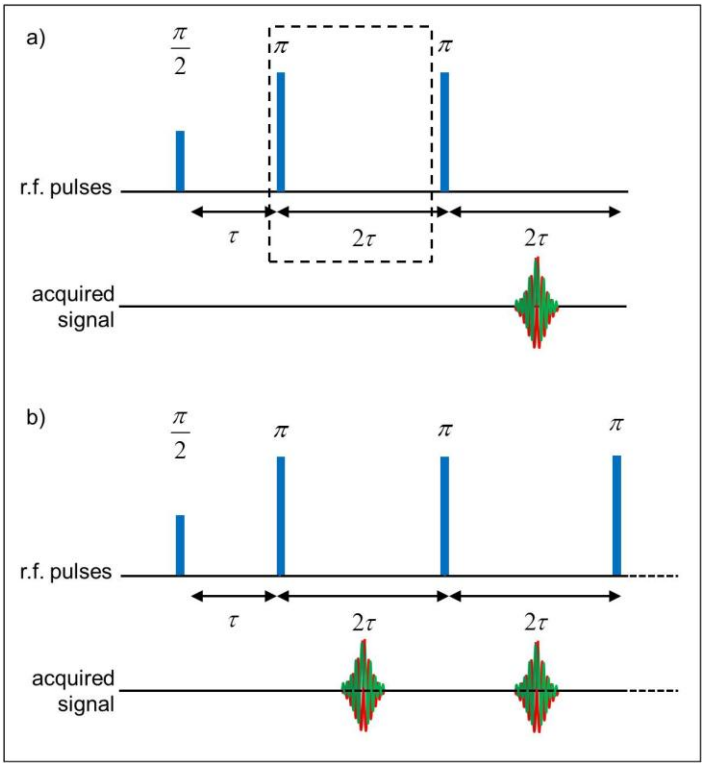

Figure 3.2. Two experimental methods for measuring T_2 relaxation. a) CPMG experiment. The dotted box indicates that the number of π pulses is changed logarithmically for each experiment. One echo is sampled for each iteration, which will be weighted by T_2 based on how many π pulses were performed in that iteration. b) One-Shot CPMG experiment. The echoes between each of the π pulses are sampled, so that an entire T_2 relaxation decay can be sampled during one iteration of the experiment.

2D Relaxation and Diffusion Correlations

In recent years, two-dimensional relaxation and displacement correlation experiments [25-31, 35-48] have become more common. Computing power has increased to the point that fast computation algorithms have been developed that enable data analysis using personal computers [49, 50]. These NMR experiments, shown in Figure 3.3, combine two types of relaxation or PGSE measurements into a single experiment to quantify the correlations between magnetic relaxation mechanisms and/or molecular motion. A 2D spectrum M_0 of molecules is obtained whereby molecular populations are resolved using the two different measurements, so more detailed information about the sample is obtained within a single experiment.

The $T_1 - T_2$ sequence in Figure 3.3.a [51] obtains the spectrum of molecules with correlated T_1 and T_2 relaxation mechanisms. The data acquired will have the form:

$$M(t_1,t_2) = \iint M_0(T_1,T_2)\left[1-2\exp\left(\frac{-t_1}{T_1}\right)\right]\exp\left(\frac{-t_2}{T_2}\right)dT_1dT_2 + E(t_1,t_2) \qquad (3.3)$$

where t_1 and t_2 are time scales of T_1 and T_2 encoding as defined in Figure 3.3.a and will define the range of T_1 and T_2 values that are sampled, and $E(t_1,t_2)$ is the noise of the measurement. The data inversion of 2D exponential decay data of this form will be discussed in the next section.

An example of a $M_0(T_1,T_2)$ spectrum of a Berea sandstone rock is shown in Figure 3.4. For samples such as rocks with large magnetic field inhomogeneities, T_1

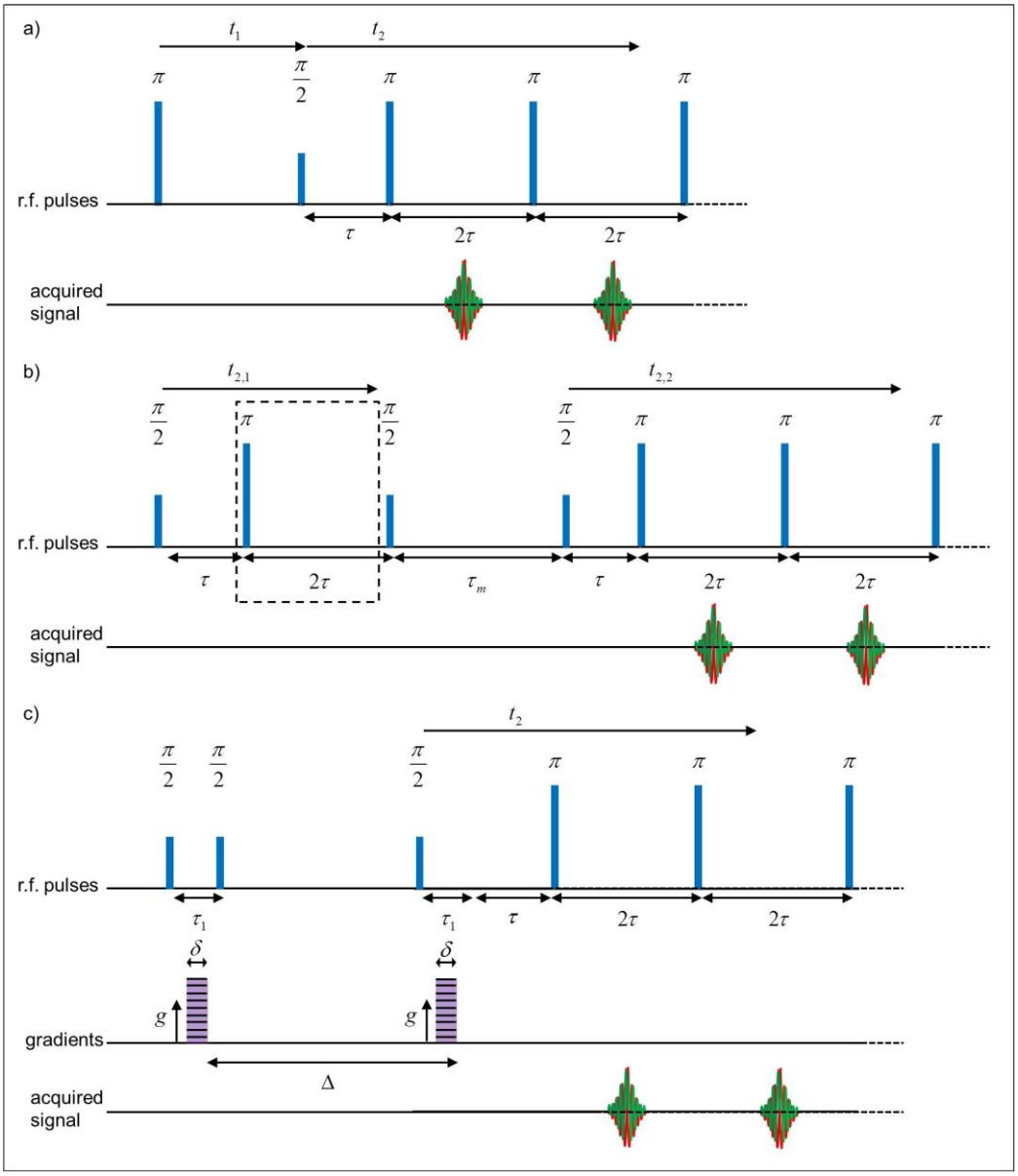

Figure 3.3. Two-dimensional correlation pulse sequences. a) $T_1 - T_2$ pulse sequence. T_2 data is acquired and is weighted by T_1 by changing t_1 for each acquisition. t_1 is varied logarithmically. b) $T_2 - T_2$ pulse sequence. T_2 is encoded by application of an initial train of π pulses; the signal is stored along the *z*-axis during a storage time τ_m; and then T_2 data is acquired. The dotted box indicates that the T_2 in the first dimension is encoded by applying a logarithmically varying number of π pulses. c) $D - T_2$ or $P(Z, \Delta) - T_2$ sequence. Diffusion or displacement is encoded in the first dimension by a PGSTE pulse sequence, then T_2 data is acquired. The magnitude of the pulsed gradient is varied linearly for each acquisition of T_2 data.

relaxation will be less affected than T_2 by magnetic susceptibility [23]. The T_1 and T_2 times will be approximately equal for large pores while for smaller pores the T_1 time will be significantly longer than the T_2 time. The range of T_2 values in Figure 3.4 is similar to the 1D distribution in Figure 3.1, but by resolving the molecular populations by T_1 as well the effects of surface relaxation and magnetic field inhomogeneities can be analyzed. For example in Figure 3.4, the smallest pores have the shortest measured T2 ~ 0.001 s and two different T_1 populations, $T_1 \sim 0.5$ s and $T_1 \sim 0.01$s. These two populations distinguish between molecules in the middle of the pores that have a T_2 that is affected by diffusion within the magnetic field inhomogeneities but have a longer T_1, from molecules which interact with the surface and have both a shorter T_1 and T_2.

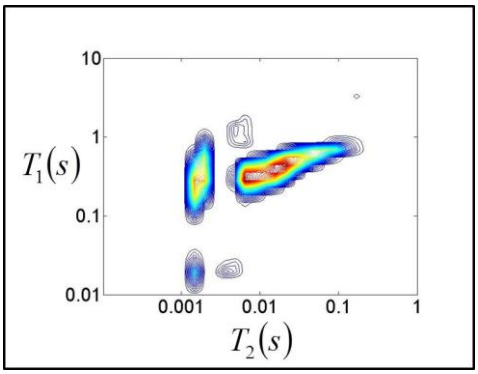

Figure 3.4. An example of a $T_1 - T_2$ spectrum of a Berea sandstone rock core saturated with brine. Experimental parameters: t_1 varied between 0.001 and 10 s in 32 logarithmically spaced steps; τ = 200 μs; 512 echoes.

The $T_2 - T_2$ sequence shown in Figure 3.3.b consists of encoding for T_2, waiting a mixing time τ_m, then measuring the T_2. If molecules have the same T_2 before and after the mixing time, the distribution in the 2D spectrum will be along the diagonal,

while if molecules have changed T_2 environments during the mixing time there will be off-diagonal peaks in the spectrum. The data will have the form:

$$M(t_{2,1},t_{2,2})=\iint M_0(T_{2,1},T_{2,2})\exp\left(\frac{-t_{2,1}}{T_{2,1}}\right)\exp\left(\frac{-t_{2,2}}{T_{2,2}}\right)dT_{2,1}dT_{2,2}+E(t_{2,1},t_{2,2}) \qquad (3.4)$$

where $t_{2,1}$ and $t_{2,2}$ are time scales of the two T_2 encoding periods as defined in Figure 3.3.b and will define the range of T_2 values that are sampled, and $E(t_{2,1},t_{2,2})$ is the noise of the measurement.

An example of a $M_0(T_2,T_2)$ spectrum for a Berea sandstone rock is shown in Figure 3.5. For this example, the magnetic field inhomogeneities are large and the off-diagonal peaks indicate the pore size distribution because molecules have had time to diffuse through the magnetic fields within the pore during the mixing time [26]. The 1D T_2 distribution is related to pore size through the pore surface to volume ratio of the rock [22], but the addition of the mixing time allows quantification of additional molecular exchange effects.

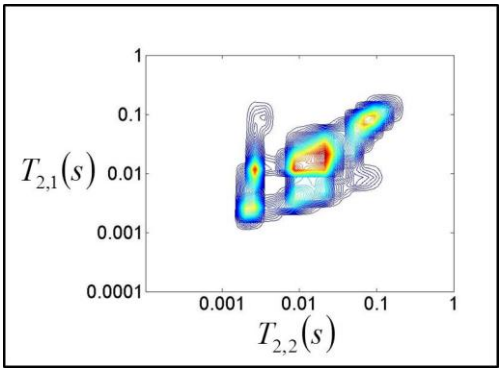

Figure 3.5. An example of a T_2-T_2 spectrum for a Berea sandstone rock core saturated with brine. Experimental parameters: number of echoes in the first dimension varied between 2 and 512 in 32 logarithmically spaced steps; τ = 200 μs; 512 echoes; τ_m = 250 ms.

The $D-T_2$ or $P(Z,\Delta)-T_2$ correlation sequence shown in Figure 3.3.c encodes the molecules of water for displacement and then measures the T_2. The data for a $D-T_2$ experiment will have the form:

$$M(g,t_2)=\iint M_0(D,T_2)\exp\left[-\gamma^2 g^2\delta^2 D\left(\Delta-\frac{\delta}{3}\right)\right]\exp\left(\frac{-t_2}{T_2}\right)dDdT_2+E(g,t_2) \qquad (3.5)$$

where g is the magnitude of the pulsed field gradient, t_2 is the time scale of T_2 sampling as defined in Figure 3.3.c and will define the range of T_2 values that are sampled, and $E(g,t_2)$ is the noise of the measurement. Depending on the range of g values that are used and the number of data points acquired, the same pulse sequence can be used to either encode for diffusion or for full propagator data. The data analysis of $D-T_2$ data is similar to T_1-T_2 and T_2-T_2 due to the exponential decay relationship between the diffusion and the applied gradient. $P(Z,\Delta)-T_2$ data analysis utilizes a Fourier transform in the displacement dimension and will be discussed in more detail in later chapters.

This sequence can be used to separate and correlate the effects of molecular motion and magnetic relaxation [52]. Figure 3.6 is an example of a $D-T_2$ spectrum for a porous rock. Smaller pores have both more restricted diffusion and a shorter T_2. Again, the measurement of diffusion and relaxation information in the same experiment gives more detailed information about the pore structure than D or T_2 information alone.

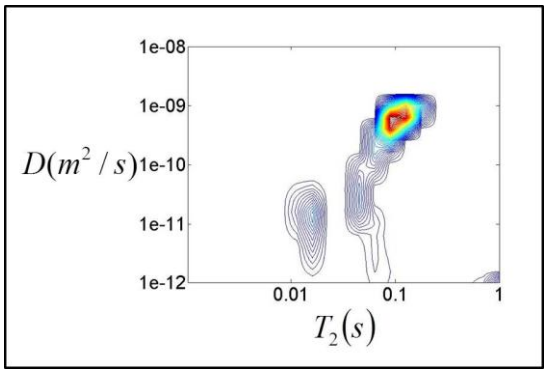

Figure 3.6. $D-T_2$ spectrum for a Berea sandstone rock core saturated with brine. Experimental parameters: g varied between 0 T/m and 1.482 T/m in 21 linearly spaced steps; δ = 1 ms; Δ = 20 ms; τ = 200 μs; 512 echoes.

Data Analysis: Inverse Laplace Transform

For complex samples with different magnetic relaxation effects that contribute to the measurement resulting in a range of relaxation decay constants, the measured decay data must be inverted to obtain the distribution of molecules M_0. The inverse Laplace transform (ILT) is the technique of choice at this time, but other methods of analysis are also possible. The 1D and 2D spectra shown in Figures 3.1, 3.4, 3.5, and 3.6 were computed using the ILT procedure described below.

If the change in time of the magnetization is represented as a sum of exponential decays, the result of a CPMG measurement may be represented by Equation 3.2, $M(t)=\int M_0(T_2)\exp\left(\frac{-t}{T_2}\right)dT_2$. Each apparent T_2 may correspond to molecules in different size pores, undergoing hydrogen exchange, or other magnetic relaxation effects, as discussed in the previous section. The form of the data in Equation 3.2 is the same as

that of a Laplace transform:

$$F(t) = \int_0^\infty f(s)\exp(-st)ds \qquad (3.6)$$

The inverse Laplace transform pair is also defined:

$$f(s) = \int_0^\infty F(t)\exp(st)dt \qquad (3.7)$$

Therefore to obtain the molecular distribution of apparent T_2 values $M_0(T_2)$, an ILT can be used:

$$M_0(T_2) = \int M(t)\exp\left(\frac{t}{T_2}\right)dt \quad (3.8)$$

The ILT is a well-known ill-posed problem [53]. The eigenfunctions do not form a complete set, so there is always at least one free variable and the problem cannot be fully defined. The algorithm for computing the ILT of a given data set begins by forming a function to minimize using non-linear least squares subject to constraints that are defined by the data set. Starting with an initial guess for the final spectrum, the solution is then compared to the given data using the minimization function until the difference between the solution and the original data is minimized. The minimization function used is very important because random error of CPMG measurements is significant due to signal to noise of the signal and will result in an infinite number of possible distributions. Smoothing algorithms are used to constrain the number of final distributions possible and obtain reproducible data inversion. CPMG experiments often contain several thousand echoes and the error minimization takes significant computing time, so reduction of the

size of the data set to be analyzed is also often desirable. The basic algorithm used to analyze exponential decay data in this thesis will first be described, followed by the modified algorithm with data size reduction used to analyze data more efficiently.

1D Inverse Laplace Transform

Consider data with the form of a sum of exponential decays as in Equation 3.2. Echo amplitude data $\vec{M}$ obtained as a function of time from t_1 to t_m with a 1D one shot CPMG experiment with *m* data points can be represented in vector form as:

$$\vec{M} = \mathbf{K}\vec{M}_0 + \vec{E} \qquad (3.9.a)$$

$$\begin{bmatrix} M(t_1) \\ \dots \\ M(t_m) \end{bmatrix} = \begin{bmatrix} \exp\left(\frac{-t_1}{T_{2,1}}\right) & \dots & \exp\left(\frac{-t_1}{T_{2,n}}\right) \\ \dots & \dots & \dots \\ \exp\left(\frac{-t_m}{T_{2,1}}\right) & \dots & \exp\left(\frac{-t_m}{T_{2,n}}\right) \end{bmatrix} \begin{bmatrix} M_0(T_{2,1}) \\ \dots \\ M_0(T_{2,n}) \end{bmatrix} + \begin{bmatrix} E(t_1) \\ \dots \\ E(t_m) \end{bmatrix} \qquad (3.9.b)$$

where $\vec{M}_0$ is the final spectrum as a function of *n* T_2 times to be calculated, $\mathbf{K}$ is the matrix of exponential relations between the time of the measurement *t* and the T_2 times, and $\vec{E}$ is the error of the measurement.

The algorithm for obtaining 1D relaxation distributions proceeds as follows:

1. Form a vector that corresponds to a "guess" for the final T_2 spectrum, for example $\vec{M}_0 = \begin{bmatrix} 1 \\ \dots \\ 1 \end{bmatrix}$.

2. Form the matrix $\mathbf{K}$ that contains the exponential relations between the range of expected T_2 values and the time of the collected data points. A typical range of expected

T_2 values is 16 values that are logarithmically spaced between 0.001 s and 10 s. The times of the data collection will depend on the 2τ value used for echo spacing in the experiment and the number of echoes, with typical values being 2τ = 400 μs and 5000 echoes, leading to $t_{m=5000}$ = 2 s. For this example:

$$\mathbf{K} = \begin{bmatrix} \exp\left(\frac{-t_1}{T_{2,1}}\right) & \cdots & \exp\left(\frac{-t_1}{T_{2,16}}\right) \\ \cdots & \cdots & \cdots \\ \exp\left(\frac{-t_{5000}}{T_{2,1}}\right) & \cdots & \exp\left(\frac{-t_{5000}}{T_{2,16}}\right) \end{bmatrix} = \begin{bmatrix} \exp\left(\frac{-0.0004}{0.001}\right) & \cdots & \exp\left(\frac{-0.0004}{10}\right) \\ \cdots & \cdots & \cdots \\ \exp\left(\frac{-2}{0.001}\right) & \cdots & \exp\left(\frac{-2}{10}\right) \end{bmatrix}$$

The matrix $\mathbf{K}$ is therefore fully defined based on experimental and calculation parameters.

3. Calculate the fit $\vec{F}$ to check against the data set with:

$$\vec{F} = \mathbf{K}\vec{M}_0 \qquad (3.10)$$

4. Calculate the error χ^2 between the fit and the original data. A simple representation of that error without smoothing is found by rearranging Equation 3.9.a:

$$\chi^2 = \sum_{j=1}^{m} \left| M(t_j) - F(t_j) - E(t_j) \right|^2 \qquad (3.11)$$

5. Iterate the M_0 spectrum until χ^2 is minimized using a non-linear least squares algorithm, such as those described by Lawson and Hanson [54].

The error $\vec{E}$ of the measurement is unknown and will be different for each experiment performed, so it is undesirable for this measurement error to be a significant factor in calculating the spectrum. There are a number of different ways to avoid this. For this thesis, a smoothing algorithm using Tikhonov regularization parameters known

as α and β was used [50]. In this case, $\vec{E}$ in Equation 3.11 is replaced by factors that are related to the calculated distribution:

$$\chi^2 = \sum_{j=1}^{m} \left| M(t_j) - F(t_j) \right|^2 + \alpha \sum_{i=1}^{n} \left| M_0(T_{2,i}) \right|^2 + \beta \sum_{i=1}^{n} \left(\left| \frac{dM_0}{dT_2} \Big|_{T_{2,i}} \right|^2 + \left| \frac{d^2 M_0}{dT_2^2} \Big|_{T_{2,i}} \right|^2 \right) \qquad (3.12)$$

where $\left| \frac{dM_0}{dT_2} \right|$ and $\left| \frac{d^2 M_0}{dT_2^2} \right|$ are the first and second derivatives of the calculated fit. The β parameter for this research was always set to a value of 1, so the last term of this equation is a measure of the smoothness of the calculated distribution. The optimal α is found by iterating the data fitting with different values of α and finding the value that just minimizes Equation 3.12.

It is this point in the analysis where knowledge of the physical limitation due to signal to noise ratio of the collected data is important. The trade-off between the error in the data fit and the smoothness of the distribution is important because a smooth distribution of molecular populations is in most cases a more physical result. This is known as the principle of parsimony, which states that the best solution is the simplest solution that fits the data [49]. The effect caused by using too large a value for α is known as "pearling of the distribution", and leads to presentation of a distribution that implies more confidence in the measurement of fine details of the spectrum than is physically possible given the measurement error. A robust method of choosing α is therefore important to the data analysis in order to have confidence that the calculated distributions are physically relevant. The L-curve method [55] was used for the data analysis described in this thesis, an example of which is shown in Figure 3.7. Calculated

χ^2 values for different α values are plotted. As α is increased above the optimal value the χ^2 will stay approximately constant, leading to an L shaped curve where the optimal value of α is found at the base of the L. At this α, the error between the fit and the data is balanced out by the smoothness of the distribution. Increasing α does not decrease the amount of error between the fit and the data but instead allows the calculated distribution to be less smooth, or "pearled".

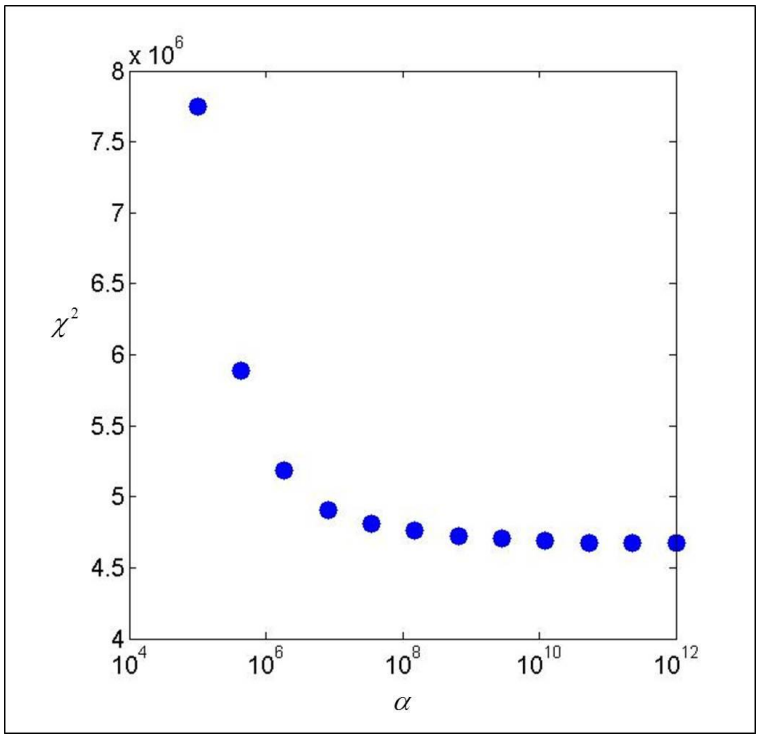

Figure 3.7. Example of the L-curve for the distribution shown in Figure 2.6. The α used to calculate the final distribution was therefore chosen to be 10^8.

As a concrete example, consider a sample containing two relaxation times T_2 = 1 s and T_2 = 0.05 s in equal proportions, so that the total magnetization is described by $M(t) = 0.5\exp\left(\frac{-t}{1}\right) + 0.5\exp\left(\frac{-t}{0.05}\right)$, as shown in Figure 3.8.a. The expected T_2

spectrum in this case would be $\bar{M}_0 = [0.5,0.5]$ for $T_2 = [0.05,1]$. In this case, there is no error in the measurement so the final T_2 distribution plotted as a function of T_2 should be two delta functions with height 0.5 centered at T_2 = 1 s and T_2 = 0.05 s.

Using the ILT algorithm described above, the computed distribution of T_2 times is shown in Figure 3.8.b. The vector for T_2 times in this case was 32 values logarithmically spaced between 0.01 and 10 s, i.e. $[0.01,...10]$. As the pictured distribution demonstrates, the algorithm leads to the expected two populations at approximately the same height and approximately centered at 0.05 and 1, but there is a distribution of possible T_2 times around each T_2. The peaks have a finite width and as a result do not have exactly a height of 0.5. An $\alpha = 10^8$ was found to be the optimal value using the L-curve method.

Figure 3.8.c demonstrates what the computed T_2 distribution will look like if a non-optimal value for α is used. Using an α that is smaller than the optimal value (LHS of Figure 3.8.c) allows for too much error χ^2 between the solution and the data, and often leads to features such as very broad distributions that do not resolve into multiple populations. The large peak seen for the smallest T_2 value considered is also a common feature of these distributions. The algorithm finds that there is a population with a short T_2, but the large χ^2 allowed at this α value means that the pictured distribution is a good enough fit even though the population is not resolved. Using an α that is larger than the optimal value (RHS of Figure 3.8.c) may lead to very sharp peaks despite the fact that the real data is noisy and the distribution is not known at such

precision. In this case, there is no error so the peaks should be highly resolved, but in most cases this is not a physical result.

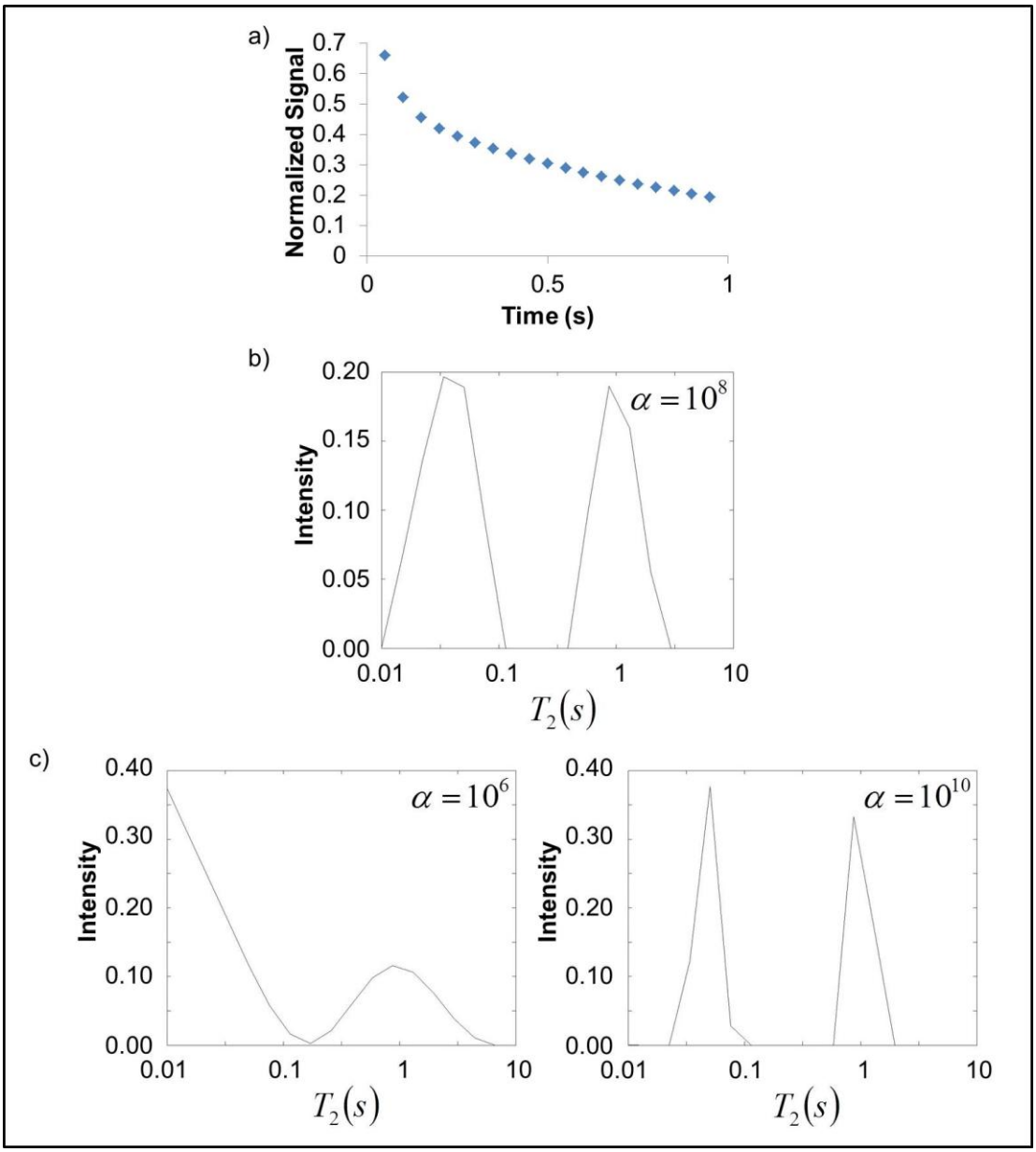

Figure 3.8. Simulated CPMG data for a sample with half of the molecules decaying with a T_2 of 1 s and half of the molecules decaying with a T_2 of 0.05 s, i.e. $M(t) = 0.5\exp\left(\frac{-t}{1}\right) + 0.5\exp\left(\frac{-t}{0.05}\right)$. a) Simulated raw data. b) T_2 distribution obtained by inverse Laplace transformation of the simulated data set. c) Demonstration of the effect of varying the α parameter on the computed distribution.

2D Inverse Laplace Transform with Data Size Reduction

The algorithm described above is suitable to compute 1D distributions, but even 1D data inversion takes multiple minutes of computation time. For 2D distributions, an algorithm that reduces the size of the data set is necessary to reduce the computation time. For example, as presented in an earlier section of this chapter, the data from a T_2-T_2 2D relaxation correlation can be represented by

$$M(t_{2,1},t_{2,2})=\int M_0(T_{2,1},T_{2,2})\exp\left(\frac{-t_{2,1}}{T_{2,1}}\right)\exp\left(\frac{-t_{2,2}}{T_{2,2}}\right)dT_{2,1}dT_{2,2}+E(t_{2,1},t_{2,2}) \quad (3.4)$$

This function has the form of a Fredholm integral of the first kind, and can be discretized and manipulated using mathematical algorithms developed for this type of function [50]. The algorithm used to perform the data analysis in this thesis was derived from the algorithm of Lawson and Hanson [41, 54]. The size of the data set is first reduced using the principles of singular value decomposition (SVD). For a matrix $\mathbf{A}\in\Re^{mxn}$, the singular value matrix $\mathbf{S}\in\Re^{mxn}$ is computed as:

$$\mathbf{A}=\mathbf{USV}^T \quad (3.13)$$

where $\mathbf{U}\in\Re^{mxm}$ and $\mathbf{V}\in\Re^{nxn}$ are orthonormal matrices. This process is analogous to finding the eigenvalues and eigenvectors of a square matrix, generalized for a non-square matrix. The original matrix $\mathbf{A}$ is reduced from a *m*x*n* matrix with values in all positions of the matrix to a singular value matrix $\mathbf{S}$ that is still *m*x*n* but can be represented as simply $\vec{S}$, a 1D vector containing the *n* computed singular values. Matrix manipulation can then be performed on $\vec{S}$, then transformed back into a 2D matrix using the computed matrices $\mathbf{U}$ and $\mathbf{V}$.

An important definition in matrix manipulation is the Frobenius norm:

$$\|\mathbf{A}\| = \sqrt{\sum_{i,j} a_{ij}^2} \qquad (3.14)$$

where a_{ij} are the elements of the matrix. An important reason for performing the SVD is that the Frobenius norm of matrix $\mathbf{A}$ is the same as the Frobenius norm of the vector $\vec{S}$. Further mathematical operations are then performed on a vector instead of a matrix, thus reducing computation time. These operations can be performed without loss of information because minimization of the Frobenius norm of the error between the data and the spectrum computed using the singular values will be the same as that which is computed using the original full data matrix. The full matrix is then recovered using inverse SVD of the known matrices $\mathbf{U}$ and $\mathbf{V}$.

The function in Equation 3.4 can be represented in discretized form as:

$$\mathbf{M} = \mathbf{K_1}\mathbf{M_0}\mathbf{K_2}^{'} + \mathbf{E} \qquad (3.15a)$$

$$\begin{bmatrix} M(t_{2,1,1}, t_{2,2,1}) & \dots & M(t_{2,1,1}, t_{2,2,m}) \\ \dots & \dots & \dots \\ M(t_{2,1,n}, t_{2,2,1}) & \dots & M(t_{2,1,n}, t_{2,2,m}) \end{bmatrix} =$$
$$\begin{bmatrix} \exp\left(\frac{-t_{2,1,1}}{T_{2,1,1}}\right) & \dots & \exp\left(\frac{-t_{2,1,1}}{T_{2,1,p}}\right) \\ \dots & \dots & \dots \\ \exp\left(\frac{-t_{2,1,n}}{T_{2,1,1}}\right) & \dots & \exp\left(\frac{-t_{2,1,n}}{T_{2,1,p}}\right) \end{bmatrix} \begin{bmatrix} M_0(T_{2,1,1}, T_{2,2,1}) & \dots & M_0(T_{2,1,1}, T_{2,2,q}) \\ \dots & \dots & \dots \\ M_0(T_{2,1,p}, T_{2,2,1}) & \dots & M_0(T_{2,1,p}, T_{2,2,q}) \end{bmatrix} \cdot$$
$$\begin{bmatrix} \exp\left(\frac{-t_{2,2,1}}{T_{2,2,1}}\right) & \dots & \exp\left(\frac{-t_{2,2,m}}{T_{2,2,1}}\right) \\ \dots & \dots & \dots \\ \exp\left(\frac{-t_{2,2,1}}{T_{2,2,q}}\right) & \dots & \exp\left(\frac{-t_{2,2,m}}{T_{2,2,q}}\right) \end{bmatrix} + \begin{bmatrix} E(t_{2,1,1}, t_{2,2,1}) & \dots & E(t_{2,1,1}, t_{2,2,m}) \\ \dots & \dots & \dots \\ E(t_{2,1,n}, t_{2,2,1}) & \dots & E(t_{2,1,n}, t_{2,2,m}) \end{bmatrix} \qquad (3.15b)$$

where $\mathbf{M} \in \Re^{mxn}$ is the data, $\mathbf{K}_1 \in \Re^{pxn}$ is the matrix of $T_{2,1}$ times to be computed, $\mathbf{K}_2 \in \Re^{qxm}$ is the matrix of $T_{2,2}$ times to be computed, $\mathbf{M}_0 \in \Re^{qxp}$ is the final spectra, and $\mathbf{E} \in \Re^{mxn}$ is the error of the measurement. The sizes of the data set $\mathbf{M} \in \Re^{mxn}$ and the matrices $\mathbf{K}_1 \in \Re^{pxn}$ and $\mathbf{K}_2 \in \Re^{qxm}$ are first reduced using SVD, then non-linear least squared minimization is used to obtain $\mathbf{M}_0 \in \Re^{qxp}$ for the given $\mathbf{M} \in \Re^{mxn}$ [50]. This could be done by minimization of a function of the Frobenius norms of each term in Equation 3.15a. This function is undesirable, however, because the error term is too significant to the solution of the problem, as discussed in the previous section. Instead, Tikhonov regularization terms are again used:

$$\chi^2 = \sum_{j=1}^{m} \left\| \mathbf{M}(t_j) - \mathbf{F}(t_j) \right\|^2 + \alpha \sum_{i=1}^{n} \left\| \mathbf{M}_0 \right\|^2 + \beta \sum_{i=1}^{n} \left(\left\| \left. \frac{d\mathbf{M}_0}{dT_2} \right|_{T_{2,i}} \right\|^2 + \left\| \left. \frac{d^2\mathbf{M}_0}{dT_2^2} \right\|_{T_{2,i}} \right|^2 \right) \qquad (3.16)$$

The second term in this equation is determined by iterating the fitting of the functions with different α parameters and determining at what point the α parameter minimizes the calculated error, as discussed earlier.

ADVANCED NMR CONCEPTS

As introduced in Chapters 2 and 3, nuclear magnetic resonance experiments involve receiving a voltage signal from an ensemble of precessing nuclear magnetic moments. In summary, hydrogen nuclei have the highest gyromagnetic ratio, and liquid molecules such as water have relaxation characteristics that allow excitation and signal collection on the order of milliseconds to seconds. Water confined within opaque solid samples such as rocks, the human body, and other porous material can then be analyzed without destroying the sample due to the fact that solids have much different relaxation and excitation characteristics. The spins can be encoded for position or displacement using magnetic field gradients, enabling the study of both spatially heterogeneous samples and dynamic systems of fluid flow and molecular diffusion. This chapter will discuss the more advanced concepts behind the use of NMR and MRI techniques to study static and dynamic systems. Experimental results are presented in the following chapters that illustrate the discussed concepts.

Bloch-Torrey Equations and Effective Gradients

As discussed briefly in Chapter 3, the Bloch-Torrey equation for the change in the sample magnetization accounts for diffusion effects, fluid flow, hydrogen exchange, and magnetic field gradients [14]. With the variables described earlier in the discussion of Equation 3.1, the complex magnetization M_+ in the rotating frame is given by:

$$\frac{dM_+}{dt} = D\nabla^2 M_+ - (\vec{v}\cdot\nabla)M_+ - \frac{M_+}{T_2} - i(\gamma\vec{r}\cdot\vec{g}M_+ - \Delta\omega M_+) \quad (4.1)$$

The solution of this equation is simplified by introducing the concept of the effective gradient of the experiment, $\vec{g}^*(t)$. The effective gradient incorporates the effects of rf pulses on the phase of the molecules as well as the effects of applied gradients [56], unknown magnetic field inhomogeneities, and constant background gradients. The magnetization is dependent on molecular positions within the sample, and the application of known magnetic field gradients allows the position of the molecules to be quantified [57, 58]. However, magnetic field inhomogeneities and constant background gradients are generally undesirable [19]. The condition for a spin echo to form in a constant background gradient is $\int_0^{2\tau} \vec{g}^*(t')dt' = 0$ because this represents the time where the evolved position dependent phase shifts are refocused, as shown in Figure 4.1. The π pulse reverses the sense of the precession of the spins so that the spins effectively experience the opposite gradient. The use of spin echoes is therefore ubiquitous for analysis of complex samples because magnetic fields are often inhomogeneous and sample surfaces can create significant magnetic fields within the liquid. These undesirable experimental artifacts can be at least partially mitigated using spin echoes.

To start to understand this equation, it is helpful to assume that each term in the equation is separable and solve for M_+ for a spatially homogeneous system without surface relaxation. The solution of equation 4.1 is then the product of exponential terms incorporating the effect of the position of the molecules, the T_2 of the system, hydrogen

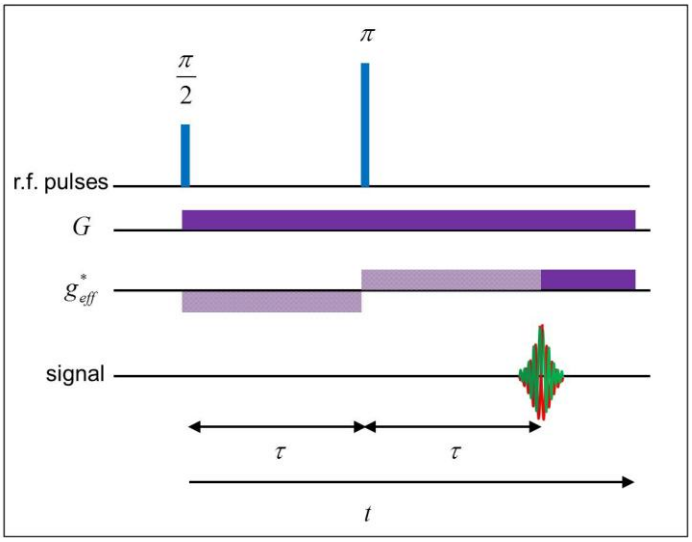

Figure 4.1. Schematic of the effective gradient for a spin echo pulse sequence. G is a constant background gradient. The π pulse reverses the precession of the spins and results in a negative effective gradient before the pulse. The shading indicates when the integrated area of the effective gradients are equal.

exchange, and molecular motion [14]:

$$M_+(\vec{r},t) = A(t)\exp\left(-i\gamma\vec{r}\cdot\int_0^t \vec{g}^*(t')dt'\right)\exp\left(\frac{-t}{T_2}\right)\exp(i\Delta\omega t) \quad (4.2.a)$$

where $A(t)$ is dependent on molecular motion and is separated into a diffusion term and a velocity term:

$$A(t) = \exp\left[-D\gamma^2\int_0^t\left(\int_0^{t'}\vec{g}^*(t'')dt''\right)^2 dt'\right]\exp\left[i\gamma\vec{v}\cdot\int_0^t\left(\int_0^{t'}\vec{g}^*(t'')dt''\right)dt'\right] \quad (4.2.b)$$

The integral of the effective gradient $\vec{g}^*(t)$ over the time of the experiment and the moments of this integral are important quantities to calculate because the influence of molecular position, diffusion, and velocity on the phase of the NMR signal can be analyzed. The phase effects of the effective gradient will be considered in detail

throughout this chapter. As an introduction to this concept, Figure 4.2 presents examples of the effective gradients for two pulse sequences used in this thesis.

Figure 4.2.a shows the effective gradients in all three directions for a basic spin echo imaging sequence. In the *z*-direction, or slice direction, the application of a gradient during a slice selective $\frac{\pi}{2}$ pulse is refocused with a gradient in the opposite direction with half of the integral of the slice selection gradient. The NMR signal is then sensitive to the positions of the molecules in the *z*-direction because only molecules within a slice specified by the gradient are excited by the pulse. In the *x*-direction, or read direction, the first negative gradient is refocused by the positive read gradient. At the echo time of 2τ, or in the center of *k*-space, $\int_0^t \vec{g}*(t')dt' = 0$. However, on either side of the echo the signal will be dependent on position in the *x*-direction, as discussed in Chapter 2. In the *y*-direction, or phase direction, the gradient is not balanced by another gradient and the signal for this experiment will have a phase shift that is sensitive to position in the *y*-direction.

Figure 4.2.b demonstrates the concept of the effective gradient for a PGSE pulse sequence. In this case, $\int_0^t \vec{g}*(t')dt' = 0$ following the application of the second pulsed gradient. However, at the echo time of 2τ, the $A(t)$ term of equation 4.2.b will be significant. The relevant ingerals are: $\int_0^t \left(\int_0^{t'} \vec{g}*(t'')dt'' \right) dt' = g\delta\Delta$ and

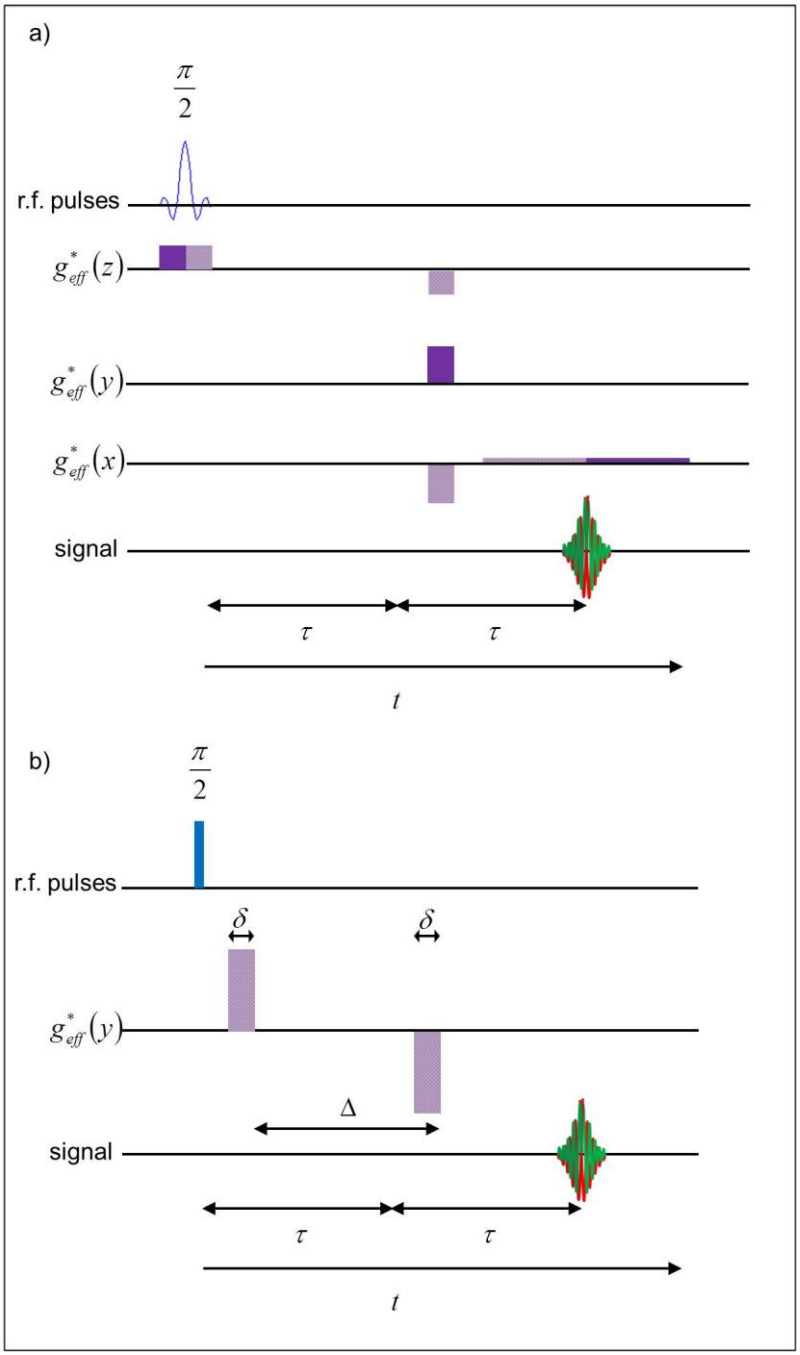

Figure 4.2. Examples of effective gradients. a) Basic imaging sequence. The shading indicates when the areas of the effective gradients are equal. b) PGSE pulse sequence. The π pulses that are used to form the spin echoes in both experiments are not shown.

$\int_0^t \left(\int_0^{t'} \vec{g} * (t'')dt'' \right)^2 dt' = g^2 \delta^2 \left(\Delta - \frac{\delta}{3} \right)$. This demonstrates how the collected signal will have a phase shift proportional to the velocity and signal attenuation proportional to the diffusion.

Experiment Optimization

Using these concepts, most imaging and molecular motion experiments can be analyzed. The effect of diffusion will be present in any experiment, particularly when the application of gradients is necessary. Whether each term of the equation is significant during a particular measurement will depend on the sample, the time scale of the measurement, and the type of experiment performed. The experiments in Figure 4.2 can be used to explain the process of experiment optimization. In the imaging experiment of Figure 4.2.a, although at the echo time the phase dependence of the signal on the position is the desired result, the integrals in Equation 4.2.b related to molecular motion will also be non-zero. As a result, images of static samples are generally analyzed using the magnitude of the signal after Fourier transformation, rather than retaining the complex phase information. Since molecular diffusion leads to additional signal attenuation, it will not impact the measured phase but instead limits the resolution attainable. For the PGSE experiment in Figure 4.2.b, T_2 relaxation during the Δ observation time is removed by analyzing the signal attenuation rather than the signal magnitude. By normalizing the data by the first experimental point, obtained with no applied gradient pulse, the relaxation effects during the experiment will be removed, so that the phase shift

and signal attenuation information is retained and can be analyzed as discussed in a later section in this chapter.

Sample effects such as surface interactions must also be taken into account when optimizing an experimental pulse sequence. For example, for a CPMG experiment of a large tube of water measured in a short amount of time, the surface effects can be neglected because a majority of molecules will not be interacting with the surface. In this case, only molecular tumbling contributes to the T_2 measurement. However, for water contained in a rock with very small pores, nearly all of the water will interact with a surface during the measurement, and the restricted diffusion term will dominate the measured T_2 decay.

The following sections will discuss the wide range of experimental techniques used for this thesis research in the context of the Bloch-Torrey equations, and the next chapter will present experimental examples that illustrate these concepts with data obtained by the author but not contained elsewhere in this thesis.

MR Imaging Experiments

NMR imaging or MRI is used for a variety of applications as discussed in Chapter 2. In the context of the Bloch-Torrey equations, $\int_0^t \vec{g}^*(t')dt' \neq 0$ so the resulting NMR signal will be sensitive to the position of the molecules within the sample with the signal having a Fourier transform relation with the spin density, see Equation 2.41. Two different types of imaging experiments were performed for this thesis research: 2D

multi-slice selection and 3D images [14]. The pulse sequence for 2D imaging was presented earlier as Figure 2.10. For 3D images, the initial slice selective $\frac{\pi}{2}$ pulse is replaced by a non-slice selective pulse and an additional phase encoding gradient in the third spatial direction is added. Experimental considerations and challenges not presented earlier are discussed below.

Image Field of View and Resolution

The field of view (FOV) of an MRI image is determined by the increment in the phase encoding gradients used and the value of the read gradient applied and the sweepwidth during data acquisition. In the read direction, (k_x in Figure 2.10) the FOV in terms of the gradient strength G_{rd} applied during data acquisition of *N* data points for a time *t* at a sampling rate known as the dwell time *dw* (or the inverse of the sweepwidth), is FOV = $\frac{N}{\gamma G_{rd} t} = \frac{1}{\gamma G_{rd}(dw)}$. The resolution is then the FOV divided by the number of data points acquired. For example, to obtain an image with a 20 mm FOV in the read direction and a resolution of approximately 20 μm, values for these parameters could be: 1024 points acquired, *dw* = 5 μs and G_{rd} = 0.235 T/m. Increasing the resolution in the read direction with the same FOV can be done without increasing the time needed for the experiment by increasing G_{rd} and increasing the number of points acquired while also decreasing the dwell time.

In the phase encoding direction (k_y in Figure 2.10), a gradient G_{ph} is applied for a time *t* to encode for position before the data acquisition during the read gradient. The

phase encoding gradient is usually varied linearly between a positive maximum gradient and the negative of the same gradient strength to sample all of *k*-space. In this case, the FOV is determined by the area of the increment of the phase encoding gradient G_{ph} and the time applied *t* with FOV = $\frac{N}{2\gamma G_{ph} t}$. The resolution is determined by the FOV divided by the number of phase encoding gradients *N*. For example, to obtain an image with a FOV of 10 mm with a resolution of approximately 20 μm, possible parameters would be 512 gradient encoding steps between -0.67 T/m and 0.67 T/m and *t* = 0.9 ms. The resolution in the read direction can be increased without significantly affecting the time of the experiment because more data points can be acquired by simply increasing the data acquisition time. However, increased resolution in the phase direction requires additional repetitions of the whole pulse sequence, including the experimental repetition time, that will significantly increase the total experiment time.

Image Acquisition Time

The overall time of an NMR experiment is often dominated by the repetition time. In general the repetition time T_R should be 5 times T_1 to ensure that the full signal has recovered to equilibrium before starting the next repetition or average of the experiment. This often means a T_R of 5 or 10 seconds for samples of liquid water. Each voxel in the phase encoding direction requires a full T_R and will increase the time required. For example, the experimental time for a 2D image with 128 phase encoding steps, 128 points in the read direction, T_R = 5 s, and 4 averages can be estimated as

$(5s)(4avg)(128steps) = 2560s = 42\min$. For a 3D image with two phase encoding gradients, the time of the experiment can therefore take many hours; for example a 128x128x128 image with the same parameters would take $(5s)(4avg)(128steps)(128steps) = 327{,}680s = 5461\min = 91hours$. Applying a strong gradient during acquisition to achieve high resolution in the read direction will also cause diffusive attenuation and will require more averaging to obtain a suitable ratio of signal to noise. In addition, the excitation of smaller slices means that there is less signal excited and will require additional averaging. Rapid imaging techniques are only advantageous when voxels are large enough that averaging to improve signal to noise is not needed [14]. As a result, it is often desirable to reduce the T_R by introducing molecules such as gadolinium ions that reduce the T_1 of the solution [59].

Magnetic Resonance Velocity (MRV) Imaging

MRV techniques are a powerful and non-invasive way to study fluid flow, such as on the pore scale of porous media [60]. There are few other ways to non-invasively study these systems on this scale, and the use of MRV measurements to quantify fluid flow through these systems can inform transport models on different time and length scales [61]. To encode the image for velocity, a PGSE gradient pair is applied in addition to the imaging gradients. Similar experimental imaging challenges to those discussed above will also come into play. Velocity is encoded in the phase of the signal by the PGSE gradient pair with $\int_0^t \left(\int_0^{t'} \bar{g} * (t'')dt'' \right) dt' = g\delta\Delta$ as discussed earlier, so care must be taken to

account for all of the phase effects on the final signal. Images taken of flowing samples are generally normalized with an image taken of an identical but non-flowing sample to cancel out the imaging gradient phase effects.

Determination of Experimental Noise Limited Velocity Resolution: The inherent signal to noise of the voltage signal acquired in a MRV experiment determines the velocity resolution. To determine the velocity resolution of MRV measurements, we acquired MRV data on a fluid flow of known velocity spatial distribution, specifically laminar flow in a capillary tube or Poiseuille flow [62]:

$$v_z(r) = \frac{2Q}{\pi R^2}\left(1 - \frac{r^2}{R^2}\right) \qquad (4.3)$$

where Q is the volumetric flow rate and R is the inner radius of the capillary.

MRV measurement of the spatial distribution of velocities at a resolution of 39.06 μm x 39.06 μm x 39.06 μm provided the expected velocity histogram for parabolic flow, and the average velocity $\langle v \rangle$ was verified by independent measurement of volumetric flow rate $Q = \langle v \rangle \pi R^2$. Thus, the velocity uncertainty may be determined directly from the capillary data.

Velocities were measured for water flowing in a 1 mm capillary at an average velocity of 3.54 mm/s. The velocity data from one slice of a 3D data set is shown in Figure 4.3.a, and the velocity histogram from data taken from the entire 3D data set is shown in Figure 4.3.b. In this simple system of Poiseuille flow in a circular capillary the expected histogram distribution of velocities is an equal amount of every velocity between 0 mm/s and v_{max} =7.04 mm/s, see the red line in Figure 4.3.b. The experimental

velocity histogram data is shown in blue in Figure 4.3.b and is fit closely when the expected velocities are convoluted with a Gaussian point spread function (GPSF) with a variance $\sigma^2 = 0.19\ mm^2/s^2 = (0.44\ mm/s)^2$, shown in black in Figure 4.3.b.

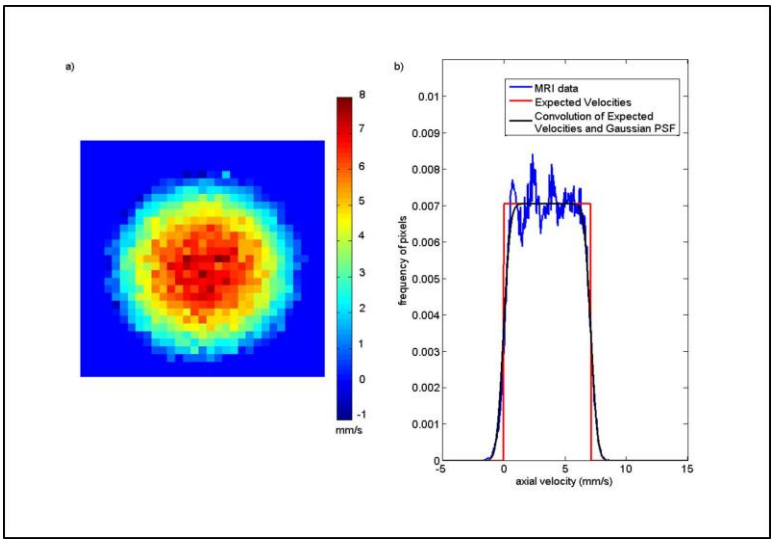

Figure 4.3. a) The MRV image shows a slice from the middle of a 3D velocity data set for water flowing in a 1 mm capillary. b) The graph shows the histogram of the distribution of velocities. The expected velocities for this system are shown in red, the experimental velocity distribution is shown in blue and the expected velocities convoluted with a Gaussian point spread function (GPSF) with a variance $\sigma^2 = 0.19\ mm^2/s^2 = (0.44\ mm/s)^2$ is shown in black.

Relaxation Mechanisms

As introduced in Chapter 3, relaxation measurements are sensitive to a range of sample effects. This section will give a background of several relaxation mechanisms: surface relaxation, magnetic field inhomogeneities, and hydrogen exchange.

Surface Relaxation

In addition to molecular interactions with other molecules which lead to T_2 relaxation, the molecules in complex samples will also interact with surfaces. The

magnetic relaxation due to surface interactions will depend on the magnetic characteristics of the surface, since NMR experiments are performed in a magnetic field. This type of relaxation is dependent on self-diffusion as the number of molecules that interact with the surface will be dependent on the time scale of the experiment. Brownstein and Tarr [34] calculated the relaxation effects for water confined in simple geometries such as between parallel plates, within spheres, and within cylinders. Their goal was to account for the increased relaxation observed for water confined within bacterial cells but their results can be generalized to model other more complex geometries. To analyze this problem they analytically solved for the magnetic relaxation after an excitation rf pulse, using the Bloch equations as modified by Torrey [32]:

$$\frac{dM_+(\vec{r},t)}{dt} = D_0\nabla^2 M_+(\vec{r},t) - \frac{M_+(\vec{r},t)}{T_2} \qquad (4.4)$$

First, they neglected the T_2 relaxation of the water itself as that simply adds a constant exponential decay to the final solution. In this case, there is no fluid flow or hydrogen exchange and no applied gradients, so the other terms in Equation 4.1 are not significant. The equation then becomes:

$$\frac{dM_+}{dt} = D_0\nabla^2 M_+ \qquad (4.5.a)$$

which is simply a Fick's law of diffusion type equation, where what is diffusing is the magnetic moments of the molecules in the sample. To completely solve this equation, a boundary condition and an initial condition are required. The boundary condition is a

surface boundary condition:

$$\left(\hat{n}\cdot D_0\nabla M_+ + \rho M_+\right)\Big|_S = 0 \qquad (4.5.b)$$

where $\hat{n}$ is the normal vector to the surface and ρ is a parameter that depends on the strength of the magnetic relaxation at the surface. This relaxation depends on the magnetic characteristics of the surface, and is a difficult parameter to quantify. Highly magnetic surfaces such as natural rocks containing iron will have higher ρ values than materials such as glass or plastic. This equation is analogous to a surface sink term in a reaction rate equation, where molecules that diffuse to the surface will relax at a rate defined by ρ. The initial condition is:

$$M_+\left(\vec{r},0\right) = \frac{\mathrm{M}(0)}{V} \qquad (4.5.c)$$

where V is the volume of the sample and

$$\mathrm{M}\left(t\right) = \int_V M_+\left(\vec{r},t\right)d\tau \quad (4.5.d)$$

This initial condition means that the magnetization at time zero is distributed uniformly throughout the sample. The quantity M(t) is the measured NMR signal of a CPMG pulse sequence, for example. By applying a series of π pulses, the change of M(t) in time is measured while other effects such as static magnetic field inhomogeneities are refocused.

Brownstein and Tarr then solve this set of partial differential equations in detail for planar, spherical, and cylindrical geometries. They obtain final solutions with the

form:

$$\mathrm{M}(t) = \mathrm{M}(0)\sum_{n=0}^{\infty} I_n \exp\left(\frac{-t}{T_n}\right) \qquad (4.6)$$

where T_n are the eigenvalues of interest and depend on complex functions of the length scale of interest *L*, diffusion *D*, and the surface relaxation ρ; and I_n are the normalized intensities corresponding to the different eigenvalues. (Note that this equation is similar to the sum of exponential decays discussed in Chapter 3, with the eigenvalues of the equation being multiple relaxation constants.)

Song et al [36] used dimensional analysis to obtain the relevant length scales. By separating Equation 4.5.a into time dependent $\Gamma(t)$ and spatially dependent $\phi(\vec{r})$ functions as $M_+(\vec{r},t) = \Gamma(t)\phi(\vec{r})$, the time dependent part of the equation can be easily solved to define the eigenvalues:

$$\Gamma_n(t) = C_n \exp\left(\frac{-t}{T_n}\right) \qquad (4.7.a)$$

The spatially dependent functions $\phi(\vec{r})$ now obey the Helmholtz equation:

$$\frac{\phi_n}{T_n} + D_0\nabla^2\phi_n = 0 \qquad (4.7.b)$$

with the boundary condition:

$$\left(D_0\hat{n}\cdot\nabla\phi_n + \rho\phi_n\right)\Big|_S = 0 \qquad (4.7.c)$$

Song et al [36] then reduce the problem to one dimension *x* and non-dimensionalize the equations using $x^* = x/L$ where *L* is a characteristic length scale of the system, such as

the pore size. The equations for the spatial eigenfunctions then become:

$$\frac{L^2}{D_0}\frac{\phi_n}{T_n}+\frac{d^2\phi_n}{dx^{*2}}=0 \qquad (4.8.a)$$

$$\left(\frac{d\phi_n}{dx^*}+\frac{L\rho}{D_0}\phi_n\right)\Bigg|_{x^*=1}=0 \qquad (4.8.b)$$

This leads in a straightforward way to the same regimes of relaxation length scales that Brownstein and Tarr also define:

1. $\frac{L\rho}{D_0} << \frac{L^2}{D_0 T_n}$, the fast diffusion regime. Relaxation is dominated by the first eigenmode, $n = 0$. For this case, the molecules have all experienced the wall relaxation, leading to the measurement of a single averaged relaxation. In this limit, a single T_2 time is measured and will correspond to:

$$T_2 = \frac{V}{\rho S} \qquad (4.9)$$

where V is the pore volume and S is the active surface area. This is the most common regime to encounter experimentally and leads to the use of T_2 measurements to quantify the surface to volume ratio.

2. $\frac{L\rho}{D_0} \sim \frac{L^2}{D_0 T_n}$, the intermediate diffusion regime. The higher eigenmodes, $n > 0$, will contribute some amount of relaxation to the decay. In this regime, small secondary populations are found in the T_2 distribution.

3. $\frac{L\rho}{D_0} >> \frac{L^2}{D_0 T_n}$, slow diffusion regime. In this regime the decay will be strongly affected by the higher eigenmodes $n > 0$.

In complex samples with a range of length scales, the measured T_2 relaxation can be related to the surface to volume ratio of the porous medium and can be used to obtain a pore size distribution [22]. Water within small pores will interact more with the surface than water within larger pores, leading to a distribution of measured T_2 times even when the length scale of all pores leads to the sample being in the fast diffusion regime. Water in smaller pores will relax faster due to increased surface effects, while larger pores will have longer water relaxation times. Figure 4.4 shows a schematic of this effect. The measurement of T_2 in porous structures with wall relaxation has been used for 20 years as a tool for obtaining the pore size distribution in rocks [22].

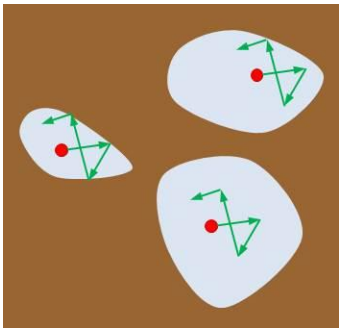

Figure 4.4. Schematic of a porous medium with a range of pore sizes. In larger pores, the diffusing water molecules are less likely to interact with the surface than in smaller pores.

Magnetic Field Inhomogeneities

In addition to surface relaxation, the presence of surface interfaces in magnetic fields will lead to magnetic field gradients that extend into the liquid phase. These are

caused by the magnetic susceptibility difference between the surface and the liquid. This effect will also be diffusion dependent, as molecules of liquid diffusing within a gradient will acquire different frequencies and dephase, as mentioned in the introduction to PGSE measurements in Chapter 2.

Hurlimann [63] calculated the effects of these gradients on measurements of rocks in magnetic fields. He defined three length scales:

1. the diffusion length $l_D = \sqrt{D_0 \tau}$, where τ is the echo spacing in the CPMG experiment.

2. the size of the pore l_S

3. the dephasing length $l_g = \sqrt[3]{\frac{D_0}{\gamma g}}$, where g is the magnitude of the magnetic field gradients.

The shortest length scale will determine which asymptotic relaxation regime describes the system. Hurlimann [63] and Mitchell et al [26] define similar asymptotic relaxation regimes:

1. $l_D << l_s, l_g$, the diffusion regime or short-time regime. If short echo times are used, or if a sample has large pores or small magnetic field inhomogeneities, the relaxation will depend only on diffusion during the echo time, leading to an exponential decay with a τ^3 dependence [20].

2. $l_s << l_D, l_g$, the motional average regime. When the length scale of the pores is the smallest, all of the molecules will have diffused throughout the pores, averaging out the

spatial dependence of the field inhomogeneities. This is analogous to the fast diffusion regime of Brownstein and Tarr.

3. $l_g << l_D, l_s$, the localization regime. The relaxation in this regime will be dependent on the diffusion of the molecules within magnetic field gradients in the pore space.

For a sample of a rock within a high magnetic field, the magnetic susceptibility difference will cause large gradients in the pore space, and the measurement of T_2 will be dominated by the dephasing of the magnetization caused by diffusion through these gradients. The value for *g* will be dependent on the magnetic field used for the measurements and the magnetic characteristics of the surfaces. For instance, sandstones have values for *g* as much as 3 orders of magnitude larger than *g* for limestones [26].

Figure 4.5 shows a schematic of diffusion through magnetic field gradients. The magnetic fields within the smaller pores will be stronger than in larger pores, again leading to faster T_2 relaxation in smaller pores than in larger pores. However, this T_2 relaxation is not dependent on surface relaxation directly, but instead dependent on diffusion through the magnetic field gradients. Measurement of T_2 relaxation at different magnetic field strengths in this localization regime will lead to different T_2 distributions for the same sample [26].

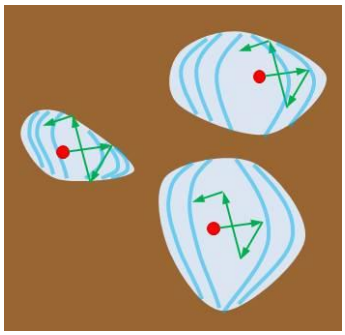

Figure 4.5. Schematic of water diffusing through magnetic field inhomogeneities caused by the applied magnetic field. As the molecules diffuse through the pore space, they will also diffuse through the magnetic field gradients and dephase, causing additional relaxation.

Hydrogen Exchange

The final relaxation effect that will be considered is the effect of molecular exchange. Take for example a sample with polymer molecules present in solution. The molecular T_2 of the polymer will be on the order of milliseconds, due to the longer correlation time of the rotational magnetic field fluctuations of a larger molecule [18]. The T_2 of water is on the order of 2 seconds. In solution, the protons on the water will exchange with protons on the polymer. Thus, the measured T_2 will have an average between the values for water and polymer, weighted by the exchange time. In addition, the hydrogen protons on the polymer will be in slightly different magnetic environments than water, leading to what is known as a chemical shift [64, 65]. As hydrogen exchange occurs, the hydrogen will have different precession frequencies, leading to additional signal dephasing analogous to diffusion within magnetic field gradients. Figure 4.6 shows a schematic of hydrogen exchange between water and a monomer block of the polymer alginate.

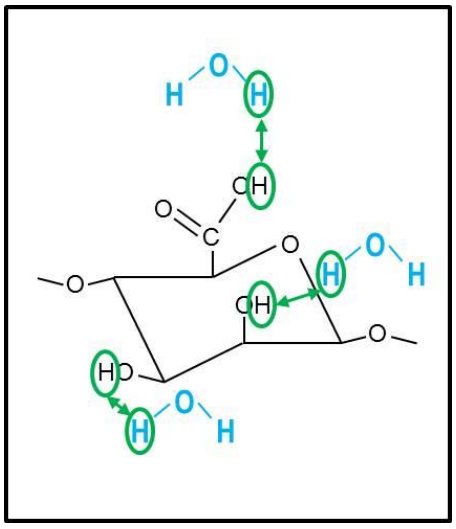

Figure 4.6. Hydrogen exchange between water and a monomer unit of the polymer alginate. The measurement of the T_2 of the solution will be influenced by both the shorter T_2 of the polymer and the chemical shift difference causing additional dephasing of the signal.

This relaxation mechanism has been utilized since the outset of NMR experimentation to study chemical reactions and polymers [24, 33, 66]. For example, considering the water protons *w* and the polymer protons *p* as the two exchangeable populations with a chemical shift difference of $\Delta\omega$ and exchange constants of $k_{wp} = k_{pw}$, the effect to the measured signal $M_+(t) = M_w(t) + M_p(t)$ can be found by solving coupled Bloch equations for each hydrogen population:

$$\frac{dM_w(t)}{dt} = \left(-\frac{1}{T_{2w}} - k_{wp}\right) M_w(t) + k_{pw} M_p(t) \qquad (4.10.a)$$

$$\frac{dM_p(t)}{dt} = \left(-\frac{1}{T_{2p}} - k_{pw} + i\Delta\omega\right) M_p(t) + k_{wp} M_w(t) \qquad (4.10.b)$$

By changing the time scale of the measurement of T_2, the effect on the magnetization due to the chemical shift difference between the different protons can be modeled [33]. The

additional effect of solvation water of the polymer leads to three coupled equations, which will be discussed in depth in Chapter 9 of this thesis.

Dynamic NMR Measurements

An introduction to PGSE experiments was provided in Chapter 2, and more advanced concepts will now be explored. Some introduction of the mathematical theory of molecular motion will first be introduced, followed by the use of PGSE experiments to measure molecular motion.

Propagator of Displacement

Self-diffusion can be related to the velocity autocorrelation function using translational motion theory [67]. The definition of an autocorrelation function $G(t)$ of a function $h(t)$ was introduced in Chapter 2 in Equations 2.16 through 2.19. In analogy with the fact that the autocorrelation function of the rotational frequency has a Fourier transform relationship with the spectral density, the self-diffusion tensor is the Fourier transform of the autocorrelation function for velocity:

$$D_{ij}(\omega) = \frac{1}{2}\int_{-\infty}^{\infty} \overline{v_i(0)v_j(t)}\exp(i\omega t)dt \qquad (4.11)$$

where i and j represent the orthogonal directions x, y, and z. The full self-diffusion tensor is then a 3x3 matrix. However, for isotropic self-diffusion the tensor will have equal non-zero values along the diagonal. The zero frequency diagonal components of

the diffusion tensor, for example in the *z*-direction, can be represented by

$$D_{zz} = \int_0^\infty \overline{v_z(0)v_z(t)}dt = \overline{v_z(0)^2}\tau_c \qquad (4.12)$$

where the definition for the correlation time τ_c was used as introduced in Equation 2.18.

For a "stationary ensemble", one particle is representative of all particles and all times, so for an arbitrary function $h(\vec{r},t)$ the average of the autocorrelation function over time is the same as the average over space. In this case, the origin of time *t* can be taken to be zero and we can say that for a particle that has moved from $\vec{r}$ at $t = 0$ to $\vec{r}'$ at $t = t'$:

$$G(t) = \overline{h(\vec{r}',t)h(\vec{r},0)} = \iint \rho(\vec{r})P_s(\vec{r},0 \mid \vec{r}',t)h(\vec{r}',t)h(\vec{r},0)d\vec{r}d\vec{r}' \qquad (4.13)$$

where $\rho(\vec{r})$ is the density of molecular spins and $P_s(\vec{r},0 \mid \vec{r}',t)$ is the transition probability or "propagator", defined as the probability that a molecule starting at position $\vec{r}$ at $t = 0$ will move to position $\vec{r}'$ at $t = t'$.

The propagator can be treated as a concentration, as it is the probability of finding a particle with a specific state. This type of treatment is known as a Smoluchowski equation or a Fokker-Planck equation [68]. Exact mathematical solutions for the propagator for a few simple sample conditions can be obtained and then generalized and used as a starting point to examine more complex conditions. For the propagator of molecular displacement, Fick's Second Law of diffusion can be written as:

$$\frac{\partial P_s}{\partial t} = -\nabla \cdot \vec{v}P_s + D_0\nabla^2 P_s \qquad (4.14)$$

For unrestricted self-diffusion with no bulk flow, the equation reduces to:

$$\frac{\partial P_s}{\partial t} = D_0 \nabla^2 P_s \qquad (4.15.a)$$

This equation can be solved exactly using the boundary conditions for unrestricted Brownian motion:

$$P_s(\vec{r},0 \mid \vec{r}',0) = \delta(\vec{r}'-\vec{r}) \qquad (4.15.b)$$

$$\lim_{\vec{r}'\to\infty} P_s(\vec{r},0 \mid \vec{r}',t) = 0 \qquad (4.15.c)$$

The first condition is equivalent to saying that the molecular displacement is uncorrelated on this time-scale, and the second condition expresses the fact that the displacement of the molecules is unrestricted. Solving these equations for diffusion along the *z*-axis and defining $Z = z'-z$, the propagator is a Gaussian function with the form:

$$P_s(Z,t) = \frac{1}{\sqrt{4\pi D_0 t}} \exp\left(\frac{-Z^2}{4D_0 t}\right) \qquad (4.16)$$

For a constant velocity in the *z*-direction v_z, the solution is obtained by adding a constant mean to the Gaussian:

$$P_s(Z,t) = \frac{1}{\sqrt{4\pi D_0 t}} \exp\left(\frac{-(Z-v_z t)^2}{4D_0 t}\right) \qquad (4.17)$$

The variance of this Gaussian function is:

$$\overline{Z^2(t)} = 2D_0 t \qquad (4.18)$$

which is consistent with Einstein's derivation [69].

Velocity Fluctuations

This Gaussian relationship can also be derived using the Langevin equation for fluctuating velocity:

$$m\frac{\partial \vec{u}(t)}{\partial t} = -\frac{m}{\tau_c}\vec{u}(t) + \vec{R}(t) \qquad (4.19)$$

where $\vec{u}(t)$ represents the randomly fluctuating velocity, τ_c is the correlation time of the velocity fluctuations, *m* is the mass of the particle that is undergoing Brownian motion, and $\vec{R}(t)$ is the random force of the surrounding fluid particles on the Brownian motion particle. This equation is simply a force balance. The force acted on the particle is divided into a viscous term $-\frac{m}{\tau_c}\vec{u}(t)$ that depends on the velocity and the stochastic force $\vec{R}(t)$ caused by collisions with the surrounding particles. When the displacement is uncorrelated as assumed in the initial conditions in Equation 4.15.b and 4.15.c, the velocity auto-correlation takes the form of an exponential decay:

$$\overline{u(0)u(t)} \sim \exp\left(-\frac{t}{\tau_c}\right) \qquad (4.20)$$

Assuming that $\vec{R}(t)$ is a Gaussian function, Kubo [70] shows how to solve these equations to obtain:

$$\overline{Z^2(t)} = 2D_0\left(t - \frac{1-\exp\left(-\frac{t}{\tau_c}\right)}{\frac{1}{\tau_c}}\right) \qquad (4.21)$$

By starting from the Langevin equation for velocity rather than the Smoluchowski equation for displacement, the effect of the correlation time of the velocity auto-correlation is derived. However, in the long time limit, the form of the variance of the displacement reduces to:

$$\overline{Z^2(t)} = 2D_0 t = 2\overline{v_z^2}\tau_c t \qquad (4.22)$$

which is again Einstein's result. For self-diffusion in liquids, the velocity autocorrelation time is on the order of 10^{-13} seconds, which is much shorter than the time scale seen using NMR so the short time limit of diffusion will not be encountered.

However, for turbulent dynamics or other applications, the velocity autocorrelation may be on the order of milliseconds and the effect may be measured using NMR, so it is useful to understand the short-time limit:

$$\overline{Z^2(t)} = \overline{v_z^2} t^2 \qquad (4.23)$$

which shows that the variance approaches the ballistic motion limit.

Time Dependent Diffusion

An ensemble system with zero flow is approximately Brownian motion $\overline{Z^2(t)} = 2D_0 t$ (see equation 4.22) and the variance of the displacement scales linearly with time. However, if some of the molecules in the sample are not undergoing Brownian motion, the variance in the displacement that is measured may no longer be linear with time. Diffusion processes that are not linear in time are sometimes referred to as anomalous diffusion [71]. For instance, for restricted diffusion within a pore space the molecules have a maximum displacement based on the size of the pore. Only after they

have diffused this maximum distance will the displacement measured be constant with time. For this situation and others, it is useful to define an "apparent" diffusion coefficient that changes with time:

$$\overline{Z^2(t)} = 2D_{app}(t)t \Rightarrow D_{app}(t) = \frac{\overline{Z^2(t)}}{2t} \qquad (4.24)$$

For example, Mitra, Sen, and Schwartz [72] demonstrate the calculation of the short time diffusion coefficient in a porous media $D_{pm}(t)$ with no bulk flow:

$$D_{pm}(t) = D_0 - AD_0\sqrt{D_0 t} + O(t) \qquad (4.25)$$

where *A* is a constant that depends on the geometry and the surface to volume ratio of the porous media. The measured diffusion is then reduced from self-diffusion due to the pore structure restrictions. The measurement of time dependent diffusion can thus be used as a tool to study porous media similar to the use of NMR relaxation measurements [5].

Hydrodynamic Dispersion

For fluids that are undergoing stationary random flow, the motion of the fluid can be separated into three different motions with three different length and time scales. The total displacement $\vec{r}_{ij}(t)$ of a molecule labeled *j* within a representative fluid element *i* can be represented as:

$$\vec{r}_{ij}(t) = \vec{v}t + \vec{u}_i t + \vec{r}_j(t) \qquad (4.26)$$

where $\vec{v}$ represents the constant bulk velocity of the fluid element *i* with a constant random velocity fluctuation of $\vec{u}_i$, and $\vec{r}_j(t)$ represents the diffusive displacement of

molecule *j*. The diffusive motion of molecule *j* is characterized by a correlation length of $L \sim \sqrt{D_0 \tau_{cr}}$ where τ_{cr} is the correlation time associated with the self-diffusion of the molecule. The correlation length of the fluid element *i* is $L \sim \sqrt{\overline{u^2}}\tau_{cu}$ where τ_{cu} is the correlation time associated with the velocity fluctuations. As long as the three terms in this equation are stochastically independent, the length scales of the fluid element and the molecule may be separated.

For instance the phase shift for a PGSE experiment of stationary random flow, i.e. when $\vec{v}$ and $\vec{u}_i$ are time independent is:

$$\phi_{ij}(t) = \gamma \int_0^t \vec{g}^*(t') \cdot \vec{r}_j(t') dt' + \gamma \int_0^t t' \vec{g}^*(t') \cdot (\vec{v} + \vec{u}_i) dt' \qquad (4.27)$$

For the time scale of interest in PGSE NMR, $\tau_{cr} << t << \tau_{cu}$ and the ensemble average of these two terms may be separated:

$$E(g) = \overline{\exp\left[i\phi_{ij}(t)\right]} = \overline{\exp\left[i\gamma \int_0^t \vec{g}^*(t') \cdot \vec{r}_j(t') dt' \right]} \; \overline{\exp\left[i\gamma \int_0^t t' \vec{g}^*(t') \cdot (\vec{v} + \vec{u}_i) dt' \right]} \qquad (4.28)$$

where the first term represents the diffusive attenuation of the signal and the second term the phase shift due to velocity. On this time scale, the correlation time of the molecular fluctuations is much less than the time of the experiment and causes a random dephasing of the signal rather than a coherent phase shift. The second term can be further separated into the phase shift caused by coherent flow and the phase shift from the random velocity

fluctuations:

$$\overline{\exp\left[i\gamma \int_0^t t' \bar{g}^*(t') \cdot (\bar{v} + \bar{u}_i) dt' \right]} = \exp\left[i\gamma \int_0^t t' \bar{g}^*(t') \cdot \bar{v} dt' \right] \overline{\exp\left[i\gamma \int_0^t t' \bar{g}^*(t') \cdot \bar{u}_i dt' \right]} \qquad (4.29)$$

The coherent velocity will contribute a phase shift, while the velocity fluctuations will contribute to random dephasing but on a different time scale than the molecular diffusion.

In this way, PGSE experiments can be used to study hydrodynamic dispersion, sometimes called Taylor dispersion [61, 73-78]. This type of fluid mixing is caused by diffusion of molecules across velocity stream lines which results in velocity fluctuations of the diffusing individual fluid elements. For laminar Pouisuelle flow through a circular capillary, the velocity distribution in an Eulerian frame of reference was shown in Equation 4.3. However, since PGSE NMR measures molecular motion in a Lagrangian sense, the effect of hydrodynamic dispersion can be seen by measuring the signal attenuation as a function of observation time [79]. As the observation time Δ is increased, the contribution to random dephasing of the signal due to the velocity fluctuations in addition to molecular self-diffusion will be observed.

For example by measuring the short-time apparent diffusion coefficient, hydrodynamic dispersion can be related to permeability *k* using Darcy's Law $k = \frac{-\varepsilon \mu v}{\nabla p}$, where ε is the porosity of the porous medium, μ is the viscosity of the fluid, *v* is the superficial velocity, and ∇p is the pressure drop across the porous medium. The short-time dispersion coefficient $D_{app}(t)$ in the case of low Reynolds number flow through a

macroscopically homogeneous porous media is derived in [4]:

$$D_{app}(t) = D_{pm}(t) + \frac{\overline{\vec{u} \cdot \vec{u}'}}{6} t - \frac{v^2 \varepsilon D_0}{18k} t^2 + O\left(t^{5/2}\right) \qquad (4.30)$$

The measurement of $D_{app}(t)$ as a function of time for water flowing through a model porous medium is shown in Figure 4.7. The model porous medium in this case is a bead pack constructed of 241 μm diameter monodispersed polystyrene beads packed into a 10 mm outer diameter glass tube. The short-time diffusion coefficient data are circles, with the solid line a fit to Equation 4.30 and the dotted line is the linear prediction using only the first two terms which do not take into account the permeability. D_0 is taken to be 2 x 10^{-9} m^2/s and $D_{pm}(t)$ was measured for the bead pack without flow. The linear term was estimated from the dotted line which is a fit to the first data points. The porosity was estimated by comparing the measured superficial velocity to the known applied constant flow rate.

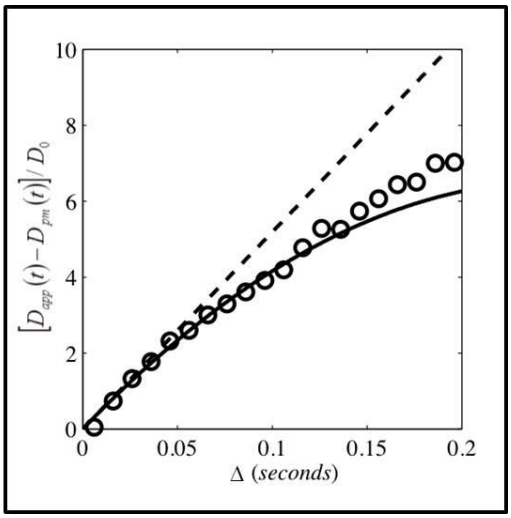

Figure 4.7. Short-time pre-asymptotic dispersion. Experimental parameters: $\delta = 0.7ms$, $\varepsilon = 0.42$, k = 7.4 x 10^{-11} m^2, v = 5.7 x 10^{-4} m/s.

Analysis of PGSE Data Using $\vec{q}$-space

Applying the propagator definition to the phase shift and signal attenuation of a PGSE experiment in the narrow gradient pulse limit, we can derive useful mathematical formulations to interpret the data [80]. If a gradient with duration δ and amplitude *g* is applied, the phase shift of a particle at position $\vec{r}$ will be $\gamma\delta\vec{g}\cdot\vec{r}$. If the particle has moved to $\vec{r}'$ during the time Δ, the phase shift will be $\gamma\delta\vec{g}\cdot(\vec{r}'-\vec{r})$. The NMR signal that will be collected by the PGSE experiment will be the ensemble average of these phase shifts weighted by the propagator:

$$E(\vec{g}) = \int \rho(\vec{r}) \int P_s(\vec{r},0 \mid \vec{r}',\Delta) \exp\left[i\gamma\delta\vec{g}\cdot(\vec{r}'-\vec{r})\right] d\vec{r}\, d\vec{r}' \qquad (4.31)$$

Defining $\vec{R} = (\vec{r}'-\vec{r})$ and $\vec{q} = \frac{\gamma\delta\vec{g}}{2\pi}$ and the average propagator as:

$$\overline{P_s}(\vec{R},\Delta) = \int \rho(\vec{r}) P_s(\vec{r},0 \mid \vec{r}',\Delta) d\vec{r} \qquad (4.32)$$

we can write the NMR signal as:

$$E(\vec{q}) = \int \overline{P_s}(\vec{R},\Delta) \exp(i2\pi\vec{q}\cdot\vec{R}) d\vec{R} \qquad (4.33)$$

which is another Fourier transform relationship, in this case between the vector $\vec{q}$ and molecular displacement $\vec{R}$. For most NMR experiments, the average propagator applies to all the spins in the sample. Combining the equation for the propagator with self-diffusion and zero velocity, and applying the gradient along the *z* direction:

$$E(q) = \int_{-\infty}^{\infty} \frac{1}{\sqrt{4\pi D\Delta}} \exp\left(\frac{-Z^2}{4D\Delta}\right) \exp(i2\pi qZ) dZ \quad (4.34)$$

This represents the Fourier transform of a Gaussian function and results in another Gaussian function:

$$E(q) = \exp\left(-4\pi^2 q^2 D\Delta\right) \qquad (4.35)$$

Sampling negative and positive values of q-space by changing the applied gradients and then applying a Fourier transform to the acquired data yields the propagator of displacement. In the simple case of molecular self-diffusion, both the propagator and the acquired data will be Gaussian distributions around a mean of 0. The addition of a constant velocity term (see Equation 4.17) results in a phase shift in the acquired signal:

$$E(q) = \exp\left(-4\pi^2 q^2 D\Delta + i2\pi q v_z \Delta\right) \quad (4.36)$$

which is the same result obtained earlier in Equation 2.48, but in terms of q and without a correction for finite gradient times. These simple examples have exact mathematical solutions, however the acquisition of propagator PGSE data for more complex systems such as flow through porous media can be interpreted using these concepts.

ADVANCED NMR CONCEPTS – EXPERIMENT

The concepts discussed in the last chapter will now be demonstrated with data obtained on several different experimental systems: natural rocks, model porous media, and gels. The data presented in this chapter will contribute to publications resulting from larger collaborative projects with the geosciences department at Montana State University and mathematical modelers at Pacific Northwest National Laboratory in Richland, Washington.

Change in the Pore Structure of Sandstones and Limestones Resulting from Dissolution due to Supercritical Carbon Dioxide

The storage of supercritical CO_2 (sc-CO_2) in depleted oil reservoirs is being investigated around the world as a way to keep CO_2 out of the atmosphere in a process known as carbon sequestration [81]. Pumping sc-CO_2 into oil reservoirs that have been pumped dry using traditional methods is also used to enhance oil recovery [82]. The effect of pumping sc-CO_2 underground into the surrounding rock cap is not well understood, but the pore structure of rocks around carbon sequestration sites is known to be altered by the presence of sc-CO_2 through dissolution processes or rock fracturing [83]. In collaboration with the geosciences department, inline chemical tests during the pumping of sc-CO_2 through a rock, referred to here as the sc-CO_2 challenge, were done to study changes to the rocks as a function of time during the challenge. MR experiments were performed before and sc-CO_2 challenge to assess pore structure changes.

Experimental System

A high pressure system was developed to analyze 25 mm diameter and 100 mm long rock cores. Two types of rock were investigated in this study: Berea sandstone (Cleveland Quarries, Ohio) and Madison limestone (Black Hills, South Dakota). The rocks were first saturated with brine and analyzed using MRI and relaxation correlations as described below. The rocks were then challenged with sc-CO_2. Brine at two different concentrations of salt (1 mg/L and 10 mg/L) saturated with sc-CO_2 was pumped through the rock at relevant temperatures (50 degrees C and 95 degrees C) and pressures (10 MPa). Cores were flooded with approximately 1700 mL of the brine and sc-CO_2 mixture. Chemical dissolution tests, permeability tests, and pH measurements were conducted inline during the sc-CO_2 challenge. The rocks were then re-saturated with brine and MRI and relaxation correlations were repeated. The sandstone was shown to change very little in the chemical dissolution, permeability, and pH tests; while the limestone had a large increase in the pH and a 6-fold increase in permeability during the sc-CO_2 challenge, indicating that the limestone dissolved. MR results that corroborate these chemical dissolution test results are presented below.

MR Imaging Experiments

Physical changes in pore volume and structure were assessed by comparing two and three dimensional Magnetic Resonance (MR) images of the cores taken before and after the experimental sc-CO_2 challenge. MR imaging has been utilized to study rocks since the development of the technique 30 years ago [84]. The use of MR images to spatially map and calculate porosity has been extensively studied [85-87]. However, due

to sample size limitations and magnetic field inhomogeneities caused by magnetic susceptibility differences in high magnetic fields, signal-to-noise ratio challenges are significant using laboratory magnets. MR imaging experiments were conducted on a Bruker 300 MHz super-wide bore magnet networked to an AVANCE spectrometer. This study utilized a novel super-wide-bore 7 T magnet (Bruker) with a radio frequency coil of 35 mm diameter. This enabled the analysis of 25 mm diameter by 100 mm length core samples, which also allowed the sc-CO_2 challenge experiments to be averaged over a large sample. MR data were obtained of the same rocks without any additional sample processing after the sc-CO_2 challenge.

Two types of imaging experiments were conducted: multi-slice spin echo and 3D spin echo images [14]. Multi-slice experiments used a slice-selective r.f. pulse to excite a slice thickness of 1.5 mm in the axial direction and each 2D slice image had an in-plane resolution of 0.27 mm x 0.27 mm. 12 slices with a gap of 2.5 mm between each slice were obtained for each experiment, for a total coverage in the axial direction of 45.5 mm. Two experiments were performed with interleaving slices to ensure complete sampling in the axial direction of the rock core. 3D spin echo images began with a r.f pulse which excited the whole sample and then used two phase-encoding gradients and a read gradient, leading to a 3D image. 3D experiments had a resolution of 0.47 mm x 0.55 mm x 0.55 mm and a FOV of 50 mm x 35 mm x 35 mm. The total experimental time for the set of experiments was about 30 hours. The bottom half of each rock core was imaged first and then the rock was repositioned to image the top half. After imaging, the cores were removed and challenged with sc-CO_2 and then the cores were placed back in the

MRI instrument and the experiments were repeated in the same order with the cores in the same positions. Images were normalized with total signal intensity from the middle part of the core, avoiding the background noise around the core.

MR Imaging Results and Discussion

Images of both the Berea sandstone and Madison limestone are shown in Figure 5.1. The differences between before and after challenge images were quantified by normalizing the images, subtracting the normalized signal intensities pixel-by-pixel, then squaring the difference. For the limestone, the greatest pixel differences are shown to correspond with regions of high pixel intensity in the pre-challenge images. This indicates that sc-CO_2 increases permeability by dissolution along preferential flow pathways. Images of the sandstone sample showed very little difference before and after challenge. This result is consistent with the chemical dissolution tests performed in parallel by our collaborators in Geosciences. The chemical dissolution tests demonstrated that the limestone dissolved while the sandstone did not, and MR images provide additional spatial information about the dissolution pathways. MR 2D relaxation correlation data was also consistent with dissolution along preferential pathways, as discussed in the next section of this chapter.

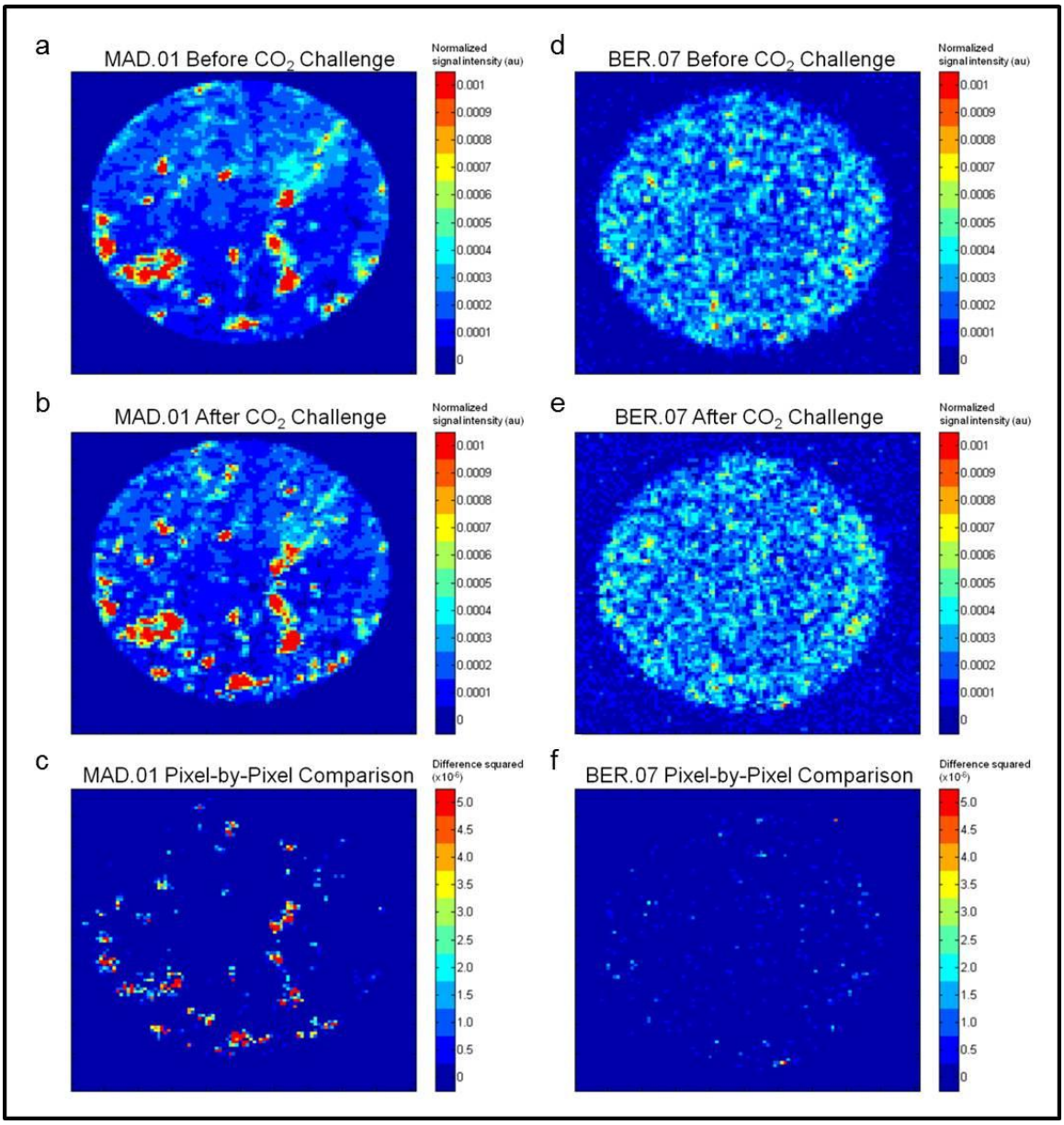

Figure 5.1. Examples of pre-challenge (a,d) and post-challenge (b,e) NMR spin echo images of selected axial slices near the middle of core samples of Madison limestone (MAD.01) (a,b) and Berea sandstone (BER.07) (d,e). (c,f) Pixel-by-pixel comparisons between the pre- and post-challenge images. The difference was quantified by subtracting the normalized intensities and squaring the difference for each pixel as discussed in the text.

Figure 5.2 shows 3D images of the Madison limestone before and after sc-CO_2 challenge. The pre- and post-challenge images shown are each combinations of two separate 3D images, one experiment for the top 50 mm of the rock core and another experiment for the bottom 50 mm of the core. The images were created using a Matlab function that creates a surface plot connecting pixels with the same intensity. The isosurfaces of all four images represent 0.025% of the total signal intensity. The images show that the pore structure is more connected after the challenge. The increase in pore space is again clustered in regions which were porous before challenge as well, in another indication that pore dissolution occurred along the preferential flow pathways.

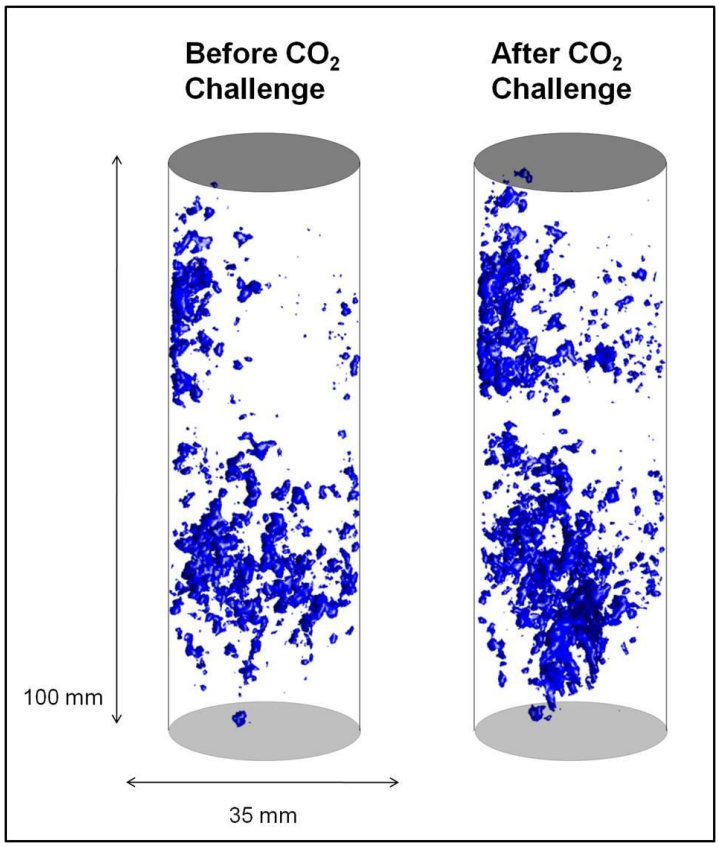

Figure 5.2. Three dimensional isosurface images derived from normalized signal intensity of pre- and post-challenge 3D spin echo image data from sample MAD.01. Resolution of images is 0.47mm x 0.55mm x 0.55mm.

Multi-Dimensional Relaxation Correlation Experiments

$T_2 - T_2$ relaxation measurements were acquired using the pulse sequence in Figure 3.3b [25, 39, 51]. These experiments used a τ of 200 μs, a CPMG echo train of 512 points, indirect encoding for T_2 of 32 points, and mixing times τ_m of 5 and 50 ms. These parameters were chosen after initial testing showed that using a shorter τ value and more points led to significant r.f. heating of the rock. For all the samples, Inverse Laplace Transform (ILT) of the data converts the spin relaxation decays into 2D relaxation maps using 2D non-negative least squares [35, 37] as discussed in Chapter 3. $T_2 - T_2$ experiments were performed before and after sc-CO_2 challenge on both the top and bottom halves of each rock.

Multi-Dimensional Correlation Results and Discussion

Example of $T_2 - T_2$ distributions for the two different rocks, limestone and sandstone, are shown in Figure 5.3. The limestone has a T_2 distribution along the diagonal centered around a higher T_2 than for the sandstone due to larger pores, as also shown in the MR images. The use of two different mixing times, 5 ms and 50 ms, allows further quantification of the pore size distribution. Cross peaks are not present in the limestone at either mixing time, indicating that molecules of water have not diffused throughout the pore, while the sandstone shows cross peaks that increase in intensity when the mixing time is increased from 5 ms to 50 ms. The sandstone has a majority of pores with diameters 1 μm to 100 μm, with a mean diameter of about 10 μm. In contrast,

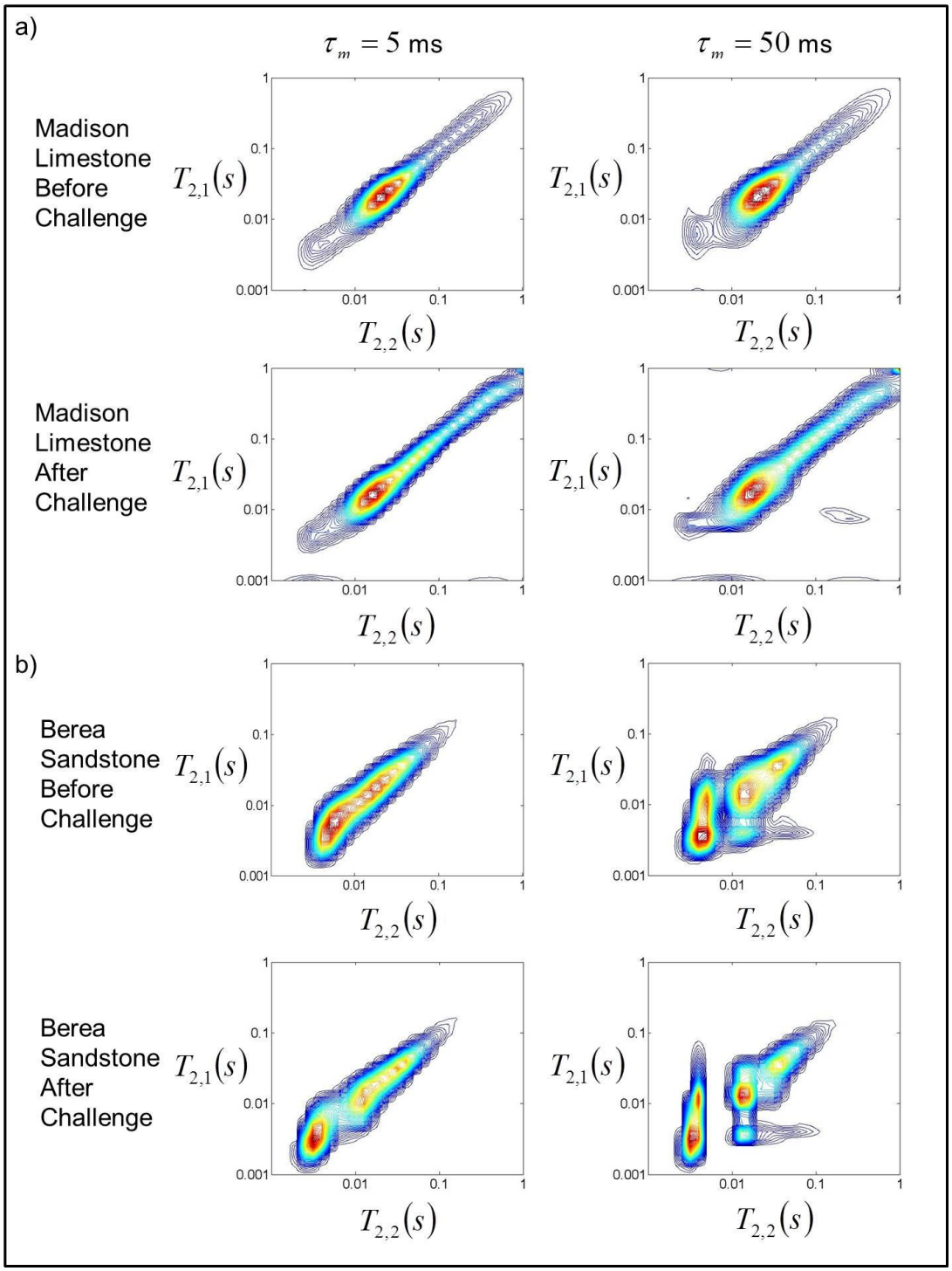

Figure 5.3. $T_2 - T_2$ distributions for two different mixing times, 5 ms and 50 ms, obtained on two different rocks, a) Madison limestone (MAD.01, bottom half of sample) and b) Berea sandstone (BER.07, top half of sample). Experiments were performed before and after rocks were challenged with sc-CO_2.

limestone has a majority of pore diameters larger than 100 μm [88]. Water molecules require over 2 seconds to diffuse 100 μm. Therefore for mixing times of 5 ms and 50 ms the molecules of water will not diffuse throughout the whole pore space and cross-peaks in the $T_2 - T_2$ distribution are not expected. In addition, the internal gradient strength for sandstones is two orders of magnitude larger than for carbonate rocks such as limestone resulting in cross peaks [63]. Due to the challenge by sc-CO_2 that dissolved some of the limestone and led to larger pores, there is a shift to longer T_2 along the diagonal for the limestone after the challenge. However, the distribution did not change for the sandstone after the challenge indicating that the pore size distribution was not affected by the sc-CO_2 challenge.

Analysis of Biofilm Growth in the Pore Structure of Sandstone

The following experiments were performed to investigate whether $T_1 - T_2$ and $T_2 - T_2$ relaxation correlation experiments could be used to detect biofilm growth in natural porous media. A biofilm is produced when certain types of bacteria attach to surfaces and start to produce and grow within a polymeric matrix called the extracellular polymeric substance (EPS) [89, 90], as shown in Figure 5.4.

This EPS matrix is composed of a number of polysaccharides, some DNA, RNA, and proteins [91]. The bacteria within the biofilm are able to communicate with each other in different ways and are much harder to remove and eradicate from the system. The growth of biofilms in porous media has negative consequences such as the biofouling of reverse osmosis membranes, but also positive potential uses such as a

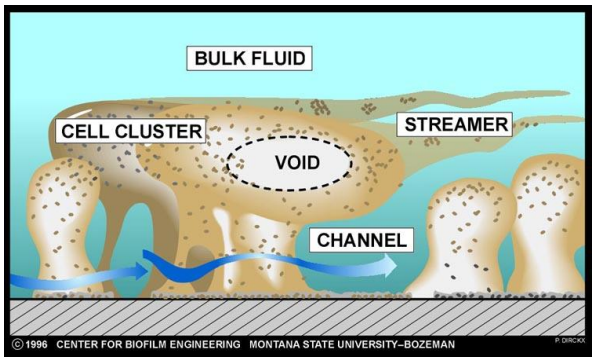

Figure 5.4. Schematic of a biofilm. The biofilm is composed of bacteria living within the EPS matrix which forms different structures depending on growth conditions.

bioremediation barrier in the subsurface [92]. Biofilm growth as a biobarrier has been investigated as a way to contain nuclear waste spills and as a means of plugging the pore structure of the rock cap around carbon sequestration sites [93, 94]. The non-invasive detection of biofilm growth in porous media is of interest for other applications as well, as will be discussed in Chapter 7 of this thesis. The hypothesis for this set of experiments was that the growth of the biofilm would alter the surface relaxation characteristics and lead to different relaxation results consistent with the theories of Brownstein and Tarr as discussed in Chapter 4.

Experimental System

Experiments were performed on a natural Berea sandstone. Samples were 6 mm in diameter and ranged from 10 to 20 mm in length. The rocks were first saturated under pressure driven flow with brine (40 g/L NaCl in distilled water) and then BHI growth media for initial testing. For biofilm growth, *Bacillus mojavensis* was chosen because it has been shown that this type of bacteria is resilient to exposure to sc-CO_2 [94]. To begin biofilm growth, *B. mojavensis* in the log growth stage was pumped into the pore structure

of the rock. Flow was then turned off for 4 hours to allow the bacteria to attach to the walls of the pores. The BHI growth media was then turned back on at a flow rate between 50 and 100 mL/hr, and biofilm was grown for 24-36 hours until pressure had built up in the flow system. The flow loop began to develop leaks at approximately 25 psi of pressure drop across the rock, so at this point the BHI flow was stopped. The rocks were then removed from the flow loop, wrapped in Teflon tape, and tested in a 10 mm NMR tube. A schematic of the flow loop is shown in Figure 5.5.

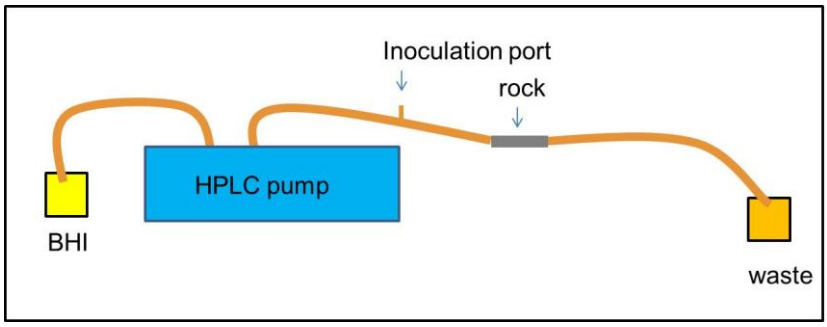

Figure 5.5. Flow system used to saturate rocks and grow biofilms using pressure driven flow.

NMR measurements were made using a Bruker AVANCE 300 MHz spectrometer, a 10 mm saddle radio frequency (rf) coil, and available magnetic field gradients of 1.5 T/m. $T_1 - T_2$ and $T_2 - T_2$ experiments were acquired using the pulse sequences in Figure 3.3.a and 3.3.b. $T_2 - T_2$ parameters used were the same as detailed above for the previous study. $T_1 - T_2$ experiments used 32 logarithmically spaced t_1 encoding points and τ of 200 μs.

Results and Discussion

Five different Berea rock samples were first saturated with brine, and $T_1 - T_2$ and $T_2 - T_2$ experiments were performed. The brine was then replaced with the growth media BHI and the measurements were repeated. A biofilm was then grown through the pore structure of the rock and measurements were repeated. The range of T_2 values was consistent in all five rocks tested indicating that the range of pore sizes was similar for all Berea samples. A representative data set is shown in Figure 5.6.

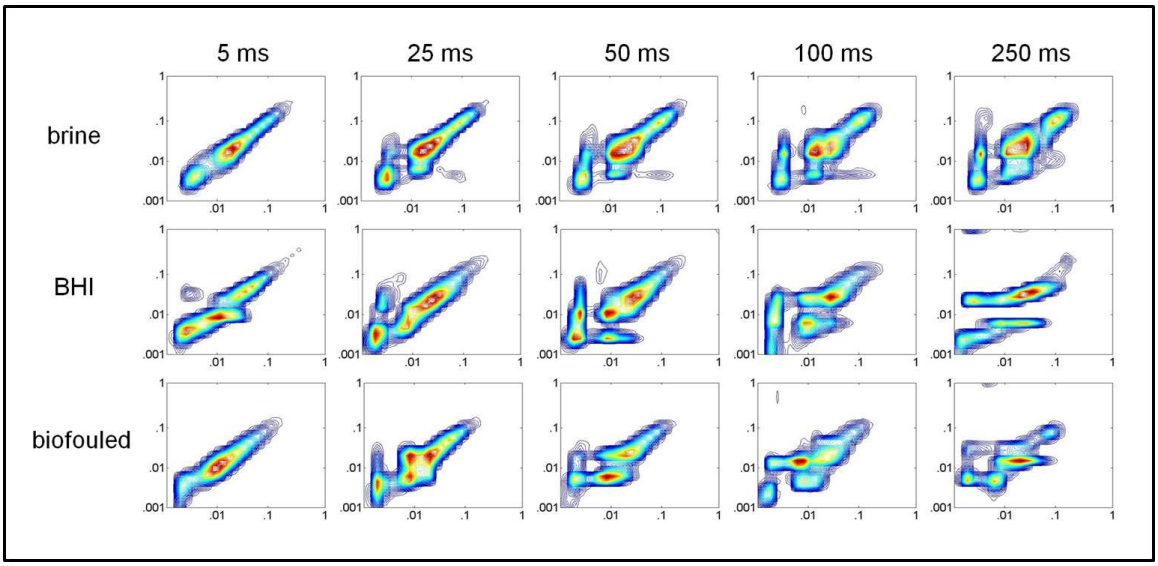

Figure 5.6. Set of $T_2 - T_2$ maps for five different exchange times for a Berea rock core sample with brine, BHI and biofilm. Five different rock samples were tested and the data set shown is representative of all five samples.

$T_2 - T_2$ experiments with a range of τ_m mixing times between 5 and 250 ms are shown. The development of cross peaks at longer exchange times is consistent with diffusion in internal gradients on the length scale of the pore sizes [95]. For example, for a 25 ms exchange time, water molecules are expected to diffuse about 10 μm, which is

the mean pore size for Berea sandstone [96]. Cross peaks continue to develop from 50 to 250 ms, also consistent with the majority of pores ranging from 10 to 40 μm in size. The T_1 of the molecules in the smaller pores is about 300 ms so longer exchange times were not possible as T_1 relaxation during the exchange time causes significant signal loss.

There were no consistent trends evident in the changes to the cross-peaks with the addition of growth media or biofilm. Statistical analysis of all five samples of Berea rock showed that there were no consistent trends in the distributions that could be attributed to either growth media or biofouling. Observed changes in any one sample were less than the variations observed between samples. For rocks with pore sizes between 10 and 100 μm tested at high field (7 T), the susceptibility difference between the rock and the fluid will cause internal gradients that will dominate the signal relaxation [63] known as the localization regime. Since the growth of the biofilm does not significantly alter the diffusion of the water in the pores [97], the diffusion within the internal gradients will still be the dominant mode of relaxation.

An example of a $T_1 - T_2$ distribution for a rock saturated with brine is shown in Figure 5.7. Although the measured T_2 varies over two orders of magnitude consistent with the $T_2 - T_2$ experiments, the T_1 only varies between 300 ms and 1 second. This result shows that the internal gradients caused by the high magnetic field affect T_2 relaxation much more than T_1 relaxation [26]. The significant impact of magnetic field inhomogeneity complicates direct interpretation of the $T_2 - T_2$ data but is consistent with samples in the localization regime. Relaxation correlation experiments performed before

and after biofilm growth were therefore unable to detect the biofilm growth within the pore structure of a rock measured in a high magnetic field.

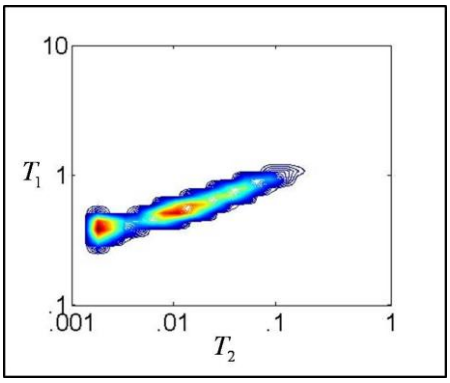

Figure 5.7. $T_1 - T_2$ of a Berea sandstone saturated with brine.

High Resolution Velocity Images of Fluid Flow through a Porous Medium

Fluid flow through porous media is of interest for a wide range of fields. Non-invasive detection of fluid flow on a pore scale is experimentally difficult so mathematical models are often developed and used to study fluid flow under different conditions [98-105]. Two approaches are commonly taken to model fluid flow: computational fluid dynamics simulations (CFD) which use finite-element analysis and lattice-Boltzmann (LB) simulations which use a particle based approach. These techniques numerically solve the Navier-Stokes equations for incompressible fluid flow:

$$\frac{\partial \vec{u}}{\partial t} + \vec{u} \cdot \nabla \vec{u} + \frac{1}{\rho} \nabla p = \eta \nabla^2 \vec{u} \quad (5.1)$$

$$\nabla \cdot \vec{u} = 0 \quad (5.2)$$

where $\vec{u}$ is the velocity of the fluid element, ρ is the density of the fluid, p is the pressure, and η is the dynamic viscosity of the fluid. These equations can be solved

analytically for simple geometries, but complex geometries such as randomly packed porous media require numerical methods to solve for the flow field. In recent years computing power has increased so that complex geometries in two and three dimensions can be simulated in a reasonable amount of time. The following experimental study used high-resolution MRV images of fluid flow through a random bead pack model porous media to validate CFD simulations developed by collaborators at Pacific Northwest National Laboratory.

Experimental System

The bead pack used for MRI measurements was constructed of a 10 mm O.D., 8.76 mm I.D. glass NMR tube with home-built PEEK fittings and PTFE tubing (GE Scientific). The tube was filled with 500 μm O.D. monodispersed polystyrene beads (Duke Scientific, Inc.). For the MRV experiments, a HPLC pump (Pharmacia) was used to flow distilled water at 100 mL/hr through the bead pack. A solution of gadolinium ions (Magnevist) was added to the water to accelerate the magnetic relaxation time to allow faster sequence repetition (T_R = 100 ms) and hence reduce experimental time.

MRI data was acquired on a 300 MHz magnet networked to a Bruker AVANCE III spectrometer and a Micro2.5 imaging probe with gradients of 1.482 T/m in all three spatial directions. 3D MRI images used for the porous media grid validation were obtained using a standard spin-echo imaging pulse sequence which was optimized to minimize the experimental echo time and hence maximize the diffusion limited resolution. Non-flowing high resolution images with a field of view (FOV) of 20 mm x 10 mm x 10 mm and 1024 x 512 x 512 pixels, resulting in an isotropic voxel size of

19.53 μm x 19.53 μm x 19.53 μm, were obtained over the course of 72 hours, see Figure 5.8.a.

3D MRV experiments with a FOV of 20 mm x 10 mm x 10 mm and 512 x 256 x 256 pixels, resulting in a voxel size of 39.06 μm x 39.06 μm x 39.06 μm were obtained with encoding for velocity in all three directions. An axial slice through the 3D velocity map is shown in Figure 5.8.b. A 3.75 ms echo time was used to accommodate the observation time for velocity $\Delta = 2$ ms with gradient duration of $\delta = 1$ ms. In order to obtain two different gradient encoded images from which to evaluate the phase difference proportional to velocity, a positive and negative g = +/-0.1482 T/m were applied, requiring 36 hours for acquisition. A gradient phase roll in the direction of fluid flow was corrected by applying a straight line correction to every voxel within each slice and

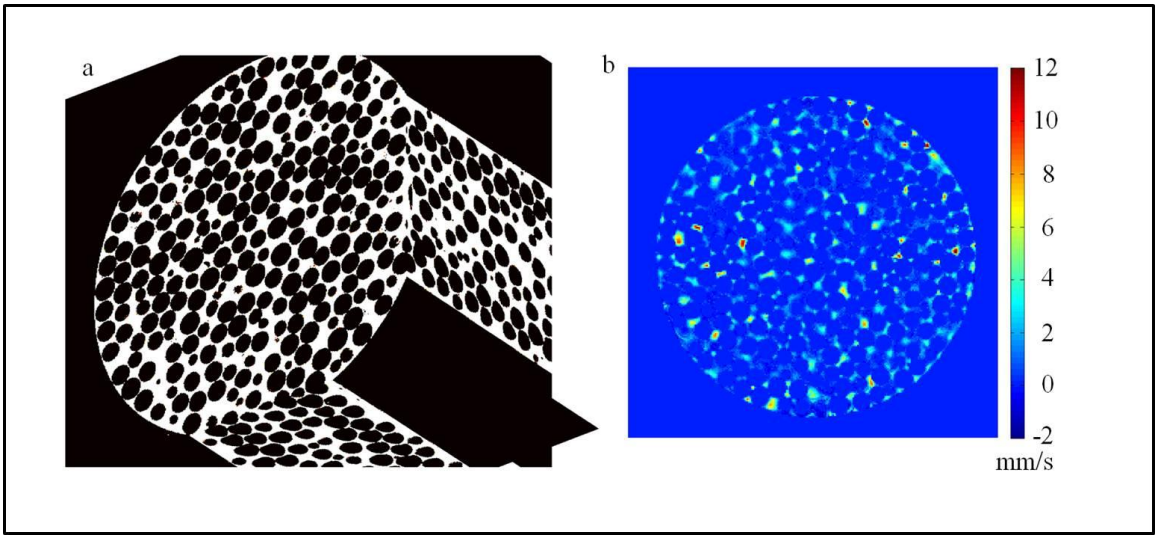

Figure 5.8. a) Orthogonal slices through a 3D MRI image with isotropic resolution of 19.53 μm^3 of a monodispersed bead pack, a model porous media. b) Axial (in the direction of fluid flow) slice through a 3D velocity MRI image with isotropic resolution of 39.06 μm^3.

enforcing the independently measured mass flux of 100 ml/hr. The MRI experimental method was validated by performing initial experiments on a circular capillary with laminar flow, see Figure 4.3.

Results and Discussion

The MRV results were compared with two CFD models, STAR-CCM+ and TETHYS, using two different resolution values for the TETHYS simulations, 20 μm^3 and 40 μm^3. The same slice for the experiments and the simulations is shown in Figure 5.9. The results compared very well spatially, in that areas of fast fluid velocity and areas of slower fluid velocity are well-correlated in the MRV images and the CFD images.

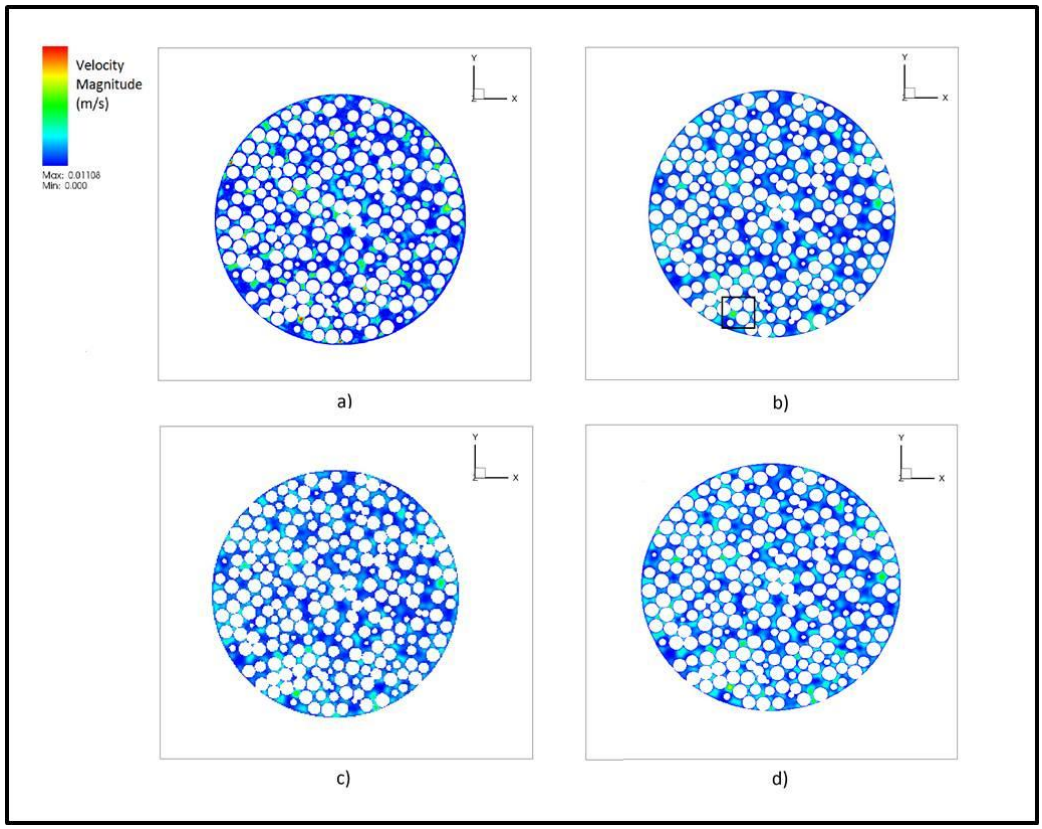

Figure 5.9. Color contour plots of velocity in slice #320: a) experimental data; b) STAR-CCM+ simulation; c) TETHYS 40 μm simulation; d) TETHYS 20 μm simulation.

However, it was shown that the magnitude of the MRV data was different from the CFD simulations. MRV data presented significant negative velocity pixels, while CFD simulations showed very few to none. In addition, the fastest velocity pixels for the experiment were significantly faster than the simulation, in some cases as much as twice as fast. This discrepancy can be explained by the limited resolution of the velocity measurement, as introduced in Chapter 4. The variance of the velocity measurements at a spatial resolution of approximately 40 μm^3 was found to be +- (0.44 mm^2/s^2) using simple Poiseulle capillary flow, see Figure 4.3. When a Gaussian Point Spread Function (GPSF) with this variance was convoluted with the histogram of velocities found using the CFD simulations, the histogram of velocities found using MRV was found to compare quite well, as shown in Figure 5.10.

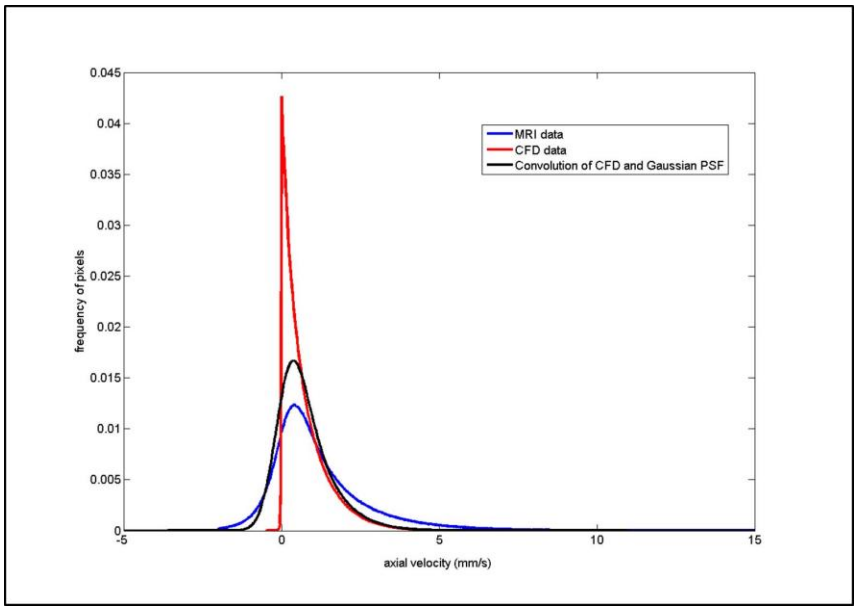

Figure 5.10. Histogram comparisons between MRI data and computational fluid dynamic simulation data. The blue line is the histogram of velocities found by MRV experiments and the red line is the histogram of velocities found by CFD simulations. The black line is the convolution of the histogram of CFD velocities (red line) with a GPSF with variance 0.44 mm^2/s^2.

Diffusion Measurements of Colloid Size
Particles Suspended in Viscous Fluids

In recent years, an exciting measurement technique called microrheology has been developed [106]. Traditional rheology involves applying a shear stress to a fluid in a known way and measuring the strain produced, or applying a prescribed strain and measuring stress, to deduce fluid properties such as viscosity. This technique is macroscopic, and for the most part is not able to study the spatial variabilities within the fluid or access high frequency information due to the limits of the mechanical equipment. Microrheology studies the properties of the fluid by measuring the displacement of small particles over time and accesses fluid information for a range of time and frequency scales. Microrheology has been demonstrated with dynamic light scattering and neutron scattering, but the use of NMR is an exciting, and thus far undemonstrated, possibility [106].

Colloid sized particles, which range from ~5 μm – 1 nm in diameter, are found in a wide variety of systems in nature and in the human body. Thus the study of their transport has many applications. The flow of red blood cells through very small capillaries in the body [107], the transport of nanoparticle size contaminants through the subsurface [108], and the deposition of bacteria in the subsurface [109] are all active areas of research. Microrheology studies the microscopic movements of colloidal particles within the fluid. The displacement of the particles is then related to the fluid properties using fluctuation-dissipation theory (FDT) [67]. When a fluid is subjected to a small perturbation, the response can be assumed to be linear if the perturbation is small

enough. The FDT says that the response of the fluid to a mechanical perturbation is the same as the thermal perturbations that occur on microscopic scales, such as the thermal motion of the molecules and Brownian motion. The relationship between an applied shear rate $\dot{\gamma}(t)$ and measured stress $\sigma(t)$ for a material is known as the relaxation modulus $G(t)$ and is defined as $\sigma(t) = \int_0^{t'} G(t')\dot{\gamma}(t')dt'$. For complex and viscoelastic fluids such as gels, the response of the fluid is dependent on the frequency of the applied shear rate and is quantified by the complex shear modulus, often denoted by $G^*(\omega)$, which is related to the complex viscosity by $\eta^* = \frac{G^*(\omega)}{i\omega}$. The real part of the modulus is the in-phase response to the perturbation and is the elastic response of the fluid. The imaginary part is the out-of-phase viscous response and is known as the loss modulus. The bulk modulus can then be manipulated mathematically and related to the displacement of a small colloidal particle (assumed to be massless) within the fluid to find the Generalized Stokes-Einstein Relationship (GSER) [110]:

$$\tilde{G}(s) = \frac{1}{6\pi a}\left(\frac{6k_BT}{s\left\langle \Delta\tilde{r}^2(s)\right\rangle}\right) \qquad (5.3)$$

where $\tilde{G}(s)$ is the Laplace transform of the bulk modulus, $\left\langle \Delta\tilde{r}^2(s)\right\rangle$ is the mean squared displacement of the colloidal probe particle, *s* is the frequency in the Laplace domain, and *a* is the particle radius. PGSE NMR directly measures $\left\langle \Delta\tilde{r}^2(s)\right\rangle$. By measuring how the mean squared displacement changes over time and then fitting this data to the equation above, values for viscosity and the bulk modulus may be obtained, depending on the time

scale of the diffusion process. The following experimental study presents exploratory data related to the use of NMR in microrheology.

Experimental System

Particle Preparation: The colloidal particles used for this project were hard-shell liquid core spheres which incorporate an oil, in this case perfluorodecalin, within a poly(methyl methacrylate) (PMMA) shell [111]. The liquid oil NMR signal can then be separated from the suspending fluid signal due to the difference in NMR spectral frequency, allowing the measurement of the dynamics of the two phases separately. A schematic of the process of making the core shell particles is shown in Figure 5.11.

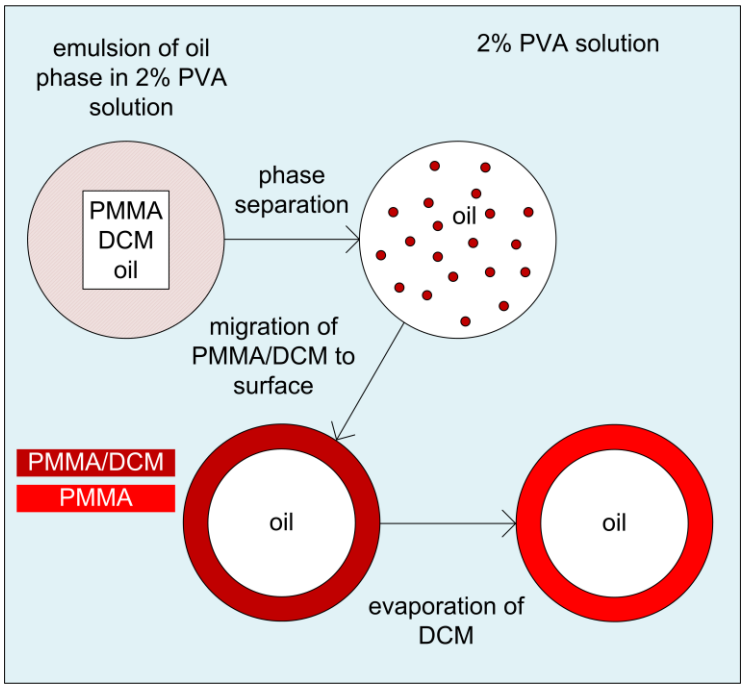

Figure 5.11. Process of producing core-shell colloidal particles, as discussed in the text.

A solution of oil, PMMA, dichloromethane (DCM), and acetone is emulsified in a solution of 2% polyvinyl alcohol. The emulsification is performed by mixing with a homogenizer at 19,000 rpm for an hour. The resulting mixture is then left to stir uncovered overnight, during which time the oil and the mixture of PMMA, DCM, and acetone will separate into two phases. The PMMA polymer with DCM and acetone then migrates to the surface of the droplets. The DCM and acetone evaporate, resulting in particles with oil encased within the PMMA shell. The perfluorodecalin core shell particles that result from this process are about 1 μm in diameter and 0.4% by weight of the resulting suspension [107, 112].

Sample Preparation: Experiments were first performed on a suspension of 0.4% wt% particles measured in its native solution of 2% polyvinyl alcohol (PVA) [111]. This suspension was then mixed with a solution of 4% wt% alginate, resulting in a fluid with 0.2% wt% particles, 1% wt% PVA, and 2% wt% alginate. Alginate is a copolymer polysaccharide that is biologically produced by certain types of algae and bacteria. It is used as a food additive and as a gelation and absorption agent. The two acid copolymers that make up alginate, α-L-guluronate and β-D-mannuronate, will arrange to form a gel structure following the addition of positive ions such as calcium [113], as will be discussed extensively in Chapters 8 and 9 of this thesis. A 1M $CaCl_2$ solution was then added to the solution of alginate and particles to induce gelation of the alginate. A gel forms when the solution stops behaving as a liquid and starts to exhibit elastic properties of a solid. The process of physical gel formation is not very well understood. Various scientists have proposed spinodal decomposition [114] or kinetic models [115], and this

is an on-going field of research. The incorporation of these particles into alginate gels and the observation of their dynamics enables the study of a model system that simulates much more complicated systems, such as nanoparticulate contaminants in the biofouled subsurface or bacterial cells moving through a biofilm matrix.

NMR Experiments: Experiments were performed using the same 300MHz Bruker magnet networked to an AVANCE spectrometer with available magnetic field gradients of 1.482 T/m in all directions, as described earlier. However for these experiments, a r.f. coil optimized for measurement of the fluorine NMR signal was used. Fluorine is a spin-1/2 nuclei, like hydrogen, with a gyromagnetic ratio γ of 40.05 MHz/T and a nearly 100% isotopic abundance. By measuring the fluorine signal of the perfluorodecalin oil encased within the particles, the dynamics of the particles themselves can be measured separately from the suspending solution.

Results and Discussion

Initial results for a suspension of 1 μm diameter perflourodecalin core-shell particles within three fluids representing different stages of alginate gelation are shown in Figure 5.12. The goal of the experiments was to measure the Brownian diffusion of the particles before and after gelation of an alginate solution in order to understand the change in fluid properties such as viscoelasticity. Figure 5.12 shows the diffusion coefficient of the particles measured at different observation times Δ. At short times, the measured diffusion is impacted by the influence of restricted diffusion of the oil within the particles, while at longer times the diffusion will asymptote to the diffusion of the

particles within the suspending fluid. The line on the graph shows the theoretical contribution of the oil diffusion within the particles themselves if the particles were stationary as in a spherical non-moving pore space [116]. The data shown follows the same trend for all fluids, with the shape of the curves following the curve for restricted diffusion of the oil within the particles. For particles in the native solution of 2% PVA the measured diffusion coefficient is more than an order of magnitude higher than that expected for stationary spherical particles, with the difference being the Brownian motion of the particles themselves. In contrast, the particles within both the solution of ungelled alginate and the gel have a lower diffusion coefficient.

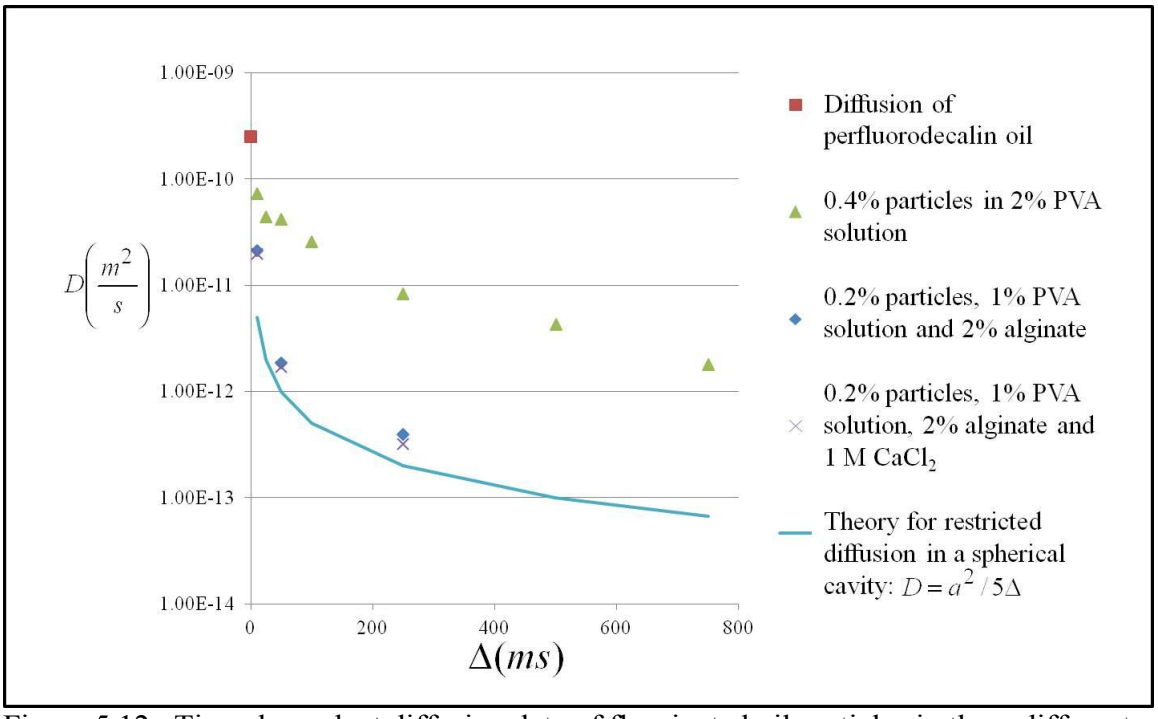

Figure 5.12. Time dependent diffusion data of fluorinated oil particles in three different samples.

The difference between the measured diffusion and the expected diffusion of the oil within the particles is the contribution of the Brownian motion of the particles. Using the Stokes-Einstein equation $D = \frac{k_B T}{6\pi\eta r}$ for 1 μm radius particles within a fluid such as water with a $\eta = 0.001$ Pa·s, the expected *D* is 4.23×10^{-12} m^2/s, while in a fluid such as 2% alginate with a viscosity on the order of 0.1 Pa·s, the expected D would be 4.23×10^{-14} m^2/s. The native solution of 2% PVA is slightly more viscous than water, so the 1.5 order of magnitude difference in the diffusion of the particles between PVA solution and alginate is very reasonable. The diffusion of the particles after gelation of the alginate is also lower than before gelation, as expected.

The acquisition of this interesting preliminary data also demonstrated the experimental challenges of using NMR PGSE techniques for microrheology. To obtain diffusion coefficient data for fluid mixtures with only 0.2% by weight particles, experiments took approximately 8 hours due to the averaging needed to obtain a reasonable signal to noise ratio. In addition, in order to measure diffusion coefficients on the order of 10^{-13} m^2/s, strong pulsed gradient amplitudes are needed. Longer observation times Δ would also be beneficial in order to reach the asymptotic time regime where the diffusion of the particles themselves dominates over the diffusion of the oil within the particles. Further work should therefore be done with larger amounts of particles within the fluid and with stronger gradients than those used in this study.

DETECTION OF BIOLOGICAL URANIUM REDUCTION

Contribution of Authors and Co-Authors

Manuscripts in Chapters 6, 7, and 8

Author: Sarah J. Vogt

Contributions: Helped conceive and implement the study design. Collected and analyzed data. Wrote manuscript.

Co-Author: Brandy D. Stewart

Contributions: Helped conceive and implement the study design. Prepared bioreactors samples. Provided feedback and comments on the manuscript.

Co-Author: Joseph D. Seymour

Contributions: Helped conceive and implement the study design. Provided feedback and comments on the manuscript.

Co-Author: Brent M. Peyton

Contributions: Helped conceive the study design. Provided feedback and comments on the manuscript.

Co-Author: Sarah L. Codd

Contributions: Helped conceive and implement the study design. Provided feedback and comments on the manuscript.

Manuscript Information Page

Sarah J. Vogt, Brandy D. Stewart, Joseph D. Seymour, Brent M. Peyton, Sarah L. Codd
Biotechnology and Bioengineering
Status of Manuscript:
___Prepared for submission to a peer-reviewed journal
___Officially submitted to a peer-review journal
___Accepted by a peer-reviewed journal
_X_Published in a peer-reviewed journal

Wiley-Blackwell
Vol. 104, No. 4, Pages 877-883, April 2012

DETECTION OF BIOLOGICAL URANIUM REDUCTION

Abstract

The conversion of soluble uranyl ions (UO_2^{2+}) by bacterial reduction to sparingly soluble uraninite ($UO_{2(s)}$) is being studied as a way of immobilizing subsurface uranium contamination. Under anaerobic conditions, several known types of bacteria including iron and sulfate reducing bacteria have been shown to reduce U (VI) to U (IV). Experiments using a suspension of uraninite ($UO_{2(s)}$) particles produced by *Shewanella putrefaciens* CN32 bacteria show a dependence of both longitudinal (T_1) and transverse (T_2) magnetic resonance (MR) relaxation times on the oxidation state and solubility of the uranium. Gradient echo and spin echo MR images were compared to quantify the effect caused by the magnetic field fluctuations (T_2*) of the uraninite particles and soluble uranyl ions. Since the precipitate studied was suspended in liquid water, the effects of concentration and particle aggregation were explored. A suspension of uraninite particles was injected into a polysaccharide gel, which simulates the precipitation environment of uraninite in the extracellular biofilm matrix. A reduction in the T_2 of the gel surrounding the particles was observed. Tests done *in situ* using three bioreactors under different mixing conditions, continuously stirred, intermittently stirred, and not stirred, showed a quantifiable T_2 magnetic relaxation effect over the extent of the reaction.

Introduction

The non-invasive detection of biogeochemical precipitation is an area of current research interest due to the role of precipitation of colloidal particles on subsurface transport processes [117-119]. In this work, the potential of magnetic resonance (MR) contrast to study the extent of reaction and spatial distribution of precipitate in the bacterial reduction of soluble uranyl ion (UO_2^{2+}) to insoluble uraninite ($UO_{2(s)}$) is explored. The data indicate a strong magnetic susceptibility contrast due to the solid precipitate, which allows gradient recalled echo imaging methods to determine spatial distributions of precipitate. Of importance for establishing *in situ* MR sensing methods to characterize biogeochemical precipitation reactions is the impact of particle size and sedimentation processes on MR contrast mechanisms. Monitoring U(VI) reducing bioreactors that were unmixed, mixed intermittently and continuously stirred demonstrated the ability of MR relaxation rates to characterize the precipitation reaction and particle sedimentation.

Several types of subsurface bacteria, *e.g. Shewanella putrefaciens* and *Shewanella oneidensis*, are being studied for use in bioremediation of uranium at nuclear waste sites [120-123]. The conversion from U(VI) to U(IV) produces uraninite $UO_{2(s)}$ which is less soluble and precipitates to form nanoparticles. Spatially resolved MR techniques may be able to visualize uraninite particles as they precipitate around or in bacteria or within a biofilm. This will provide pertinent information on the nature of metal precipitation and subsequent immobilization in biofilms and allow for measurement of potential reoxidation within reduced-metal biofilms. Currently, there is not a technique to quantify

or visualize this reductive immobilization process in a non-destructive manner. The ability to measure both the size and spatial distribution of the precipitate particles is important in modeling the transport of the contaminant. Whether bacterially produced uraninite particles undergo sorption processes to the microbes themselves, to the biofilm extracellular polymeric substance (EPS), or both can impact whether transport is enhanced or reduced. In the context of a conceptual model of transport [108] for sorption of contaminants to organic colloidal particles, this research provides a technique to provide new data to develop analogous models for bio-precipitate colloidal contaminants and their role in transport.

MR studies of bioreactors have been undertaken for batch reactors of cell suspensions [124-127], packed beds [76, 128-130], and capillary reactors [131]. Recent studies using MR have also been conducted considering the transport of colloids through porous media [132, 133]. This work extends these studies to consider the impact of mobile nanoparticle precipitate reaction products. Direct MR of uranium has been measured [134], however due to the MR active isotope (spin=7/2) also being the radioactive isotope (^{235}U) with low natural abundance and low inherent signal, direct detection of uranium resonance is limited in its application.

Materials and Methods

MR Relaxation

MR relaxation experimental techniques have been used for years as a non-invasive and non-destructive tool to study, for example, the pore size distribution in rocks

[22] and as a contrast mechanism in medical MR imaging [59]. The relaxation of MR signals occurs due to spin-lattice interaction in the longitudinal direction along the applied magnetic field (T_1), and spin-spin dipolar interactions (T_2). The T_2 relaxation is dependent on rotational mobility of the proton (^{1}H) spins, *e.g.* in a solid T_2 is short, on the order of μs whilst in liquids it is long, on the order of seconds. Paramagnetic ions in solution provide dipole interactions that decrease T_2 [18]. Inhomogeneity in magnetic fields is caused by interfaces of materials with different magnetic susceptibilities, such as water and solid nanoparticle interfaces, generating additional spin-spin relaxation termed T_2*. The relaxation caused by inhomogeneity in the magnetic field can be refocused if the time scale associated with the magnetization dephasing is long enough, but will contribute to the measured T_2 relaxation if the dephasing occurs over short time scales. Thus differences between T_2 and T_2* effects is an indication of the presence of nanoparticles. T_1 relaxation is dependent on the applied magnetic field, translational mobility, and paramagnetic ions, but is less sensitive to these effects than T_2 at laboratory-strength magnetic fields.

Washed $UO_{2(s)}$ Particle and UO_2^{2+} Solution Experiments

To determine the impact of the uraninite nanoparticles on water proton relaxation in the absence of biomass or solution UO_2^{2+}, a set of experiments was performed using a suspension of $UO_{2(s)}$ particles produced anaerobically by *Shewanella putrefaciens* CN32 in an anoxic chamber (Coy Laboratory Products Inc.) containing a pre-mixed gas of 90% N_2, 5% H_2, and 5% CO_2 (by volume), and then thoroughly washed to remove bacterial matter following the method described by Ulrich et al [135]. The solution was

centrifuged and then treated with 1 M NaOH to destroy intact cells, followed by incubation with anoxic hexane to separate any remaining organic matter. The reduced U was then re-suspended in 100 mM anoxic $KHCO_3$ to remove any remaining U (VI) adsorbed on the $UO_{2(s)}$ particles. The suspension was then transferred into 5 mm MR tubes and sealed within the anoxic chamber. MR relaxation experiments were conducted to determine the relaxation dependence on the presence of $UO_{2(s)}$ particles. Lee et al [136] have shown using high-resolution transmission electron microscopy that while individual $UO_{2(s)}$ particles produced by *Shewanella putrefaciens* CN32 are about 3 nm in diameter, most nanocrystals occurred in aggregates 100 nm in diameter or larger. T_2 (CPMG) experiments [20], spin echo images, gradient echo images [14], and T_1-T_2 relaxation correlation experiments were used to quantify these effects. MR experiments were performed at 5.9 T (250 MHz) using a DRX spectrometer (Bruker) and microimaging Micro5 probe with 2 T/m magnetic field gradients in all 3 coordinate axes.

T_2 Experiments: The suspension of $UO_{2(s)}$ particles was shaken and T_2 experiments were performed every 12 minutes as the particles settled to observe the effect of particle concentration within the r.f. coil during the measurement. The CPMG experiments used 4096 echoes at a spacing of $2\tau = 70$ μs.

Imaging Experiments: Gradient echo and spin echo images were compared to observe the spatial distribution of the T_2* effect [14]. The spin and gradient echo images had a slice thickness of 0.5 mm, echo time (T_E) of 6.2 ms, and repetition time (T_R) of 1 s. Gradient echo images are attenuated by T_2* to which T_2 processes contribute, while spin

echo techniques, as in the CPMG pulse sequence, partially refocus the inhomogeneous T_2* broadening of the signal and are primarily attenuated by T_2. Gradient and spin echo images were obtained using the same resolution, receiver gain, and echo time for direct comparison. The two images, gradient (G) and spin echo (S), were then repeated every 10 minutes over the course of an hour (i=10…60min) as the nanoparticles were sedimenting through the active region of the r.f. coil. The signal from the same region of each image was integrated and the difference between the images in which particles had sedimented ($I_{(G,S),s}$) and images with particles suspended ($I_{(G,S),i=10\ldots60\text{min}}$) was calculated using:

$$\Delta(G,S)_{i=10..60\,\text{min}} = \left(\frac{I_{(G,S),s} - I_{(G,S),i=10..60\,\text{min}}}{I_{(G,S),s}} \right) \quad (6.1)$$

The change in the spin echo image intensity was then subtracted from the gradient echo change in intensity to quantify the increased attenuation in the gradient-recalled image ($\Delta G_{i=10\ldots60\text{min}}$ -$\Delta S_{i=10\ldots60\text{min}}$), which reflects the inhomogeneous dephasing of the signal due to the magnetic susceptibility T_2* effect of the nanoparticles.

Relaxation Correlation Experiments: Two dimensional T_1-T_2 relaxation correlation experiments were also conducted as the uraninite particles were settling through the r.f. coil. These 2-D correlations have been shown to probe surface relaxation mechanisms in porous media and other applications [25, 27, 35, 41]. T_1-T_2 experiments use an inversion recovery 180 degree pulse followed by a varying time to encode for the T_1 of the sample, followed by a CPMG pulse train to measure the T_2, as shown in Figure 6.1. An inverse Laplace transform is then performed, and the spectrum $F(T_1,T_2)$ is found

by reducing the size of the data $M(t_1,t_2)$, then using a non-linear least squares algorithm and:

$$M(t_1,t_2) = \iint \left(1 - 2\exp\left(\frac{-t_1}{T_1}\right)\right)\exp\left(\frac{-t_2}{T_2}\right)F(T_1,T_2)dT_1T_2 + E(t_1,t_2) \qquad (6.2)$$

where $E(t_1,t_2)$ represents the noise of the experiment [25]. Relaxation measurements were also performed on several different concentrations of the uranyl ion UO_2^{2+}, and a linear dependence on both the T_1 and T_2 of the water protons was found (results not shown).

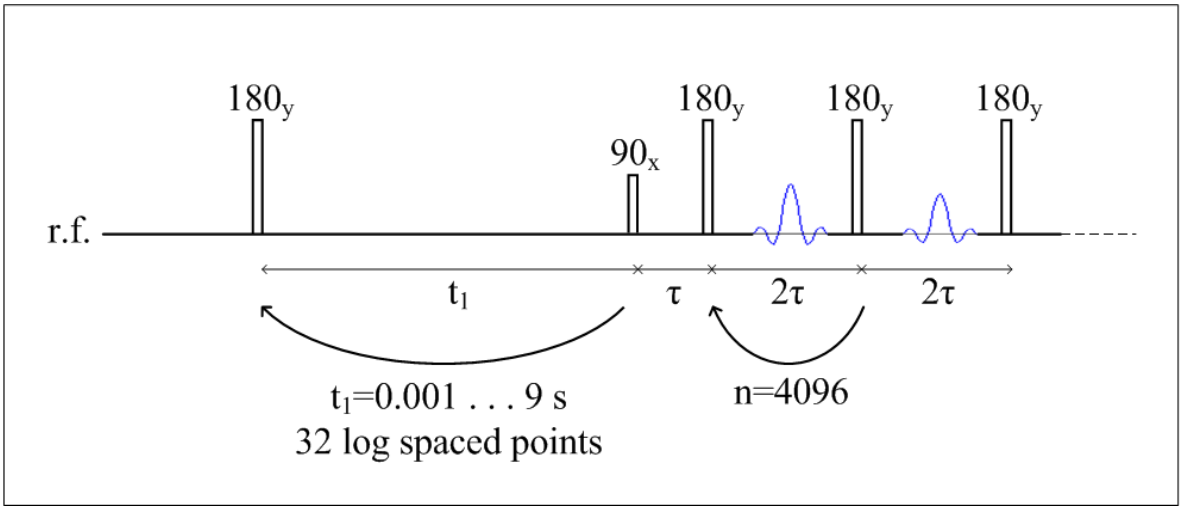

Figure 6.1. T_1-T_2 correlation pulse sequence. Experimental parameters: T_2 direction – τ = 200 μs, 2048 echoes; T_1 direction – t_1 varied from 1 ms to 9 s in 32 logarithmic steps.

Detection in Hydrogel Experiments

The suspension of $UO_{2(s)}$ particles was injected into a xanthan gum/locust bean gum biomolecular hydrogel to simulate the precipitation of uraninite in the extracellular polymeric substance (EPS) of a biofilm. Spin and gradient echo images were again obtained with slice thickness 0.5 mm, echo time (T_E) of 6.2 ms, and repetition time (T_R)

of 1 s. Visual inspection indicated that the particles were in the wall region of the sample, as indicated by the image contrast in Figure 6.2. Note the strong refocusing of the susceptibility induced by the nanoparticles in the spin echo experiment relative to the gradient echo. This demonstrates the ability to use magnetic susceptibility contrast to determine the spatial distribution of biogeochemical reaction precipitates in biopolymer hydrogels similar to biofilm EPS. Previous studies have also shown the ability to use signal contrast due to heavy metal molecules to measure diffusion of the molecules into an alginate gel [137].

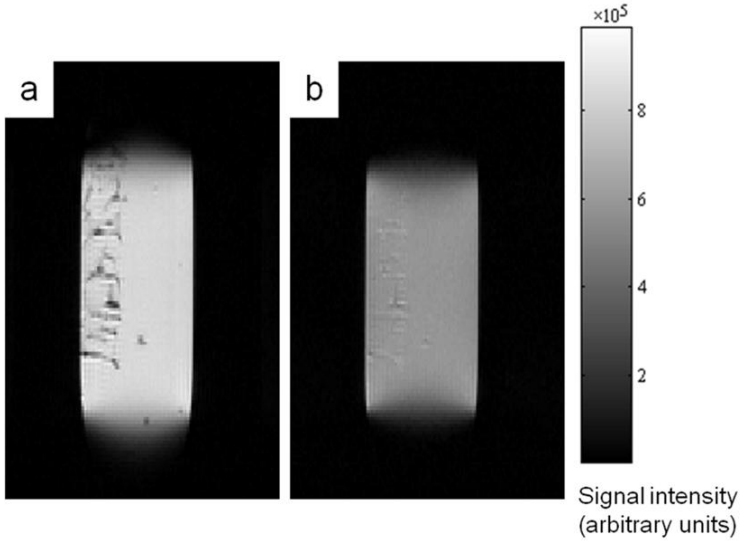

Figure 6.2. Uraninite particles ($UO_{2(s)}$) injected into a xantham gum/locust bean gum gel. The enhanced signal attenuation around the injected particles in the gradient-recalled echo image (a) compared to the spin echo image (b) shows the T_2* effect on the gel surrounding the injected particles. Both images have the same intensity scale. Experimental parameters: 25 mm x 10 mm FOV, 128x128, 0.5 mm slice thickness, T_E = 6.2 ms, T_R = 1 s.

Bioreactor Experiments

Finally, an experiment was conducted to validate the use of these concepts on an active bioreactor system. Two 10 mm NMR tubes were prepared with an initial concentration of 4 mM UO_2^{2+} as UO_2Cl_2, artificial groundwater medium (3 g/L $KHCO_3$, 1.5 mL/L mineral solution, 3 g/L PIPES buffer, 0.005 g/L KCl, 0.05 g/L $MgSO_4$, 0.03 g/L NaCl, 1 mL/L NH_4Cl, 1 mL/L KH_2PO_4, 30 mM Na-lactate) and approximately 10^8 cells/mL *Shewanella putrefaciens* CN32 bacteria and sealed within the anoxic chamber. A 1 L stirred reactor was also prepared in the anoxic chamber and run concurrently with the tube reactors as a control experiment. Initially, it was not clear that the reaction would proceed within the sealed NMR tubes which were not stirred constantly, so samples were taken from the larger stirred reactor every 24 hours and tested with the two tube reactors to make sure that the reaction was proceeding as expected.

One of the two NMR tube reactors, referred to as "Reactor #1", was frequently shaken to approximate the "stirred" reactor, and the other reactor, "Reactor #2", was allowed to settle and was never shaken. This was done to determine if this reaction would also proceed in a static "biofilm" state as opposed to only occurring under stirred conditions. The reduction reaction from UO_2^{2+} to $UO_{2(s)}$ clearly still proceeded without shaking, as shown by the presence of dark particles in both Reactor #1 and Reactor #2 in Figure 6.3. A tube of the initial solution of media and UO_2^{2+} is shown in Figure 6.3 for comparison.

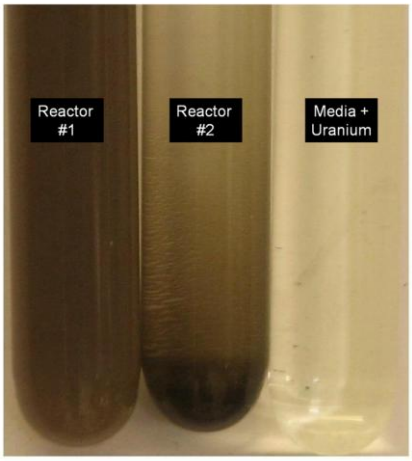

Figure 6.3. Two "reactors" that were compared during the bacterial reduction tests, with a tube of the starting media and UO_2^{2+} solution for comparison. Reactor #1 was mixed intermittently during the experiment, while Reactor #2 was not mixed. The dark particles in both Reactor #1 and #2 are the solid UO_2 precipitate. These two reactors, as well as samples from a larger 1 L reactor, were tested in the bioreactor experiments. A tube of the initial solution of media and UO_2^{2+} is shown on the right for comparison.

Results and Discussion

Washed $UO_{2(s)}$ Particle and UO_2^{2+} Solution Experiments

The linear dependence of both T_1 and T_2 relaxation on UO_2^{2+} ion concentration is consistent with treatment of the uranium as a paramagnetic species that enhances the relaxation of the surrounding solvent protons [59]. This paramagnetism is due to the unpaired "f" and "d" electrons in the uranium atom [138]. Water molecules around the UO_2^{2+} ions exchange between the coordination sphere around the ion and the bulk water, which causes increased magnetization relaxation [66].

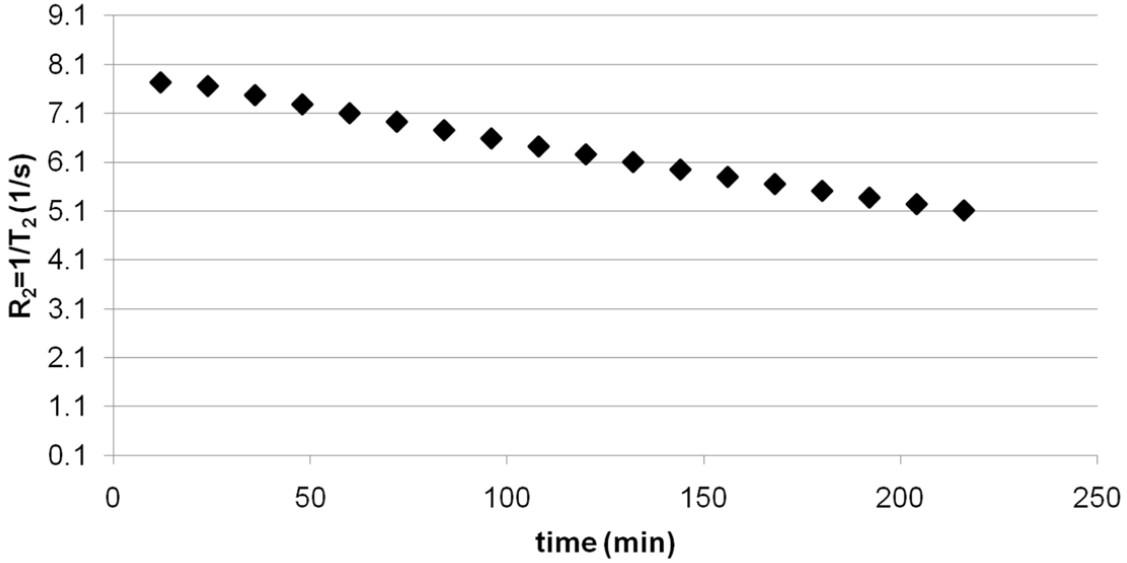

Figure 6.4. Relationship between relaxation rate ($R_2=1/T_2$) and the amount of time that the particles have been settling. The relaxation rate decreases with the decreasing presence of uranium nanoparticles. Experimental parameters: CPMG pulse sequence, τ = 35 μs, 4096 echoes.

T_2 Experiments: The transverse relaxation rate $R_2=1/T_2$, as shown in Figure 6.4, was increased by the presence of $UO_{2(s)}$ nanoparticles. This is due to the strong magnetic susceptibility of the particles causing both homogeneous and inhomogeneous dephasing of the signal, resulting in a T_2* effect that is not refocused by the CPMG sequence due to susceptibility induced spin relaxation on a time scale less than the CPMG refocusing pulse spacing, *i.e.* $\tau_{inhomogeneous} < 2\tau_{CPMG}$= 70 μs. As the larger particles settled out of the active region of the r.f. coil during the experiment, the relaxation rate continued to decrease approximately linearly.

Imaging Experiments: The maximum diameter of the particles settling through the active region was calculated by finding the maximum terminal settling velocity v_t for each experiment using the length of the r.f. coil (15 mm) and the experiment time

($v_t = 15mm/i = 10...60\,\text{min}$), and then using the force balance for a particle sedimenting in a viscous fluid [62]:

$$D_p = \sqrt{\frac{18 v_t \mu_f}{g\left|\rho_p - \rho_f\right|}} \qquad (6.3)$$

where subscript "p" refers to the particle and "f" refers to the suspending fluid water. The dependence of the T_2* signal weighting ($\Delta G_{i=10\ldots60\text{min}}$ -$\Delta S_{i=10\ldots60\text{min}}$) calculated from the images of Figure 6.5 on the size of the particles is shown in Figure 6.6. The linear relationship shown between the T_2* relaxation and length scale is consistent with the well known dependence of relaxation rate on surface to volume ratio of surface magnetization sinks [34].

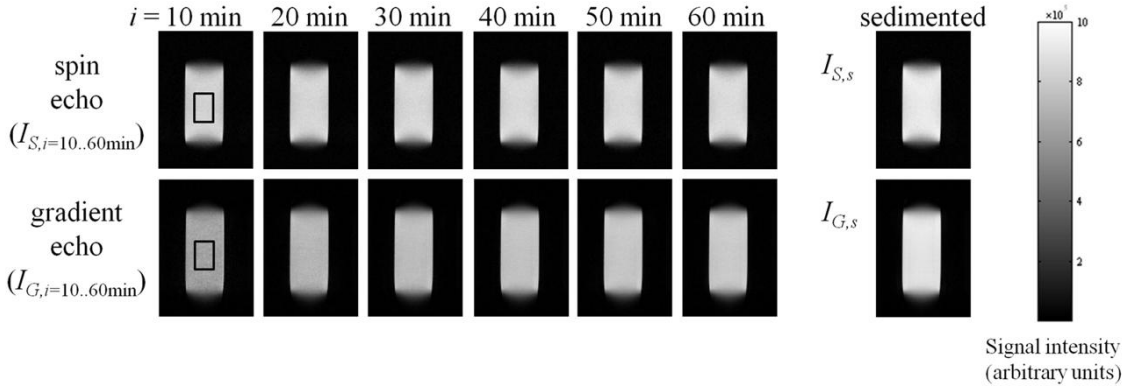

Figure 6.5. Images used to quantify T_2* effect of sedimenting particles. Spin echo (top row) and gradient echo (bottom row) images were taken after the particles had been settling overnight (far left) and were repeated for an hour after the sample had been stirred (i=10…60min). Images are shown using the same intensity scale. The region shown by the box in the images on the far right (i=10min) was integrated to find the image intensity of each image. Experimental parameters: 25 mm x 10 mm FOV, 128x128, 0.5 mm slice thickness, T_E = 6.2 ms, T_R = 1 s.

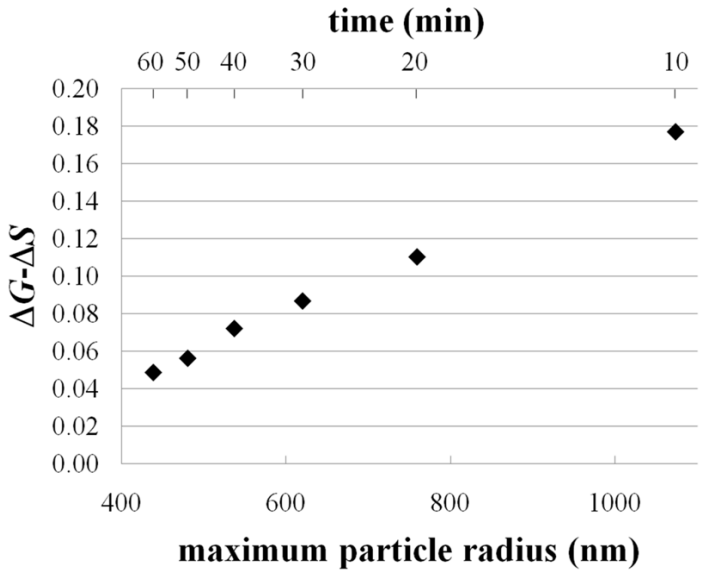

Figure 6.6. Demonstration of T_2* effect vs. largest particles still suspended within the coil during the experiment, calculated using equations 6.1 and 6.3 in the text and the images shown in Figure 6.5.

Relaxation Correlation Experiments: The T_1-T_2 correlation results in Figure 6.7 show that while the T_1 of the solution surrounding the settling particles stays essentially constant at approximately the T_1 of pure water, the T_2 varies by an order of magnitude between the unshaken sample and the shaken sample. While the peaks are about the same order of magnitude, the ratio T_1/T_2 varies from 12.8 for the freshly shaken sample to 1.5 for the "settled" sample. Even after allowing about one year for the particles to settle to the bottom of the sample tube, particles with a diameter of 9 nm or less were still suspended, and the effect of this is shown by the fact that T_1/T_2 ratio is still above the expected value of 1 for pure water. This demonstrates the quantification of the presence of $UO_{2(s)}$ by MR relaxation.

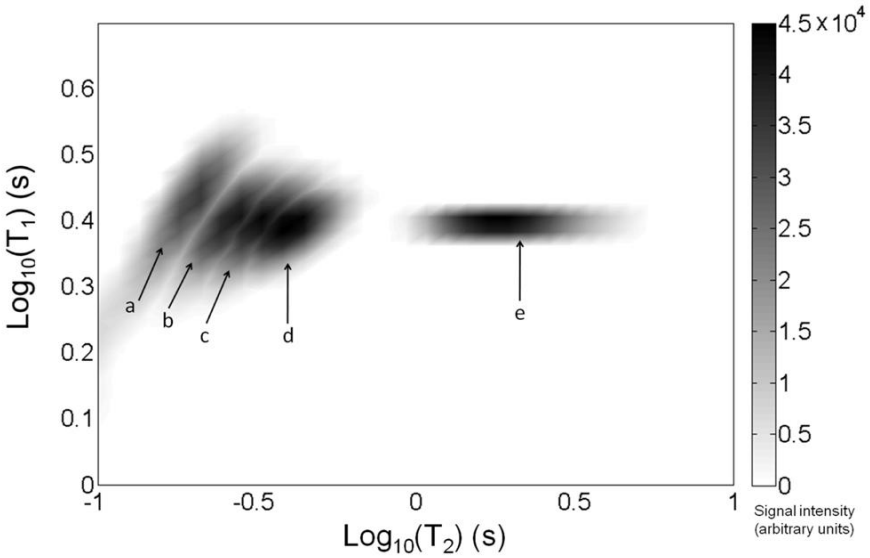

Figure 6.7. T_1-T_2 correlation spectra of solution surrounding settling washed uranitite ($UO_{2(s)}$) particles at five different times, overlaid onto the same graph: (a) 0-1.5 hours after shaking the sample (b) 1.5-3 hours (c) 3-4.5 hours (d) 4.5-6 hours and (e) 9000 hours (1 year) after shaking.

Bioreactor Experiments

The T_2* effect of the particles is shown in the gradient recalled echo images in Figure 6.8, indicating the increasing concentration of sedimented particles in the bottom of Reactor #2, generating signal dephasing.

The effects of the bacterial reduction of U(VI) to U(IV) on the T_1 and T_2 of the solution are shown in Figures 6.9 and 6.10. The T_1 result does not show a strong dependence on the presence of $UO_{2(s)}$ particles within the coil, consistent with the T_1-T_2 correlation results shown in Figure 6.7. However, the dependence on T_1 of the depletion of soluble UO_2^{2+} ions can be seen in the increase exhibited after 10,000 minutes for the two stirred reactors, Reactor #1 and the 1L constantly stirred reactor. The three reactors show a similar decrease of T_2 during the first 2 days of the reaction, and while the two

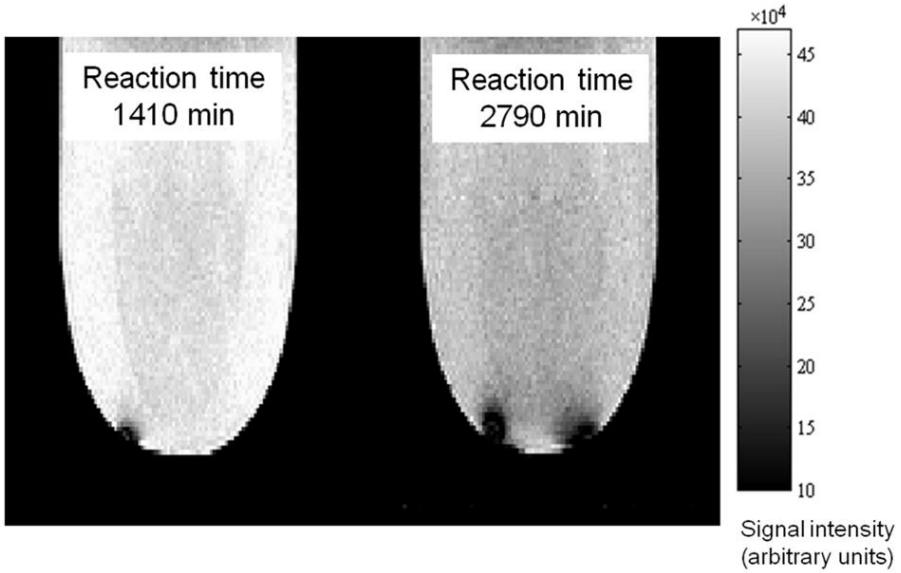

Figure 6.8. Gradient echo images of the bottom of Reactor #2. The increasing concentration of uraninite ($UO_{2(s)}$) particles settling into the bottom of the tube is shown by increased signal attenuation, both throughout the tube and particularly along the bottom surface. Both images have the same intensity scale. Experimental parameters: 25 mm x 10 mm FOV, 128x128, 0.5 mm slice thickness, T_E = 6.2 ms, T_R = 1 s.

stirred reactors continue to show the same trend the settled reactor diverges. This is due to the increase in particle concentration due to reaction extent generating aggregation and sedimentation of the particles to the bottom of the reactor and causing them to cease affecting the T_2 of the solution. Because the stirred reactors always have particles of $UO_{2(s)}$ within the coil during the experiment, the effect of the decreased concentration of the UO_2^{2+} dissolved in the solution is not visible. The error in the fit for the T_2 experiments is about 0.1%, and the error for the T_1 experiments is 2%.

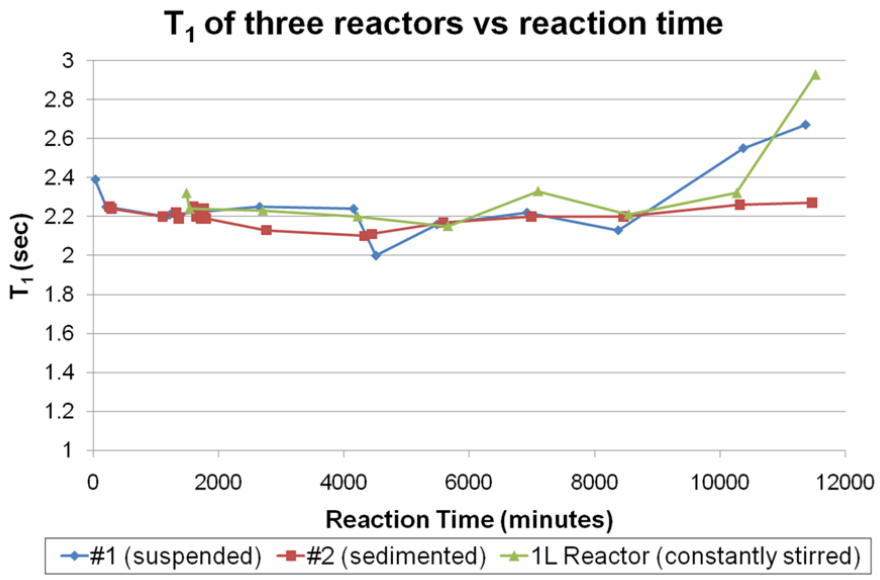

Figure 6.9. T_1 of the two 10 mm NMR tube bioreactors and samples from the 1 L continuously stirred bioreactor vs. total bacterial reduction reaction time. T_1 was measured using an inversion recovery pulse sequence with 32 logarithmic spaced inversion times up to 5 s. The T_1 for all three reactors throughout the extent of the reaction remains about constant.

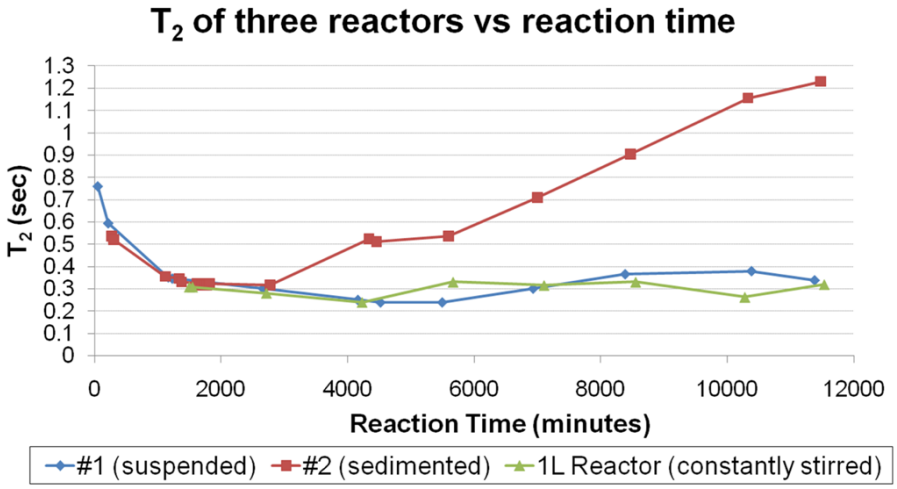

Figure 6.10. T_2 of the two 10 mm NMR tube bioreactors and samples from the 1 L continuously stirred bioreactor vs. total bacterial reduction reaction time. T_2 was measured using a CPMG pulse sequence with $\tau = 35$ μs, 4096 echoes. The continued presence of $UO_{2(s)}$ particles within the coil for the two stirred reactors is shown by the divergence of the T_2 of the sedimented reactor (Reactor #2) after about 3000 minutes.

Conclusion

The MR contrast of $UO_{2(s)}$ nanoparticles formed by biological reduction of UO_2^{2+} by the bacteria *Shewanella putrefaciens* CN32 is shown to impact T_2 and T_2* MR relaxation. The MR techniques described provide a non-destructive means of measuring and understanding the complex process of microbially mediated U (VI) reduction to $UO_{2(s)}$, as well as the potential reoxidation and remobilization back to U (VI) and associated species. Using this method, spatial and temporal characterization of U precipitate formation in geological systems would provide insight into the nanoparticle nature of reduction products and their distribution within complex, multi-phase systems. More traditional imaging techniques are often limited to providing information at the end of experiments and generally require termination and destruction of sample systems to obtain information. Data provided by non-invasive MR methods will provide valuable insights into the factors promoting uranium immobilization and has potential to improve the design of effective *in situ* remediation systems.

PERMEABILITY OF A GROWING BIOFILM IN A POROUS MEDIA FLUID FLOW ANALYZED BY MAGNETIC RESONANCE DISPLACEMENT-RELAXATION CORRELATIONS

Contribution of Authors and Co-Authors

Manuscripts in Chapters 6, 7, and 8

Author: Sarah J. Vogt

Contributions: Helped conceive and implement the study design. Helped collect and analyze data. Wrote manuscript.

Co-Author: Alexis B. Sanderlin

Contributions: Helped implement the study design. Helped collect and analyze data. Provided feedback and comments on the manuscript.

Co-Author: Joseph D. Seymour

Contributions: Helped conceive and implement the study design. Provided feedback and comments on the manuscript.

Co-Author: Sarah L. Codd

Contributions: Helped conceive and implement the study design. Provided feedback and comments on the manuscript.

Manuscript Information Page

Sarah J. Vogt, Alexis B. Sanderlin, Joseph D. Seymour, Sarah L. Codd
Biotechnology and Bioengineering
Status of Manuscript:
___Prepared for submission to a peer-reviewed journal
___Officially submitted to a peer-review journal
_X_Accepted by a peer-reviewed journal
___Published in a peer-reviewed journal

Wiley-Blackwell
Accepted November, 2012

PERMEABILITY OF A GROWING BIOFILM IN A POROUS MEDIA FLUID FLOW ANALYZED BY MAGNETIC RESONANCE DISPLACEMENT-RELAXATION CORRELATIONS

Abstract

Biofilm growth in porous media is difficult to study non-invasively due to the opaqueness and heterogeneity of the systems. Magnetic resonance is utilized to non-invasively study water dynamics within porous media. Displacement-relaxation correlation experiments were performed on fluid flow during biofilm growth in a model porous media of mono-dispersed polystyrene beads. The spin-spin T_2 magnetic relaxation distinguishes between the biofilm phase and bulk fluid phase due to water - biopolymer interactions present in the biofilm, and the flow dynamics are measured using PGSE NMR experiments. By correlating these two measurements, the effects of biofilm growth on the fluid dynamics can be separated into a detailed analysis of both the biofilm phase and the fluid phase simultaneously within the same experiment. Within the displacement resolution of these experiments, no convective flow was measured through the biomass. An increased amount of longitudinal hydrodynamic dispersion indicates increased hydrodynamic mixing due to fluid channeling caused by biofilm growth. The effect of different biofilm growth conditions was measured by varying the strength of the bacterial growth medium.

Introduction

In diverse growth environments, microorganisms including bacteria and algae will attach to surfaces and grow in a phenotypically different state known as a biofilm. Biofilm growth occurs after the microorganisms attach to a surface by excreting and then growing within the extracellular polymeric substance (EPS) [91]. The EPS consists of proteins, polymers, and DNA material and both enables the bacterial colony to adhere to the surface and inhibits the killing of the bacteria by limiting the diffusion of antimicrobials within the polymer matrix and promoting dormant growth states for the microbial cells. When bacterial colonies grow in biofilms, bacteria are difficult to remove and lead to negative consequences such as persistent infections on medical implants [89]. Positive attributes such as the growth of biobarriers to contain harmful environmental contaminants such as nuclear waste are also of interest [118, 139].

The experimental observation of biofilm growth in porous media is complicated by the heterogeneous nature of the biofilm, the opaqueness and heterogeneity of porous media growth environments, and the diversity of nutrient conditions and colony species compositions. Thus there are a large number of computer models that have been developed to enable variation of parameters such as growth rates and substrate geometries numerically [105]. Recent numerical models utilize either computational fluid dynamics simulations (CFD) [99] or lattice-Boltzmann simulations (LB) [100, 101] to calculate the velocity field of the fluid and to model bacterial transport and attachment. In particular, recent modeling research has been focused on understanding the effect of the permeability of the biomass on the flow through biofouled media [140, 141].

Understanding the biofilm permeability is important for analyzing the change in the overall permeability of the biofouled porous media and for analyzing the transport of nutrients or antimicrobials into the biofilm.

CFD and LB simulations numerically solve the Navier-Stokes equations for incompressible fluid flow:

$$\frac{\partial \vec{u}}{\partial t} + \vec{u} \cdot \nabla \vec{u} + \frac{1}{\rho} \nabla p = \eta \nabla^2 \vec{u} \quad (7.1)$$

$$\nabla \cdot \vec{u} = 0 \quad (7.2)$$

where $\vec{u}$ is the velocity of the fluid element, ρ is the density of the fluid, p is the pressure, and η is the dynamic viscosity of the fluid. Nutrient transport and consumption in the biofilm are modeled using a mass transfer convection-diffusion-reaction equation [101]:

$$\frac{\partial C_s}{\partial t} + \vec{u} \cdot \nabla C_s - D_s \nabla^2 C_s = r_s \qquad (7.3)$$

where C_s is the nutrient concentration, D_s is the nutrient diffusion coefficient, and r_s is the local consumption rate of the nutrient . The impact of permeability of the biofilm on convection and diffusion of nutrients is therefore important to quantify in order to model biofilm growth kinetics.

Simulations of biofilm growth in porous media have taken different approaches to the modeling of the permeability of the biofilm. Some models [99, 104] account for the permeability of the biofilm by incorporating the Brinkman flow equations [142] into the model calculations. Brinkman flow equations model the flow through the biofilm by

assuming that the biofilm is a dense array of spherical bacteria in a fluid. Radu et al. [99] include the full equation in their model:

$$\frac{\eta}{\kappa}\bar{u} + \nabla p = \frac{1}{\varepsilon}\left[\eta \cdot \nabla^2 \bar{u} - \left(\frac{2\eta}{3} - \kappa\right)(\nabla \cdot \bar{u})\right] \quad (7.4)$$

where ε and κ are the porosity and permeability of the biofilm, respectively. Kapellos et al. [104] simplify the calculation by combining equations 7.1 and 7.4 and considering the biofilm and fluid as a continuous fluid with spatially varying properties. The use of the Brinkman equations requires the assumption of values for the porosity, permeability, and viscosity of the biofilm and for the bacterial cell size.

Pintelon et al. [100] take the simpler approach of solving equations 7.1 and 7.2 assuming an increased value of viscosity of the biofilm in relation to the bulk fluid [143, 144]. The authors found the predicted relationship between the permeability of the biomass and the velocity of fluid through the biofilm, the growth rate of the biofilm, and the transport of nutrients into the biomass [100]. They demonstrated that the value for the permeability of the biomass significantly affected both the properties of the fluid flow throughout the porous medium and growth rate of the biofilm due to the varying amount of nutrient transport into the biofilm [100].

The amount of convective flow through the biofilm in a biofouled porous media is currently an open question. Due to the heterogeneity and the different length and time scales for fluid flow through the biofilm and in the bulk, experimental data for realistic systems is difficult to obtain. The work presented here utilizes a recently developed magnetic resonance (MR) experimental technique to study these systems.

Magnetic Resonance

Magnetic resonance (MR) experimental techniques such as spectroscopy [97, 145], imaging [125, 131, 146-148], and dynamic measurements [128, 130, 149] have found increasing use in recent years as a non-invasive way to study biofilm growth. The work presented here uses the correlation between molecular motion and MR relaxation to study the growth of a biofilm. These displacement-relaxation correlation experiments [42] have been utilized in recent years to study the flow through rocks [40, 150, 151], the transport of water through trees [152], and water flow through a packed bed of alginate polymer beads [153]. This technique has been used previously to study a biosystem of packed methanogenic sludge particles [154] but to our knowledge has not been used to study convection through a growing biofilm.

Previous studies have utilized dynamic MR measurements to study the transport through biofouled porous media [103, 128, 129] but were unable to distinguish between the dynamics within the biomass and in the bulk fluid flow. The biofilm was shown to grow in preferential flow pathways but the degree of flow through the biomass itself was not quantified. MR relaxation measurements have been used to separately study the biofilm and the bulk fluid [1] but did not measure the fluid dynamics. The research presented here utilizes these two MR phenomena to study the dynamics within the biomass separately from the bulk fluid at the same time and within the same experiment. By obtaining signal from the entire sample and using the ability to separate the biofilm and fluid phases using relaxation phenomena, complicated and heterogeneous biofouled porous media samples may be analyzed.

Measurement of Molecular Motion Using MR: The MR pulse sequences known as pulsed gradient spin echo (PGSE) and pulsed gradient stimulated echo (PGSTE) are the building blocks for most sequences that measure molecular motion [21, 42]. These experiments are able to quantify molecular motion by applying a sequence of radio frequency (rf) pulses and magnetic field gradients to encode molecules for their positions at different points in time. The frequency of the precession of the magnetic moments of molecules is encoded for position by applying a linearly varying magnetic field gradient g for a duration δ, a specific waiting time Δ is then applied during which the molecules move randomly due to diffusion and hydrodynamic dispersion or coherently due to convection, and then the new positions are encoded by applying the same gradient of opposite polarity. The effect of the molecular motion on the phase and amplitude of the total MR signal can then be analyzed. A Fourier relationship is found [14, 42] between the MR signal and the transition probability, or propagator of motion, $P(z \mid z', \Delta)$ in one direction, defined as the probability that a molecule starting at position z at $t = 0$ will move to position z' at $t = \Delta$. When we define $Z=z'-z$ as the displacement and $q = \frac{\gamma \delta g}{2\pi}$ as its Fourier conjugate, we can write the signal as:

$$E(q) = \int P(Z, \Delta) \exp(i 2\pi q Z) dZ \qquad (7.5)$$

where $E(q)$ is the measured MR signal voltage. For example, the propagator for

molecular self-diffusion D with a coherent velocity in the z direction is a Gaussian function:

$$P(Z,\Delta) = \frac{1}{\sqrt{4\pi D\Delta}} \exp\left[\frac{-(Z-\bar{v}\Delta)^2}{4D\Delta}\right] \qquad (7.6)$$

By performing a Fourier transform the form for the MR signal is then predicted to be:

$$E(q) = \exp\left(-4\pi^2 q^2 D\Delta + 2\pi i q\bar{v}\Delta\right) \quad (7.7)$$

which demonstrates that diffusion will cause an attenuation of the signal while velocity will result in a phase shift [14]. The data obtained using the propagator of motion contains information about self-diffusion and flow directly, but also spatial and temporal information in more indirect ways [155]. The resolution in the displacement measurement enables the measurement of both slow flow which may be present through the biofilm and fast flow of the bulk fluid through non-biofouled pores in the same experiment.

MR Relaxation Theory: The relaxation of the MR signal occurs after an rf pulse excites the molecular magnetic moments and relaxes back to equilibrium due to spin-lattice T_1 interaction in the longitudinal direction along the applied magnetic field, and spin-spin T_2 dipolar interactions. The T_2 relaxation occurs due to both interactions with the other molecules in the solution and also the environment around them. In solution, the T_2 is dependent on rotational mobility of the proton (^{1}H) spins [18], so that on a polymer molecule the T_2 of the protons is short, on the order of tens to hundreds of ms, but for protons on liquid molecules such as water the T_2 is long, on the order of seconds. Molecular exchange occurring on a time scale of μs or ms between polymer protons and

water protons will affect the measured T_2 [156], resulting in the measured T_2 being a time and weighted average of the polymer and water proton T_2 times. For water within the EPS of a biofilm, the molecular exchange between the protons on the polymer molecules and the protons of the water will result in a decrease in the measured T_2, from a T_2 of approximately 2 s in pure water to a T_2 on the order of 100 ms in biofilms [1, 128, 131, 157, 158]. The displacement-relaxation correlation experiments presented here utilize the capability of MR to quantify both dynamics and molecular relaxation to study the dynamics of the bulk water and the biofilm separately within the same experiment as discussed below.

Materials and Methods

Biofilm Growth

Bacillus mojavensis was chosen for these experiments due to the ease with which it produces a relatively thick biofilm and environmental importance [94]. Brain Heart Infusion (BHI, Becton, Dickenson and Company, Sparks, MD) used as the bacterial growth medium was prepared according to the recipe given by Mitchell et al [40 g/L NaCl, 3 g/L $NaNO_3$, 0.75 g/L NH_4Cl (Fisher, Pittsburgh, PA), and 28 g/L, 18 g/L, 9 g/L, or 4.5 g/L BHI for 65%, 50%, 25%, and 12.5% strength, respectively] and autoclaved. Following preparation and cooling of the media, 1 mL of a frozen stock culture of the bacteria was warmed to room temperature and added to 100 mL of 100% strength BHI. This culture was incubated in a 1L media bottle (Kimax, Vineland, NJ) at room temperature on a horizontal shaker for 24 hours.

A model porous media was constructed with a 8.76 mm inner diameter chromatography column (Omnifit) that was packed with 240 μm diameter monodispersed polystyrene spheres (Duke Scientific). The flow loop was constructed using PTFE tubing and HPLC fittings (GE Scientific). The bead column was saturated with distilled water and was monitored to ensure that there were no leaks or bubbles in the system before being loaded into the MR magnet. The fluid was then switched from water to BHI pumped at a rate of 50 mL/hr with a HPLC pump (Pharmacia P-500) to both create the proper pH and osmotic conditions for the bacterium *B. mojavensis* within the column and to perform experiments as a base line before the introduction of the bacteria.

After the bacteria grew sufficiently in the 1L media bottle on the shaker, the column was inoculated and incubated for four hours to allow for bacterial attachment to the beads. The flow of the growth media (BHI) was then re-started and was continuously pumped through the column at 50 ml/hr for the duration of the experiments. For the measured initial porosity of $\phi = 0.43$, this flow rate gives a superficial velocity $\langle v_0 \rangle =$ 0.53 mm/s corresponding to a pore Reynolds number $\mathrm{Re} = \dfrac{\langle v_0 \rangle l \rho}{\mu} = 9.6 \cdot 10^{-5}$ for water based on a pore length scale $l = \dfrac{d_p \phi}{1-\phi} = 180$ μm, where $d_p = 240$ μm is the diameter of the bead particles. This indicates a Peclet number for the relative contribution of convective to diffusive transport rate of $\mathrm{Pe} = \dfrac{\langle v_0 \rangle l}{D_0} = 48$.

The amount of growth media provided for bacteria growth will affect the growth rate of the biofilm through the column. This was varied by using four different strengths

of BHI, 65%, 50%, 25%, and 12.5%. For the 65% and 50% strength BHI trials, the biofilm grew quickly and plugged the system and caused leaks after 24 hours of data was obtained. The majority of the data discussed in this work was obtained with 25% and 12.5% strength BHI which allowed for biofilm growth to be monitored for 2 or 3 days.

Displacement-Relaxation Correlation Experiments

Two dimensional $P(Z, \Delta)$-T_2 displacement-relaxation correlation experiments were conducted as the biofilm was grown within a 300 MHz Bruker super-wide bore superconducting magnet networked to an AVANCE III spectrometer and a Micro2.5 micro-imaging probe with maximum gradients in all three directions of 1.482 T/m. $P(Z, \Delta)$-T_2 experiments begin with a pulsed gradient, stimulated echo sequence (PGSTE) to encode the spins for displacement followed by a CPMG pulse train [14, 20] to measure the T_2, as shown in Figure 7.1 [42]. A τ_2 value of 200 μs was used to minimize the effects of exchange during the T_2 measurement [154]. The PGSTE sequence is a variant of the PGSE except that the magnetization is stored along the *z*-axis during the observation time Δ, minimizing the influence of T_2 relaxation during the observation time Δ [14]. Experimental details are discussed in the caption to Figure 7.1. The resulting 2D data set from each experiment included 51 gradient steps in one dimension and 4096 echoes in the second dimension. The data was zero-filled to 64 points and a Fourier transform was performed in the PGSTE direction to obtain a propagator of motion for each echo that was collected. An inverse Laplace transform (ILT) was then performed

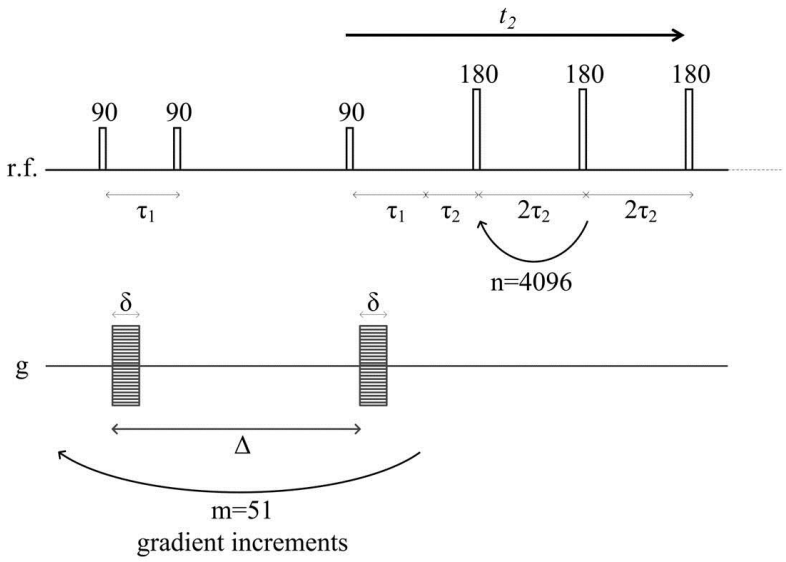

Figure 7.1. *P(Z ,Δ)-T_2* displacement-relaxation correlation pulse sequence. A PGSTE sequence encoded the spins for displacement before a CPMG sequence was used to measure the T_2. Experimental parameters: δ = 1 ms; Δ = 500 ms, 250 ms, or 50 ms; 51 linearly spaced gradient increments from -0.2964 T/m to 0.2964 T/m for Δ = 500 ms, -0.5928 T/m to 0.5928 T/m for Δ = 250 ms, and -1.482 T/m to 1.482 T/m for Δ = 50 ms; t_2 from 0 to 1.64 s with τ_2 = 200 μs and 4096 echoes collected.

for each point in the propagator direction to obtain the spectrum *F(P(Z, Δ),T_2)*. The ILT was performed using a non-linear least squares algorithm and:

$$M(Z,\Delta,t_2) = \int P(Z,\Delta)\exp\left(\frac{-t_2}{T_2}\right)F(P(Z,\Delta),T_2)dT_2 + E(Z,t_2) \quad (7.8)$$

where *E(Z,t_2)* represents the noise of the experiment [50]. Each experiment was 3 hours in length to allow for signal averaging. Experiments with displacement observation times Δ = 500 ms, 250 ms, and 50 ms were performed sequentially as the biofilm was growing within the magnet, resulting in a complete experimental series that required 9 hours to

acquire. Biofilms were grown for from one day to three days depending on the growth media strength and the corresponding extent of biofouled clogging of the system.

Results and Discussion

The data obtained for the biofilm grown using 12.5% strength BHI growth media is presented in detail and is representative of all the data. At this media strength, the growth reached a pseudo-steady state and was monitored for about 3 days without plugging the system and causing leaks. Figure 7.2 presents the results of 2D $P(Z, \Delta)$-T_2 correlation experiments for displacement times Δ = 500 ms and 250 ms. The first column shows the data for BHI growth media flowing through the system before introduction of

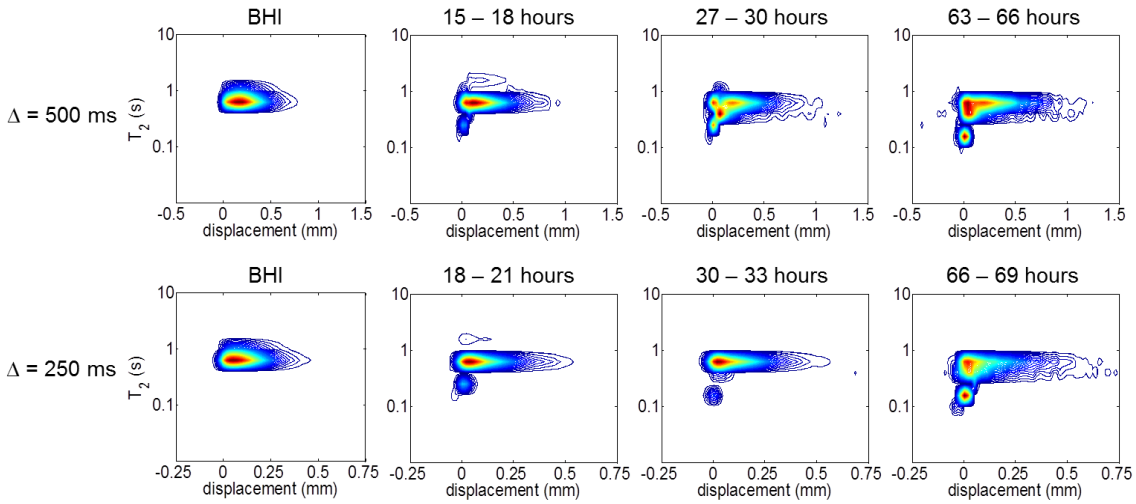

Figure 7.2. $P(Z, \Delta)$-T_2 data as a function of biofilm growth time for 12.5% strength BHI for observation times Δ of 250 ms and 500 ms. The shorter T_2 peak at ~ 150 ms corresponding to biofilm growth increases over time and shows no convective flow. The longer T_2 peak at 700 ms corresponding to the bulk fluid exhibits longer displacements as the biofilm grows indicating that there is channeling occurring where the biofilm is plugging up some of the pores and other pores are showing increased velocity due to the fixed volumetric flow rate.

the bacteria. There is a T_2 shift to a lower value from distilled water (not shown) from 1.2 s to 700 ms due to the carbohydrates and proteins in the BHI, and all of the BHI liquid showed the same T_2 value. The shape of the curve in the propagator dimension will be discussed further below, note the difference in the displacement axis with longer displacement range for Δ = 500 ms.

At t = 15-18 hours, after the column was inoculated with the bacteria, a shorter T_2 peak at approximately 100 ms appears in the distribution and then increases in intensity with increasing biofilm growth time. The integral of the intensity of the $T_2 \sim$ 100 ms peak over growth time is shown in Figure 7.3. This peak is located at the T_2 of the water within the EPS of the biofilm and its amplitude corresponds to the quantity of biofilm in the column. While the peak amplitude tends to increase in amplitude over time, between 30 and 33 hours the peak amplitude decreases before again increasing until 60 hours.

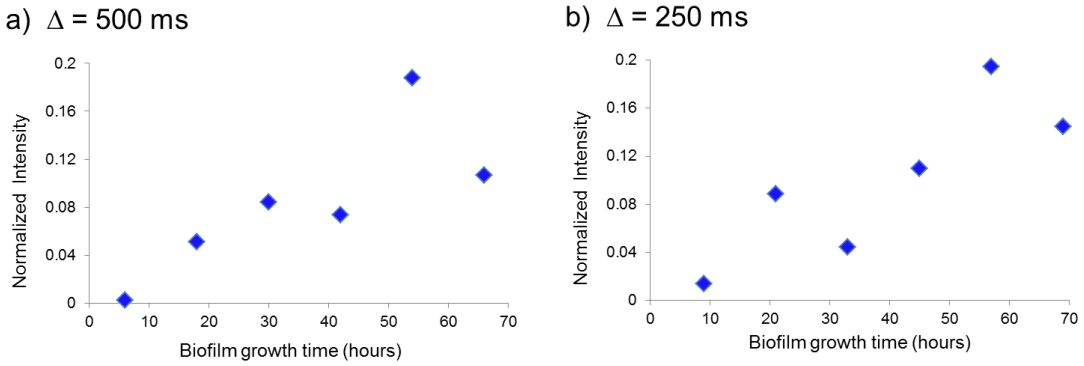

Figure 7.3. Integral of the intensity of the $T_2 \sim$ 150 ms peak as a function of biofilm growth time for a) Δ = 500 ms and b) Δ = 250 ms. The peak was integrated over the same area of each $P(Z,\Delta)$-T_2 plot and then normalized to the total signal intensity of each experiment. Each experimental data point is averaged over a 3 hour growth time period. A sloughing event appears to have occurred after about 30 hours of biofilm growth and is shown by the decrease in signal intensity of the T_2 component that corresponds to the biomass. The biofilm then continued to grow and the signal intensity increased until after 60 hours when the biofilm appears to have sloughed again. Note the Δ = 250 ms data points occur 3 hours after the Δ = 500 ms data points.

This corresponds to a sloughing event [159] which occurs when part of the biofilm is dispersed due to shear stresses and thus flows out of the bead pack. The distribution of T_2 values in the data set for $\Delta = 500$ ms at 33 hours shows an intermediate value for T_2 between the bulk liquid and the biofilm. This likely corresponds to biomass which detached during the sloughing event and moved through the bead pack. While the experiment acquisition times are too long to pinpoint exactly when the sloughing occurred, there is clearly a transition between 30 and 36 hours in the flow pattern consistent with this interpretation. In addition, the T_2 distribution shifts to longer values, the shorter T_2 peak has a smaller intensity, and the bulk flowing peak shows shorter displacements after sloughing indicating reduced biomass and increase in pore spaces which allow flow at fixed volumetric flow rate.

Figure 7.4 shows detailed analysis of the profiles of T_2 distributions at zero displacement $Z = 0$ and of the propagators at two specific T_2 values corresponding to bulk fluid ($T_2 \sim 700$ ms) and biomass ($T_2 \sim 150$ ms). Further evidence of a sloughing event occurring around 30-33 hours of biofilm growth is shown in the decrease in the signal amplitude of the shorter T_2 peak between the second and third rows in Figure 7.4.b. The propagator at the longer T_2 of approximately 700 ms corresponds to the flow of the bulk fluid and is not shifted significantly from the initial value of the T_2 of the BHI growth media. As the biofilm grew and plugged some of the pores of the bead pack, the distributions of displacements include longer displacements. This indicates a channeling effect, where the bulk fluid is not flowing through the biofilm-clogged pores and as a result is flowing faster through the clear pores to maintain the conservation of mass at the

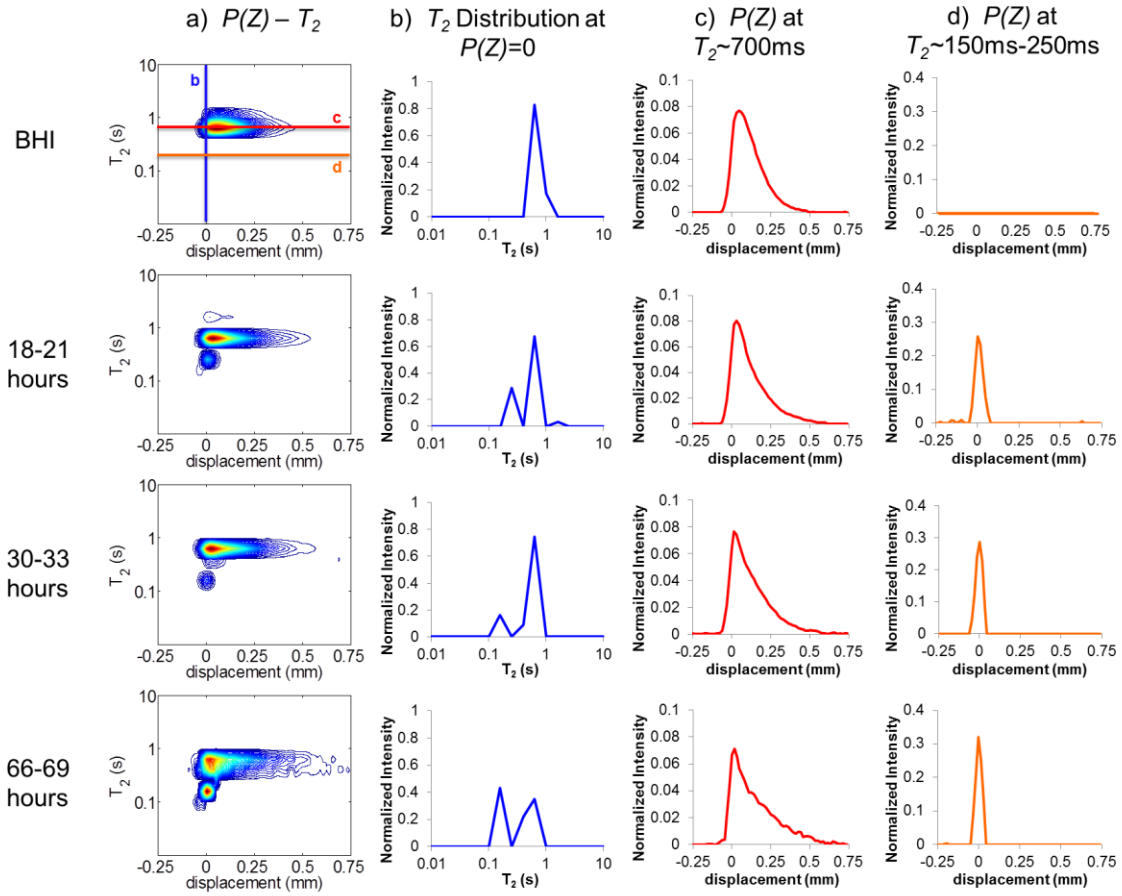

Figure 7.4. T_2 and $P(Z,\Delta)$ profiles at selected biofilm growth times for Δ of 250 ms. a) $P(Z,\Delta)$-T_2 plots at three time points in the biofilm growth. b) T_2 profile taken at the Z = 0 displacement, showing the growth in the shorter T_2 peak over time. c) $P(Z,\Delta)$ profile through the longer T_2 value, demonstrating that bulk fluid exhibits longer displacement values as the biofilm plugs some of the pores of the porous media. d) $P(Z,\Delta)$ profile through the shorter T_2 value, demonstrating that there is zero flow through the biomass.

set volumetric flow rate [128]. At the shorter T_2 of ~ 150 ms that corresponds to the biofilm, there is no flow and the propagator is narrow and centered at Z = 0. This is quantitative experimental evidence that there is no convective flow through the biomass within the displacement resolution of the measurement of +/- 15.6 μm over Δ = 250 ms, or v = +/- 62 μm/s.

Figure 7.5 presents an alternative analysis of the difference between the dynamics in the bulk fluid and within the biomass. Rather than performing a Fourier transform on the data, the positive pulsed magnetic field gradient displacement data was fitted with a 2D inverse Laplace transform corresponding to equation 7.7 in the *q*-space direction and an exponential decay in the T_2 direction. These 2D plots are correlations between

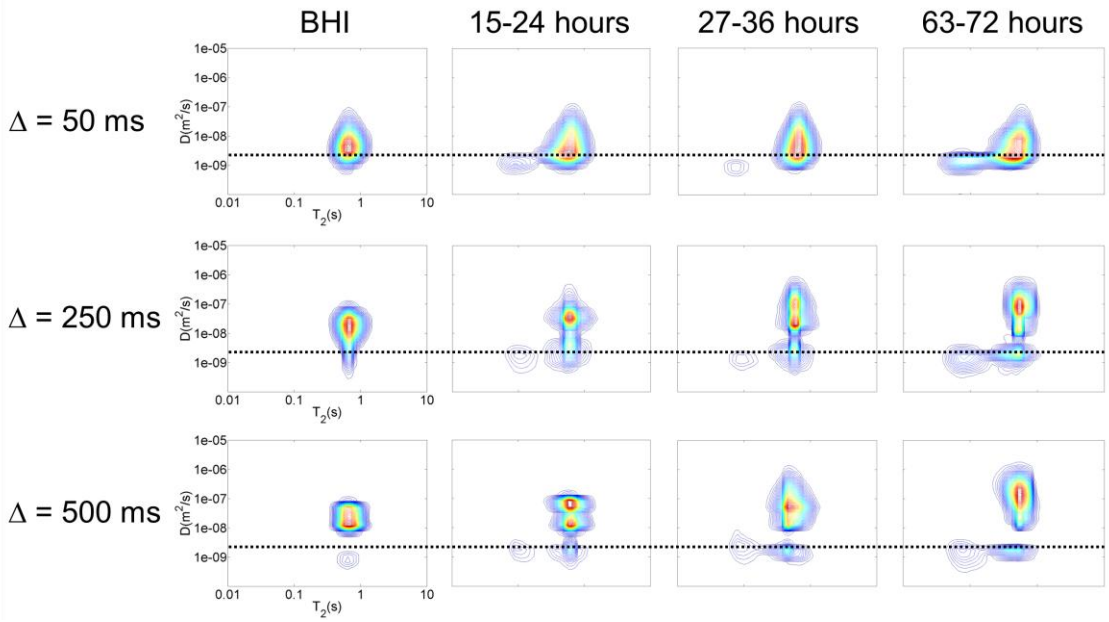

Figure 7.5. $D(\Delta)$-T_2 effective diffusion–spin-spin relaxation correlation plots of longitudinal hydrodynamic dispersion and fluid type for three different observation times and at four different times during biofilm growth. The dotted lines are shown as a guide to the eye at the self-diffusion of water at 25C, $D_0 = 2.2\text{x}10^{-9}\text{m}^2/\text{s}$. Note the presence of a bimodal distribution in hydrodynamic dispersion at $\Delta = 500$ ms before the inoculation of bacteria. As the biofilm grew, the $\Delta = 50$ ms data continue to show about the same amount of hydrodynamic dispersion at $T_2 \sim 700$ ms, while the 250 ms and 500 ms data show larger amplitude hydrodynamic dispersion more broadly distributed in amplitude as the biofilm grew. The spread in the vertical direction indicates the increase in hydrodynamic dispersion over biofilm growth for the bulk fluid indicating increased hydrodynamic mixing. The bimodal distribution of dispersion at $T_2 \sim 700$ ms also indicates the presence of dead end pores due to bioclogging. The spins at the shorter T_2 values however show no hydrodynamic dispersion on these time scales, indicating that there is no convective motion through the biomass.

longitudinal hydrodynamic dispersion coefficients $D(\Delta)$ (m^2/s) along the vertical axis and magnetic spin-spin relaxation T_2(s) along the horizontal axis. The absolute value of the data is analyzed so all phase information is lost and instead of a phase shift corresponding to the velocity induced displacement, only hydrodynamic dispersion information is retained [61]. Before the bacteria were inoculated into the system, the results for the three displacement observation times Δ show the well-known increase in preasymptotic hydrodynamic dispersion $D(\Delta)$ [73] and the same T_2 of 700ms. As the biofilm grew, the Δ = 50 ms data continue to show about the same amount of hydrodynamic dispersion at $T_2 \sim$ 700 ms, while the 250 ms and 500 ms data show larger amplitude hydrodynamic dispersion more broadly distributed in amplitude as the biofilm grew. The decrease in signal intensity of the shorter T_2 peak in the 50 ms and 250 ms data is evident between the second and third columns, again demonstrating that a sloughing event most likely occurred at about 30 hours of biofilm growth. At these flow rates and Δ times, the protons on the water molecules have transited only $\left\langle Z^2(\Delta)\right\rangle^{1/2} = \langle \xi_0 \rangle = \langle v_0 \rangle \Delta =$ 27, 130, and 270 μm for Δ = 50, 250, and 500 ms respectively, which provides displacement data in the clean bead pack ranging from within a single pore to several pores for the pore length scale l = 180 μm. The increasing amount of dispersion is a result of the growth of biofilm in parts of the bead pack and channeling in other parts of the bead pack causing increased mixing and dispersion. In contrast, at all biofilm growth times and all three Δ times, the peak at the $T_2 \sim$ 150 ms corresponding to the biofilm shows no increased dispersion and is approximately along the line for the self-diffusion of water, again

indicating that there is no convective flow generating dispersion within the biomass. An interesting feature of the data in Figure 7.5 is the evolution as a function of displacement time of a bimodal distribution of hydrodynamic dispersion in the BHI at the bulk fluid T_2 ~ 700 ms. At displacement time Δ = 500 ms, for which $\langle \xi_0 \rangle = 270$ μm, the flowing fluid has a mean dispersion of $D \sim 5\text{x}10^{-8}$ m^2/s while a smaller percentage of fluid has a value slightly slower than free water in BHI due to the no slip zero velocity layer at the bead surfaces. This restricted diffusion bulk fluid peak increases in concert with the biofilm peak at T_2 ~ 150 ms indicating increased hold-up of the bulk fluid contained in pore centers of biofouled pores and in dead end pores blocked by biofouled pores downstream. In addition, exchange occurring between the biofilm phase and the bulk phase in dead end pores may also result in cross-peaks in the $D(\Delta)$-T_2 spectrum. This effect may be seen in the data for 63-72 hours, which shows a range of T_2 values with restricted diffusion. Hydrodynamic dispersion on the pore scale will impact Darcy scale reactive transport simulations and measurements [98], so this ability to non-invasively measure dispersion of the biofilm phase and bulk fluid phase on the pore scale may provide data useful for a wide range of applications.

Figure 7.6 presents the T_2 distributions at $P(Z, \Delta) = 0$ for Δ = 250 ms and 21 hours of biofilm growth for four different strengths of BHI. The dotted lines indicate the T_2 of the BHI before biofilm growth with decreasing T_2 = 690, 520, 440 and 350 ms for 12.5%, 25%, 50%, and 65% BHI respectively. The T_2 of all of the water in the bead pack is shown to shift to shorter times for all BHI strengths because the bulk fluid interacts with

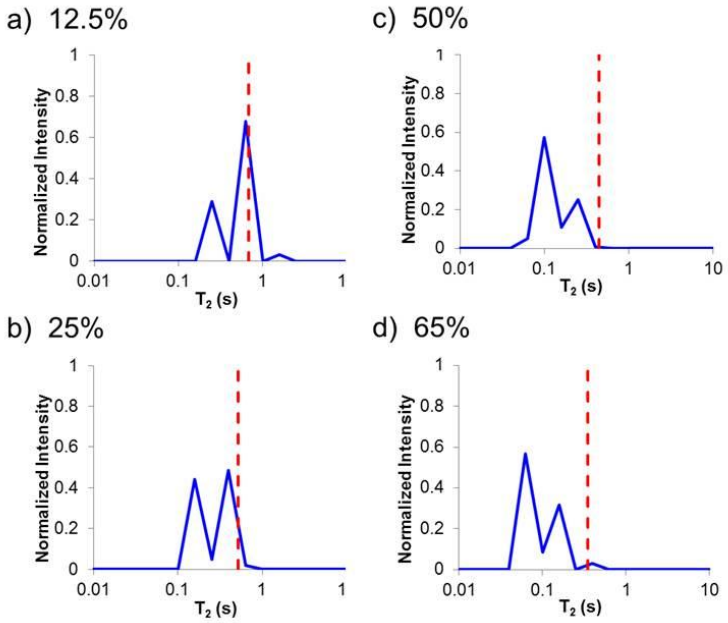

Figure 7.6. T_2 distributions at $P(Z,\Delta) = 0$ and 18-21 hours of biofilm growth for four different strengths of growth media: a) 12.5%, b) 25%, c) 50%, and d) 65%. The dotted lines indicate the T_2 of the growth media before biofilm growth: 690 ms for 12.5% BHI, 520 ms for 25% BHI, 440 ms for 50% BHI, and 350 ms for 65% BHI. The T_2 in the BHI is affected by the concentration of the carbohydrates and proteins in the growth media.

the polymers in the EPS of the biofilm and the T_2 is shifted due to hydrogen exchange [160]. The ratio between the amplitudes of the two peaks changes for the larger strengths of BHI indicating that more biofilm has grown in the bead pack. By providing more nutrient to the system by increasing the strength of BHI fed to the system, more bacteria will reproduce and grow within the biofilm and produce EPS, leading to a denser polymer matrix which will decrease the T_2 [3]. In addition the entire T_2 distribution shifts to shorter T_2 values for increased biofilm growth, again indicating that the water interacts with more polymers in the biofilm, providing an additional measure for the extent of biofouling.

Conclusion

In this paper we presented MR displacement-relaxation correlation experiments which are able to separate the effects on fluid flow of biofilm growth and enable the separate analysis of the convective flow through the biomass and through the channels of a biofouled porous media. We demonstrated the wealth of information that may be obtained from the same experimental data, including the analysis of fluid flow, biofilm growth, and hydrodynamic dispersion. Within the displacement resolution of these experiments, no convective flow was measured through the biomass. An increased amount of longitudinal hydrodynamic dispersion indicates increased hydrodynamic mixing due to increased channeling effects caused by biofilm growth. Increasing the velocity resolution of the experiments is possible by increasing the number of displacement encoding steps but comes at the expense of longer experiments, resulting in data with high velocity resolution but very course resolution in the time of biofilm growth. Studies with different flow rates, different geometries, or different organisms have the potential to yield relevant data for the understanding of biofilm growth, flow dynamics, and hydrodynamic dispersion in porous media.

MICROBIAL AND ALGAL ALGINATE GELATION CHARACTERIZED BY MAGNETIC RESONANCE

Contribution of Authors and Co-Authors

Manuscripts in Chapters 6, 7, and 8

Author: Hilary T. Fabich

Contributions: Helped conceive and implement the study design. Helped collect and analyze data. Helped write manuscript.

Author: Sarah J. Vogt

Contributions: Helped conceive and implement the study design. Helped collect and analyze data. Helped write manuscript.

Co-Author: Matthew L. Sherick

Contributions: Helped implement the study design. Provided feedback and comments on the manuscript.

Co-Author: Joseph D. Seymour

Contributions: Helped conceive and implement the study design. Provided feedback and comments on the manuscript.

Co-Author: Jennifer R. Brown

Contributions: Helped conceive and implement the study design. Provided feedback and comments on the manuscript.

Co-Author: Michael J. Franklin

Contributions: Helped conceive and implement the study design. Provided feedback and comments on the manuscript.

Co-Author: Sarah L. Codd

Contributions: Helped conceive and implement the study design. Provided feedback and comments on the manuscript.

Manuscript Information Page

Hilary T. Fabich, Sarah J. Vogt, Matthew L. Sherick, Joseph D. Seymour, Jennifer R. Brown, Michael J. Franklin, Sarah L. Codd
Journal of Biotechnology
Status of Manuscript:
___Prepared for submission to a peer-reviewed journal
___Officially submitted to a peer-review journal
___Accepted by a peer-reviewed journal
_X_Published in a peer-reviewed journal

Elsevier
Vol. 161, Pages 320-327, 2012

MICROBIAL AND ALGAL ALGINATE GELATION CHARACTERIZED BY MAGNETIC RESONANCE

Abstract

Advanced magnetic resonance (MR) relaxation and diffusion correlation measurements and imaging provide a means to non-invasively monitor gelation for biotechnology applications. In this study, MR is used to characterize physical gelation of three alginates with distinct chemical structures; an algal alginate, which is not O-acetylated but contains poly guluronate (G) blocks, bacterial alginate from *Pseudomonas aeruginosa*, which does not have poly-G blocks, but is O-acetylated at the C2 and/or C3 of the mannuronate residues, and alginate from a *P. aeruginosa* mutant that lacks O-acetyl groups. The MR data indicate that diffusion-reaction front gelation with Ca^{2+} ions generates gels of different bulk homogeneity dependent on the alginate structure. Shorter spin-spin T_2 magnetic relaxation times in the alginate gels that lack O-acetyl groups indicate stronger molecular interaction between the water and biopolymer. The data characterize gel differences over a hierarchy of scales from molecular to system size.

Introduction

Alginate is a biologically synthesized polymer that is commonly used as a food additive, for biomedical applications, including tissue constructs [161], microfluidic device manufacture [162] and in some bandages to promote wound healing. Alginates are mixed polysaccharides composed of α-L-guluronate residues and β-D-mannuronate

residues linked by ß-1-4 glycosidic bonds, produced by brown algae and by bacteria of the genera, *Pseudomonas* and *Azotobacter*. The chemical structures of the alginate subunits are shown in Figure 8.1, and the mechanism of bacterial alginate biosynthesis was described in a recent review [163].

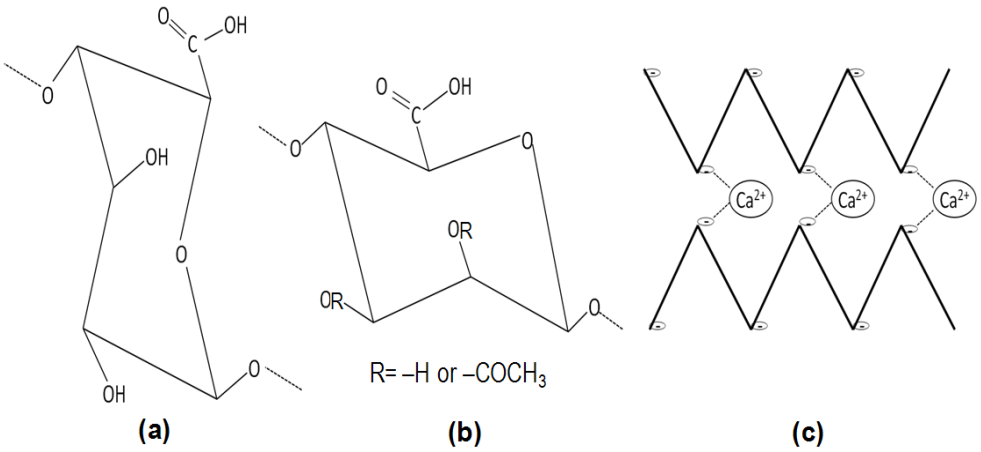

Figure 8.1. (a) α-L-guluronate (G), and (b) β-D-mannuronate (M), form the anionic polysaccharides that make up alginate. (c) Alginate (indicated by the bold lines) is known to order into an "egg box" formation when a divalent cation is introduced, forming a gel. The cation, such as Ca^{2+}, will covalently bond (indicated by the dashed lines) with the negative charges on the deprotanated carboxyl groups (indicated by the (-)) of the G units in the alginate chain.

The gelation properties of alginate, which are important for its biotechnological applications, are dependent on the alginate structure and on its molecular weight [164, 165]. The structures of alginates vary depending on their source. Rather than repeating polymers of the two uronic acid subunits, the G and M residues are interspersed randomly, with algal alginates containing blocks of repeating G subunits. *Azotobacter vinlandii* alginate also contains G-blocks, but G-blocks are not found in alginates from *Pseudomonas spp*. Another structural difference is that the bacterial alginates are often

O-acetylated at the C2 and/or C3 positions of the D-mannuronate residues, whereas the algal alginate does not contain O-acetyl groups. Research on algal alginate since the 1970s has shown that G-blocks will align and bind to the positive ions in an ordered "egg-box" structure [113](Fig 8.1). However, the M units are also known to be important to gel formation and structure, particularly in high molecular weight alginates such as the bacterial alginates studied in this research [166, 167]. The degree of O-acetylation of the alginate also affect the gelation properties, but the mechanism for this is not well understood [168]. Deacetylated alginates produce gels that are stronger than acetylated alginates [169]. As shown in the magnetic resonance (MR) images presented below in Figure 8.2, O-acetylation also appears to affect the homogeneity of the gel.

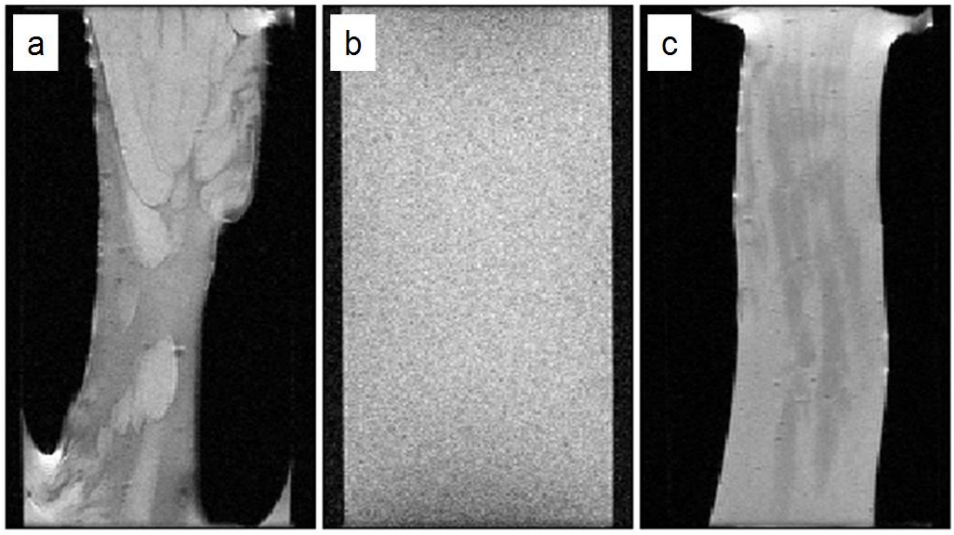

Figure 8.2. MRI images of alginate gels obtained from (a) FRD1153, (b) algae, and (c) FRD1. These T_2 maps demonstrate the variation in heterogeneity between the three gels prepared in the same fashion. These images were obtained after the gelation process had been completed and the bulk water drained. The images have a FOV of 20 mm in the frequency encode direction and 13 mm in the phase encode direction, the resulting resolution being 78 x 102 μm over a slice thickness of 1 mm. Sixteen echoes were collected with a TE = 11 ms and the TR = 1 s.

In addition to its importance for biomaterials and as a food additive, gelation of alginate may also be important for a certain infectious disease process. *Pseudomonas aeruginosa* causes chronic pulmonary infections of patients with the genetic disorder, cystic fibrosis (CF) [170]. CF patients are prone to many acute bacterial infections, including from strains of *P. aeruginosa*. Over time the *P. aeruginosa* strains convert to an alginate overproduction (mucoid) phenotype. Mucoid *P. aeruginosa* strains often cause chronic pulmonary infections. When the alginate comes in contact with divalent cations, most commonly calcium in the body, it forms a rigid gel. Gel formation may play a role in chronic infections by contributing to the protection of the bacterial cells from the host immune response, since the structure of alginate is important for chronic infections. In particular, the presence of O-acetyl groups on the alginate provides the bacteria with greater resistance to opsonic phagocytosis [171] than does alginate lacking O-acetyl groups. Enhanced understanding of the molecular origin of physical gelation behavior in microbial and algal alginates will impact both biomedical and biotechnology applications.

Nuclear magnetic resonance (NMR) techniques including spectroscopy [166, 172], imaging [115, 168], and pulsed-field-gradient spin-echo (PGSE) [97, 173, 174] have been utilized for many years to study alginate and other biopolymer systems including biofilms. The study of MR relaxation processes of biopolymer systems provides unique data on molecular dynamics and interactions [24]. MR relaxation measurements are affected by hydrogen exchange between the water and the biopolymer and diffusive exchange between the bulk water and water interacting with the

biopolymer. Recently, two dimensional MR relaxation and diffusion correlation experiments have been performed on a number of diverse systems, including real and model porous media, food, gels, and protein solutions [25, 27, 29, 44, 46, 47, 175]. In this work, we use MR properties and techniques to compare gels formed by physical gelation with calcium ions added to 2% by weight solutions of three alginates produced from different organisms: brown algae, *P. aeruginosa* FRD1, and the O-acetyl mutant derivative *P. aeruginosa* FRD1153.

Materials and Methods

Alginate Solution and Gel Preparation

Alginate Isolation: The bacterial strains used in this study were *P. aeruginosa* FRD1 and the O-acetylation deficient derivative, FRD1153 [176]. Alginate was purified from these strains using the procedure described previously [176], but scaled up to increase the mass of alginate purified. The bacteria were first cultured on agar plates and incubated for 20 h. at 37°C. A mucoid colony was selected from the plate, and inoculated into 10 ml of Luria Broth (LB) (Difco) in a 125 ml baffled flask. The culture was incubated with shaking at 220 rpm for 24 h. at 37°C. Two ml of the culture was used to inoculate a 400 ml volume of LB in a 1000 ml baffled flask. The culture was incubated with shaking for 24 h. at 200 rpm. The culture was diluted with an equal volume of 0.85% NaCl to reduce viscosity and the culture supernatant containing the secreted alginate was separated from the cells by centrifugation at 10,000 rpm for 20 min at 20°C. Cetyl-pyridinium chloride ($C_{21}H_{38}ClN$), 200 ml of a 2 wt% solution, was used

to precipitate the alginate from the culture supernatants. The precipitates were dissolved in 200 ml of 1 M NaCl by shaking at 37°C for 24 h. The samples were centrifuged to remove the remaining cellular debris, and an equal volume of isopropanol was added to the supernatant to precipitate the alginate again. The precipitated polymer was then dissolved in 200 ml of 0.85% NaCl. The isopropanol precipitation and resuspension procedure was repeated several times until the alginate solution was clear and colorless. The polysaccharide was then dialyzed for 24 h. against distilled water using Spectra/Por dialysis membrane with a molecular weight cutoff of 10,000. The purified polymer was then lyophilized to allow for rehydration at a controlled weight percent.

Alginate and Ion Solution Preparation: Alginates were prepared as 2 wt% solutions by dissolving sodium alginate powder from a brown algae source (Acros Organics, Geel, Belgium), or lyophilized FRD1 or FRD1153 into deionized water with stirring. Once dissolved, the solutions were stored in a refrigerator until use. An ion solution of 1M calcium chloride ($CaCl_2$) was prepared with nanopure water. $CaCl_2$ and algal alginate were used without further purification.

Gel Sample Preparation: Glass NMR tubes (inner diameter 11.4 mm, length 10 cm) were cleaned with ethanol before being coated twice with a thin layer of alginate solution dried onto the tubes in a 110°C oven for 1 hour. In previous research [115] this technique was used to adhere the gel to the tube walls. The coated tubes were then filled with the alginate solution and stored overnight to allow degassing. A polystyrene annulus with an outer diameter of 9.5 mm and an inner diameter of 5.3 mm was then

placed on top of the alginate solution to stabilize the ion – alginate solution interface. Approximately 2 ml of the 1 M $CaCl_2$ solution was added with a pipette. After 2-5 minutes, the tube was gently placed in the MR probe to start the measurements. MR measurements were then conducted as Ca^{2+} ions diffused into the alginate solution causing gelation along the reaction front. After it was fully gelled, the bulk water was drained from the tube to more accurately measure the differences between the gels without the influence of the surrounding water resulting in gels of slightly denser weight percent polymer.

Magnetic Resonance (MR) Techniques and Experiments

MR Relaxation: Spin-lattice (T_1) relaxation of the MR signal occurs due to interaction in the longitudinal direction along the applied magnetic field (B_0), and spin-spin dipolar (T_2) relaxation occurs due to interactions transverse to B_0. The T_2 relaxation is dependent on rotational mobility of the proton (^{1}H) nuclei. For protons on the polymer, T_2 is on the order of milliseconds while in the bulk water it is on the order of seconds. The measurement of T_2 using a standard CPMG pulse sequence [20], shown in Figure 8.3, is also sensitive to the time scale of the measurement, in particular the 2τ time spacing between the 180 radio frequency (rf) pulses. The relaxation data are impacted by this spacing, depending on several complex mechanisms that contribute to T_2 relaxation in polymer systems, including hydrogen exchange between the polymer protons and water protons [156] and water interactions with the polymer chains [177].

MR Experiments: MR experiments were conducted using a 15 mm diameter rf coil on a Micro 2.5 imaging probe with maximum gradient strengths of 1.48 T/m in three directions on a 300 MHz (^{1}H frequency) Bruker magnet networked to an AVANCE III spectrometer. After $CaCl_2$ was added to the alginate solution, a series of MR experiments including relaxation time weighted 2D images, 1D spatial profiles, and diffusion measurements with acquisition times totaling 15 minutes were repeated for approximately 10 hours to monitor gel formation [115]. After the gelation process was complete, a series of 2D relaxation and diffusion correlation measurements were conducted. The water surrounding the gel was then drained and the same set of experiments was repeated. The gels were then aged for 10 days and the experiments were, again, repeated. This same experiment sequence was followed for all three alginate samples.

MR Experimental Details: 2D images of a slice of the tube reactor spatially resolved in radial and axial directions were collected with a standard multi-echo (CPMG) spin-warp imaging sequence. Sixteen echoes (n_E) were collected over the 1 mm sample slice and the echo attenuation of each image pixel fit to $\exp\left(\frac{-(n_E)TE}{T_2}\right)$ to determine the T_2 and form the T_2 map with an echo time (TE) of 11 ms, the longest echo time being $n_E \cdot TE$ = 176 ms. The repetition time (TR) of the sequence was 1 s and two averages were collected resulting in a total image acquisition time of 4 minutes. The image had a field of view (FOV) of 20 mm in the axial frequency encode direction and 13 mm in the phase

encode direction. The spatial resolution of the image was 78 μm x 102 μm over a 256 x 128 pixel domain.

1D spatially resolved T_2 relaxation weighted axial profiles of the sample were acquired. The 1D spatially resolved experiment was exactly the same as the 2D image with the exception of the elimination of the phase encoding which reduced total experiment time in order to monitor rapid changes during gelation. The profiles represent an integration over the radial phase encoded direction of the sample. The 1D spatial profiles with a TR of 1 s were repeated four times during the 15 minute cycle to determine variation during the 15 minute experimental suite. The 1D profiles were each acquired in 2 s.

The three 2D correlation experiments used in this study, diffusion - relaxation D-T_2, spin-spin relaxation correlation/exchange T_2-T_2, and spin-lattice – spin-spin relaxation correlation T_1-T_2, utilize the direct measurement of T_2 using a CPMG pulse train with 4096 echoes at a spacing of $2\tau = 400$ μs. The indirect dimension for each type of experiment is encoded using either a pulsed gradient stimulated echo sequence (D-T_2), a 180 rf inversion pulse (T_1-T_2), or a series of CPMG pulses (T_2-T_2). The pulse sequences are shown in Figure 8.3. The parameters for the D-T_2 experiments were: $\delta = 1$ ms, $\Delta =$ 50 ms, 26 magnetic field gradient points between $g = 0$ and 1.482 T/m and 32 step phase cycle with a total acquisition time of 3.5 hours. For the T_1-T_2 experiments, the inversion recovery time was varied between 0.001 and 3.6 seconds in 32 logarithmically spaced steps with a 16 step phase cycle and a total acquisition time of 2 hours. The T_2-T_2 experiments used the same 2τ time in the indirect dimension as the direct dimension (400

μs) and the number of pulses was varied logarithmically from 2 to 4096 in 32 steps with a 16 step phase cycle and a total acquisition time of 2 hours. The 2D correlation data were analyzed using a 2D inverse Laplace transform algorithm [37, 50].

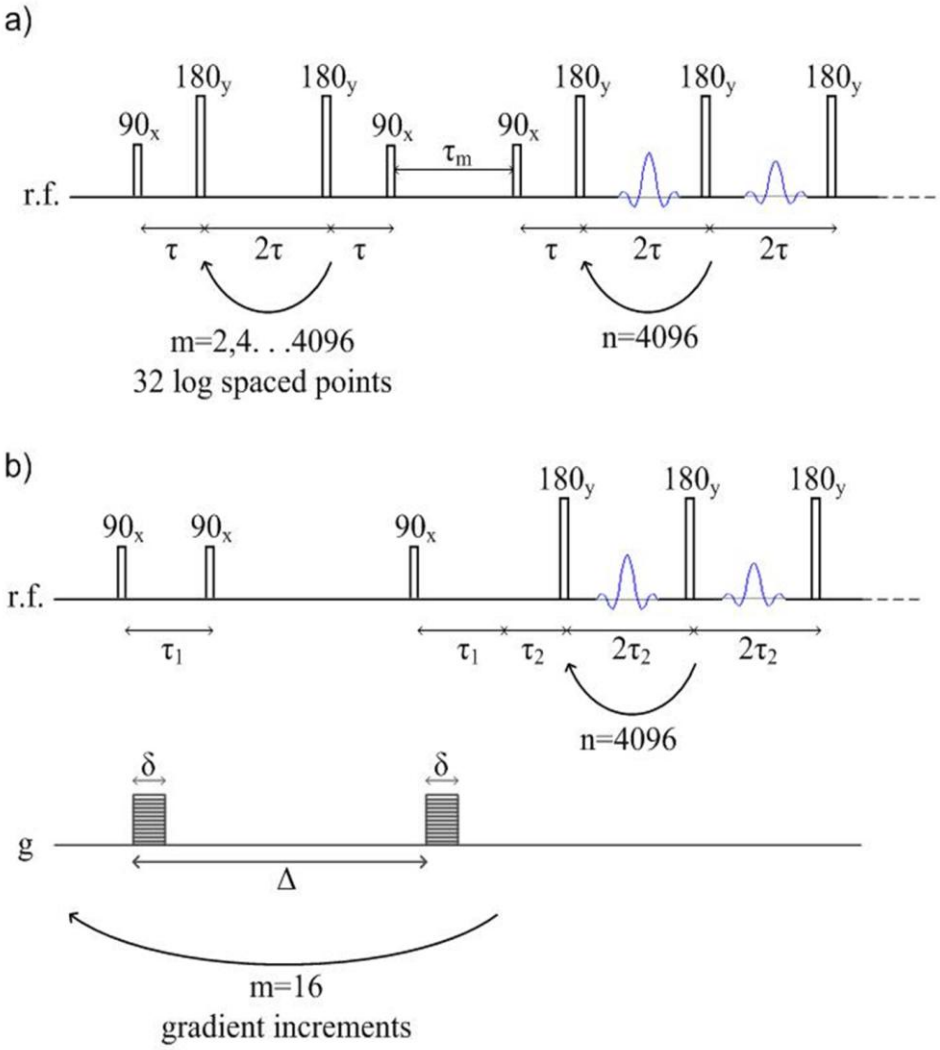

Figure 8.3. 2D diffusion and relaxation correlation MR pulse sequences. Both utilize a CPMG measurement with a 2τ spacing of 400 μs and 4096 echoes in the direct dimension. a) T_2-T_2 pulse sequence, which encodes for T_2 relaxation in the indirect dimension by applying a logarithmically varying number between 2 and 4096 series of 180 pulses. b) D-T_2 pulse sequence, which encodes for diffusion in the indirect direction using a stimulated echo PGSE sequence with 26 linearly varying gradient pulses between g = 0 and 1.48 T/m.

Results and Discussion

Gelation Front

MR measurements were performed as the gels were forming. The signal and T_2 relaxation as a function of gelation time is shown in Figure 8.4. As time progresses and calcium diffuses into the sample, a drop is seen in both the T_2 and signal amplitude (M_0) due to gelation. This is due to the change from the alginate solution to a gel as the calcium diffuses into the sample. As can be seen from the relaxation contrast in the MR relaxation images in Figures 8.2 and 8.4, the gel produced by the FRD1153 bacterial alginate is more heterogeneous than that produced by the FRD1 bacterial alginate. Figure 8.2 shows the bacterial alginate gels contract during gelation. The algal gel adheres to the alginate coated tube wall, while the bacterial gels do not. This indicates larger molecular stresses are generated in the bacterial gels during gelation. Restriction of rotational mobility causes more rapid T_2 relaxation, so pixels of less signal indicate regions with a tighter gel network. For the FRD1153 solution, T_2 and M_0 decrease more rapidly (Figure 8.4) indicating that the gelation front motion is faster. Faster gelation is related to increased heterogeneity.

2D Correlations

After gel formation was complete, T_2-T_2 relaxation measurements were conducted. Mixing times (τ_m) of 5 ms and 250 ms, sequence in Figure 8.3a, were obtained for the three alginate solutions before gelation, after gelation, after draining of the bulk water, and after aging for 10 days. Results for the three alginate gels after aging

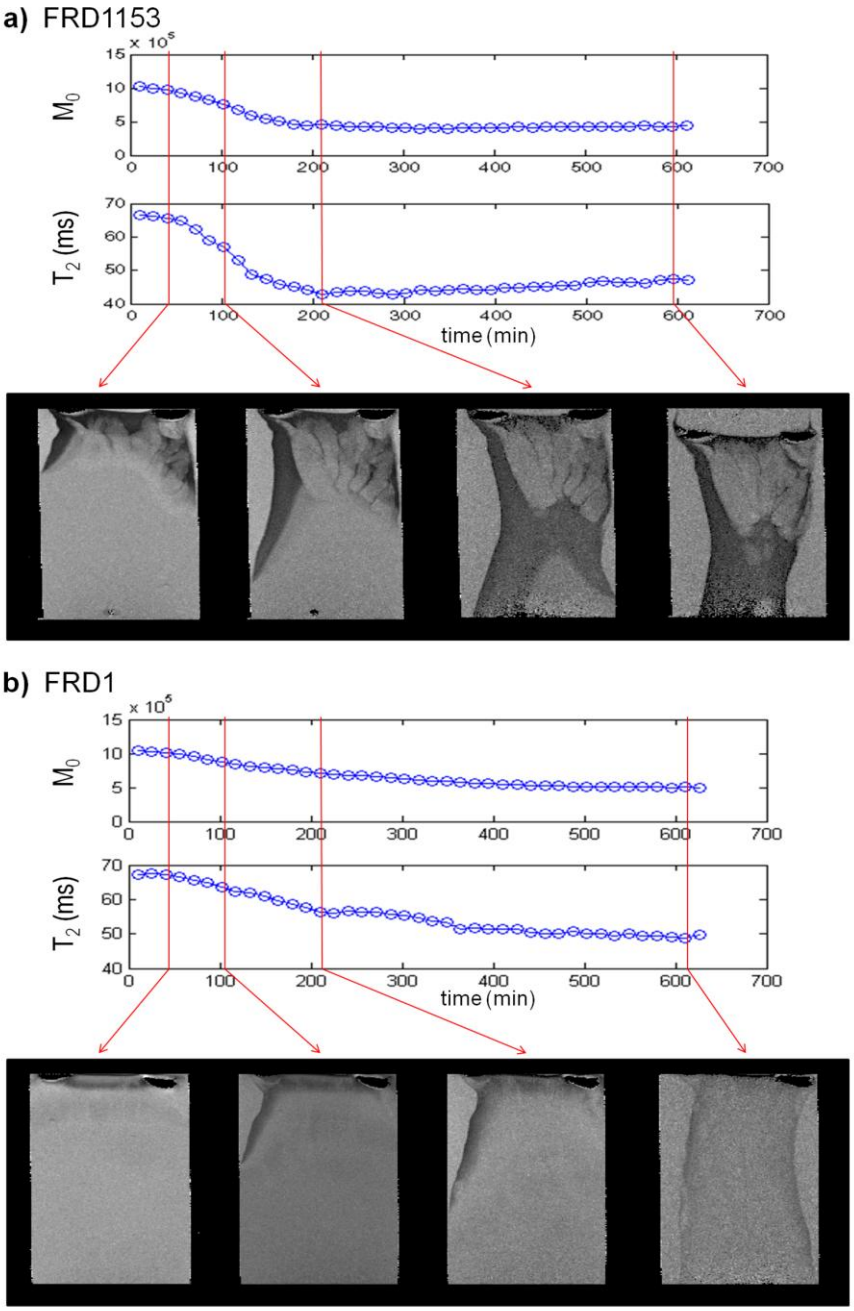

Figure 8.4. Magnetization amplitude (M_0), spin-spin relaxation (T_2) and images with increasing time during gelation for (a) FRD1153 and (b) FRD1 alginates showing a difference in rate of gelation as well as heterogeneity. The MR images have a resolution of 78 x 102 μm^2 over a 1 mm thick slice. The FRD1153 gel shows more heterogeneity in the images. The faster decay in both the M_0 and T_2 indicate the gel formed by the FRD1153 also forms more quickly than the FRD1.

for 10 days are shown in Figure 8.5. Note that since the bacterial alginate gels contracted more than the algal gel, they are of higher polymer weight percent. Off-diagonal peaks in T_2-T_2 spectra are an indication of exchange of protons between different T_2 environments. Chemical exchange of protons between water and biopolymer occur on timescales shorter than 5 ms and so are not present [24]. For the more homogeneous algal and FRD1 alginates, no off-diagonal peaks were observed for any of the mixing times. However the heterogeneous FRD1153 gel exhibited off-diagonal peaks that increased in intensity as the mixing time was increased, indicating exchange between the mesoscale gel domains exhibited in the images in Figure 8.2. The data clearly demonstrate the quantitative differentiation of gel heterogeneity by T_2-T_2 measurements.

Results of D-T_2 experiments for all three gels are shown in Figure 8.6 and further indicate the detail 2D correlations provide for monitoring gelation. All three solutions have similar T_2 and diffusion coefficient distributions prior to gelation. After gelation the distributions are unique for each alginate source. The distribution of T_2 values for each type of gel is consistent with the 2D and 1D T_2 results. In the diffusion direction, the results show that for each of the three gels, the proton molecules with the shortest T_2 values also have the smallest diffusion coefficients. This indicates a coupling between restricted rotational and translational mobility of protons interacting with the more polymer dense or rigid parts of the gel, thus exhibiting restricted diffusion and faster relaxation. A common feature in the D-T_2 data of all three alginates is the broadening of

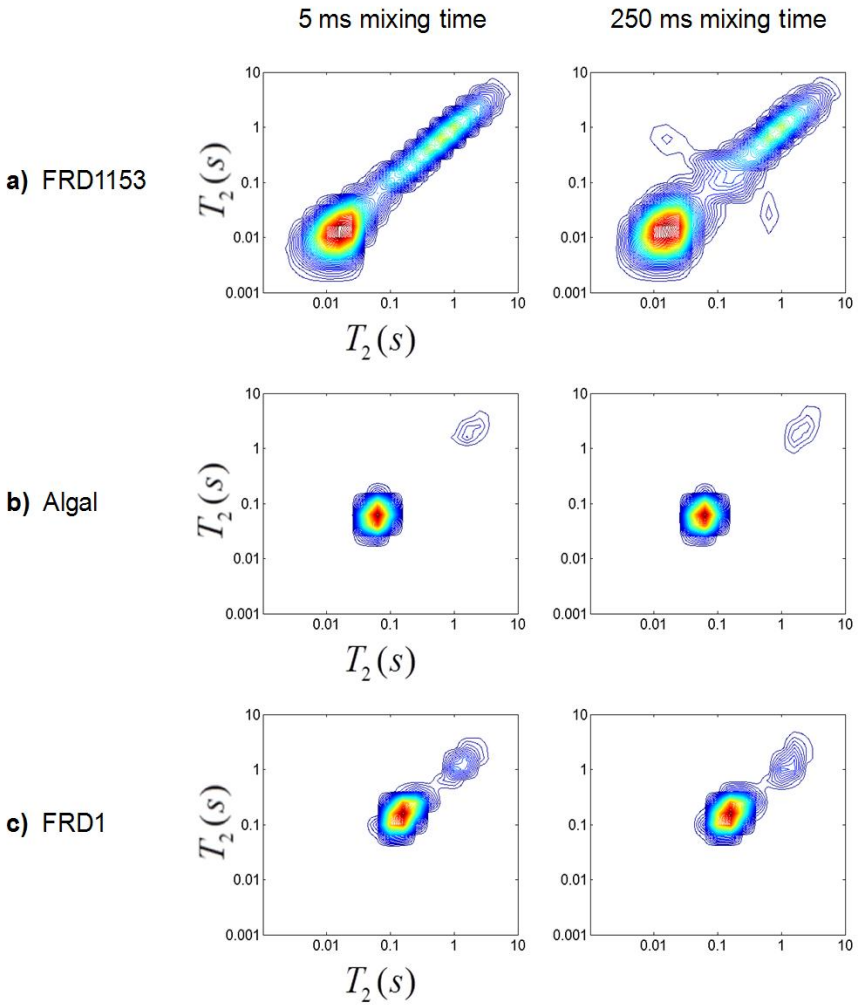

Figure 8.5. T_2-T_2 correlations for mixing times of 5 ms (left column) and 250 ms (right column) for a) FRD1153, b) algal, and c) FRD1 gels after draining of bulk water and aging for 10 days. 2D T_2-T_2 experiments were integrated in the vertical direction to obtain the 1D T_2 profiles shown in Figure 8.7 and 8.8.

the distribution of effective diffusion coefficients in the transition from the sol to the gel phase. As in the T_2-T_2 data, the heterogeneous FRD1153 gel has distinct features indicating the multiple water domains not present in the more homogeneous FRD1 and algal gel.

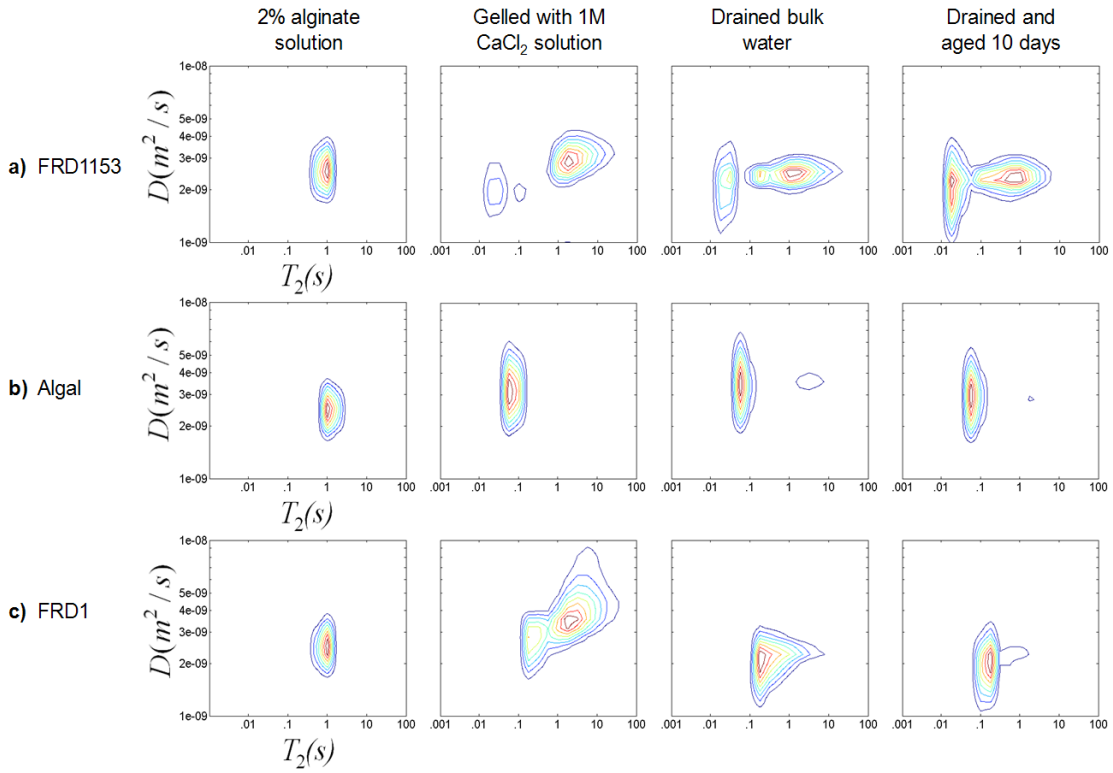

Figure 8.6. D-T_2 correlations for the three alginate biopolymers a) FRD1153, b) algal and c) FRD1 in solution, post gelation, drained of bulk water after gelation and gel aged for 10 days (columns left to right). Experimental details are discussed in the text.

T_1-T_2 correlation experiments were conducted. The 2D plots are not shown due to the fact that all experiments exhibited a single peak in the T_1 direction. All three gels have approximately the same $T_1 = 2.3$ s over the same range of T_2 values shown in all the 2D correlation data. The FRD1153 with the shorter T_2, has a larger ratio between T_1 and T_2 than the algal gel, another indication of a more dense or rigid gel structure.

1D Relaxation Distributions

The 2D T_2-T_2 spectra shown in Figure 8.5 for $\tau_m = 250$ ms were integrated over the indirect dimension to obtain 1D T_2 relaxation distributions. The results for all three gels are shown in Figure 8.7. The two non-acetylated alginate gels, FRD1153 and algal,

have shorter T_2 populations than the acetylated alginate FRD1. This is in spite of the fact that due to contraction the FRD1 gel is at slightly higher polymer concentration than the algal gel. Shorter T_2 spin-spin relaxation indicates stronger dipolar coupling between ^1H protons due to more restricted rotational mobility. The ^1H signal is dominated by the 98 wt% water signal and so polymer protons are not directly observed. However, the water relaxation in a gel is reduced from the free bulk water value due to exchange of water protons and biopolymer exchangeable protons and restricted mobility of water interacting with the gel matrix [24] an indirect detection of the polymer gel network structure.

The non O-acetylated FRD1153 and algal gels have lower T_2 indicating stronger interaction with the solvent water through biopolymer network rigidity and enhanced proton exchange. The increased heterogeneity of the FRD1153 gel, as shown in the MR images in Figure 8.2, is apparent in the broader distribution of T_2 populations in comparison with the much narrower range of populations in the FRD1 gel. The homogenous algal alginate gel has the narrowest distribution of T_2 populations. As T_2 distributions can be acquired in 10 minutes, MR T_2 relaxation measurements are viable as real time monitors for gelation processes on-line. With aging over ten days the algal gel T_2 distribution stays constant. In contrast, the two bacterial alginate gels show shifts to shorter T_2 values after draining of the bulk water and further shifts after aging. The FRD1153 and FRD1 have a larger peak at approximately $T_2 \sim 3$ s due to the presence of bulk water after the contraction of the gel phase during the reaction as shown in the images of Figure 8.4. Draining this water alters the proportion of proton spins in the 1 s peak and the ~100 ms peak for the FRD1 and the ~10 ms peak for FRD1153 as expected.

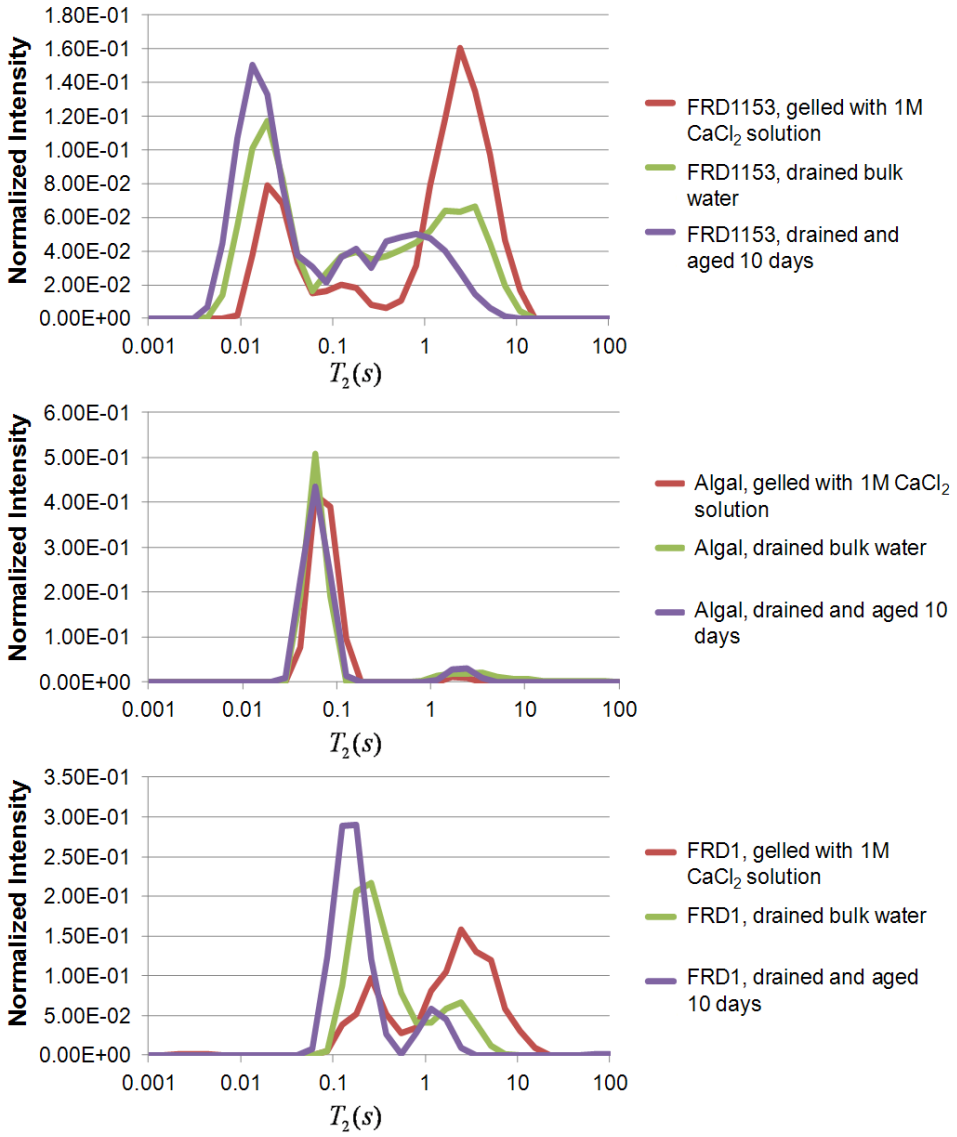

Figure 8.7. 1D T_2 profiles for the three alginate gels immediately after gelation with $CaCl_2$, after draining excess water, and after aging for 10 days.

The reduced proportion of proton spins in the bulk water allow for a better comparison between the two bacterial alginates and the algal alginate. The FRD1 and algal gels have a bimodal distribution indicating two populations of proton relaxation in contrast to the FRD1153 which has a broader distribution due to multiple relaxation domains in the more heterogeneous gel. An interesting feature of the aging in the bacterial alginate gels

is the shift to shorter relaxation time of both the short and long components of the distributions. This indicates that while the algal alginate gel is stable over time, the bacterial alginate gels are contracting or more highly associating water and biopolymer over time.

The entire set of experiments was repeated twice for each type of gel, and the results obtained were reproducible. T_2 distributions for the two trials of the bacterial alginate gels are shown in Figure 8.8. The heterogeneity of the FRD1153 gels causes some variation in the distributions, however, the range of T_2 values for each gel was similar for each repetition. The two trials of the more homogeneous FRD1 gels showed even more similar T_2 distributions indicating the ability to quantifiably monitor the degree of homogeneity or heterogeneity during gelation.

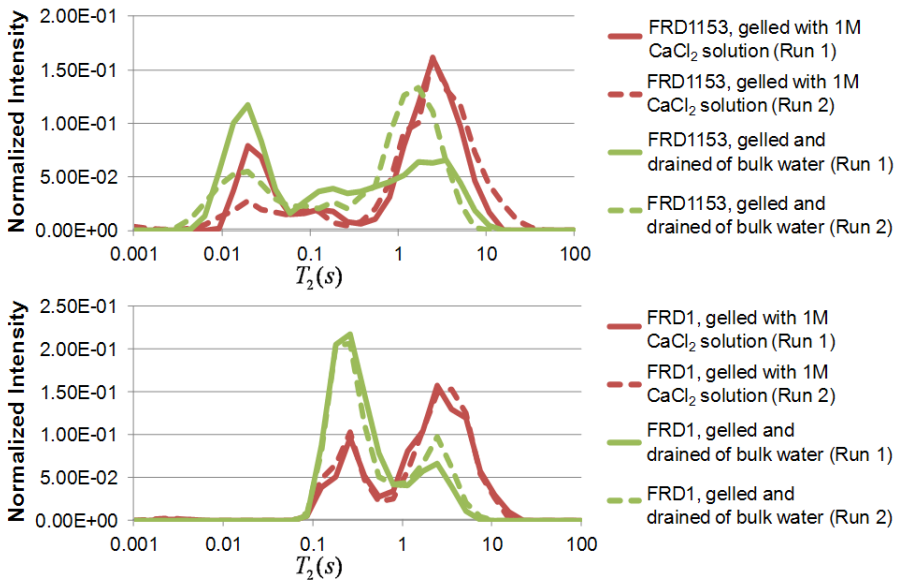

Figure 8.8. 1D T_2 profiles showing two trials of measurements for FRD1153 and FRD1 bacterial alginate gels, demonstrating the repeatability of the reaction front experimental process.

Conclusions

Alginates are broadly used in food and biomedical applications in biotechnology. This work presents direct, non-invasive comparison of gels generated by a diffusion-reaction front for alginates from brown algae and *Pseudomonas aeruginosa* microbes. The ability of magnetic relaxation and diffusion correlation experiments to quantify the differences in gelation behavior of the different precursor alginate biopolymers is demonstrated. The MR data show that the deacetylated algal and FRD1153 have shorter T_2 relaxation times due to stronger molecular interaction between water and biopolymer than the acetylated FRD1. MR data also readily differentiates the formation of mesoscale heterogeneous structures in the FRD1153 from the more homogeneous algal and FRD1 alginate gels. Further characterization of gels from microbial alginate sources provides the potential to develop genetically tailored alginate biopolymers for particular gel biotechnology applications.

ALGINATE SOLUTIONS AND HOMOGENEOUS GELS CHARATERIZED USING RELAXATION DISPERSION MEASUREMENTS

Introduction

Polymers are molecules of long chains of repeating subunits known as monomers. They are found in nature as biopolymers (rubbers, alginates), used in biotechnology applications and industries ranging from pharmaceuticals to food. There is a wide range of research devoted to understanding the molecular level interactions, rheological properties, and electrostatic interactions of these types of molecules [165, 167, 177-186]. An interesting property of some polymers is that in certain circumstances polymers may form a system spanning network of molecules that behaves as a solid, called a gel, as discussed in the previous chapter.

This chapter presents research on solutions and homogeneous gels of the biopolymer alginate. Sodium alginate is a solid salt which dissociates and dissolves in solution to form a negatively charged polyelectolyte. Polyelectrolytes in dilute solutions behave differently than uncharged polymers due to electrostatic interactions between the charges on the chains [181]. The material properties of polyelectrolytes are affected by the addition of salts such as sodium chloride (NaCl) due to electrostatic screening of the polymers by the counterions [187]. The addition of ions with a positive charge of two, such as calcium or copper, will cause the alginate to associate and form a gel [115, 188-190]. The previous chapter presented research which was conducted on gels made from a diffusive reaction which resulted in heterogeneous gels. The results presented were

primarily interesting due to the ability to detect the mesoscale heterogeneities. This chapter presents research on homogeneous gels, in which NMR relaxation measurements are shown to be sensitive to molecular level dynamics. This research was done in collaboration with undergraduate students who are currently performing additional research on these systems. As such, the following discussion will present data that is in the process of being analyzed and will result in a publication including the author in the next few months.

Background

Alginate

Alginate is copolymer made up of β-D-mannuronate (M units) and α-L-guluronate (G units), the molecular structure of which are shown in Figure 9.1. Alginate is produced by certain types of algae, such as brown algae, as well as bacteria such as *Pseudomonas aeruginosa*, as discussed in the last chapter. The research presented here compares O-acetylated and non-acetylated alginates. O-acetylated alginate is produced

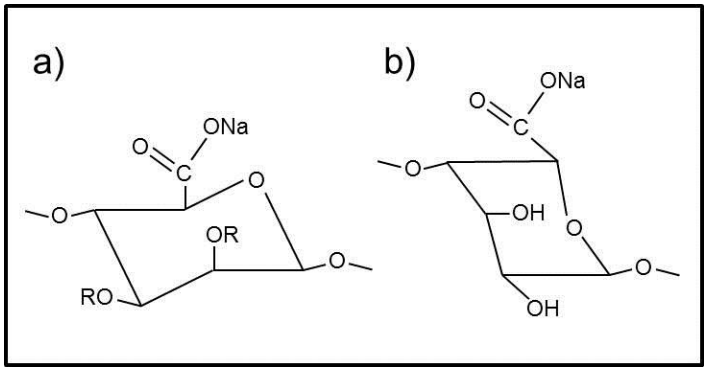

Figure 9.1. Monomer units that make up the copolymer known as alginate. a) sodium salt of mannuronate (M unit). The R units may be either –H or $–COCH_3$ (acetyl). b) sodium salt of guluronate (G unit). The monomer units are epimers.

by *P. aeruginosa* FRD1 isolated from the lungs of cystic fibrosis patients. Non-acetylated alginates produced by brown algae are the primary source for industrial uses of alginate. The reason for the evolutionary production of O-acetylated alginate by P. aeurignosa in CF patients is not known. Understanding the differences in the material properties of O-acetylated and non-acetylated alginates provides a basis for a biomimetic approach to molecular level biopolymer design for biotechnology applications. To this end a genetic mutant *P. aeruginosa* FRD1153 which produces a non-acetylated alginate is used to compare material properties.

The three different types of alginate allow several comparisons to be made. The differences between non-acetylated alginates produced by algae and FRD1153 are the molecular weights of the alginate chains and the ratio between M and G units of the alginate chains [166]. The difference between the two bacterially produced alginates is primarily the degree of acetylation, as the molecular weights and the ratio of M to G units are known to be essentially identical [166]. The degree of acetylation is known to affect the properties of alginate, but the molecular level interactions that cause these differences are not well characterized.

The study of homogeneous solutions and gels allows us to study the molecular level interactions caused by the differences in molecular weights, monomer compositions, and degrees of acetylation. The experiments presented compare solutions with three different concentrations of added salt (NaCl) and two concentrations of alginate (0.58wt% and 1wt%). The 1wt% solutions are then gelled with a homogeneous reaction process which results in gels of 0.58wt% alginate with three concentrations of

salt. The salt concentrations chosen were 0M, 0.0577M, and 0.1M NaCl for the solutions and gels at 0.58wt% alginate; and 0M, 0.1M, and 0.1733M NaCl for the 1wt% solutions. Concentrations were chosen because the gelation process dilutes the initial solution of 1wt% alginate with these salt concentrations and results in 0.58wt% alginate gels with the specified salt concentrations. The comparisons between alginates of varying molecular weight and degree of acetylation in both the solution and gel state as a function of salt and polymer concentration allow the study of polymer conformational changes using NMR relaxation measurements.

Polymers and Polyelectrolytes

In the dilute regime, uncharged polymers will have a size that corresponds to [182]:

$$\left\langle R^2 \right\rangle^{1/2} = \sqrt{N}b \qquad (9.1)$$

where R is the length of the polymer, N is the number of monomer units in the chain, and b is the bond length between monomers. This result is derived using Gaussian chain random walk theory [182]. To take into account the excluded volume effect where polymer monomers cannot bend back into the same exact place, the b is replaced by b_{eff} [182]. In the dilute concentration regime, the length of the polymer varies as the square root of the molecular weight and the polymers chains are not interacting with other polymer molecules. In the semi-dilute concentration regime above the overlap polymer concentration, the polymer chains will begin to interact and entangle with other polymer molecules [180].

Dilute solutions of polyelectrolytes such as alginate have much different material properties than uncharged polymers due to electrostatic interactions between the charges on the polymer backbone dominating interaction between polymers. In an ideal solution, all ions are homogeneously distributed, but the effect of polyelectrolyte interactions leads to non-ideality of the solution properties [181]. This non-ideality is described by the Debye-Huckel theory [191]. Poisson's equation describes the electric field ϕ within a medium with uniform dielectric constant ε and charge density ρ_E:

$$\nabla^2 \phi = \frac{-\rho_E}{\varepsilon} \quad (9.2)$$

The Debye-Huckel theory makes the approximation that for small electric potentials, the solution to this equation reduces to:

$$\phi = \phi_w \exp\left(\frac{-x}{r_D}\right) \quad (9.3)$$

with r_D known as the Debye screening length:

$$r_D = \frac{1}{\sqrt{4\pi l_B c_s q_s^2}} \quad (9.4)$$

where c_s is the concentration of ions, q_s is the charge of the ion, and l_B is the length scale for which the thermal energy of the charged molecule is equal to the electrostatic interaction within a medium with uniform dielectric constant. This length scale is known as the Bjerrum length:

$$l_B = \frac{e^2}{4\pi\varepsilon k_B T} \quad (9.5)$$

For water at 278K (5C), the Bjerrum length is 0.7 nm, using a relative permittivity for water of 85.83 [192].

The Debye screening length is the length scale for which the electric potential has exponentially decayed to 1/*e*. For a solution of polyelectrolyte without added salt, this screening length is longer than the polymer chains and the negative charges on the polymers repel each other. The addition of salt to a solution of polyelectrolytes reduces the Debye screening length associated with the charged polymers. As the salt concentration is increased, the polymers will no longer repel each other, allowing conformational changes as the polymers are less likely to be linear. As the salt concentration is further increased, the monomers of the polymer are less likely to repel each other, causing the polymer to become more spherical. As the salt concentration is further increased, the counterions may interact with the charged polymers to the point which the counterions are so closely associated with the polymers as to effectively be bonded, known as counterion condensation [187]. Figure 9.2 shows a schematic of the screening effect on polyelectrolyte conformation.

In a salt-free solution without added ions and dilute polymer concentration, the charges on the polymer backbone will repel other charges and the polymer will be in a rod-like conformation doe to long range Coulomb interactions. The polymer in the rod-like conformation can be modeled as a series of electrostatic “blobs” [180]. The number of monomer units within each blob will depend on the characteristics of the solvent. Each blob will repel the other blobs on the same polymer chain, leading to the rod-like

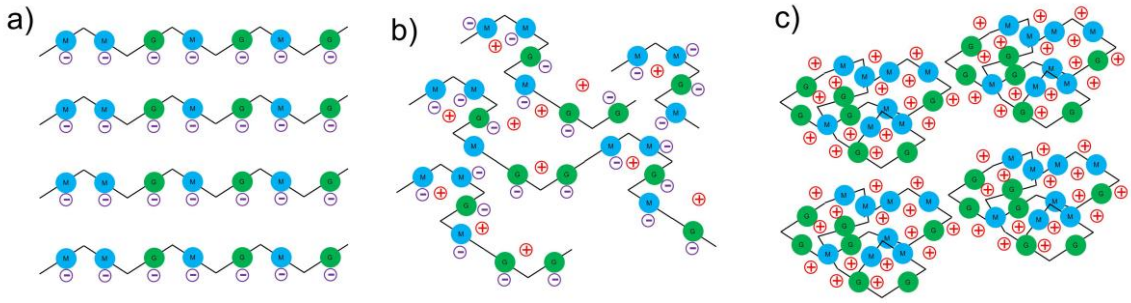

Figure 9.2. Conformation changes as counterions are added. a) Dilute solution of alginate with no added salt. Blue dots represent mannuronate monomers, green dots represent guloronate monomers, and purple dashes represent the negative charges on the monomer units. b) Dilute solution of alginate with a small amount of added salt. The positive counterions are represented by red crosses. c) Dilute solution of alginate with increased salt. The screening of the counterions allows the alginate to self-associate to form a more spherical blob.

conformation. If the polymer is in a good solvent (known as a theta solvent), the diameter of the polymer blob is:

$$D_b = \sqrt{N_b} b \quad (9.6)$$

with $N_b = \left(\frac{A^2 b}{l_B} \right)^{2/3}$ and A the number of monomers between charges [180, 181]. The total length of the polymer will then be:

$$L = Nb \left(\frac{l_B}{A^2 b} \right)^{1/3} \quad (9.7)$$

For polyelectrolytes, this derivation shows how the length of the polymer does not vary as the square root of the molecular weight but rather linearly with the molecular weight. Equation 9.7 also shows how the ratio between the bond length and the Bjerrum length and the charge density impact the length of the polymer chains.

Gelation

The addition of ions with a positive two charge, such as Ca^{2+} or Cu^{2+}, induces another electrostatic effect known as physical gelation. In this case, the positively charged ion will interact with two separate monomer units. For alginate, consecutive G unit groups will align in a linear way and bind with the calcium to form what is known as an "egg-box" structure [113]. A schematic of this structure is shown in Figure 9.3. Mannuronate units are also known to associate with the positively charged ions and form a gel, but the gel is less ordered and therefore less rigid than a gel formed with G units [167].

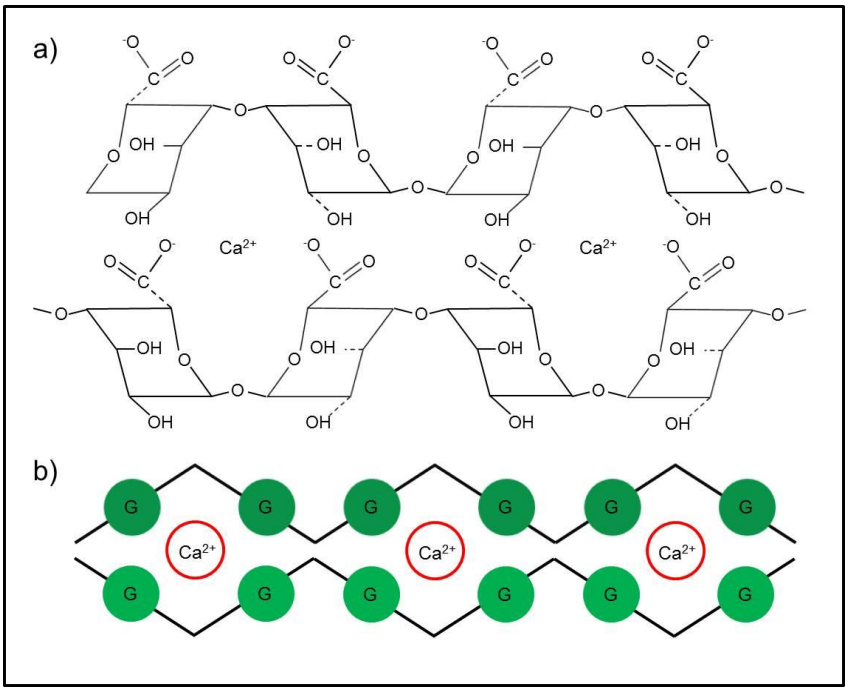

Figure 9.3. Gelation of alginate caused by addition of calcium ions. a) Consecutive G units will align to form linear chains. b) Schematic of the egg-box structure.

NMR Hydrogen Exchange

The effect to NMR relaxation caused by hydrogen exchange was discussed in Chapter 4. In summary, the protons on water will exchange with certain protons on the polymer. When the proton is on the polymer, it will have a different frequency than when in water, known as the chemical shift [18]. In addition, the T_2 of polymer protons is several orders of magnitude shorter than protons on water. Exchange between these populations will thus effect the measured T_2 in two ways: the time scale of the exchange will impact the measured T_2 of the surrounding water due to averaging with the shorter T_2 of the polymer; and the exchange between the two different frequency environments will cause additional dephasing of the signal, leading to a difference in the measured T_2, known as relaxation dispersion [24, 156, 160, 193, 194].

In addition to the effect of hydrogen exchange, in polymer solutions there is a relaxation effect caused by water that is highly associated with the polymer, which will be referred to in this discussion as coordinated water [66]. This water is in close contact with the polymer and therefore will have additional relaxation due to the fluctuating magnetic fields caused by the other molecular species contained in the polymer such as carbon and oxygen. This water is available for hydrogen exchange. The hypothesis for the following discussion is that the polymer conformation will affect both the amount of coordinated water and the hydrogen exchange with the polymer. The bulk water will also exchange with the coordinated water on the time scale of diffusion. A schematic of the coordinated water for M units is shown in Figure 9.4.

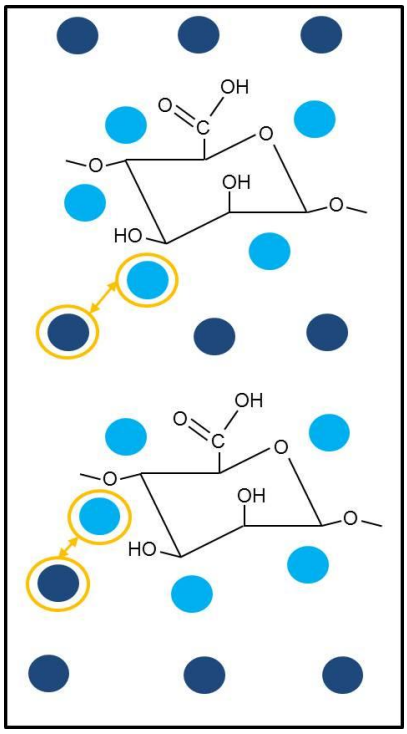

Figure 9.4. Bulk water and coordinated water around mannuronate monomer units of two alginate chains. The light blue dots represent coordinated water and the dark blue dots are bulk water. The yellow circles represent diffusive exchange between the bulk and coordinated water populations.

Materials and Methods

Homogeneous Gelation

A 2% wt/vol alginate solution is mixed, and 2.1 g of the solution is added to an 11 mm outer diameter NMR tube. Insoluble calcium carbonate (Mikhart 2 from Provencale S.A.) is mixed with water to a concentration of 55 mM. 0.77 mL of the resulting solution is dispersed throughout the alginate solution using a vortex mixer. Gluconic acid δ-lactone (GDL) is mixed to a concentration of 109 mM and 0.77 mL is added to the alginate and calcium carbonate, again dispersed with a vortex mixer. The tube is placed in ice under vacuum for an hour to remove entrapped air bubbles, after which a uniform

physical gel is formed. A MR image showing the spatial homogeneity of the three alginate gels is shown in Figure 9.5.

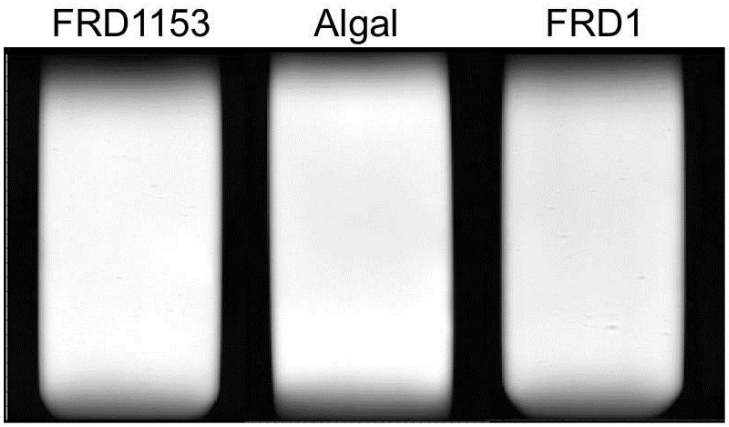

Figure 9.5. MR images of homogeneous gels of the three different alginates. T_E = 11 ms, T_R = 1 s, FOV 20 mm x 13 mm, 256 x 128 pixels.

T_2 Experiments

CPMG experiments with varying numbers of pulses and varying echo times were performed in order to access the relaxation dispersion information. 16 experiments were performed for each solution and gel in an experimental set that took approximately 4 hours to acquire. The number of echoes for each experiment was calculated in order to have a total echo train time of approximately 2 s and to acquire an even number of echoes. The timing for each experiment is shown in Table 9.1. Pulse lengths were optimized to be as short as possible for the rf coil which was used. For gels and solutions without added salt, the pulse times were 20 μs for π/2 pulses and 40 μs for π pulses. With addition of salt, the pulse times were increased to 22 μs and 44 μs for the π/2 and the π pulses respectively due to amplifier power limitations.

Table 9.1. CPMG echo train pulse spacing parameters used for T_2 dispersion experiments.

Tau (μs)	No. of echoes	Acq. time (s)
64	15626	2.000128
88	11364	2.000064
96	10418	2.000256
128	7814	2.000384
160	6250	2
192	5210	2.00064
224	4466	2.000768
256	3908	2.000896
320	3126	2.00064
384	2606	2.001408
448	2234	2.001664
512	1954	2.000896
1024	978	2.002944
2048	490	2.00704
4096	246	2.015232
9216	110	2.02752

Results and Discussion

Solutions

The NMR relaxation dispersion results for solutions are presented in Figures 9.6 – 9.9. Each plot shows the relaxation rate ($1/T_2$) vs $1/\tau$. Figure 9.6 and 9.7 present the same data in two different comparisons. Figure 9.6 shows the three different 0.58wt% alginate solutions on the same plot for each of three salt concentrations: 0M NaCl, 0.0577M NaCl, and 0.1M NaCl. Figure 9.7 shows the three different salt concentrations on the same plot for each different type of alginate.

In Figure 9.6, the three alginate types at 0.58wt% are compared at three different salt (NaCl) concentrations. For 0M added NaCl, algal alginate and FRD1153 alginate are essentially the same, while the FRD1 alginate has a lower relaxation rate. The change in relaxation as the echo time changes shows the effect of dephasing caused by hydrogen exchange. The FRD1 alginate has only 80% as many exchangeable protons due to O-acetylation of the M units, and thus decreased hydrogen exchange between the polymer and coordinated water leads to a lower relaxation rate for FRD1 than FRD1153 or algal. The effect of molecular weight and of the different ratios of M and G units are not apparent in this data, indicating that for solutions with out added salt the primary effect to the T_2 dispersion curve is the effect of hydrogen exchange.

As NaCl is added to the solution, there are several interesting effects to note. For 0.0577M NaCl, the FRD1153 alginate has a much lower relaxation rate than algal or

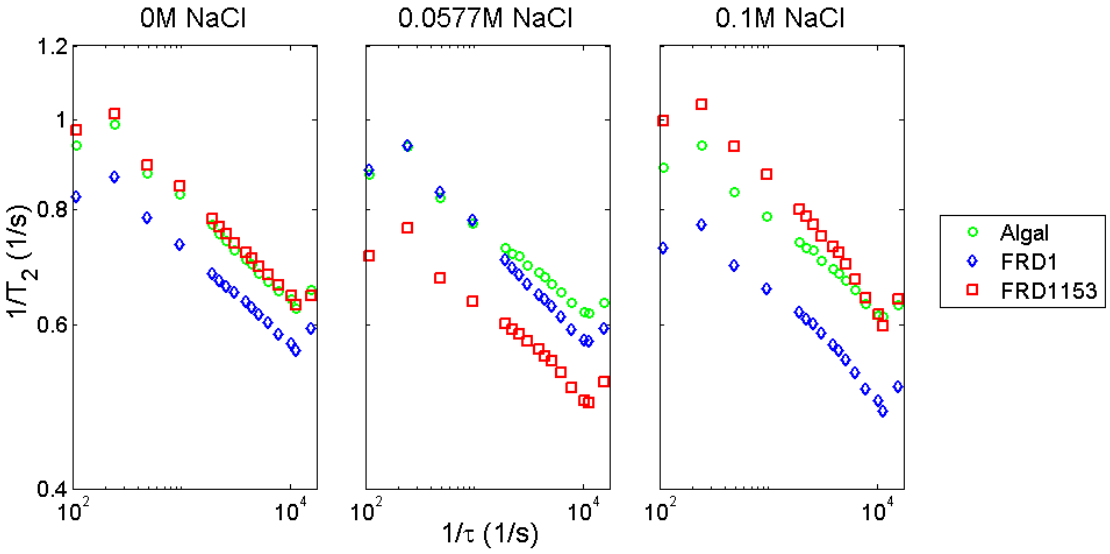

Figure 9.6. 0.58% by weight solutions of three different alginates with three different added NaCl concentrations: 0M, 0.0577M, and 0.1M.

FRD1 alginates. In this case, the difference cannot be explained by hydrogen exchange alone, as it is assumed that the hydrogen exchange will be similar. However, the conformation of the polymer chains will change with increased electrostatic screening, as discussed above. The smaller relaxation rate may be because the Debye screening length is on the order of the bond length for the FRD1153 alginate, causing a conformational change in the chains so that the chains have transitioned from a linear rod-like conformation to a coiled conformation. In this case, the amount of coordinated water around each chain could be less, causing a shift to longer T_2. At a salt concentration of 0.1M, the FRD1 alginate shows this abrupt change to shorter relaxation rate, indicating a transition to a coiled conformation. The difference between FRD1 and FRD1153 alginates is primarily that FRD1 alginate is partially O-acetylated. The increased screening needed for FRD1 to transition to coils may be due to the additional ions needed to screen out interactions caused by the acetyl groups on the M units.

Figure 9.7 shows the same data as Figure 9.6, but as a comparison of each alginate at the separate salt concentrations. The algal alginate does not change significantly for any of the salt concentrations, which indicates that for a lower molecular weight polymer, the effect of screening caused by added salt needs to be stronger before the chains will transition from linear to coiled. The FRD1153 alginate shows the abrupt change from 0M to 0.0577M NaCl, then at 0.1M NaCl again has a similar relaxation rate to the 0M NaCl. However, the slope of the change in the relaxation rate changes slightly. This may be an indication that the coiled polymers are screened more and may be interacting more closely, causing additional relaxation due to partial gelation [167]. The

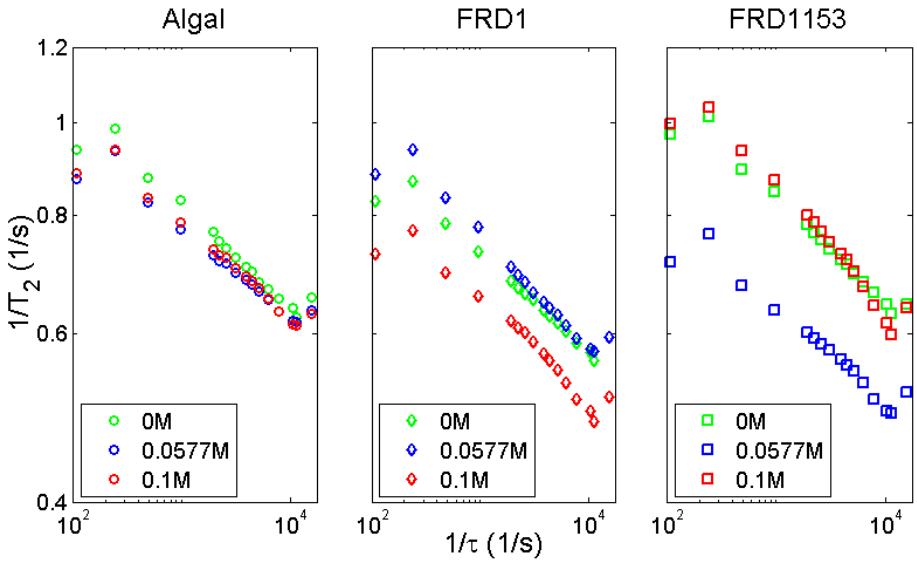

Figure 9.7. 0.58% by weight solutions with three different added NaCl concentrations for three different alginates: algal, FRD1, and FRD1153.

FRD1 alginate has relaxation similar at the two lower salt concentrations, but abruptly shifts to slower relaxation rates at the highest salt concentration.

Figure 9.8 presents results for 1wt% alginate at three different salt concentrations: 0M NaCl, 0.1M NaCl, and 0.1733M NaCl. The first trend to notice, in comparison with Figure 9.6, is that all of the distributions are shifted to higher relaxation rates. This difference is due to the increased amount of alginate available for hydrogen exchange, in addition to an increased amount of coordinated water. The comparisons between the different alginates are quite different however. At 0M added NaCl, the algal and FRD1153 alginates are no longer the same. The algal alginate has a slower relaxation rate than the FRD1153, indicating that at this polymer concentration, the increased molecular weight of the polymer chains results in stronger inter-polymer electrostatic interactions which affect the relaxation rate. The comparison between FRD1153 and FRD1 alginates is again straightforward however, as the decreased hydrogen exchange

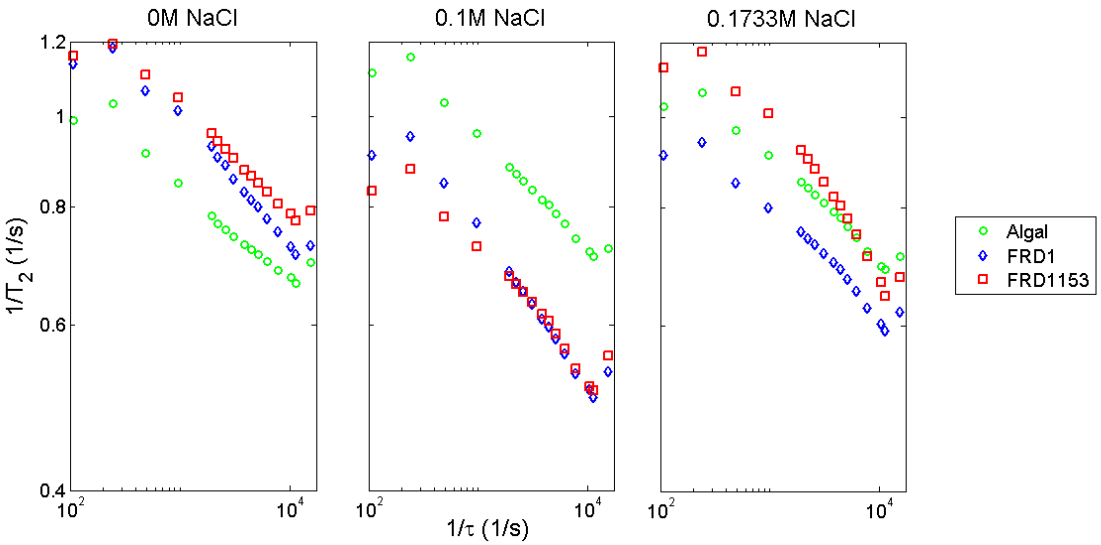

Figure 9.8. 1% by weight solutions of three different alginates with three different added NaCl concentrations: 0M, 0.1M, and 0.1733M.

due to O-acetylation for the FRD1 results in a slightly slower relaxation rate than for the non-acetylated FRD1153.

When NaCl is added at 0.1M, the algal alginate does not change significantly, while both FRD1 and FRD1153 show decreased relaxation rates. This may again correspond to the transition to a coiled conformation. However, in contrast with the 0.58wt% data, this transition appears to occur for both bacterial alginates at 0.1M NaCl. At the increased alginate concentration, the interactions between the longer bacterial alginate chains cause screening effects that overwhelm the additional screening effect of the acetyl groups. At the highest added salt concentration, the coiled polymers are again able to interact more due to the increased screening, resulting in faster relaxation rates. The effect of reduced hydrogen exchange for the FRD1 acetylated alginate is again evident in the reduced relaxation rate in comparison with the algal and FRD1153 alginates. Figure 9.9 again presents the same data, but comparing the different salt

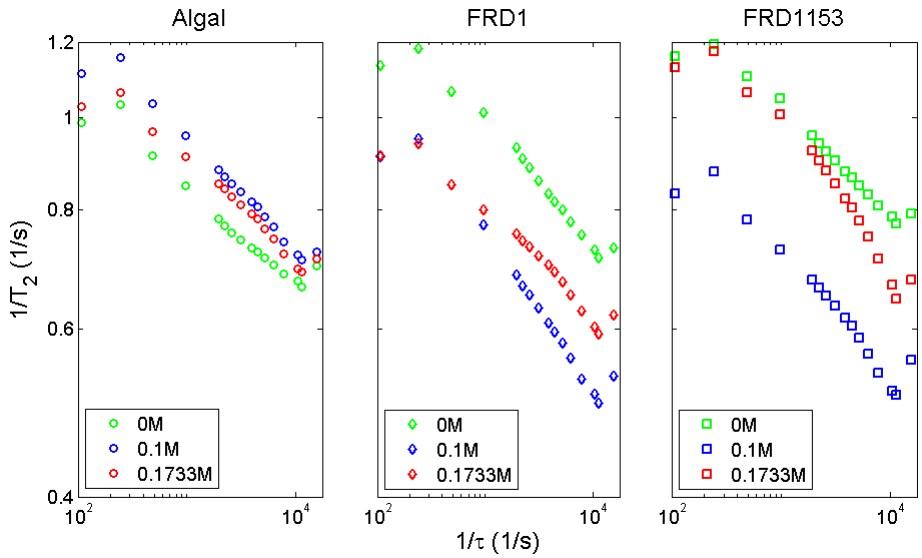

Figure 9.9. 1% by weight solutions of three different added NaCl concentrations with three different alginates: algal, FRD1, and FRD1153.

concentrations for each alginate. The algal data shows little difference due to salt, while the two bacterial alginates show significant screening effects.

Gels

The 1wt% solutions were then gelled using the described process for homogeneous gelation. This process resulted in gels that were 0.58% alginate and the same added NaCl concentrations that were tested in solution form, 0M, 0.0577M, and 0.1M. The results for T_2 dispersion experiments are shown in Figures 9.10 and 9.11.

Figure 9.10 shows the results for the three different alginates at the three different salt concentrations. The algal alginate has a significantly faster relaxation rate than either of the bacterially produced alginates. This effect is due to the fact that algal alginate has more consecutive G unit blocks that are able to align and form the ordered egg-box structures. The bacterially produced alginate gels have faster relaxation rates than in

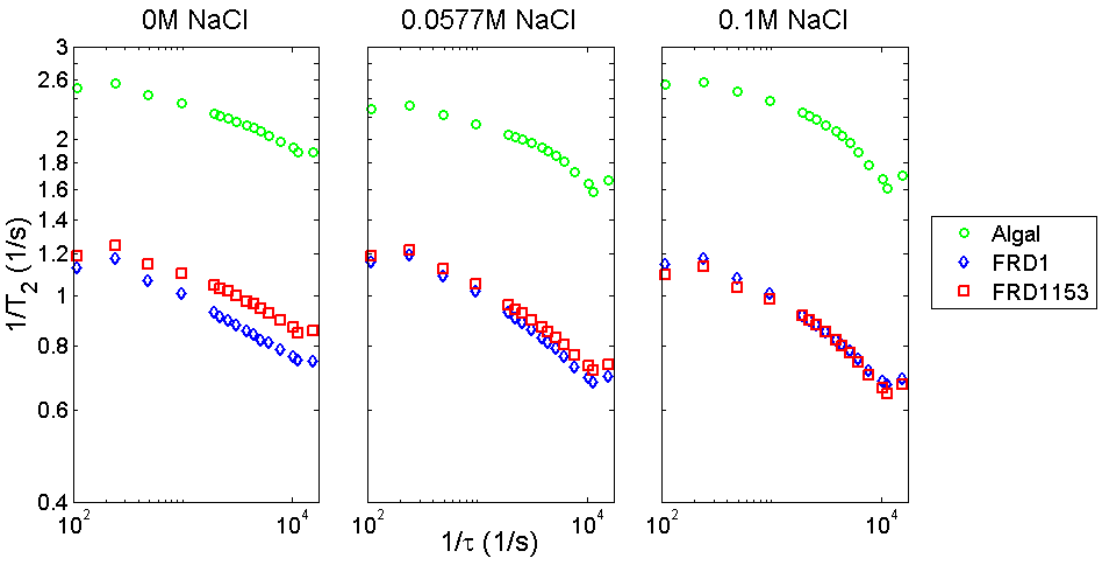

Figure 9.10. 0.58% by weight gels of three different alginates with three different added NaCl concentrations: 0M, 0.0577M, and 0.1M.

solution form, indicating a difference in the coordinated water due to gelation. However, the effect is much less than for algal alginate. The effect of hydrogen exchange and amount of coordinated water is also seen in the 0M salt data, as the O-acetylated FRD1 gel has a slower relaxation rate than the FRD1153 gel. With the addition of salt, the data continues to show the same trends. The algal alginate gel has much faster relaxation due to increased ordered structure. The relaxation dispersion results of the two bacterially produced alginates become closer together, indicating that the effect of hydrogen exchange mediated by O-acetylation is less influential and relaxation is instead dominated by the change in the coordinated water and added salt induced screening changing the proton interactions.

Figure 9.11 presents the same data again with each type of alginate compared at the three different salt concentrations. The algal alginate gels all show very similar

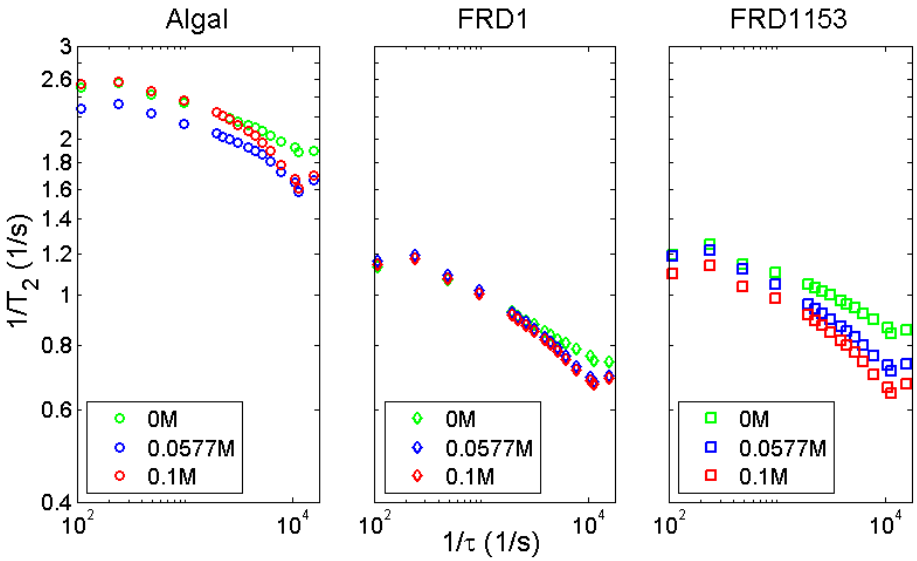

Figure 9.11. 0.58% by weight gels of three different added NaCl concentrations for three different alginates: algal, FRD1, and FRD1153.

relaxation properties. However, at the highest added salt, the slope of the curve is slightly different. This may indicate that a different structure has formed, perhaps due to conformational changes in the alginate chains. FRD1 gels show very little difference with salt concentration, while the FRD1153 gels show a consistent decreasing trend in relaxation as salt concentration increases.

Data Fitting

In order to quantify the qualitative changes to the relaxation dispersion curves caused by polymer conformation discussed above, a system of equations is solved and fitted to the data. The Bloch equations are used to describe the time evolution of the magnetization [24, 33, 66, 156, 160, 193]. A three population model was considered incorporating bulk water protons, coordinated water protons, and polymer protons. Bulk water is water that does not interact at all with the polymer during the time of the

experiment and has a T_2 of approximately 2 s. Coordinated water is water that is interacting with the polymer and is available for hydrogen exchange. Hydrogen exchange occurs between the coordinated water and the alcohol (OH) protons on the alginate chain. Hydrogen exchange affects the NMR relaxation by lowering the measured T_2 of the water surrounding the polymer and also dephasing of the magnetization caused by the exchange on the time scale of the measurement between species with different chemical shift values. The coordinated water will also have a smaller rotational diffusion and a corresponding reduce T_2 relative to bulk water. The coupled Bloch equations for the evolution of the transverse magnetization *M* of the three populations are:

$$\frac{dM_b}{dt} = \left(-R_b - k_{bc}\right)M_b + k_{cb}M_c \qquad (9.8.a)$$

$$\frac{dM_c}{dt} = \left(-R_c - k_{cb} - k_{cp}\right)M_c + k_{bc}M_b + k_{pc}M_p \qquad (9.8.b)$$

$$\frac{dM_p}{dt} = \left(-R_p - k_{pc} + i\Delta\omega\right)M_p + k_{cp}M_c \qquad (9.8.c)$$

where the subscript *b* refers to the bulk water, subscript *c* refers to coordinated water, and subscript *p* refers to the polymer; k_{ij} are exchange constants between the three different populations, where $k_{ij}=k_{ji}$; R_i are the relaxation rates $1/T_{2i}$ for each population; and $\Delta\omega$ is the chemical shift difference between the polymer protons and the solvation water.

This set of coupled differential equations was solved using a Matlab program. The coupled differential equations for the change in magnetization were solved for each echo time using the function "ode45". The resulting simulated T_2 decay was then fit to a

single exponential fit using the function "fit". Reasonable initial guesses were made for each parameter, as discussed below, and the fits were iterated until the error between the data and the simulated T_2 decay was minimized. Efforts are ongoing to fit all the data presented in the last section. These efforts are complicated by the need to determine physically based initial estimates for the model parameters. The results at this point for solutions and gels with 0M added salt are presented in Figure 9.12, with the parameters used to produce the fits in the graph shown in Table 9.2.

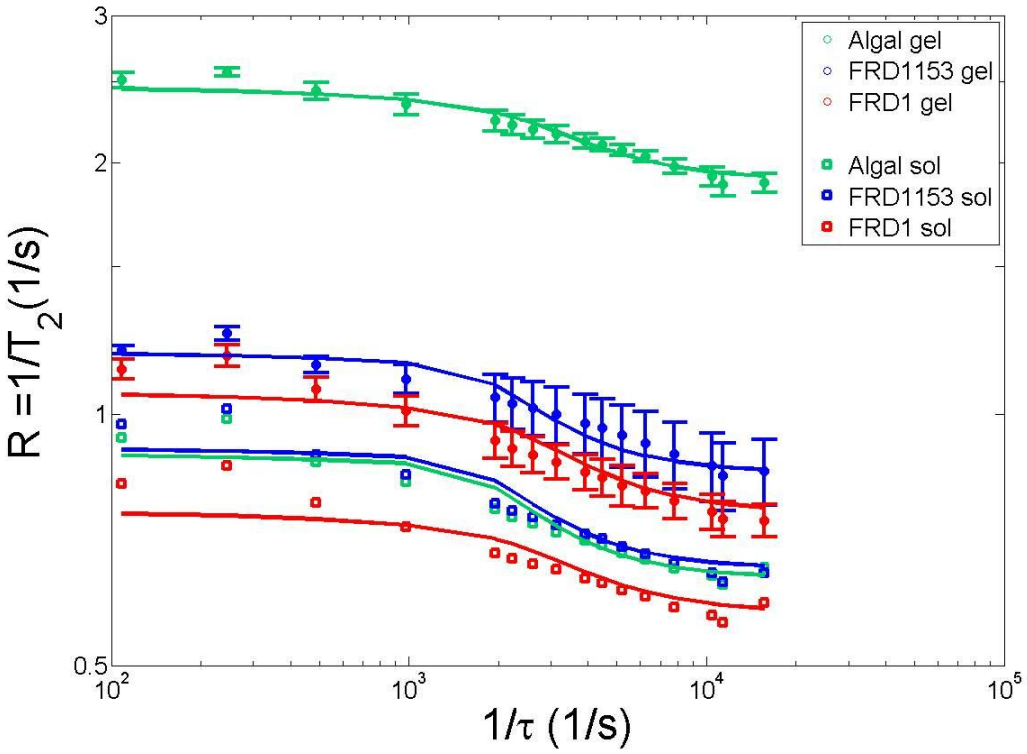

Figure 9.12. Data fitting for solutions and gels of 0.58wt% alginates and no additional NaCl (0M). Error bars shown are calculated from the standard deviation of four different gels.

Table 9.2. Data fitting parameters used for data fits in Figure 9.12.

Parameter	Algal sol	FRD1153 sol	FRD1 sol	Algal gel	FRD1153 gel	FRD1 gel
M_b	80	80	80	80	80	80
M_c	19.945	19.945	19.985	19.945	19.945	19.975
M_p	0.055	0.055	0.015	0.055	0.055	0.025
R_b	0.5	0.5	0.5	0.5	0.5	0.5
R_c	1.7	1.8	1.8	9.7	2.9	2.7
R_p	333	333	333	333	333	333
$\Delta\omega$	3500	3500	3500	3500	3500	3500
k_{bc}	12	11.8	11.8	21.9	21.9	25.6
k_{cp}	2.4	2.4	2.4	9	3.1	3.7

These initial fits were performed by keeping as many parameters constant as possible. In this case, the chemical shift difference, the amount of bulk water, the relaxation rate of the bulk water, and the relaxation rate of the polymer protons were kept constant for all solutions and gels. The amount of exchangeable polymer protons [194] was kept constant for all non-acetylated gels and solutions, while the number was allowed to vary for the acetylated solution and gel (FRD1). The free parameters for each fit were then the exchange rates between the bulk water and coordinated water, the exchanges rates between the coordinated water and the polymer protons, and the relaxation rate of the coordinated water.

These initial results show the potential of this type of data fitting to obtain useful quantitative information. The only difference between the three different solutions was the amount of exchangeable hydrogen protons, as discussed in the earlier section. For the gels, the relaxation rate of the coordinated water was faster for all three alginates, with the fastest relaxation rate being for the algal alginate. This is consistent with the idea that

the algal alginate forms a more rigid and ordered gel due to the larger numbers of G units available to form the egg-box structure, which results in longer range interactions of the polymer with the coordinated water.

Conclusions and Future Work

This chapter presented relaxation dispersion results for homogeneous solutions and gels. Additional research is being done within the author's research group by several undergraduates to study the rheology of the solutions and the gels. Rheology will give information about the viscosity, material properties, and molecular weights of the different forms of alginate. These rheological results will be used to corroborate and inform the NMR data. In addition to this ongoing research, the data fitting presented here is preliminary. If all parameters are allowed to vary, the three coupled differential equations considered would have nine adjustable variables. The fits obtained for Figure 9.12 were restricted to only three free variables, but efforts are ongoing to further restrict the free parameters to obtain more meaningful comparisons. By focusing on the effect on relaxation dispersion curves due to the amount and the relaxation rate of the coordinated water, the conformational changes to the polymer chains caused by addition of salt may be further quantified.

REFERENCES

1. Codd, S. L.; Vogt, S. J.; Hornemann, J. A.; Phillips, A. J.; Maneval, J. E.; Romanenko, K. R.; Hansen, L.; Cunningham, A. B.; Seymour, J. D., NMR relaxation measurements of biofouling in model and geological porous media. *Organic Geochemistry* **2011,** *42*, (8), 965-971.

2. Vogt, S. J.; Stewart, B. D.; Seymour, J. D.; Peyton, B. M.; Codd, S. L., Detection of biological uranium reduction using magnetic resonance. *Biotechnol. Bioeng.* **2012,** *109*, (4), 877-883.

3. Fabich, H. T.; Vogt, S. J.; Sherick, M. L.; Seymour, J. D.; Brown, J. R.; Franklin, M. J.; Codd, S. L., Microbial and algal alginate gelation characterized by magnetic resonance. *Journal of Biotechnology* **2012,** *161*, (3), 320-327.

4. Brosten, T. R.; Vogt, S. J.; Seymour, J. D.; Codd, S. L.; Maier, R. S., Preasymptotic hydrodynamic dispersion as a quantitative probe of permeability. *Phys. Rev. E* **2012,** *85*, (4), 045301-1-4.

5. Brown, J. R.; Brox, T. I.; Vogt, S. J.; Seymour, J. D.; Skidmore, M. L.; Codd, S. L., Magnetic resonance diffusion and relaxation characterization of water in the unfrozen vein network in polycrystalline ice and its response to microbial metabolic products. *J. Magn. Reson.* **2012,** *225*, 17-24.

6. Vogt, S. J.; Sanderlin, A. B.; Seymour, J. D.; Codd, S. L., Permeability of a Growing Biofilm in a Porous Media Fluid Flow Analyzed by Magnetic Resonance Displacement-Relaxation Correlations. *Biotechnol. Bioeng.* **2012,** *Accepted*.

7. Sanderlin, A. B.; Vogt, S. J.; Grunewald, E.; Bergin, B. A.; Codd, S. L., Biofilm detection in natural unconsolidated porous media using a low-field magnetic resonance system. *Environmental Science & Technology* **2012,** *Accepted*.

8. Yang, X.; Scheibe, T. D.; Richmond, M. C.; Perkins, W. A.; Vogt, S. J.; Codd, S. L.; Seymour, J. D.; McKinley, M. I., Direct Numerical Simulation of Pore-Scale Flow in a Bead Pack: Validation against Magnetic Resonance Imaging Observations. *Adv. Water Resour.* **2012,** *Submitted*.

9. Shaw, C. A.; Vogt, S. J.; Maneval, J. E.; Brox, T. I.; Skidmore, M. L.; Codd, S. L.; Seymour, J. D., Petrophysical Evolution of Carbonate and Clastic CCS Reservoir Rocks: Supercritical CO2 Flood Experiments. *Manuscript in Preparation*.

10. Vogt, S. J.; Smith, J.; Codd, S. L.; Seymour, J. D.; Carr, A.; Golding, M., Assessment of the changes in the structure and component mobility of Mozzarella and Cheddar cheese during heating using magnetic resonance techniques. *Manuscript in Preparation*.

11. Smith, J.; Vogt, S. J.; Codd, S. L.; Seymour, J. D.; Carr, A.; Golding, M., Probing water migration in Mozzarella cheese during storage and heating utilizing magnetic resonance techniques. *Manuscript in Preparation*.

12. Proceedings of the American Physical Society. *Physical Review* **1946,** *69*, (11-12), 674-674.

13. Bloch, F., Nuclear Induction. *Physical Review* **1946,** *70*, (7-8), 460-474.

14. Callaghan, P. T., *Principles of Nuclear Magnetic Resonance Microscopy*. Clarendon Press: Oxford, 1991.

15. Levitt, M. H., *Spin Dynamics: Basics of Nuclear Magnetic Resonance*. 2 ed.; John Wiley & Sons: Chichester, England, 2008.

16. Zwanzig, R., *Nonequilibrium Statistical Mechanics*. Oxford University Press: Oxford, England, 2001.

17. Fukushima, E.; Roeder, S. B. W., *Experimental Pulse NMR: A Nuts and Bolts Approach*. Westview Press: Boulder, CO, 1981.

18. Abragam, A., *The Principles of Nuclear Magnetism*. Clarendon Press: Oxford, 1961.

19. Hahn, E. L., Spin Echoes. *Physical Review* **1950,** *80*, (4), 580-594.

20. Carr, H. Y.; Purcell, E. M., Effects of Diffusion on Free Precession in Nuclear Magnetic Resonance Experiments. *Physical Review* **1954,** *94*, (3), 630-638.

21. Stejskal, E. O.; Tanner, J. E., Spin Diffusion Measurements: Spin Echoes in the Presence of a Time-Dependent Field Gradient. *J. Chem. Phys.* **1965,** *42*, (1), 288-292.

22. Kleinberg, R. L., Kenyon, W.E., Mitra, P.P., Mechanism of NMR Relaxation of Fluids in Rock. *J. Magn. Reson. Ser. A* **1994,** *108*, 206-214.

23. Kleinberg, R. L.; Farooqui, S. A.; Horsfield, M. A., T_1/T_2 Ratio and Frequency-Dependence of Nmr Relaxation in Porous Sedimentary-Rocks. *Journal of Colloid and Interface Science* **1993,** *158*, (1), 195-198.

24. Hills, B. P.; Wright, K. M.; Belton, P. S., Proton NMR - Studies of Chemical and Diffusive Exchange in Carbohydrate Systems. *Mol. Phys.* **1989,** *67*, (6), 1309-1326.

25. Washburn, K. E.; Callaghan, P. T., Tracking Pore to Pore Exchange Using Relaxation Exchange Spectroscopy. *Physical Review Letters* **2006,** *97*, 175502-1-4.

26. Mitchell, J.; Chandrasekera, T. C.; Johns, M. L.; Gladden, L. F.; Fordham, E. J., Nuclear magnetic resonance relaxation and diffusion in the presence of internal gradients: The effect of magnetic field strength. *Phys. Rev. E* **2010,** *81*, (2), 026101-1-19.

27. Song, Y. Q., A 2D NMR method to characterize granular structure of dairy products. *Prog. Nucl. Magn. Reson. Spectrosc.* **2009,** *55*, (4), 324-334.

28. Austin, D. T. R., Hills, B.P., Two-Dimensional NMR Relaxation Study of the Pore Structure in Silicone Hydrogel Contact Lenses. *Appl. Magn. Reson.* **2009,** *35*, 581-591.

29. Monteilhet, L.; Korb, J. P.; Mitchell, J.; McDonald, P. J., Observation of exchange of micropore water in cement pastes by two-dimensional T_2-T_2 nuclear magnetic resonance relaxometry. *Phys. Rev. E* **2006,** *74*, (6), 061404-1-9.

30. McDonald, P. J., Korb, J.-P., Mitchell, J., Monteilhet, L., Surface relaxation and chemical exchange in hydrating cement pastes: A two-dimensional NMR relaxation study. *Phys. Rev. E* **2005,** *72*, 011409-1-9.

31. McDonald, P. J.; Mitchell, J.; Mulheron, M.; Aptaker, P. S.; Korb, J. P.; Monteilhet, L., Two-dimensional correlation relaxometry studies of cement pastes performed using a new one-sided NMR magnet. *Cement and Concrete Research* **2007,** *37*, (3), 303-309.

32. Torrey, H. C., Bloch Equations with Diffusion Terms. *Physical Review* **1956,** *104*, (3), 563-565.

33. McConnell, H. M., Reaction Rates by Nuclear Magnetic Resonance. *J. Chem. Phys.* **1958,** *28*, (3), 430-431.

34. Brownstein, K. R., Tarr, C.E., Importance of classical diffusion in NMR studies of water in biological cells. *Physical Review A* **1979,** *19*, (6), 2446-2453.

35. Song, Y.-Q., Venkataramanan, L., Hurlimann, M.D., Flaum, M., Frulla, P., Straley, C., T_1-T_2 Correlation Spectra Obtained Using a Fast Two-Dimensional Laplace Inversion. *J. Magn. Reson.* **2002,** *154*, 261-268.

36. Song, Y.-Q.; Zielinski, L.; Ryu, S., Two-Dimensional NMR of Diffusion Systems. *Physical Review Letters* **2008,** *100*, 248002-1-4.

37. Godefroy, S.; Callaghan, P. T., 2D relaxation/diffusion correlations in porous media. *Magn. Reson. Imaging* **2003,** *21*, 381-383.

38. Callaghan, P. T.; Godefroy, S.; Ryland, B. N., Diffusion-relaxation correlation in simple pore structures. *J. Magn. Reson.* **2003,** *162*, (2), 320-327.

39. Galvosas, P.; Callaghan, P. T., Multi-dimensional inverse Laplace spectroscopy in the NMR of porous media. *C. R. Phys.* **2010,** *11*, (2), 172-180.

40. Burcaw, L. M.; Hunter, M. W.; Callaghan, P. T., Propagator-resolved 2D exchange in porous media in the inhomogeneous magnetic field. *J. Magn. Reson.* **2010,** *205*, (2), 209-215.

41. Callaghan, P. T.; Arns, C. H.; Galvosas, P.; Hunter, M. W.; Qiao, Y.; Washburn, K. E., Recent Fourier and Laplace perspectives for multidimensional NMR in porous media. *Magn. Reson. Imaging* **2007,** *25*, (4), 441-444.

42. Callaghan, P. T., *Translational Dynamics and Magnetic Resonance: Principles of Pulsed Gradient Spin Echo NMR*. Oxford University Press: Oxford, 2011.

43. Mitchell, J.; Hurlimann, M. D.; Fordham, E. J., A rapid measurement of T_1/T_2: The DECPMG sequence. *J. Magn. Reson.* **2009,** *200*, (2), 198-206.

44. Mitchell, J.; Griffith, J. D.; Collins, J. H. P.; Sederman, A. J.; Gladden, L. F.; Johns, M. L., Validation of NMR relaxation exchange time measurements in porous media. *J. Chem. Phys.* **2007,** *127*, (23), 234701-1-9.

45. Marigheto, N., Venturi, L., Hibberd, D., Wright, K.M., Ferrante, G., Hills, B.P., Methods for peak assignment in low-resolution multidimensional NMR cross-correlation relaxometry. *J. Magn. Reson.* **2007,** *187*, 327-342.

46. Venturi, L.; Woodward, N.; Hibberd, D.; Marigheto, N.; Gravelle, A.; Ferrante, G.; Hills, B. P., Multidimensional cross-correlation relaxometry of aqueous protein systems. *Appl. Magn. Reson.* **2008,** *33*, (3), 213-234.

47. Iuliano, C.; Piggott, R. B.; Venturi, L.; Hills, B. P., A Two-Dimensional Relaxation Study of the Evolving Microstructure in a Mixed Biopolymer Gel. *Appl. Magn. Reson.* **2010,** *38*, (3), 307-320.

48. Van Landeghem, M.; Haber, A.; de Lacaillerie, J. B. D.; Blumich, B., Analysis of Multisite 2D Relaxation Exchange NMR. *Concepts in Magnetic Resonance Part A* **2010,** *36A*, (3), 153-169.

49. Provencher, S. W., A Constrained Regularization Method for Inverting Data Represented by Linear Algebraic or Integral Equations. *Comput. Phys. Commun.* **1982,** *27*, (3), 213-227.

50. Venkataramanan, L.; Song, Y.-Q.; Hurlimann, M. D., Solving Fredholm Integrals of the First Kind With Tensor Product Structure in 2 and 2.5 Dimensions. *IEEE Transactions on Signal Processing* **2002,** *50*, (5), 1017-1026.

51. Lee, J. H.; Labadie, C.; Springer, C. S.; Harbison, G. S., 2-Dimensional Inverse Laplace Transform NMR - Altered Relaxation-Times Allow Detection of Exchange-Correlation. *J. Am. Chem. Soc.* **1993,** *115*, (17), 7761-7764.

52. Song, Y.-Q., Novel NMR techniques for porous media research. *Magn. Reson. Imaging* **2003,** *21*, 207-211.

53. Epstein, C. L.; Schotland, J., The bad truth about Laplace's transform. *SIAM Rev.* **2008,** *50*, (3), 504-520.

54. Lawson, C. L.; Hanson, R. J., *Solving least squares problems*. Prentice-Hall: Englewood Cliffs, NJ, 1974.

55. Hansen, P. C., Analysis of Discrete Ill-Posed Problems by Means of the L-Curve. *SIAM Rev.* **1992,** *34*, (4), 561-580.

56. Mansfield, P.; Pykett, I. L., Biological and Medical Imaging by NMR. *J. Magn. Reson.* **1978,** *29*, (2), 355-373.

57. Mansfield, P., Multi-Planar Image Formation using NMR Spin Echoes. *Journal of Physics C-Solid State Physics* **1977,** *10*, (3), L55-L58.

58. Lauterbur, P. C., Image Formation by Induced Local Interactions - Examples Employing Nuclear Magnetic Resonance. *Nature* **1973,** *242*, (5394), 190-191.

59. Lauffer, R. B., Paramagnetic Metal-Complexes as Water Proton Relaxation Agents for Nmr Imaging - Theory and Design. *Chemical Reviews* **1987,** *87*, (5), 901-927.

60. Elkins, C. J.; Alley, M. T., Magnetic resonance velocimetry: applications of magnetic resonance imaging in the measurement of fluid motion. *Exp. Fluids* **2007,** *43*, (6), 823-858.

61. Seymour, J. D.; Callaghan, P. T., Generalized approach to NMR analysis of flow and dispersion in porous media. *Aiche J.* **1997,** *43*, (8), 2096-2111.

62. Wilkes, J. O., *Fluid Mechanics for Chemical Engineers, Second Edition*. Prentice Hall: Upper Saddle River, NJ, 2006.

63. Hurlimann, M. D., Effective Gradients in Porous Media Due to Susceptibility Differences. *J. Magn. Reson.* **1998,** *131*, 232-240.

64. Ramsey, N. F., Magnetic Shielding of Nuclei in Molecules. *Physical Review* **1950,** *78*, (6), 699-703.

65. Schneider, W. G.; Bernstein, H. J.; Pople, J. A., Proton Magnetic Resonance Chemical Shift of Free (Gaseous) and Associated (Liquid) Hydride Molecules. *J. Chem. Phys.* **1958,** *28*, (4), 601-607.

66. Swift, T. J.; Connick, R. E., NMR-Relaxation Mechanisms of O-17 in Aqueous Solutions of Paramagnetic Cations and Lifetime of Water Molecules in First Coordination Sphere. *J. Chem. Phys.* **1962,** *37*, (2), 307-320.

67. Boon, J. P.; Yip, S., *Molecular Hydrodynamics*. McGraw-Hill: New York, 1980.

68. van Kampen, N. G., *Stochastic Processes in Physics and Chemistry*. North-Holland Publishing Company: New York, 1981.

69. Einstein, A., The motion of elements suspended in static liquids as claimed in the molecular kinetic theory of heat. *Ann. Phys.-Berlin* **1905,** *17*, (8), 549-560.

70. Kubo, R.; Toda, M.; Hashitsume, N., *Statistical Physics II: Nonequilibrium Statistical Mechanics*. Springer Verlag: 1991.

71. Metzler, R.; Klafter, J., The random walk's guide to anomalous diffusion: a fractional dynamics approach. *Physics Reports-Review Section of Physics Letters* **2000,** *339*, (1), 1-77.

72. Mitra, P. P.; Sen, P. N.; Schwartz, L. M., Short-time Behavior fo the Diffusion Coefficient as a Geometrical Probe of Porous Media. *Phys. Rev. B* **1993,** *47*, (14), 8565-8574.

73. Codd, S. L.; Seymour, J. D., Nuclear magnetic resonance measurement of hydrodynamic dispersion in porous media: preasymptotic dynamics, structure and nonequilibrium statistical mechanics. *The European Physical Journal - Applied Physics* **2012,** *60*, (02), 24204-1-9.

74. Manz, B.; Gladden, L. F.; Warren, P. B., Flow and dispersion in porous media: Lattice-Boltzmann and NMR studies. *Aiche J.* **1999,** *45*, (9), 1845-1854.

75. Fridjonsson, E. O.; Seymour, J. D.; Schultz, L. N.; Gerlach, R.; Cunningham, A. B.; Codd, S. L., NMR measurement of hydrodynamic dispersion in porous media subject to biofilm mediated precipitation reactions. *Journal of Contaminant Hydrology* **2011,** *120-21*, 79-88.

76. Tallarek, U.; van Dusschoten, D.; Van As, H.; Bayer, E.; Guiochon, G., Study of transport phenomena in chromatographic columns by pulsed field gradient NMR. *J. Phys. Chem. B* **1998,** *102*, (18), 3486-3497.

77. Taylor, G., Conditions under Which Dispersion of a Solute in a Stream of Solvent can be Used to Measure Molecular Diffusion. *Proceedings of the Royal Society of London. Series A. Mathematical and Physical Sciences* **1954,** *225*, (1163), 473-477.

78. Taylor, G., Dispersion of Soluble Matter in Solvent Flowing Slowly through a Tube. *Proceedings of the Royal Society of London. Series A. Mathematical and Physical Sciences* **1953,** *219*, (1137), 186-203.

79. Codd, S. L.; Callaghan, P. T., Spin echo analysis of restricted diffusion under generalized gradient waveforms: Planar, cylindrical, and spherical pores with wall relaxivity. *J. Magn. Reson.* **1999,** *137*, (2), 358-372.

80. Karger, J.; Heink, W., The Propagator Representation of Molecular Transport in Microporous Crystallites. *J. Magn. Reson.* **1983,** *51*, (1), 1-7.

81. Jenkins, C. R.; Cook, P. J.; Ennis-King, J.; Undershultz, J.; Boreham, C.; Dance, T.; de Caritat, P.; Etheridge, D. M.; Freifeld, B. M.; Hortle, A.; Kirste, D.; Paterson, L.; Pevzner, R.; Schacht, U.; Sharma, S.; Stalker, L.; Urosevic, M., Safe storage and effective monitoring of CO_2 in depleted gas fields. *Proc. Natl. Acad. Sci. U. S. A.* **2012,** *109*, (2), E35-E41.

82. Orr, F. M.; Taber, J. J., Use of Carbon Dioxide in Enhanced Oil Recovery. *Science* **1984,** *224*, (4649), 563-569.

83. Kharaka, Y. K.; Cole, D. R.; Hovorka, S. D.; Gunter, W. D.; Knauss, K. G.; Freifeld, B. M., Gas-water-rock interactions in Frio Formation following CO_2 injection: Implications for the storage of greenhouse gases in sedimentary basins. *Geology* **2006,** *34*, (7), 577-580.

84. Rothwell, W. P.; Vinegar, H. J., Petrophysical Applications of NMR Imaging. *Appl. Optics* **1985,** *24*, (23), 3969-3972.

85. Merrill, M. R., Porosity Measurements in Natural Porous Rocks using Magnetic Resonance Imaging. *Appl. Magn. Reson.* **1993,** *5*, (3-4), 307-321.

86. Borgia, G. C.; Bortolotti, V.; Dattilo, P.; Fantazzini, P.; Maddinelli, G., Quantitative determination of porosity: A local assessment by NMR imaging techniques. *Magn. Reson. Imaging* **1996,** *14*, (7-8), 919-921.

87. Marica, F.; Chen, Q.; Hamilton, A.; Hall, C.; Al, T.; Balcom, B. J., Spatially resolved measurement of rock core porosity. *J. Magn. Reson.* **2006,** *178*, (1), 136-141.

88. Molina, E.; Cultrone, G.; Sebastian, E.; Alonso, F. J.; Carrizo, L.; Gisbert, J.; Buj, O., The pore system of sedimentary rocks as a key factor in the durability of building materials. *Eng. Geol.* **2011,** *118*, (3-4), 110-121.

89. Costerton, J. W.; Stewart, P. S.; Greenberg, E. P., Bacterial biofilms: A common cause of persistent infections. *Science* **1999,** *284*, (5418), 1318-1322.

90. Stoodley, P.; Debeer, D.; Lewandowski, Z., Liquid Flow in Biofilm Systems. *Applied and Environmental Microbiology* **1994,** *60*, (8), 2711-2716.

91. Sutherland, I. W., Biofilm exopolysaccharides: a strong and sticky framework. *Microbiology-(UK)* **2001,** *147*, 3-9.

92. Lovley, D. R.; Phillips, E. J. P.; Gorby, Y. A.; Landa, E. R., Microbial Reduction of Uranium. *Nature* **1991,** *350*, (6317), 413-416.

93. Mitchell, A. C.; Phillips, A. J.; Hiebert, R.; Gerlach, R.; Spangler, L. H.; Cunningham, A. B., Biofilm enhanced geologic sequestration of supercritical CO_2. *International Journal of Greenhouse Gas Control* **2009,** *3*, (1), 90-99.

94. Mitchell, A. C.; Phillips, A. J.; Hamilton, M. A.; Gerlach, R.; Hollis, W. K.; Kaszuba, J. P.; Cunningham, A. B., Resilience of planktonic and biofilm cultures to supercritical CO_2. *Journal of Supercritical Fluids* **2008,** *47*, (2), 318-325.

95. Deswiet, T. M.; Sen, P. N., Decay of Nuclear Magnetization by Bounded Diffusion in a Constant Field Gradient. *J. Chem. Phys.* **1994,** *100*, (8), 5597-5604.

96. Padhy, G. S.; Lemaire, C.; Amirtharaj, E. S.; Ioannidis, M. A., Size distribution in multiscale porous media as revealed by DDIF-NMR, mercury porosimetry and statistical image analysis. *Colloids and Surfaces A - Physicochemical and Engineering Aspects* **2007,** *300*, (1-2), 222-234.

97. Hornemann, J. A.; Lysova, A. A.; Codd, S. L.; Seymour, J. D.; Busse, S. C.; Stewart, P. S.; Brown, J. R., Biopolymer and water dynamics in microbial biofilm extracellular polymeric substance. *Biomacromolecules* **2008,** *9*, (9), 2322-2328.

98. Battiato, I.; Tartakovsky, D. M.; Tartakovsky, A. M.; Scheibe, T., On breakdown of macroscopic models of mixing-controlled heterogeneous reactions in porous media. *Adv. Water Resour.* **2009,** *32*, (11), 1664-1673.

99. Radu, A. I.; Vrouwenvelder, J. S.; van Loosdrecht, M. C. M.; Picioreanu, C., Effect of flow velocity, substrate concentration and hydraulic cleaning on biofouling of reverse osmosis feed channels. *Chem. Eng. J.* **2012,** *188*, 30-39.

100. Pintelon, T. R. R.; Picioreanu, C.; van Loosdrecht, M. C. M.; Johns, M. L., The effect of biofilm permeability on bio-clogging of porous media. *Biotechnol. Bioeng.* **2012,** *109*, (4), 1031-1042.

101. von der Schulenburg, D. A. G.; Pintelon, T. R. R.; Picioreanu, C.; Van Loosdrecht, M. C. M.; Johns, M. L., Three-Dimensional Simulations of Biofilm Growth in Porous Media. *Aiche J.* **2009,** *55*, (2), 494-504.

102. Pintelon, T. R. R.; von der Schulenburg, D. A. G.; Johns, M. L., Towards Optimum Permeability Reduction in Porous Media Using Biofilm Growth Simulations. *Biotechnol. Bioeng.* **2009,** *103*, (4), 767-779.

103. Pintelon, T. R. R.; Creber, S. A.; von der Schulenburg, D. A. G.; Johns, M. L., Validation of 3D Simulations of Reverse Osmosis Membrane Biofouling. *Biotechnol. Bioeng.* **2010,** *106*, (4), 677-689.

104. Kapellos, G. E.; Alexiou, T. S.; Payatakes, A. C., Hierarchical simulator of biofilm growth and dynamics in granular porous materials. *Adv. Water Resour.* **2007,** *30*, (6-7), 1648-1667.

105. Klapper, I.; Rupp, C. J.; Cargo, R.; Purvedorj, B.; Stoodley, P., Viscoelastic fluid description of bacterial biofilm material properties. *Biotechnol. Bioeng.* **2002,** *80*, (3), 289-296.

106. Squires, T. M.; Mason, T. G., Fluid Mechanics of Microrheology. *Annual Review of Fluid Mechanics* **2010,** *42*, 413-438.

107. Brown, J. R.; Seymour, J. D.; Codd, S. L.; Fridjonsson, E. O.; Cokelet, G. R.; Nyden, M., Dynamics of the solid and liquid phases in dilute sheared Brownian suspensions: Irreversibility and particle migration. *Physical Review Letters* **2007,** *99*, (24), 240602-1-4.

108. Flury, M.; Qiu, H. X., Modeling colloid-facilitated contaminant transport in the vadose zone. *Vadose Zone J.* **2008,** *7*, (2), 682-697.

109. Harvey, R. W.; Garabedian, S. P., Use of Colloid Filtration Theory in Modeling Movement of Bacteria through a Contaminated Sandy Aquifer. *Environmental Science & Technology* **1991,** *25*, (1), 178-185.

110. Mason, T. G.; Weitz, D. A., Optical Measurements of Frequency-Dependent Linear Viscoelastic Moduli of Complex Fluids. *Physical Review Letters* **1995,** *74*, (7), 1250-1253.

111. Loxley, A.; Vincent, B., Preparation of poly(methylmethacrylate) microcapsules with liquid cores. *Journal of Colloid and Interface Science* **1998,** *208*, (1), 49-62.

112. Wassenius, H.; Callaghan, P. T., Nanoscale NMR velocimetry by means of slowly diffusing tracer particles. *J. Magn. Reson.* **2004,** *169*, (2), 250-256.

113. Grant, G. T.; Morris, E. R.; Rees, D. A.; Smith, P. J. C.; Thom, D., Biological Interactions between Polysaccharides and Divalent Cations - Egg-Box Model. *FEBS Lett.* **1973,** *32*, (1), 195-198.

114. Onuki, A.; Puri, S., Spinodal decomposition in gels. *Phys. Rev. E* **1999,** *59*, (2), R1331-R1334.

115. Maneval, J. E.; Bernin, D.; Fabich, H. T.; Seymour, J. D.; Codd, S. L., Magnetic resonance analysis of capillary formation reaction front dynamics in alginate gels. *Magn. Reson. Chem.* **2011,** *49*, (10), 627-640.

116. Tanner, J. E.; Stejskal, E. O., Restricted Self-Diffusion of Protons in Colloidal Systems by Pulsed-Gradient Spin-Echo Method. *J. Chem. Phys.* **1968,** *49*, (4), 1768-&.

117. Dong, W., Xie, Guibo, Miller, Todd R., Franklin, Mark P., Oxenberg, Tanya Palmateer, Bouwer, Edward J., Ball, William P., Halden, Rolf U., Sorption and bioreduction of hexavalent uranium at a military facility by the Chesapeake Bay. *Environmental Pollution* **2006,** *142*, 132-142.

118. Fang, Y. L.; Yabusaki, S. B.; Morrison, S. J.; Amonette, J. P.; Long, P. E., Multicomponent reactive transport modeling of uranium bioremediation field experiments. *Geochim. Cosmochim. Acta* **2009,** *73*, (20), 6029-6051.

119. Novikov, A. P.; Kalmykov, S. N.; Utsunomiya, S.; Ewing, R. C.; Horreard, F.; Merkulov, A.; Clark, S. B.; Tkachev, V. V.; Myasoedov, B. F., Colloid transport of plutonium in the far-field of the Mayak Production Association, Russia. *Science* **2006,** *314*, (5799), 638-641.

120. Abdelouas, A., Lu, Yongming, Lutze, W., Nuttall, H.E., Reduction of U(VI) to U(IV) by indigenous bacteria in contaminated ground water. *Journal of Contaminant Hydrology* **1998,** *35*, 217-233.

121. Neal, A. L.; Amonette, J. E.; Peyton, B. M.; Geesey, G. G., Uranium complexes formed at hematite surfaces colonized by sulfate-reducing bacteria. *Environmental Science & Technology* **2004,** *38*, (11), 3019-3027.

122. Sani, R. K.; Peyton, B. M.; Dohnalkova, A., Comparison of uranium(VI) removal by Shewanella oneidensis MR-1 in flow and batch reactors. *Water Res.* **2008,** *42*, (12), 2993-3002.

123. Suzuki, Y., Kelly, S. D., Kemner, K. M., Banfield, J. F., Nanometre-size products of uranium bioreduction. *Nature* **2002,** *419*, 134.

124. As, H. V.; Lens, P., Use of H-1 NMR to study transport processes in porous biosystems. *Journal of Industrial Microbiology & Biotechnology* **2001,** *26*, (1-2), 43-52.

125. Bartacek, J.; Vergeldt, F. J.; Gerkema, E.; Jenicek, P.; Lens, P. N. L.; Van As, H., Magnetic resonance microscopy of iron transport in methanogenic granules. *J. Magn. Reson.* **2009,** *200*, (2), 303-312.

126. Majors, P. D.; McLean, J. S.; Scholten, J. C. M., NMR bioreactor development for live in-situ microbial functional analysis. *J. Magn. Reson.* **2008,** *192*, (1), 159-166.

127. Nott, K. P.; Paterson-Beedle, M.; Macaskie, L. E.; Hall, L. D., Visualisation of metal deposition in biofilm reactors by three-dimensional magnetic resonance imaging (MRI). *Biotechnology Letters* **2001,** *23*, (21), 1749-1757.

128. Seymour, J. D.; Gage, J. P.; Codd, S. L.; Gerlach, R., Anomalous fluid transport in porous media induced by biofilm growth. *Physical Review Letters* **2004,** *93*, (19), 198103-1-4.

129. Seymour, J. D.; Gage, J. P.; Codd, S. L.; Gerlach, R., Magnetic resonance microscopy of biofouling induced scale dependent transport in porous media. *Adv. Water Resour.* **2007,** *30*, (6-7), 1408-1420.

130. von der Schulenburg, D. A. G.; Holland, D. J.; Paterson-Beedle, M.; Macaskie, L. E.; Gladden, L. F.; Johns, M. L., Spatially resolved quantification of metal ion concentration in a biofilm-mediated ion exchanger. *Biotechnol. Bioeng.* **2008,** *99*, (4), 821-829.

131. Seymour, J. D.; Codd, S. L.; Gjersing, E. L.; Stewart, P. S., Magnetic resonance microscopy of biofilm structure and impact on transport in a capillary bioreactor. *J. Magn. Reson.* **2004,** *167*, (2), 322-327.

132. Creber, S. A.; Pintelon, T. R. R.; Johns, M. L., Quantification of the velocity acceleration factor for colloidal transport in porous media using NMR. *Journal of Colloid and Interface Science* **2009,** *339*, (1), 168-174.

133. Brosten, T. R.; Fridjonsson, E. O.; Codd, S. L.; Seymour, J. D., NMR measurement of the transport dynamics of colloidal particles in an open cell polymer foam porous media. *Journal of Colloid and Interface Science* **2010,** *349*, (1), 384-391.

134. Ikushima, K.; Tsutsui, S.; Haga, Y.; Yasuoka, H.; Walstedt, R. E.; Masaki, N. M.; Nakamura, A.; Nasu, S.; Onuki, K., First-order phase transition in UO_2: U-235 and O-17 NMR study. *Phys. Rev. B* **2001,** *63*, (10), 104404-1-11.

135. Ulrich, K. U.; Singh, A.; Schofield, E. J.; Bargar, J. R.; Veeramani, H.; Sharp, J. O.; Bernier-Latmani, R.; Giammar, D. E., Dissolution of biogenic and synthetic UO_2 under varied reducing conditions. *Environmental Science & Technology* **2008,** *42*, (15), 5600-5606.

136. Lee, S. Y.; Baik, M. H.; Choi, J. W., Biogenic Formation and Growth of Uraninite (UO2). *Environmental Science & Technology* **2010,** *44*, (22), 8409-8414.

137. Nestle, N., Kimmich, R., Heavy metal uptake of alginate gels studied by NMR microscopy. *Colloids and Surfaces A: Physicochemical and Engineering Aspects* **1996,** *115*, 141-147.

138. Blume, M., Theory of First-Order Magnetic Phase Change in UO_2. *Physical Review* **1966,** *141*, (2), 517-524.

139. Beveridge, T. J.; Makin, S. A.; Kadurugamuwa, J. L.; Li, Z. S., Interactions between biofilms and the environment. *Fems Microbiol. Rev.* **1997,** *20*, (3-4), 291-303.

140. Stewart, P. S., Mini-review: Convection around biofilms. *Biofouling* **2012,** *28*, (2), 187-198.

141. Kim, D. S.; Fogler, H. S., Biomass evolution in porous media and its effects on permeability under starvation conditions. *Biotechnol. Bioeng.* **2000,** *69*, (1), 47-56.

142. Brinkman, H. C., A Calculation of the Viscous Force Exerted by a Flowing Fluid on a Dense Swarm of Particles. *Applied Scientific Research Section a-Mechanics Heat Chemical Engineering Mathematical Methods* **1947,** *1*, (1), 27-34.

143. Thullner, M.; Baveye, P., Computational pore network modeling of the influence of biofilm permeability on bioclogging in porous media. *Biotechnol. Bioeng.* **2008,** *99*, (6), 1337-1351.

144. Dupin, H. J.; Kitanidis, P. K.; McCarty, P. L., Pore-scale modeling of biological clogging due to aggregate expansion: A material mechanics approach. *Water Resour. Res.* **2001,** *37*, (12), 2965-2979.

145. McLean, J. S.; Majors, P. D.; Reardon, C. L.; Bilskis, C. L.; Reed, S. B.; Romine, M. F.; Fredrickson, J. K., Investigations of structure and metabolism within Shewanella oneidensis MR-1 biofilms. *Journal of Microbiological Methods* **2008,** *74*, (1), 47-56.

146. Manz, B.; Volke, F.; Goll, D.; Horn, H., Measuring local flow velocities and biofilm structure in biofilm systems with magnetic resonance imaging (MRI). *Biotechnol. Bioeng.* **2003,** *84*, (4), 424-432.

147. Renslow, R. S.; Majors, P. D.; McLean, J. S.; Fredrickson, J. K.; Ahmed, B.; Beyenal, H., In Situ Effective Diffusion Coefficient Profiles in Live Biofilms Using Pulsed-Field Gradient Nuclear Magnetic Resonance. *Biotechnol. Bioeng.* **2010,** *106*, (6), 928-937.

148. Hoskins, B. C.; Fevang, L.; Majors, P. D.; Sharma, M. M.; Georgiou, G., Selective imaging of biofilms in porous media by NMR relaxation. *J. Magn. Reson.* **1999,** *139*, (1), 67-73.

149. von der Schulenburg, D. A. G.; Vrouwenvelder, J. S.; Creber, S. A.; van Loosdrecht, M. C. M.; Johns, M. L., Nuclear magnetic resonance microscopy studies of membrane biofouling. *J. Membr. Sci.* **2008,** *323*, (1), 37-44.

150. Mitchell, J.; von der Schulenburg, D. A. G.; Holland, D. J.; Fordham, E. J.; Johns, M. L.; Gladden, L. F., Determining NMR flow propagator moments in porous rocks without the influence of relaxation. *J. Magn. Reson.* **2008,** *193*, (2), 218-225.

151. Washburn, K. E.; Callaghan, P. T., Propagator resolved transverse relaxation exchange spectroscopy. *J. Magn. Reson.* **2007,** *186*, (2), 337-340.

152. Windt, C. W.; Vergeldt, F. J.; Van As, H., Correlated displacement-T_2 MRI by means of a Pulsed Field Gradient-Multi Spin Echo method. *J. Magn. Reson.* **2007,** *185*, (2), 230-239.

153. Britton, M. M.; Graham, R. G.; Packer, K. J., NMR relaxation and pulsed field gradient study of alginate bead porous media. *J. Magn. Reson.* **2004,** *169*, (2), 203-214.

154. Homan, N. M.; Venne, B.; Van As, H., Flow characteristics and exchange in complex biological systems as observed by pulsed-field-gradient magnetic-resonance imaging. *Phys. Rev. E* **2010,** *82*, (2), 026310-1-9.

155. Callaghan, P. T.; Codd, S. L.; Seymour, J. D., Spatial coherence phenomena arising from translational spin motion in gradient spin echo experiments. *Concepts Magn. Resonance* **1999,** *11*, (4), 181-202.

156. Carver, J. P.; Richards, R. E., General 2-Site Solution for Chemical Exchange Produced Dependence of T_2 upon Carr-Purcell Pulse Separation. *J. Magn. Reson.* **1972,** *6*, (1), 89-105.

157. Lens, P.; Vergeldt, F.; Lettinga, G.; Van As, H., H-1 NMR characterisation of the diffusional properties of methanogenic granular sludge. *Water Sci. Technol.* **1999,** *39*, (7), 187-194.

158. Lens, P.; Pol, L. H.; Lettinga, G.; Van As, H., Use of H-1 NMR to study transport processes in sulfidogenic granular sludge. *Water Sci. Technol.* **1997,** *36*, (6-7), 157-163.

159. Picioreanu, C.; van Loosdrecht, M. C. M.; Heijnen, J. J., Two-dimensional model of biofilm detachment caused by internal stress from liquid flow. *Biotechnol. Bioeng.* **2001,** *72*, (2), 205-218.

160. Hills, B. P.; Cano, C.; Belton, P. S., Proton NMR Relaxation Studies of Aqueous Polysaccharide Systems. *Macromolecules* **1991,** *24*, (10), 2944-2950.

161. Langer, R. S.; Vacanti, J. P., Tissue engineering: The challenges ahead. *Sci.Am.* **1999,** *280*, (4), 86-89.

162. Cabodi, M.; Choi, N. W.; Gleghorn, J. P.; Lee, C. S. D.; Bonassar, L. J.; Stroock, A. D., A microfluidic biomaterial. *J. Am. Chem. Soc.* **2005,** *127*, (40), 13788-13789.

163. Franklin, M. J.; Nivens, D. E.; Weadge, J. T.; Howell, P. L., Biosynthesis of the Pseudomonas aeruginosa extracellular polysaccarides, alginate, Pel, and Psl. *Frontiers in Microbiology* **2011,** *2*, (167), 167-1-16.

164. Storz, H.; Muller, K. J.; Ehrhart, F.; Gomez, I.; Shirley, S. G.; Gessner, P.; Zimmermann, G.; Weyand, E.; Sukhorukov, V. L.; Forst, T.; Weber, M. M.; Zimmermann, H.; Kulicke, W. M.; Zimmermann, U., Physicochemical features of ultra-high viscosity alginates. *Carbohydr. Res.* **2009,** *344*, (8), 985-995.

165. Windhues, T.; Borchard, W., Effect of acetylation on physico-chemical properties of bacterial and algal alginates in physiological sodium chloride solutions investigated with light scattering techniques. *Carbohydr. Polym.* **2003,** *52*, (1), 47-52.

166. Schurks, N.; Wingender, J.; Flemming, H. C.; Mayer, C., Monomer composition and sequence of alginates from Pseudomonas aeruginosa. *Int. J. Biol. Macromol.* **2002,** *30*, (2), 105-111.

167. Donati, I.; Holtan, S.; Morch, Y. A.; Borgogna, M.; Dentini, M.; Skjak-Braek, G., New hypothesis on the role of alternating sequences in calcium-alginate gels. *Biomacromolecules* **2005,** *6*, (2), 1031-1040.

168. Degrassi, A.; Toffanin, R.; Paoletti, S.; Hall, L. D., A better understanding of the properties of alginate solutions and gels by quantitative magnetic resonance imaging (MRI). *Carbohydr. Res.* **1998,** *306*, (1-2), 19-26.

169. Skjakbraek, G.; Zanetti, F.; Paoletti, S., Effect of Acetylation on Some Solution and Gelling Properties of Alginates. *Carbohydr. Res.* **1989,** *185*, (1), 131-138.

170. Lyczak, J. B.; Cannon, C. L.; Pier, G. B., Establishment of Pseudomonas aeruginosa infection: lessons from a versatile opportunist. *Microbes Infect.* **2000,** *2*, (9), 1051-1060.

171. Pier, G. B.; Coleman, F.; Grout, M.; Franklin, M.; Ohman, D. E., Role of alginate O acetylation in resistance of mucoid Pseudomonas aeruginosa to opsonic phagocytosis. *Infect. Immun.* **2001,** *69*, (3), 1895-1901.

172. Shapiro, Y. E., Structure and dynamics of hydrogels and organogels: An NMR spectroscopy approach. *Prog. Polym. Sci.* **2011,** *36*, (9), 1184-1253.

173. Walderhaug, H.; Soderman, O.; Topgaard, D., Self-diffusion in polymer systems studied by magnetic field-gradient spin-echo NMR methods. *Prog. Nucl. Magn. Reson. Spectrosc.* **2010,** *56*, (4), 406-425.

174. Vogt, M.; Flemming, H. C.; Veeman, W. S., Diffusion in Pseudomonas aeruginosa biofilms: a pulsed field gradient NMR study. *Journal of Biotechnology* **2000,** *77*, (1), 137-146.

175. Qiao, Y.; Galvosas, P.; Adalsteinsson, T.; Schonhoff, M.; Callaghan, P. T., Diffusion exchange NMR spectroscopic study of dextran exchange through polyelectrolyte multilayer capsules. *J. Chem. Phys.* **2005,** *122*, (21), 214912-1-9.

176. Franklin, M. J.; Ohman, D. E., Identification of Algf in the Alginate Biosynthetic Gene-Cluster of Pseudomonas-Aeruginosa Which Is Required for Alginate Acetylation. *J. Bacteriol.* **1993,** *175*, (16), 5057-5065.

177. Turco, G. T. G.; Donati, I.; Grassi, M.; Marchioli, G.; Lapasin, R.; Paoletti, S., Mechanical Spectroscopy and Relaxometry on Alginate Hydrogels: A Comparative Analysis for Structural Characterization and Network Mesh Size Determination. *Biomacromolecules* **2011,** *12*, (4), 1272-1282.

178. Degennes, P. G.; Pincus, P.; Velasco, R. M.; Brochard, F., Remarks on Polyelectrolyte Conformation. *Journal De Physique* **1976,** *37*, (12), 1461-1473.

179. Rubinstein, M.; Dobrynin, A. V., Associations leading to formation of reversible networks and gels. *Curr. Opin. Colloid Interface Sci.* **1999,** *4*, (1), 83-87.

180. Dobrynin, A. V.; Colby, R. H.; Rubinstein, M., Scaling Theory of Polyelectrolyte Solutions. *Macromolecules* **1995,** *28*, (6), 1859-1871.

181. Dobrynin, A. V.; Rubinstein, M., Theory of polyelectrolytes in solutions and at surfaces. *Prog. Polym. Sci.* **2005,** *30*, (11), 1049-1118.

182. Doi, M., *Introduction to Polymer Physics*. Oxford University Press: Oxford, 1996.

183. Fuoss, R. M.; Katchalsky, A.; Lifson, S., The Potential of an Infinite Rod-like Molecule and the Distribution of the Counter Ions. *Proc. Natl. Acad. Sci. U. S. A.* **1951,** *37*, (9), 579-589.

184. Donati, I.; Paoletti, S., Material Properties of Alginates. In *Alginates: Biology and Applications*, Rehm, B., Ed. Microbiology Monographs, Springer-Verlag: Berlin Heidelberg, 2009; Vol. 13, pp 1-53.

185. Witten, T. A.; Pincus, P., Structure and Viscosity of Interpenetrating Polyelectrolyte Chains. *Europhys. Lett.* **1987,** *3*, (3), 315-320.

186. Braccini, I.; Grasso, R. P.; Perez, S., Conformational and configurational features of acidic polysaccharides and their interactions with calcium ions: a molecular modeling investigation. *Carbohydr. Res.* **1999,** *317*, (1-4), 119-130.

187. Manning, G. S., Limiting Laws and Counterion Condensation in Polyelectrolyte Solutions I. Colligative Properties. *J. Chem. Phys.* **1969,** *51*, (3), 924-933.

188. Draget, K. I., Homogeneous Alginate Gels: A Technical Approach. *Carbohydr. Polym.* **1991,** *14*, 159-178.

189. Funami, T.; Fang, Y. P.; Noda, S.; Ishihara, S.; Nakauma, M.; Draget, K. I.; Nishinari, K.; Phillips, G. O., Rheological properties of sodium alginate in an aqueous system during gelation in relation to supermolecular structures and Ca(2+) binding. *Food Hydrocolloids* **2009,** *23*, (7), 1746-1755.

190. Fang, Y. P.; Al-Assaf, S.; Phillips, G. O.; Nishinari, K.; Funami, T.; Williams, P. A.; Li, L. B., Multiple steps and critical behaviors of the binding of calcium to alginate. *J. Phys. Chem. B* **2007,** *111*, (10), 2456-2462.

191. Probstein, R. F., *Physicochemical Hydrodynamics: An Introduction*. Butterworth-Heinemann: Stoneham, MA, 1989.

192. Ellison, W. J.; Lamkaouchi, K.; Moreau, J. M., Water: A dielectric reference. *J. Mol. Liq.* **1996,** *68*, (2-3), 171-279.

193. Hills, B. P., The Proton-Exchange Cross-Relaxation Model of Water Relaxation in Biopolymer Systems. *Mol. Phys.* **1992,** *76*, (3), 489-508.

194. Gottwald, A.; Creamer, L. K.; Hubbard, P. L.; Callaghan, P. T., Diffusion, relaxation, and chemical exchange in casein gels: A nuclear magnetic resonance study. *J. Chem. Phys.* **2005,** *122*, (3), 034506-1-10.